Functional and Anatomical study of the Inferior Olive: From slice physiology to in vivo recordings

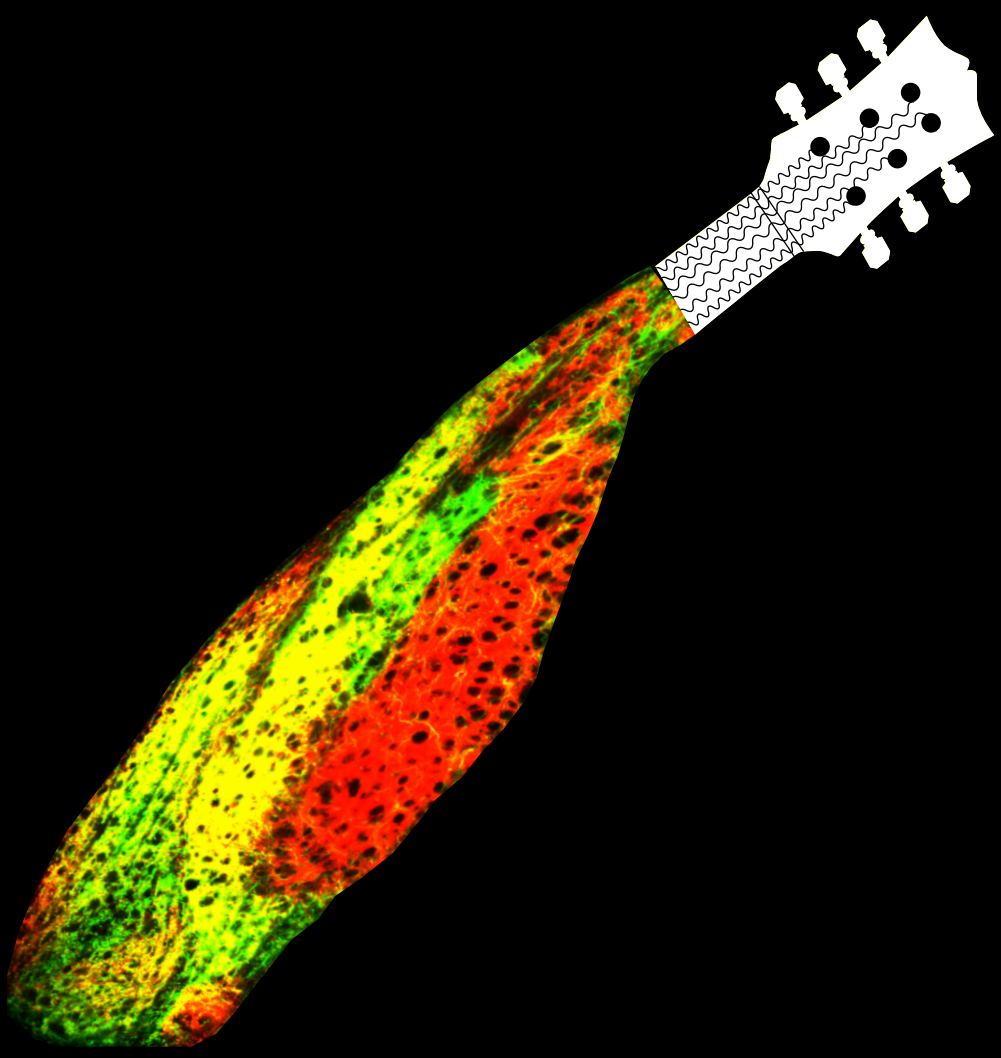

Sebastián Loyola Arroyo

Functional and Anatomical study of the Inferior Olive: From slice physiology to in vivo recordings

Sebastián Loyola Arroyo

Functional and anatomical study of the inferior olive:
From slice physiology to in vivo recordings

The author's work described herein was done at:

Netherlands Institute for Neuroscience (NIN), Amsterdam

&

Department of Neuroscience, Erasmus MC, Rotterdam

Cover art: "The inferior olive is like an ingenious guitar" by Sebastián Loyola. It was inspired by that statement which was said by my supervisor, Chris De Zeeuw, during a data discussion meeting. it was also inspired for the love I have for the guitar, the music, and the inferior olive.

Copyright © 2021 Sebastián Loyola Arroyo

All rights reserved. No part of this publication may be reproduced, stored in a retrieval system, or transmitted, in any form or by any means, electronic, mechanical, photocopying, recording, or otherwise, without permission of the author.

Printed by Gildeprint || www.gildeprint.nl

ISBN: 978-94-6419-126-4

Functional and Anatomical study of the Inferior Olive: From slice physiology to in vivo recordings

Functionele en anatomische studie van de onderste olijf:
Van in vitro fysiologie tot in vivo opnames

Thesis

to obtain the degree of Doctor from the
Erasmus University Rotterdam
by command of the
Rector Magnificus

Prof. dr. F.A. van der Duijn Schouten,

and in accordance with the decision of the Doctorate board.

The public defence shall be held on

March 23rd, 2021 at 13:00 hrs

by

Sebastián Loyola Arroyo

born in Santiago, Chile

Erasmus University Rotterdam

Doctoral committee

Promotor:	Prof.dr. C.I. de Zeeuw
Other members:	Dr. T.J.H. Ruigrok Prof. dr. Y. Yarom Dr. P. Isope
Copromotor:	Dr. T.M. Hoogland

For all the people who care about me and for the ones who care about our old and well conserved friend across evolution, the inferior olive….

Table of contents

1 General Introduction…… 1

1.1 Abstract…… 2

1.2 Development of the inferior olive and climbing fibers

1.2.1 The origin of inferior olivary neurons…… 3

1.2.2 Migration of inferior olivary neurons……6

1.2.3 Inferior olivary subdivisions and cell types……7

1.2.4 Climbing fiber outgrowth and elimination…….....8

1.3 Ultrastructure of the inferior olivary neuropil

1.3.1 Glomeruli and gap junctions……..…….. 12

1.3.2 Inputs and origin……...15

1.3.3 Neurotransmitters and receptors……...16

1.4 Cell physiology of inferior olivary neurons

1.4.1 Subthreshold oscillations and spike Timing……18

1.4.2 Electrical synapses in the inferior Olive……20

1.4.3 Synaptic modification of oscillations and coupling…… 21

1.4.4 Action potential waveforms……24

1.5 Models of the olivary Neurons

1.5.1 Single-cell models……25

1.5.2 Network models……27

1.6 Climbing fibers patterns and behavioral consequences

1.6.1 Spatiotemporal patterms……28

1.6.2 Behavioral consequences…….....30

1.7 Functional models of the olivocerebellar system

1.7.1 Marr-Albus-Ito learning models……..34

1.7.2 Motor timing models……37

1.8 Pathology of the inferior olive……39

1.9 Inferior olive and sleep…… 40

1.10 Conclusions……42

1.11 Scope of the thesis……42

1.13 References……43

2 Variability and directionality of inferior olive neuron dendrites revealed by detailed 3D characterization of an extensive morphological library

Abstract…… 74
Introduction……..75
Materials and methods……..76
Results…… 81
Discussion……94
References……..100
Supplementary figures…… 105

3 Impact of temporal interplay of excitatory and inhibitory inputs on sub- and suprathreshold activity of inferior olivary neurons and motor learning

Abstract ……..108
Introduction……109
Results
Physiological properties of IO neurons……...111
Impact of subthreshold CN input on IO neurons…….. 113
Impact of suprathreshold CN input on IO neurons……...116
Impact of subthreshold MDJ input on IO neurons……118
Impact of suprathreshold MDJ input on IO neurons…….122
Interaction of CN and MDJ inputs and their impact on IO neurons……124
Interaction of CN and MDJ inputs and their impact on motor learning……..126
Discussion……..129
References……134
Supplementary figures…… 138
Supplementary tables……...147
Appendix……153
Materials and Methods……153

4 Sleep stage dependent modularion of complex spike activity ensemble activity

Abstract……...160
Introduction……161
Results…… 162

Discussion……...170
Materials and methods……..175
References…… 178

5 General Discussion

5.1 A morphological map of IO neuron morphology
5.1.1 IO dendritic morphology…… 185
5.1.2 Anamotical clustering of IO neurons……... 185
5.2 The role of cerebellar nuclei and midbrain afferents in shaping the STOs and output of IO neurons
5.2.1 Impact of CN and MDJ afferents on conditional oscillators……..186
5.2.2 Impact of CN and MDJ afferents on oscillating neurons……...187
5.2.3 Temporal interactions of CN and MDJ afferents and their impact on STOs and output …… 189
5.2.4 Temporal interactions of CN and MDJ afferents and their impact on motor learning……190
5.3 Modulation of complex spike activity during sleep……...191
5.4 Future perspectives…….. 194
5.5 References…… 195

Summary …… 201

Samenvatting…… 203

Curriculum Vitae……205

Acknowledgments……211

Chapter 1

General Introduction

This chapter is the thoroughly revised and updated second edition of the book chapter:

Inferior Olive: All Ins and Outs. Handbook of the Cerebellum and Cerebellar disorders. Springer, Cham.

Authors of the first edition: De Gruijl JR, Bosman LWJ, De Zeeuw CI, De Jeu MTG

Year of publication of the first edition of the book chapter: 2013
Year of publication of the second edition of the book chapter: 2019

Sebastián Loyola, Laurens Bosman, Jornt De Gruijl, Marcel De Jeu, Mario Negrello, Tycho Hoogland, Chris De Zeeuw

1.1 Abstract

The inferior (IO) is a structure located in the ventrolateral part of the brainstem that plays a fundamental role in motor learning and motor coordination by providing one of the two major excitatory inputs to the cerebellar cortex: the climbing fibers. These climbing fibers elicit an all or none response in Purkinje cells named the “complex spike”. In addition, the olivary axons provide collaterals to the cerebellar nuclei, further modulating the cerebellar output.

IO neurons have several distinguishing features one of them is exhibiting complex dendritic arbor morphologies with particular spatial orientations. Another striking feature is the presence of dendro-dendritic gap junctions in which electrotonically coupled dendritic spines receive both excitatory and inhibitory inputs. Due to this unique synaptic arrangement of the glomerulus, which forms the core of the hallmark of the olivary neuropil (De Zeeuw, 1990), temporal interaction of both inputs would have a big impact on synaptic integration and spatiotemporal activity patterns (Segev and Parnas, 1983; De Zeeuw et al., 1995). Furthermore, IO neurons also show subthreshold oscillations (STOs) that may well play an important role in motor learning and motor coordination by controlling spike timing (Van der Giessen et al., 2008; Yarden-Rabinowitz and Yarom, 2019). Due the low spike frequency of individual IO neurons (~1Hz), coordination of complex behaviors, such as eating, grooming or digging, is mediated by ensembles of IO neurons that generate dynamic spatiotemporal patterns of complex spikes in the cerebellar cortex (Welsh et al., 1995).

Despite the multiple studies focused on olivary function, there is little knowledge about the morphology of IO neurons and the anatomical organization of their inputs. Likewise, the impact of the temporal interaction of excitatory and inhibitory inputs on STOs, spike output and motor learning remains to be elucidated. In this thesis I will address those topics using in vitro and in vivo techniques that will allow us to have a better understanding of this structure. Furthermore, I will provide new insights in the engagement of olivo-cerebellar activity during sleep.

1.2 Development of the inferior olive and climbing fibers

1.2.1 The origin of Inferior olivary neurons

Neurons of the inferior olive (IO) arise from the neural tube in the embryonic hindbrain and migrate subsequently to the ventral site of the brainstem. During embryonic development, the neural tube becomes increasingly partitioned, with each partition giving rise to a specific part of the developing brain (Fig. 1a). Such partitioning is under strict genetic control. The segregation of the hindbrain from the midbrain is largely controlled by two homeodomain transcription factors: Otx2 and Gbx2. Initially, the expression domains of Otx2 and Gbx2 overlap (Fig. 1b1), but (in mice) around embryonic day 7.5 (E7.5), Otx2 becomes restricted to the forebrain and midbrain and Gbx2 to the hindbrain (Fig. 1b2) (Joyner et al., 2000; Rubenstein et al., 1994; Simeone et al., 1992). Otx2 and Gbx2 act antagonistically. While Otx2 inhibits formation of the hindbrain, thus allowing the midbrain to be formed, Gbx2 inhibits formation of the rostral brain, permitting the hindbrain to develop (Acampora et al., 1995; Hidalgo-Sánchez et al., 1999, 2005; Kikuta et al., 2003; Millet et al., 1996, 1999; Sakurai et al., 2010; Wassarman et al., 1997). At the border of the Otx2 and Gbx2 expression domains, the isthmic organizer develops (Fig. 1b3) (Broccoli et al., 1999; Joyner et al., 2000; Leto et al., 2016; Martinez et al., 2013; Simeone, 2000).

Around E8, the hindbrain becomes segmented into eight compartments, the rhombomeres (Lumsden and Krumlauf, 1996; Osumi-Yamashita et al., 1996; Vaage, 1969). Due to an alternating expression pattern of Eph receptors and their membrane-bound ephrin ligands, which exert a repelling effect, cell migration between rhombomeres is no longer possible (Fig. 1b4) (Becker et al., 1994; Bergemann et al., 1995; Dahmann et al., 2011; Egea and Klein, 2007; Kania and Klein, 2016; Kemp et al., 2009; Lumsden and Krumlauf, 1996). This compartmentalization of the neural tube allows region-specific differentiation (Fraser et al., 1990). The anterior rhombomere, r1, will develop into the cerebellum (Altman and Bayer, 1978a; Larsell, 1947; Leto et al., 2016; ten Donkelaar and Lammens, 2009; Zervas et al., 2004). The caudal rhombomeres (r2–r8) give rise to the neurons of the hindbrain nuclei, including the IO (Altman and Bayer 1978b; Ray and Dymecki, 2009).

The fate of the individual rhombomeres is largely determined by the specific sets of Hox genes expressed. A complex signaling cascade leads to the correct spatial pattern of Hox gene expression. Already during the formation of the rhombomeres, the first Hox genes are expressed. Retinoic acid, which is formed in the mesoderm of the trunk and underlies a concentration gradient decreasing in the rostral direction, induces the expression of among others Hoxa1 and Hoxb1

(Fig. 1b4) (Alexander et al., 2009; Carpenter et al., 1993; Cunningham and Duester, 2015; Mark et al., 1993; Rossel and Capecchi, 1999; Shimozono et al., 2013; Studer et al., 1998).

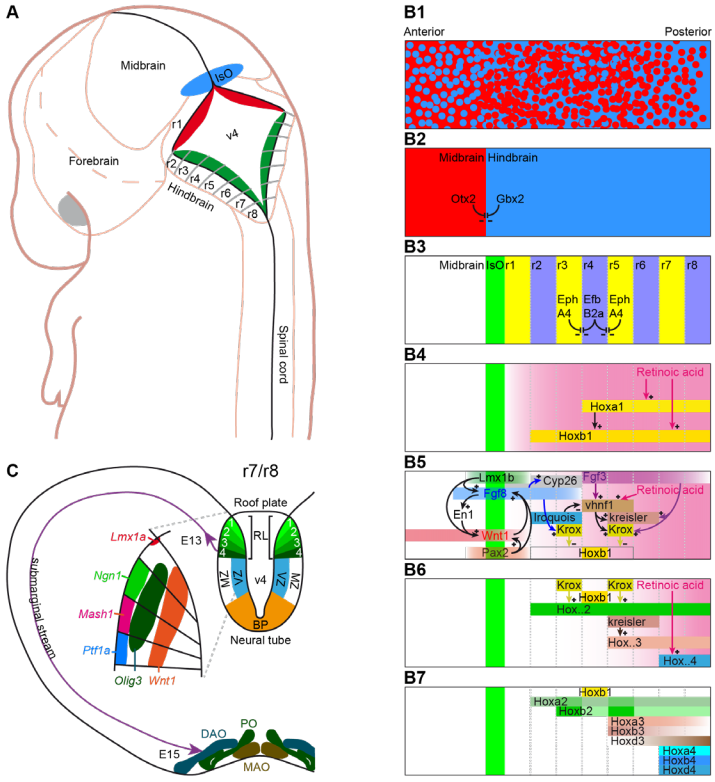

Fig. 1 Development of the inferior olivary neurons. A – The neural tube of the hindbrain is transiently divided into eight segments (“rhombomeres”) (r1–r8). The neural tube does not close completely over the fourth ventricle (v4). The border of the neural tube lining the fourth ventricle is called the “rhombic lip” (red and green zones). The neurons of the IO originate from the rhombic lip in r7 and r8. At the border between the hindbrain and the midbrain, the isthmic organizer (IsO) develops. B1 – During early development, the expression domains of the homeodomain transcription factors Otx2 (red) and Gbx2 (blue) overlap. B2 – Later on they become segregated, and Otx2 and Gbx2 have a mutually repulsive action. B3 – The hindbrain transiently forms eight rhombomeres. Cell migration between the rhombomeres is prevented by the alternated expression pattern of membrane-bound ephrins (EphA4) and their receptors (EfbB2a). The combination of EphA4 and EfbB2a has a repulsive action, preventing mixture of neuronal progenitor cells from different rhombomeres. B4 – Retinoic acid is formed in the trunk and diffuses into the hindbrain. It stimulates directly the expression of the early Hox genes Hoxa1 and Hoxb1. Due to the higher retinoic acid concentration in the posterior hindbrain, the expression domains of Hoxa1 and Hoxb1 are predominantly posterior. B5 – Interactions of fibroblast growth factors, released by the IsO, and the posterior rhombomeres and of retinoic acid, released by the trunk, with several transcription factors create an anteroposterior pattern, which serves as a template (B6) to induce the late Hox genes. B7 – Ultimately, a nested pattern of Hox genes is established. Concentration gradients are indicated by different color intensities: the darker, the higher the concentration. Altogether, each rhombomere has now a unique set of Hox genes, with the borders between the rhombomeres serving as anterior borders of the expression domains. C – Schematic drawing of a coronal transection of the embryonic hindbrain at the level of the posterior hindbrain (r7/r8). The neural tube is composed of two plates: the basal plate (BP) and the alar plate. The alar plate, in turn, is composed of the mantle zone (MZ), the ventricular zone (VZ), and the rhombic lip (RL). Following the expression pattern of several basic helix-loop-helix transcription factors, the rhombic lip can be subdivided into four compartments along the dorsoventral axis (inset). Upon completion of mitosis, the IO neurons start to migrate around E13 (in rat) from their site of origin (r7/r8, compartment 4 of the rhombic lip) to the site of the IO. The first neurons that complete the migration along the submarginal stream reach the IO at E15. Around E18, migration is complete, and the three main compartments of the IO can be recognized: the DAO (dorsal accessory olive), the PO (principal olive), and the MAO (medial accessory olive).

Next, the isthmic organizer starts, stimulated by the homeodomain transcription factors Lmx1b and Pax2, to secrete the signaling proteins Wnt1 and Fgf8 (Adams et al., 2000; Guo et al., 2007; Ye et al., 2001). Wnt1 and Fgf8 stimulate, directly or via En1, each other's expression (Fig. 1b5) (Chi et al., 2003; Ciani and Salinas, 2005; Lee et al., 1997; Ye et al., 2001). Wnt1 and Fgf8 stimulate, directly or via En1, each other's expression (Fig. 1b5) (Chi et al., 2003; Ciani and Salinas 2005; Lee et al., 1997; Ye et al., 2001). Wnt1 promotes the development of the midbrain and the cerebellum (Amoyel et al., 2005; Ciani and Salinas, 2005; Klaus and Birchmeier, 2008; Mastick et al., 1996; Mcmahon and Bradley, 1990). It is also secreted by the rhombomere borders, where it contributes to neurogenesis in the hindbrain (Amoyel et al., 2005). Fgf8 is also transiently produced by r4 (Maves et al., 2002; Walshe et al., 2002). In addition, Fgf3 is secreted, first by r4, and later also by the more posterior rhombomeres (Mahmood et al., 1996; Maves et al., 2002; Walshe et al., 2002). Fgf and retinoic acid together activate vhnf1 (Hernandez et al., 2004). The expression domain of vhnf1 is anteriorly limited by the suppressive action of Iroquois (Lecaudey et al., 2004). vhnf1 promotes, together with the Fgf's, the expression of Krox20 and kreisler (Aragón et al., 2005; Kim et al., 2005; Marin and Charnay, 2000; Sun and Hopkins, 2001; Wiellette and Sive, 2003). Krox20 is exclusively expressed in r3 and r5 (Oxtoby and Jowett, 1993) and kreisler in r5 and r6 (Frohman et al., 1993). In addition, Fgf8 stimulates the degradation of retinoic acid in the more anterior rhombomeres by Cyp26 enzymes (Dueste,r 2007; White and Schilling, 2008). This has implications for the expression pattern of Hoxb1. While it is no longer induced by retinoic acid in the anterior rhombomeres, it is also suppressed by Krox20 in r3 and r5 (Garcia-Dominguez et al., 2006), limiting Hoxb1 expression to r4 (Fig. 1b5) (Wilkinson et al., 1989).

Taken together, there is now a spatial framework which imposes the nested expression pattern of Hox genes (Fig. 1b6). Hoxb1 remains restricted to r4 (Wilkinson et al., 1989). Hoxa2 spans the largest area, r2–r8, but is enriched in r3 and r5 due to the positive action of Krox20 (Nonchev et al. 1996; Sham et al. 1993). Under the influence of kreisler, Hoxa3, Hoxb3, and Hoxc3 are expressed from r5 onward (Manzanares et al., 1997, 1999). The neurons of the IO are generated in r7 and r8 (Ambrosiani et al. 1996; Yamada et al. 2007). These rhombomeres express Hoxa4, Hoxb4, and Hoxd4 under the influence of retinoic acid (Fig. 1b7) (Alexander et al., 2009; Packer et al., 1998). Either a deficiency or an excess of retinoic acid, a vitamin A derivative, leads to a malformed IO (Yamamoto et al., 2005). Once the Hox genes are activated, they can sustain their expression by auto- and cross-regulation (Alexander et al., 2009; Tümpel et al., 2009). Thus, there are complicated, often mutual, interactions between rhombomere-specific transcription factors and signaling molecules that impose a nested expression of Hox genes along the anteroposterior axis of the developing hindbrain, determining the fate of each rhombomere.

In addition to the anteroposterior patterning, partitioning also occurs along the dorsoventral axis of the neural tube. The dorsoventral patterning is largely imposed by two antagonistic gradients, including sonic hedgehog (SHH) secreted by the floor plate and Wnt and bone morphogenetic proteins (BMPs) by the root plate (Hernandez-Miranda et al., 2017; Ulloa and Martí, 2010). The dorsal part of the neural tube, the “alar plate,” is composed of an outer layer, the “mantle zone,” and an inner layer, the “ventricular zone.” The dorsal part of the alar plate, thus the part forming the borders of the fourth ventricle, is referred to as the “rhombic lip” (Essick, 1912; His, 1891; Ray and Dymecki, 2009). The rhombic lip extends over the whole hindbrain, spanning the eight rhombomeres, and is therefore also affected by the rhombomere-specific expression of Hox genes. Next to the Hox genes, several other transcription factors are expressed in the alar plate of the hindbrain neural tube. The whole rhombic lip is characterized by the expression of Wnt1, while several other transcription factors occur in restricted areas along the dorsoventral axis (Landsberg et al., 2005; Ray and Dymecki, 2009). The homeodomain transcription factor Lmx1a is found only in the dorsal layer (dA1) (Chizhikov et al., 2010; Landsberg et al., 2005). Ventral to the Lmx1a expression area are those of the basic helix-loop-helix (bHLH) transcription factors Math1, Ngn1, and Ptf1a, respectively (Landsberg et al., 2005; Liu et al., 2008; Ray and Dymecki, 2009; Wang et al., 2005). The expression domain of the bHLH transcription factor Olig3 overlaps with those of Math1, Ngn1, and Pft1a (Storm et al., 2009; Takebayashi et al., 2002). The neurons of the IO develop in the Ptf1a-expressing region dA4 (Hernandez-Miranda et al., 2017; Iskusnykh et al., 2016; Storm et al., 2009; Yamada et al., 2007). Ptf1a expression is required for the formation of IO neurons, probably by the induction of the direct downstream targets Nephrin and Neph3 (Iskusnykh et al., 2016; Nishida et al., 2010; Yamada et al., 2007). During formation of the IO neurons, Ptf1a and Olig3 act synergistically. Deletion of one of these bHLH transcription factors prevents the formation of the IO (Storm et al., 2009). This complicated network of gene expression ultimately leads to the generation of IO neurons in dA4 of r7 and r8.

1.2.2 Migration of Inferior olivary neurons

IO neurons are the first neurons that originate from the rhombic lip. In rats, they are formed at embryonic day 12 (E12) and E13 (Altman and Bayer, 1978b; Bourrat and Sotelo, 1988). After their last mitosis, the newly formed neurons start to migrate tangentially to their destinations (Altman and Bayer, 1978b; Bourrat and Sotelo, 1988). This migration occurs via well-defined streams. While the streams leading to the other precerebellar nuclei at some point cross the

midline, the so-called submarginal strand that leads to the site of the IO does not (Fig. 1c) (Altman and Bayer, 1978b; Bourrat and Sotelo, 1988; Ellenberger et al., 1969; Harkmark, 1954; Sotelo and Chédotal ,2005).

Neuronal migration is under tight control of tissue-dependent cues. The actual effects of these chemotactic molecules, being either chemo-attractive or chemorepellant, depend on the specific receptors of the migrating neurons. Multiple mechanisms are at stake. Netrin-1, secreted by the floor plate, attracts the migrating IO neurons (Bloch-Gallego et al., 1999; Marcos et al., 2009; Sotelo and Chédotal 2005; Yee et al., 1999). Once the IO neurons reach their destination between E15 and E19 (Altman and Bayer,1978b; Bourrat and Sotelo, 1988; Ellenberger et al., 1969), further migration of their somata across the midline is prevented by repulsive action of Slit and Robo as well as of EphA4 and EphrinB3 (Fig. 3a) (Di Meglio et al., 2008; Ypsilanti et al., 2010). Upon arrival at the IO primordium, between E15 and E18, the somata become more rounded, and the dendritic trees develop (Bourrat and Sotelo, 1988).

1.2.2 Inferior olivary subdivisions and cell types

When the first neurons arrive at the site of the IO, no subdivisions can be recognized yet in the IO primordium (Bourrat and Sotelo, 1988). The medial accessory olive (MAO) is the first part of the IO to develop (Bourrat and Sotelo, 1988). Gradually, also the other two main divisions, the principal olive (PO) and dorsal accessory olive (DAO) become clearly discernible, and by E19 (in rats), upon completion of the migration, the IO has reached its adult shape (Altman and Bayer, 1987; Bourrat and Sotelo, 1988).

Both the PO and DAO are composed of two parts: a dorsal and a ventral leaf. The MAO can be subdivided into a rostral and a caudal halve. At its caudal margin, the MAO has three cell groups, termed “a,” “b,” and “c” (Bowman and Sladek, 1973; Gwyn et al., 1977; Martin et al., 1975). Next to the three main subdivisions, there are also a few minor subnuclei: the dorsal cap of Kooy (DCK), the ß nucleus, the ventrolateral outgrowth (VLO), and the dorsomedial cell column (DMCC). The basic organization of the IO is similar in all mammals, although the relative size of the nuclei differs across species (Bowman and , 1973; Kooy, 1917). In porpoises the MAO is dominant, whereas in primates the PO is highly expanded and gyrated (Cozzi et al., 2016; Glickstein et al., 2007). Elephants also have an expanded PO, but lack the gyrations seen in the human IO (Cozzi et al., 2016). It is likely that such differences in olivary organization reflect the behavioral repertoire dictated by the animal’s ecological niche and specialized sensory systems.

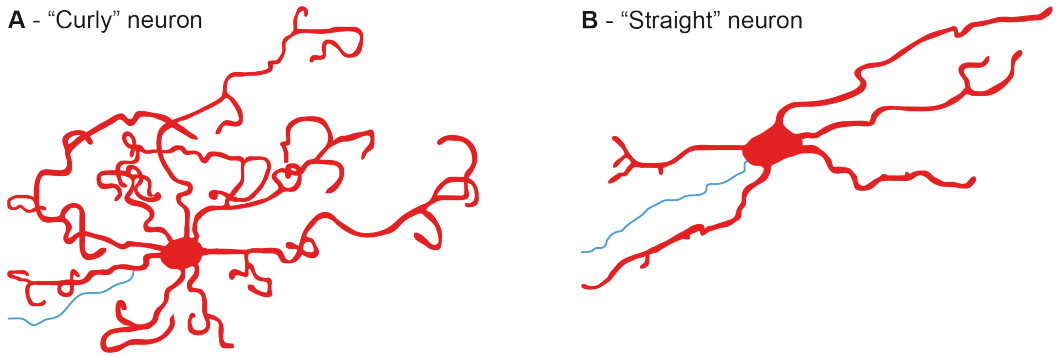

Fig. 2 Morphology of inferior olivary neurons. A – Schematic drawing of a “curly” neuron. The axon (blue) usually branches of from a first-order dendrite. B – Schematic drawing of a “straight” neuron. The axon originates at the soma.

The cellular composition of the IO is homogeneous with the majority of cells being glutamatergic. GABAergic interneurons may account for less than 0.1% of all neurons in the IO (Nelson and Mugnaini, 1988; Walberg and Ottersen, 1989). IO neurons have been classified according to their dendritic morphology as being “straight” and “curly” (Fig. 2) (De Zeeuw et al., 1990b; Devor and Yarom, 2002a; Foster and Peterson, 1986; Ruigrok et al., 1990; Scheibel and Scheibel, 1955). Furthermore, some studies have suggested that neurons in the intermediary and caudal MAO have straighter dendritic morphologies, while cells with more curly morphologies are found predominantly in other regions of the IO (Foster and Peterson,1986; Ruigrok et al., 1990). A typical IO neuron has a spherical soma with a diameter of about 15–30 µm and highly branched dendrites, curling back toward the soma, at times creating spirals (Foster and Peterson, 1986; Ruigrok et al., 1990; Scheibel and Scheibel, 1955). The axon of the “curly” neurons branches frequently off from a first-order dendrite (Ruigrok et al., 1990). Since the dendrites of “straight” neurons tend to grow away from the soma, their axons usually start directly at the soma (Fig. 2) (Ruigrok et al., 1990). Due to the subjective estimations used in these studies, it is important to have a more quantitative and robust approach in order to obtain a better objective classification of IO neurons based on their dendritic morphologies.

1.2.3 Climbing fiber outgrowth and elimination

In contrast to most of the somata (De Zeeuw et al., 1996), inferior olivary axons cross the midline, reaching out for the contralateral cerebellum. Axon growth starts before reaching the IO primordium, and midline crossing occurs around E15 (Bourrat and Sotelo, 1988) under control of Robo3 and its Slit receptor (Badura et al., 2013; Marillat et al., 2004; Renier et al., 2010). Around E18 the olivocerebellar fibers reach the caudal part of the cerebellar plate (Chédotal and Sotelo,

1992; Morara et al., 2001; Wassef et al., 1992). After passing through the brainstem, some axon collaterals innervate the cerebellar nuclei and some axons provide terminal branches in the cerebellar cortex (in addition to their climbing fiber terminals) (Fig. 3a) (Ruigrok and Voogd, 2000; Sugihara et al., 1999; Van der Want et al., 1989; Wiklund et al., 1984; Voogd et al., 2003). There is some evidence for the existence of direct synapses of olivary axons onto stellate cells (Scheibel and Scheibel, 1954; Sugihara et al., 1999), but this is contradicted by an electron-microscopic study (Hámori and Szentágothai, 1980). Nevertheless, stellate cells do respond to activity of olivocerebellar axons (Ohtsuki et al., 2004), possibly in response to glutamate spillover (Szapiro and Barbour, 2007). In addition, there is anatomical evidence for the formation of synapses onto Golgi cells (Chan-Palay and Palay, 1971; Hámori and Szentágothai, 1966; Sugihara et al., 1999), but electrophysiological studies showed inhibition, rather than excitation, of Golgi cells by olivocerebellar axons (Schulman and Bloom, 1981; Xu and Edgley, 2008).

The immature climbing fibers creep between the multilayered Purkinje cells (“creeper stage”) (Chédotal and Sotelo, 1993; Morara et al., 2001; Sugihara, 2005), establishing the first functional synaptic contacts with the postsynaptic Purkinje cells around postnatal day 3 (P3) in rats (Altman, 1972; Crepel, 1971; Woodward et al., 1971). The number of presynaptic climbing fibers increases to on average five per Purkinje cell at P5 (Fig. 3b) (Crepel et al., 1981; Mariani and Changeux, 1981).

These early climbing fiber synapses are formed at the somata or at the small dendritic protrusions of Purkinje cells (Altman, 1972; Hashimoto et al., 2009a; Mason et al., 1990; Morara et al., 2001). Around P7, some of the climbing fibers start to form nest-like structures around the somata (Fig. 3b) (Altman, 1972; Hashimoto et al., 2009a; Mason et al., 1990; O’Leary et al., 1971; Ramón y Cajal, 1911; Sugihara, 2005). Of about 100 “creeper” climbing fibers per IO axon, only about 10 form nest-like structures (Sugihara, 2005; Sugihara, 2006).

Simultaneously, the premature dendritic protrusions disappear, and the apical dendrite, which is so characteristic of the adult Purkinje cells, starts to grow (Altman, 1972; Bosman et al., 2008; Hashimoto et al., 2009a; Mason et al., 1990; McKay and Turner, 2005). The first climbing fibers start to expand their innervation area to the proximal part of the nascent dendritic tree (Hashimoto et al., 2009a; Scelfo et al., 2003). It is possible that more than one climbing fiber translocates to the dendritic tree, but in most instances, the “largest” (or “winner”) climbing fiber rapidly increases in size and synaptic strength, whereas the other climbing fibers become atrophic and degenerate (Bosman and Konnerth, 2009; Bosman et al., 2008; Hashimoto et al., 2009a; Hashimoto and Kano 2005; Scelfo et al., 2003; Sugihara, 2005, 2006). Around P15, perisomatic nests are no longer observed, although a few somatic release sites may persist until P20 (Fig. 3b) (Hashimoto

et al., 2009a). By P20, the large majority of Purkinje cells is innervated by a single climbing fiber only, with numerous release sites all over the thick branches of the Purkinje cell dendritic tree (Hashimoto and Kano, 2003; Ramón y Cajal, 1911). A single, mature olivocerebellar axon gives rise to, on average, six to seven climbing fibers. These climbing fibers are strictly organized in a single, parasagittal plane spanning multiple lobules (Sugihara et al., 2001).

Selective elimination of redundant synaptic contacts, in combination with strengthening of those that survive, is a common theme in neuronal development (Bleckert and Wong, 2011; Katz and Shatz, 1996; Purves and Lichtman, 1980). The developmental elimination of redundant climbing fiber synapses probably depends on a combination of a genetic blueprint and activity-dependent synaptic competition (Bosman and Konnerth, 2009; Kano and Hashimoto, 2009). At P7, when the first climbing fiber synapses translocate to the Purkinje cell dendritic tree (Hashimoto et al., 2009a; Sugihara, 2005), also the first parallel fiber synapses are formed (Scelfo and Strata, 2005). These early parallel fiber synapses are located at the thick branches of the Purkinje cell dendritic tree (Altman, 1972). Thus, at the onset of the second postnatal week, both the climbing fibers and the parallel fibers project to the same dendritic compartment.

A process of heterosynaptic axonal competition ensues between the parallel fibers and the climbing fibers (Hashimoto et al., 2009b). During normal development, the climbing fiber establishes contact sites all over the proximal, thick, and smooth branches of the dendritic tree, while the parallel fiber synapses translocate to the distal, spiny branches (Altman, 1972; Robain et al., 1981). When, following experimental manipulation, functional parallel fibers do not develop, or develop only partially, the climbing fiber territory is expanded to the distal spiny branches, which are normally the exclusive domain of the parallel fiber synapses (Altman and Anderson 1972; Crepel 1982; Hashimoto et al., 2001; Hirai et al., 2005; Ichikawa et al., 2002; Watanabe, 2008). The reverse is also true: when climbing fibers do not develop normally, parallel fiber synapses persist abnormally also on the thick smooth branches (Miyazaki et al., 2004). The adult situation, with the climbing fiber synapses on the thick branches and the parallel fibers on the thin branches, seems to be a dynamic equilibrium. Weakening of one of the two afferent systems leads to an increased innervation by the other, even in adults (Cesa et al., 2005, 2007; Kakizawa et al.,, 2005; Miyazaki et al. 2010; Sotelo et al., 1975).

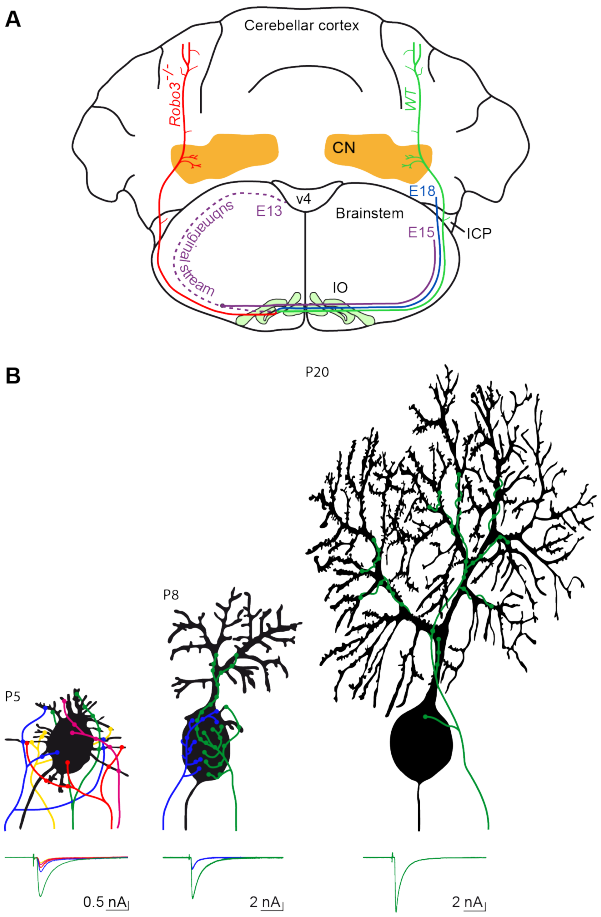

Fig. 3 Development of the olivocerebellar axons. A – Schematic drawing of a coronal slice of a mature rat. As shown in Fig. 1c, the IO neurons migrate from the rhombic lip, bordering the fourth ventricle (v4) along the submarginal stream to the IO primordium. Before they reach the IO, the migrating neurons start to grow axons that pass the midline and a part of the contralateral brainstem at E15 (in rats). Around E18, the first olivocerebellar axons reach the cerebellar anlage. Please note that at that developmental stage, the cerebellum is much less developed as on the schematic drawing shown here. A few days later, the first contacts with the cerebellar Purkinje cells are formed. On its way to the Purkinje cells, olivocerebellar axons form collaterals at the level of the inferior cerebellar peduncle (ICP), the cerebellar nuclei (CN), the cerebellar white matter, and the cerebellar granule layer. In the absence of Robo3, olivocerebellar axons do not cross the midline, but form ipsilateral connections. B – The thick ramifications of the olivocerebellar axons are the climbing fibers that innervate Purkinje cells. At P5 (in rats), each postsynaptic Purkinje cell is innervated by several, on average five, climbing fibers, originating from different olivocerebellar axons. The synapses are formed at the perisomatic protrusions and on the soma. This is called the "creeper" stage. The Purkinje cells still lack their apical dendrite. The synaptic strength of these "creeper" climbing fiber synapses are approximately equal, as shown by their EPSCs (bottom). Later on, the perisomatic protrusions disappear, and the apical dendrite starts to grow. Some of the climbing fibers are already lost, and the remaining ones form nests ("nest stage") around the soma. They may even start to translocate to the nascent dendritic tree. The synaptic strength of the presynaptic climbing fibers is no longer equal (note the different y-scale). Around P20, the adult situation has almost been reached. There is only one, surviving climbing fiber, making hundreds of contact sites with the thick branches of the Purkinje cell. The last somatic contact site is lost around this day. Horizontal scale bar: 20 ms.

Other forms of axonal competition also exist, such as between climbing fibers impinging on the same immature Purkinje cells (Bosman and Konnerth 2009; Bosman et al. 2008; Ohtsuki and Hirano 2008). Voltage-gated Ca^{2+} channels are primarily found at the growing apical dendrite (Llano et al. 1994; Llinás et al. 1989) to which the climbing fibers translocate (Hashimoto et al. 2009a; Sugihara 2005). As postsynaptic Ca^{2+} is required for normal climbing fiber development

and elimination (Kawamura et al. 2013; Mikuni et al. 2013; Miyazaki et al. 2004), the unequal distribution of both voltage-gated Ca^{2+} channels in combination with the spatial distribution of immature climbing fibers across the developing Purkinje cell is likely to be a strong driving factor of climbing fiber development (Bosman and Konnerth 2009). BDNF and semaphorins provide retrograde signals to the climbing fibers that are required for their proper development (Bosman et al., 2006; Choo et al., 2017; Uesaka et al., 2014).

In addition, there are indications for the existence of heterosynaptic competition between climbing fibers and cerebellar stellate cells (Bosman et al., 2006; Bosman and Konnerth, 2009). One should note that, at that age, the input of the GABAergic stellate cells to the Purkinje cells is excitatory (Eilers et al., 2001), while their synapses are still at the same dendritic compartment as the climbing fiber and parallel fiber synapses (Ramón y Cajal, 1911; Smirnow, 1897).

1.3 Ultrastructure of the Inferior olivary neuropil

1.3.1 Glomeruli and gap junctions

The ultrastructure of the mammalian IO neuropil has been described in many studies of various animals (De Zeeuw 1990). The segments of IO dendrites as well as the hillocks of IO axons bear pedunculated club-shaped and/or racemose spiny appendages (De Zeeuw et al., 1990a, b, c; Gwyn et al., 1977; Ruigrok et al., 1990; Sotelo et al., 1974). While it is clear that the dendritic spines are frequently electrotonically coupled by gap junctions formed by connexin36 (Cx36; Fig. 4) (De Zeeuw et al., 1989a, b, 1990b, 1995; Sotelo et al., 1974), it remains to be demonstrated whether this also holds true for the axonal spines (De Zeeuw et al., 1990c). Both the dendritic and axonal spines have unusually long spine necks. Because of their long necks, the spine heads can cluster together and form the core of what is the most characteristic feature of the IO neuropil: the glomerulus (De Zeeuw et al., 1990b; Gwyn et al., 1977; Nemecek and Wolff, 1969; Sotelo et al., 1974). In general, a glomerulus contains a core of five to ten dendritic and/or axonal spiny appendages derived from different neurons (De Zeeuw, 1990; De Zeeuw et al., 1990b, c). This core is surrounded by four or five terminals and several glial sheaths. Serial section analysis has demonstrated that virtually all spines are located in glomeruli. When the expression of Cx36 is blocked, the formation of gap junction plaques is disturbed (Fig. 4a–b), but the remnants of gap junction-like structures are still visible in the center of the glomeruli (Fig. 4c–d) (De Zeeuw et al., 2003).

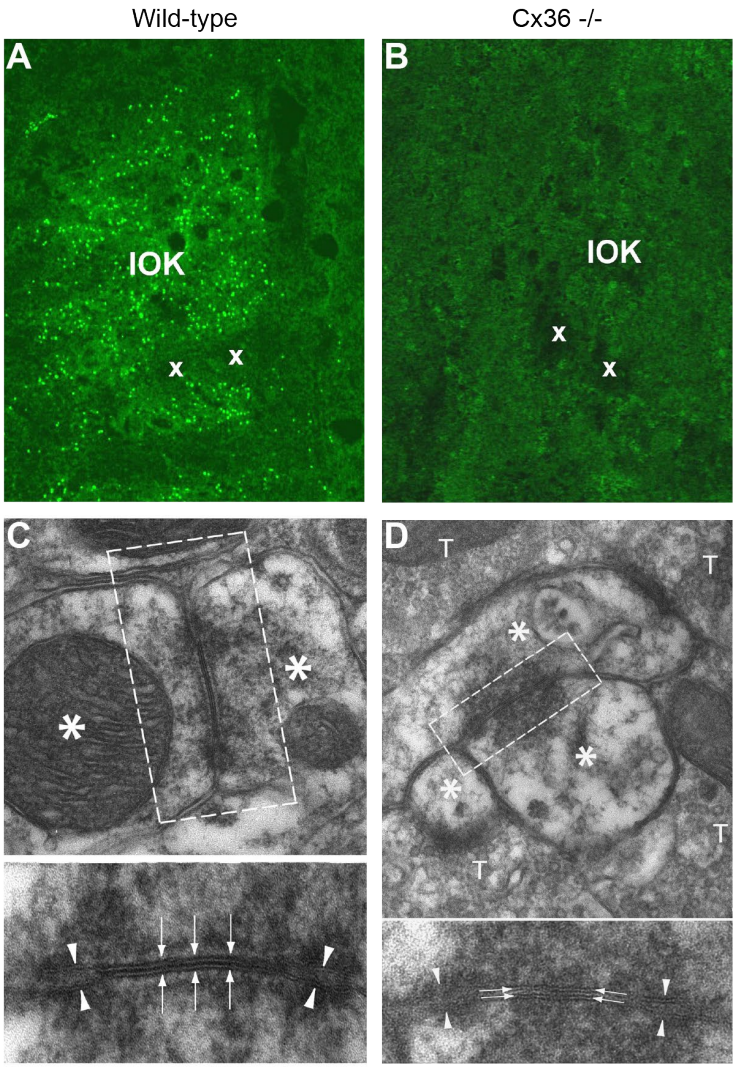

Fig. 4 Inferior olivary gap junctions. A – Punctate labeling in IO neuropil of wild-type mouse after immunocytochemistry staining with anti-Cx36. B – In Cx36 / mutant mice, the IO neuropil could not be labeled by anti-Cx36. IOK, dorsal cap of Kooy; x, examples of cell bodies. C – Ultrastructural characteristics of a dendrodendritic gap junction in the IO of a wild-type mouse. The gap junctions between IO dendritic spines (*) showed electron-dense deposits in the cytoplasm at both sides of the membrane. Arrowheads, attachment plaques. Arrow, gap junction plaque. D – Ultrastructural characteristics of a dendrodendritic gap junction-like structure in the IO of a CX36-deficient mouse. The dendrites show numerous gap junction-like structures with a widened interneuronal gap (arrows). *, dendritic spines. T, terminals. (Reprinted with permission of De Zeeuw et al. 2003).

Several attempts have been made to estimate the extent of electrotonic coupling of IO neurons via gap junctions. A number of groups have been able to demonstrate the existence of clusters of coupled neurons through intracellular injections of small molecules such as biocytin (see also section: “Subthreshold Oscillations and Spike Timing”) or Neurobiotin that readily cross gap junctions (Benardo and Foster, 1986; De Zeeuw et al., 2003; Hoge et al., 2011; Leznik and Llinás, 2005). Typical cluster sizes range from a few to more than ten coupled IO neurons in a slice of several hundred µm. Given that these studies have been performed in sectioned tissue and thus include neurons with severed dendrites, the actual number of connected neurons is likely

to be larger. Performing multiple unit recordings following application of harmaline and picrotoxin, Llinás and colleagues have demonstrated that in the intact IO, synchronous firing can be induced in coupled cellular aggregates of tens of neurons (Lang et al., 1996; Llinás and Volkind, 1973). In addition, population level imaging of neighboring Purkinje cell dendrites has revealed large-scale coherence of complex spikes in awake behaving rodents, suggesting that during certain types of behavior, synchrony may encompass tens of climbing fibers and thus many synchronized IO neurons (De Gruijl et al., 2014a; Hoogland et al., 2015; Ozden et al., 2012). In fact, bilateral multiple unit recordings from the cerebellar cortex demonstrated that an ensemble of coupled IO neurons in the rat can even extend beyond the midline (De Zeeuw et al., 1996). In the same study, it was estimated that one IO neuron may have 500–1000 gap junctions and that two individual IO neurons may be coupled by 10–20 gap junctions (De Zeeuw et al., 1996). Estimates of the density of neuronal gap junctions with the use of antibodies against Cx36 are in line with these counts (Fig. 4a).

Usually the types of IO neurons that are coupled are of the same subtype (see section "Inferior Olivary Subdivisions and Cell Types"; Devor and Yarom 2002a). However, the coupling shows a striking level of heterogeneity and asymmetry (Lefler et al., 2014), which may serve to finely influence the synchronization of IO neurons (Hoge et al., 2011). This raises the possibility that variations in coupling could result from glomerulus-specific short- and long-term modulation of gap junctions, which is supported by studies investigating the impact of excitatory synaptic inputs to the IO (Mathy et al., 2014; Turecek et al., 2014). Another promiinent, possibly related feature of the IO neuropil is the presence of dendritic lamellar bodies (De Zeeuw et al., 1995). This organelle consists of stacks of membranous cisternae with electron-dense deposits in between, and it occurs exclusively in the varicose dilatations that are abundant in the peripheral IO dendrites just outside the glomeruli. Although other possible functions cannot be excluded such as intracellular Ca^{2+} control or the exchange of excitable dendritic membranes (De Zeeuw et al., 1997a), various lines of evidence suggest that the dendritic lamellar bodies may serve to control the turnover or assembly of dendrodendritic gap junction channels. The fact that the density of dendritic lamellar bodies in the IO is higher than in any other area of the brain points to the importance of electrotonic coupling between IO neurons (De Zeeuw et al., 1995).

1.3.2 Inputs and origin

Although some of the IO subnuclei have some unique characteristic features, they all share the presence of glomeruli, dendrodendritic gap junctions, and dendritic lamellar bodies, and they all receive both excitatory and inhibitory inputs (De Zeeuw et al., 1989a, 1990b, c, d, 1993, 1994, 1996; Strata, 1989). The IO receives sensory and motor signals from nuclei such as the trigeminal nuclei, dorsal column nuclei, pretectal complexes, and red nuclei as well as direct feedback signals from the cerebellar nuclei and indirect feedback signals that are relayed via the meso-diencephalic junction (De Zeeuw and Ruigrok, 1994; Garden et al., 2017; Onodera and Hicks 1995; Swenson, 1983). Sensory and motor inputs are partially segregated, but also converge within parts of the IO (Berkley and Worden, 1978). For example, motor inputs deriving from the nucleus of Darkschewitsch and nucleus of Bechterew, part of the mesodiencephalic junction, as well as the primary motor cortex innervate the PO and rostral MAO (Onodera, 1984; De Zeeuw and Ruigrok, 1994; Garden et al., 2017; Berkley and Worden, 1978), whereas somatosensory inputs coming from the spinal cord, dorsal column nuclei, pretectum, and lateral cervical nucleus innervate the DAO and caudal MAO (Berkley and Worden, 1978; Bull et al., 1990; Boesten and Voogd, 1975). An overlap of motor and sensory fibers coming from the primary motor cortex, spinal cord, dorsal column nuclei, and lateral cervical nucleus, is observed in the medial part of the rostral DAO and a small area in the middle of the caudal MAO (Berkley and Worden, 1978). Supporting these latter findings, olivary cells located in the DAO respond to cerebral cortex and spinal cord stimulation, exhibiting a high degree of convergence of motor and sensory inputs in this subnucleus of the IO (Crill and Kennedy, 1967). Whether in this case the excitatory responses of IO cells vary depending on the type of input – motor or sensory - requires further investigation. However, it has been observed that excitatory synaptic responses to motor inputs coming from the primary motor cortex and MDJ differed in that synaptic responses to cortical afferents were smaller. This could reflect a scarce direct innervation from that cortical region (Garden et al., 2017). Regardless of whether the responses of IO neurons to convergent inputs are different or not, the location of the IO cells also dictates the way the information is processed, since a specific area of an IO subnucleus projects to a particular longitudinal microzone of the cerebellar cortex, which can be involved in either a motor or non-motor task (Apps and Hawkes, 2009; De Zeeuw, 2020). Likewise, a specific area of an IO subnucleus projects and receives afferents back from specific regions of the cerebellar nuclei (Apps and Hawkes, 2009; Ruigrok and Voogd, 1990, 2000). Therefore, the spatial distribution of sensory and motor inputs within the IO will determine which microzones of the cerebellar cortex and specific areas of the cerebellar nuclei are engaged

with particular functional consequences for motor program adjustment or cognitive processes. How IO neurons integrate sensory and motor information requires further investigation.

As mentioned above, In the PO and MAO, all terminals derived from the mesodiencephalic junction are excitatory and display the corresponding morphological features consisting of rounded vesicles and asymmetric synapses. In contrast, all the cerebellar terminals in the PO and MAO are GABAergic and have pleiomorphic vesicles and symmetric synapses (De Zeeuw et al., 1988). Approximately half of both types of terminals contact dendritic elements inside glomeruli (De Zeeuw, 1990; De Zeeuw et al., 1989a, 1990b, c, d; Strata, 1989). The large majority of the remaining terminals contact the proximal and intermediate dendrites, while relatively few terminate on the somata and axon hillock; presynaptic axo-axonal contacts have not been observed in the IO. The innervation of the IO by the non-GABAergic mesodiencephalic terminals and GABAergic cerebellar terminals is apparently random, because neither type of terminal has a preference for either the extra- or intra- glomerular neuropil and there is no obvious pattern in the distribution of the two types of terminals within the individual glomeruli (Strata, 1989). Every spine on the dendrites and axon hillock of all IO neurons in the PO and rostral MAO receives a synaptic input from both an excitatory mesodiencephalic terminal and an inhibitory cerebellar terminal. Since in most regions of the central nervous system the vast majority of dendritic spines are contacted solely by asymmetric synapses, the ubiquitous, combined excitatory and inhibitory input to the IO spines can also be considered as one of the characteristic features of its neuropil. The other subnuclei such as the DAO, β nucleus, DCK, VLO, and DMCC follow the same configuration, but with different origins of the inputs involved (De Zeeuw et al., 1993, 1994, 1996). Despite the fact that we have a reasonably detailed view on which afferents project to what subnuclei in the inferior olive, we still lack sufficient detailed insight as to how these afferents are distributed with respect to the different cell types in the inferior olive.

1.3.3 Neurotransmitters and receptors

Apart from the glutamatergic and GABAergic inputs and receptors present in the IO glomeruli (Garden et al., 2017; Hoge et al., 2011; Lefler et al., 2014; Mathy et al., 2014; Turecek et al., 2014), there is also a widespread indolaminergic and catecholaminergic innervation present in the IO (Bishop and Ho, 1984; Paré et al., 1987). These inputs generally serve as level setting systems, determining the membrane potential of the olivary neurons and thereby controlling ensemble oscillations and rhythmic activity (Barragan et al., 1983). Even though the signaling

through these pathways is more diffuse and generally takes place outside the olivary glomeruli through termi- nals with abundant dense core vesicles, the distribution of the receptors involved appears to be strictly organized within the IO complex and usually at least partly overlaps with that of the inputs and transmitters. However, there are substantial differences among species. For instance, in cat, indolaminergic receptors appear to be most densely present in the MAO and DAO, whereas in rats these are restricted to the lateral DAO (Wiklund et al., 1977). Likewise, the catecholaminergic innervation (norepinephrine and dopamine) of the IO is generally also not spread evenly and also differs among species (Sladek and Hoffman, 1980). In rat, the dopaminergic projections from the mesodiencephalic junction target the VLO, which is involved in vertical compensatory eye movements (Toonen et al., 1998), whereas in cat, the dopaminergic nerve terminals are most prominent in the DAO, which may be involved in sensorimotor processing during locomotion (Horn et al., 2010, 2013; Maqbool et al., 1993). And again, differently, in nonhuman primates, catecholaminergic fibers are mostly seen in the MAO and lateral lamella of the PO (Kamei et al., 1981; Sladek and Bowman, 1975), whereas in humans the noradrenergic fibers in the IO are much more homogeneously distributed than in rat, cat, and monkey (Powers et al., 1990).

In many extraglomerular terminals with dense core vesicles, one can find a coexistence of a classical neurotransmitter like an indolamine or catecholamine with some neuropeptide. For example, in the DAO of the rat, many terminals have both serotonin and substance P, while the corresponding receptors can be found in adjacent dendrites (Bishop and Ho, 1984; Paré et al., 1987). However, some of the inferior olivary subnuclei appear to receive peptidergic inputs without concomitant indolaminergic or catecholaminergic substances in the same terminals. Indeed, in the DCK, the β nucleus, and the DMCC of the rat, there are many substance P fibers and varicosities as well as related receptors, but little trace of serotonin immunoreactive elements (Bishop and Ho, 1984). Possibly, neuropeptides like substance P can also serve relevant functions without co-release of one of the classical neurotransmitters. Substance P can exert its effects through tachykinin neurokinin-1 receptor (NK1R), which plays an integral role in the modulation of homeostatic functions in the medulla, including regulation of respiratory rhythm generation, integration of cardiovascular control, and modulation of the baroreceptor reflex and mediation of the chemoreceptor reflex in response to hypoxia (Bright et al., 2017).

1.4 Cell physiology of inferior olivary neurons

1.4.1 Subthreshold oscillations and spike timing

One of the distinguishing features of IO neurons is that they can exhibit prominent membrane potential subthreshold oscillations (Fig. 5a; Benardo and Foster 1986; Llinás et al. 1974; Llinás and Yarom 1981b, 1986). Such oscillations are generated through the sequential activation of various voltage-gated ionic conductances such as a dendritic high-threshold Ca^{2+} conductance, a somatic low-threshold Ca^{2+} conductance, a Ca^{2+}-activated K^+ conductance, and a hyperpolarization-activated cationic conductance (IH) (Bal and McCormick, 1997; Benardo and Foster, 1986; Llinás and Yarom, 1981b, 1986; Matsumoto-Makidono et al., 2016; Zhang et al., 2017). Electrophysiological experiments on IO neurons of mutant mice lacking either the CaV2.1 gene (P /Q-type) or the CaV3.1 gene (T-type Ca^{2+} channel) have shown that these channels support the generation of IO membrane potential oscillations (Choi et al., 2010; Matsumoto-Makidono et al., 2016; Park et al., 2010). Indeed, immunohistochemical stainings confirmed that T-type Ca^{2+} channels are only expressed in IO neurons displaying subthreshold oscillations (Bazzigaluppi and de Jeu, 2016). The Ca^{2+}-activated K^+ conductances are responsible for the after- hyperpolarization (AHP), and blocking these channels prevents the rhythmogenesis of the membrane potential in IO neurons (Bal and McCormick, 1997; Llinás and Yarom, 1981a, b). The IH conductance mainly determines the pacemaker potential and the oscillation frequency (Bal and McCormick, 1997; Matsumoto-Makidono et al., 2016). In rodents, IO neurons can exhibit two prevalent types of subthreshold oscillation (Fig. 5a): 3–10 Hz sinusoidal subthreshold oscillation (SSTO) and rhythmic 1–3 Hz low-threshold Ca^{2+} oscillations (LTO). IO cells can express either one or a mixture of these oscillations (Khosrovani et al., 2007; Lampl and Yarom, 1997; Llinás and Yarom, 1986). Only IO neurons from the DCK and the VLO do not express subthreshold oscillations (Urbano et al., 2006). In non-human primates, SSTOs and LTOs are found in similar proportions, but the overall oscillation frequency is in general significantly slower (1–2 Hz), most likely due to the increased capacitive load of the more elaborate IO dendrites (Turecek et al., 2016). With such slow oscillations, phase differences in populations of IO neurons might be important to confer the temporal precision required for rapid motor adaptation. Frequency modulation of subthreshold oscillations has been observed within IO recordings, but it is more frequently seen in vitro than in vivo (Devor and Yarom, 2002b; Khosrovani et al., 2007). The origin of shifts activation of NMDA receptors in the IO can support and modulate subthreshold rhythmogenesis in IO neurons. In vivo IO recordings from animals anesthetized by ketamine

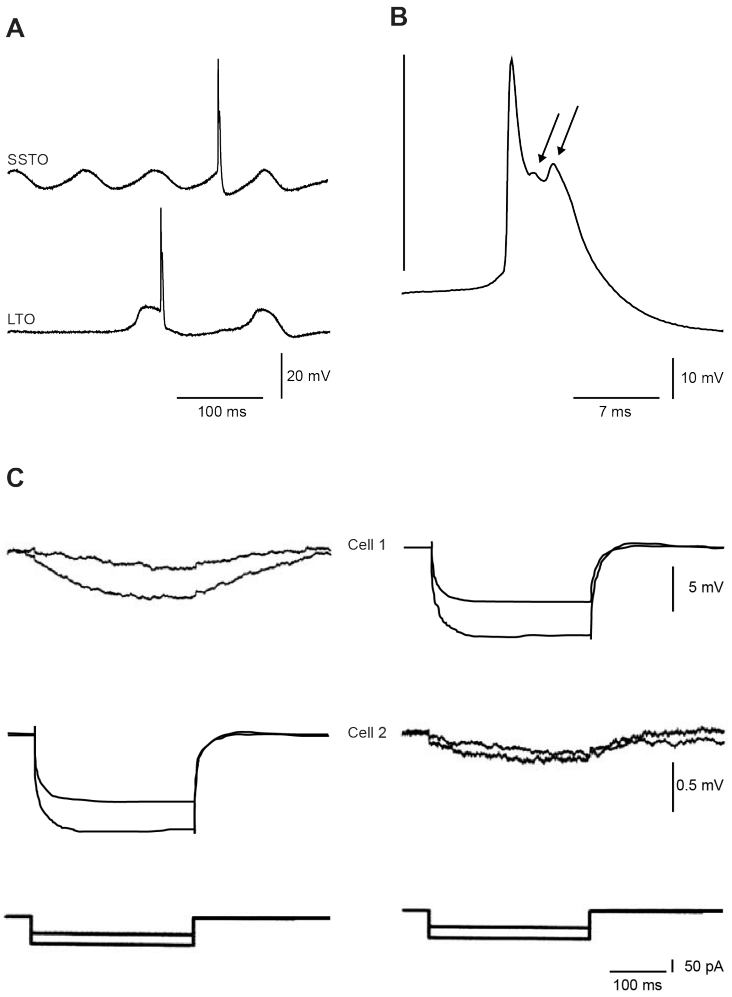

Fig. 5 Electrophysiological properties of inferior olivary neurons. A – Membrane potentials of IO neurons can express different spontaneous subthreshold oscillations. In the top trace, a spontaneous sinusoidal subthreshold oscillation (SSTO) was recorded from an IO neuron in vivo, whereas the bottom trace shows an IO neuron that expresses spontaneous low-threshold Ca^{2+} depolarizations (LTO). B – Enlargement of a typical IO action potential. The arrows indicate IO wavelets on top of the after depolarization (ADP). C – Electrotonic coupling between two adjacent IO neurons was measured using a dual whole-cell patch-clamp technique. Current injections into cell 2 (left panel) induced direct voltage responses in cell 2 and indirect responses in cell 1. This current flow was bidirectional (right panel). (Reprinted with permission of Bazzigaluppi et al. (2012a) and De Zeeuw et al. (2003)).

(blocker of NMDA receptors) show more often LTOs than SSTOs, whereas IO recordings of animals in which the anesthetics used does not block the NMDA receptors (medetomidine/midazolam/ fentanyl mixture) report more often SSTOs than LTOs (Bazzigaluppi et al., 2012a). By contrast, pharmacological stimulation of NMDA receptors can, through a concomitant increase in coupling between IO neurons, amplify or even initiate IO oscillations (Devor and Yarom, 2002b) (Turecek et al., 2014). Thus, in individual IO neurons, synaptic activation of NMDA receptors could provide a means to dynamically change a cell's oscillatory behavior and the number of synchronized neighboring cells. The fact that freeze-fracture analysis of IO glomeruli shows close proximity of glutamatergic postsynaptic densities and Cx36-

containing gap junctions further supports this idea (Hoge et al., 2011). Several studies revealed that a number of neuroactive substances are able to modulate the amplitude of the sub- threshold oscillations. For example, serotonin suppresses the amplitude of the subthreshold oscillation (Placantonakis et al., 2000), whereas harmaline, like NMDA, can amplify oscillation amplitude (Llinás and Yarom, 1986).

Subthreshold oscillations determine the firing behavior of IO neurons in a temporal manner. During the peak of the oscillation, there is an enhanced spiking probability, which in turn is reduced at the trough. IO neurons do not generate an action potential at every depolarizing phase of the oscillation, but on average only spike once every ten cycles. Harmaline facilitates the spiking behavior of IO neurons by increasing the amplitude of the oscillation, resulting in the generation of a spike on every depolarizing phase of the oscillation (Llinás and Volkind, 1973; Llinás and Yarom, 1986). The harmaline-induced firing is, therefore, very rhythmic and brings the IO neurons up to their maximal firing rate. The interaction (phase locking of spikes) between the subthreshold oscillations and spiking is not unidirectional. The phase of the subthreshold oscillation influences the probability of spiking, but spiking also influences the phase of the following oscillation (Khosrovani et al., 2007; Leznik et al., 2002). IO spikes consistently lead to a shift in the subthreshold oscillation phase such that the spike would have occurred at the peak of the phase- shifted subthreshold oscillation (i.e., at 90°). Choi et al. (2010) showed that CaV2.1 and CaV3.1 are also required for the phase resetting of oscillations in IO neurons. Thus, IO neurons are equipped with a self-regulating temporal pattern generator.

1.4.2 Electrical synapses in the inferior olive

IO neurons are interconnected by dendrodendritic gap junctions formed by Cx36 proteins, while Cx45 and Cx47 are also found in oligodendrocytes in the IO (Fig. 6) (Condorelli et al. 1998; Weickert et al., 2005). Gap junctional coupling allows direct communication across multiple neurons. The electrophysiological properties of Cx36 gap junctions are characterized by a low unitary conductance of 10–15 pS, weak voltage sensitivity, and low-pass filter function (Srinivas et al. 1999). These properties ensure that low-frequency membrane oscillations are preferentially transmitted from one IO neuron to another (Fig. 5c) and that subthreshold oscillations can be synchronized among coupled IO neurons. Both dual whole-cell recordings and voltage-sensitive dye imaging in the IO have demonstrated that coupled IO neurons can synchronize their subthreshold oscillations (Devor and Yarom, 2002a, b; Leznik and Llinás, 2005). Optical imaging

has confirmed that such activity can propagate across the olivary nucleus (Devor and Yarom, 2002b).

It is important to note that the electrotonic coupling between IO neurons is not a prerequisite for the generation and maintenance of oscillations in IO neurons. Both genetic and pharmacological uncoupling of IO neurons do not abolish the generation of subthreshold oscillations (De Zeeuw et al., 2003; Leznik and Llinás, 2005; Long et al., 2002), suggesting that oscillations are generated by the intrinsic conductances of individual neurons. However, genetic uncoupling of IO neurons does abolish the synchrony of subthreshold oscillations and the synchrony of firing among IO neurons (Long et al., 2002). Synchronization of subthreshold oscillations and synchrony of firing among IO neurons are often considered the most critical function of gap junctional coupling. In fact, the ability to synchronize membrane oscillations across IO neurons through Cx36 gap junctions may have functional consequences, as the crispness of reflexive movements is impaired in Cx36 global knockout mice (De Gruijl et al., 2014a).

The uncoupling of IO neurons does affect one of the oscillatory properties; their oscillatory behavior is limited to a smaller range of membrane potential levels (De Zeeuw et al., 2003; Leznik and Llinás, 2005; Long et al., 2002). Therefore, the gap junctions (or coupled network) act to stabilize the subthreshold oscillatory activity in the olive cell by making the oscillations less sensitive to the membrane potential with respect to frequency and amplitude. The uncoupling of the IO network also increases the excitability of IO neurons at hyperpolarized levels (De Zeeuw et al., 2003; Leznik and Llinás, 2005), which results in an altered timing of climbing fiber activities in the cerebellar cortex (Van Der Giessen et al., 2008).

1.4.3 Synaptic modification of oscillations and coupling

Sensory and motor signals reach the IO via excitatory projections, which are most likely glutamatergic (Onodera and Hicks, 1995; Swenson ,1983). The feedback projection that connects the cerebellar nuclei via the mesodiencephalic junction with the IO is also excitatory (De Zeeuw and Ruigrok 1994), whereas the direct pathway is inhibitory and uses GABA as neurotransmitter (De Zeeuw et al.,, 1989a). The contribution of GABA and glutamate to the activity of IO neurons is subtle (Duggan et al. 1973; Lang 2002; Lang et al. 1996). Application of glutamate in the IO increased the spiking activity of IO neurons by only 2–3 Hz (Duggan et al. 1973), and blocking

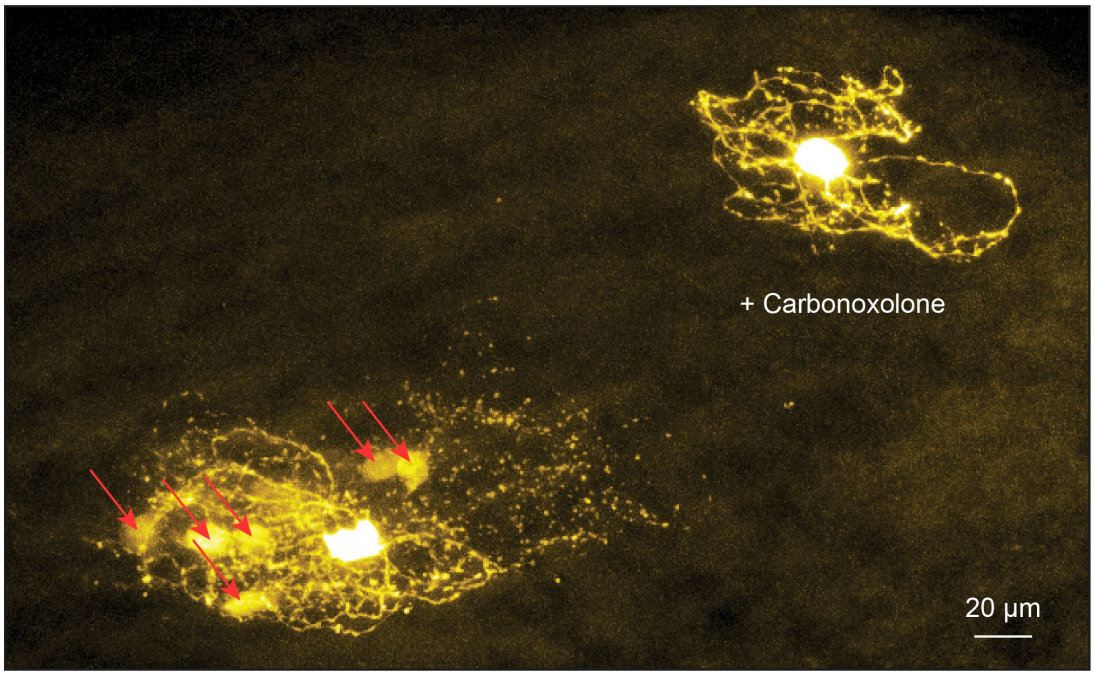

Fig. 6 Modification of coupling of olivary cells. The panel shows two intracellular injections of biocytin in the same slice, one before (left) and one after (right) application of broad-spectrum gap junction blocker carbenoxolone into the bath. Without the blocker the biocytin diffused to a whole cluster of at least six other cells (red arrows), but after blocker application, the biocytin remained localized to a single cell. Scalebar: 20 µm.

GABAergic inhibition increased the spiking activity of IO neurons by only 1–2 Hz (Lang, 2002; Lang et al., 1996). This limited modulatory capacity of these neurotransmitters on IO activity can be attributed to the unique membrane properties of IO neurons (Llinás and Yarom 1981a; Llinás and Yarom, 1981b). Furthermore, depriving the IO from inputs does not abolish the intrinsic spiking activity of IO neurons. Thus, IO neurons are intrinsically active and do not require the glutamatergic or GABAergic inputs to spike (Lang 2001, 2002).

Stimulation of excitatory projections to the IO results in phase resetting of the subthreshold oscillation without affecting the amplitude or frequency of the oscillation (Leznik et al., 2002). Somatosensory stimulations in vivo reveal a similar phase resetting mechanism, except that under these conditions, no IO cell can be stimulated during the hyperpolarizing phase of their subthreshold oscillations (Khosrovani et al. 2007). This resetting mechanism allows IO neurons to adjust their spiking patterns in a temporal manner by using online sensory and motor (“reference”) feedback.

Activation of the CN *in vivo* induces a biphasic response in IO neurons. First, a depolarization occurs which can evoke an action potential. Subsequently, a long-lasting GABAergic hyperpolarization is generated (Bazzigaluppi et al., 2012b). This hyperpolarization blocks the supra- and subthreshold activity of the IO neurons for the duration of one subthreshold oscillation

cycle, and after this hyperpolarizing block has been raised, all subthreshold oscillations are restarted (inducing a 0o resetting point). Under these conditions, The input from the CN did not alter the amplitude or frequency of the reappearing subthreshold oscillations. Thus, the direct GABAergic, nucleo-olivary pathway gates information during specific time windows (i.e., approximately one subthreshold oscillation cycle) and resets very bluntly the subthreshold oscillation. Such resetting has also been demonstrated in optogenetic experiments where nucleo-olivary axons to the IO neurons were stimulated directly and repeated stimulation could transiently silence subthreshold oscillations (Lefler et al., 2014).

IO neurons receive GABA and glutamatergic inputs that terminate close to the electrical synapse (at IO glomeruli, see section “Glomeruli and Gap Junctions”.), and these inputs may, therefore, also control the electrotonic coupling between IO neurons (Lang et al., 1996; Llinás and Sasaki, 1989). Imaging studies (Leznik and Llinás, 2005; Leznik et al., 2002) showed that blocking GABAA receptors in the IO increased the number of neurons oscillating inphase, indicating an expansion of the number of electrotonically coupled neurons. This increment of cluster size has also been observed in Purkinje cells after blocking the GABA receptors in the IO (Lang, 2002). By contrast, stimulation of GABAergic nucleo-olivary afferents can transiently reduce coupling between IO neurons (Lefler et al., 2014). The role of glutamatergic inputs on IO coupling is a bit less clear. Low-frequency electrical stimulation of glutamatergic projections was shown to reduce coupling (Mathy et al., 2014), whereas pharmacological activation of NMDA receptors was shown to increase coupling strength (Turecek et al., 2014). In another study, a pharmacological block of glutamatergic input resulted in an overall reduction in IO coupling (Lang, 2002). Gap junctional plasticity could be mediated by the PKA and CaMKII pathways, where activation of the PKA pathway most likely reduces the opening probability of Cx36 gap junctions, whereas the CaMKII pathway could increase the number of Cx36 gap junctions (Bazzigaluppi et al., 2017). Discrepancies in these results could in fact be explained by considering the Ca^{2+} levels in IO spine heads evoked by the different stimulus paradigms (De Gruijl et al., 2014b, 2016). Overall, these results suggest that activity of the intra-glomerular chemical synapses dynamically regulates the efficacy of electrotonic coupling and therefore the patterns of synchronous activity in the olivocerebellar system (Llinás et al., 1974). Despite all the studies addressing these topics, it is still unknown how postsynaptic integration of both responses modulates STOs, electrical coupling and spike probability of IO neurons.

1.4.4 Action potential waveforms

IO neurons have action potentials with a characteristic waveform (Fig. 5b): a sharp spike is followed by a prolonged afterdepolarization (ADP) and a long-lasting AHP (Llinás and Yarom, 1981a, b). The discharge rate is low: only once or twice per second (Benardo and Foster 1986; Llinás and Yarom, 1981a, b). Although IO neurons are sensitive to sensory stimulation, their responsiveness is limited. Stimulating excitatory afferents to the IO either from sensory nuclei such as the trigeminal nucleus or from higher systems such as the mesodiencephalic junction evokes only a single action potential in IO neurons. Using a chemical excitant, such as harmaline, IO firing can be driven to a maximum of approximately 10 Hz (Llinás and Volkind, 1973; Llinás and Yarom, 1986). The low discharge rate and limited responsiveness of IO neurons are unique features in the generally very active olivocerebellar circuit.

The fast IO spike is mediated by Na^+, whereas the ADP is generated by the activation of dendritic high-threshold Ca^{2+} conductances (Llinás and Yarom, 1981a, b). Choi et al. (2010) have shown the involvement of the P/Q-type Ca^{2+} channel CaV2.1 in this process. However, there also is evidence that CaV3.1 affects spike repolarization (Matsumoto-Makidono et al., 2016). The influx of Ca^{2+} activates dendritic Ca^{2+}-activated K^+ conductances inducing subsequently the slow AHP (Bal and McCormick, 1997; Llinás and Yarom, 1981a). During this hyperpolarization, two processes are initiated: hyperpolarization-activated cationic conductances (IH) are activated, and somatic low-threshold Ca^{2+} conductances become de-inactivated (T-type; Bal and McCormick, 1997; Llinás and Yarom, 1986). It is likely that both processes are involved in the termination of the AHP and the generation of a rebound spike. The long duration of the AHP and the de-inactivation process of the T-type Ca^{2+} conductances are probably responsible for the low discharge rate and poor responsiveness following high-frequency stimulation.

One to seven small wavelets (<10 mV) are superimposed on the ADP of IO neurons (Fig. 5b, arrows) and occur at very high frequencies ranging from 200 to 500 Hz. They represent a high-frequency bursts of action potentials that are most likely generated in the axon of IO neurons by the ADP (Crill, 1970; Crill and Kennedy, 1967; Maruta et al., 2007; Mathy et al. 2009). Propagation of the ADP to the axon leads to the initiation of a burst of action potentials, which in turn propagate back to the soma. Here, they give rise to attenuated wavelets. Na^+ spikes are not evoked because the Na^+ channels are still inactivated at the soma (Mathy et al., 2009). IO burst firing is transmitted to the Purkinje cells via the climbing fibers, where they can modify the Purkinje cell complex spike itself or the synaptic transmission between the parallel fibers and Purkinje cells (Hansel, 2009; Mathy et al., 2009).

Information about spike timing relative to the phase of the subthreshold oscillation may be conveyed by axonal burst activity of IO neurons (Mathy et al., 2009). The timing of the IO activity is encoded by the number of spikes in the IO axonal burst. Such bursts might provide the olivocerebellar system with a mechanism that allows timing-dependent learning of parallel fiber input patterns in Purkinje neurons. However, in vivo studies (Bazzigaluppi et al., 2012a) suggest that the amplitude of the IO subthreshold oscillations also contributes to the size of the IO axonal burst. The bursts are reduced when a spike is evoked on top of a subthreshold oscillation with a large rather than a small amplitude. This amplitude coding might provide the olivocerebellar system with a mechanism to grade the expectancy (or saliency) of an event, gating only relevant information to Purkinje cells. There now is some evidence that the climbing fiber axons that originate from IO neurons indeed respond in a graded manner to sensory stimuli of different duration and strength (Najafi et al., 2014; Najafi and Medina, 2013).

1.5 Models of olivary neurons

1.5.1 Single-cell models

In addition to research conducted in vitro (Bleasel and Pettigrew, 1992; Leznik and Llinás, 2005; Leznik et al., 2002), in silico studies of the IO have investigated the spectrum of cellular and network behavior as a function of crucial parameters. A small number of dynamical system models of IO neurons exist, with each model being characterized by its level of detail, such as ionic conductances and number of compartments (Manor et al., 1997; Schweighofer et al., 1999; Van Der Giessen et al., 2008; Velarde et al.,, 2002). Based on its electrophysiological characteristics, the oscillating IO neuron can be classified as a so-called resonator: a cell that is highly sensitive to the frequency at which sequential inputs arrive (Izhikevic, 2007).

Among the most detailed is the compartmental model by Schweighofer et al. (1999), later modified by De Gruijl et al. (2012) to include an axonal compartment. The original Schweighofer IO cell model includes a somatic and a dendritic compartment, each with its own ionic currents (section “Subthreshold Oscillations and Spike Timing”) as illustrated in Fig. 7a. Across a large range of parameters, the single IO cell model neuron reproduces a number of properties of its biological counterpart, such as (1) that the cell shows SSTOs with a frequency range of 7 to 9 Hz and an amplitude of 10 to 20 mV, (2) that the IO cell basically does not generate a spike in the trough of the oscillation, (3) that the IO cell shows differentially damped oscillations after an

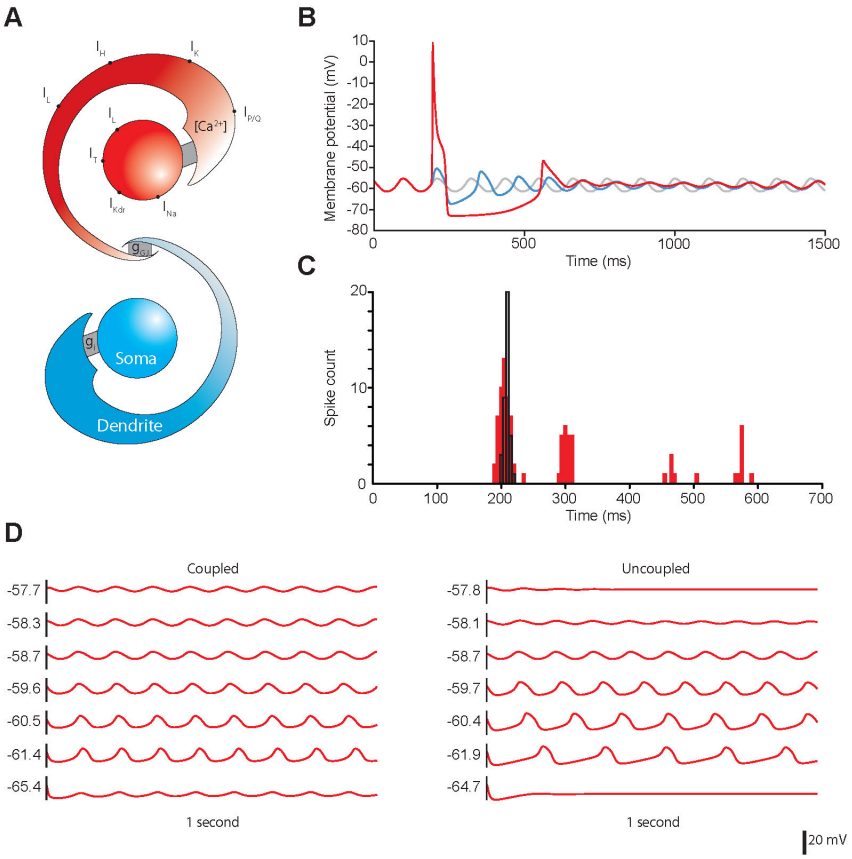

Fig. 7 Two-compartment model of two electrotonically coupled olivary neurons. A – Coupled cell pair with compartments separated by gray-shaded areas. For the red cell, the currents used in the model are depicted at the appropriate compartment. Somatic currents are T-type Ca^{2+} (IT), sodium (INa), delayed rectifier potassium (IKdr), and a passive leak current (IL). Dendritic currents are P /Q- type Ca^{2+} (IP/Q), cation h-current (Ih), a passive leak current (IL), and Ca^{2+}-dependent K^{+} (IK). For IK internal Ca^{2+} concentration ($[Ca^{2+}]$) is also modeled in the dendritic compartment. In the blue cell, the values for internal conductance (gint) and gap junctional conductance (gGJ) are indicated. B – Reaction of depicted coupled IO neurons to a stimulus. The red cell is stimulated and shows the distinct spike-shaped, long AHP and differentially damped SSTOs of its biological counterpart. The blue cell receives no input, but its state is changed due to the electrotonic coupling between the cells. As can be deduced from the gray reference trace, the action potential causes a shift in the phase of the SSTOs of both coupled cells after the event. C – Tendency of uncoupled cells (red) to fire doublets and respond rhythmically to repeated input. This is less apparent in coupled cells (black outline). Cells received temporally randomized input at 200 10 ms and 300 10 ms. Uncoupled cells often respond to one or both of the inputs but can also fire one or even two additional action potentials afterward. Coupled cells fire only on the first input and tend to synchronize their spikes, as is apparent from the narrower distribution. (Adapted from Van Der Giessen et al. 2008). D – Oscillations in cells at different injected currents. In coupled cells (left), oscillations in a cell can be sustained over a wider range of injected currents and resulting membrane potentials than in uncoupled cells (right). Depicted cell in the coupled network is the center cell of a 3 3 network, connected to all other cells. Values on the left side of the graphs are the average membrane potential in mV, taken from the last 500 ms of the simulation.

action potential, and (4) that the IO cell undergoes strong phase resetting following an action potential (Fig. 7). Dynamical systems analysis indicates that oscillatory characteristics are driven by the coupled interplay between dendritic and somatic conductances (Schweighofer et al., 1999; Van Der Giessen et al., 2008). Both the prevalence of SSTO and the SSTO frequency of the model cell are probably mainly controlled by the conductance of the low-threshold (T-type) somatic Ca^{2+} channels and the somato-dendritic coupling. When IO model neurons are uncoupled, they exhibit an increased excitability, shorter firing windows, and an increased voltage

dependency of the SSTOs (Fig. 7c–d). All these alterations can be explained by the removal of the gap junctional leak current and the thwarting of the transmission of the oscillatory behavior of coupled neighboring neurons (De Zeeuw et al., 2003; Van Der Giessen et al., 2008). In addition to the properties above, the extended model including an axonal compartment was also able to display high-threshold Ca^{2+} spikes, which produced bursts of axonal spikelets that were partly dependent on the network state (De Gruijl et al., 2012).

1.5.2 Network models

The network properties of the IO can change dramatically depending on the conductance value of the gap junctions, controlling both synchrony and the presence of network-wide oscillations. At high gap junctional conductances, ensembles of IO neurons operate in synchrony (i.e., their membrane potentials all oscillate in sync). The high gap junctional conductances also increase the input resistance of the model cell by increasing the leak to neighboring cells, preventing the IO neuron from generating a spike and making it more difficult to excite. At very low gap junctional conductances, the ensembles start to desynchronize, and the individual neurons become more excitable. Gap junctional coupling may bring a pair of non-oscillating cells to the oscillatory domain (Lefler et al., 2013). The coupling coefficient between IO neurons in situ, generated by Cx36 gap junctions, ranges from relatively small to significant (0.002–0.17; Devor and Yarom, (2002a). Simulations of small networks in that range show that electrotonic coupling yields the most versatile and interesting network properties (Schweighofer et al., 2004). In a low to moderately coupled network, a volley of excitatory events sent to an ensemble of IO neurons does not need to arrive in perfect synchrony for the IO network in order to generate a more synchronized output due to multiple cell phase resetting (Fig. 7c; Van Der Giessen et al., 2008). In low to moderately coupled networks, the synchrony is transient, as cells retain some of their abilities to operate individually. Due to local electrotonic coupling, neighboring cells can also tangentially change the state of other close-by cells. For instance, a network IO model demonstrated to produce quasi-synchronous spatiotemporal wavefronts in SSTOs (Latorre et al., 2013). By applying noisy inputs to a low to moderately electrotonically coupled IO network, Schweighofer et al. (2004) were able to simulate low-firing IO network behavior. In a series of in silico experiments, they showed that under certain assumptions, the low-frequency signals generated by the IO show a higher degree of mutual information with the input (Schweighofer et al., 2004). Not only the low-frequency firing can carry information, but also the high-frequency pattern of the climbing fiber bursts produced by individual IO axons can contain important information. In that context, a network model by De

Gruijl et al. (2014b) showed that the number of spikelets in a climbing fiber burst (Mathy et al., 2009) transmits information about amplitude – more so than the phase – of the network subthreshold oscillation. Network state is subject to Ca^{2+}-dependent modulation of gap junctional plasticity, which was experimentally demonstrated and subsequently modeled in De Gruijl et al. (2016).

1.6 Climbing fiber patterns and behavioral consequences

1.6.1 Spatiotemporal patterns

Purkinje cells produce two types of spikes: complex and simple spikes. Simple spikes are produced endogenously, but their firing pattern is modulated by excitatory and inhibitory synaptic input from parallel fibers and molecular layer interneurons (MLI), respectively (Häusser and Clark, 1997; Llinás and Sugimori, 1980; Miyashita and Nagao, 1984; Raman and Bean, 1999; Wada et al., 2007; Wulff et al., 2009). Simple spikes occur at a sustained, high frequency (10–200 Hz). Complex spikes are evoked by the climbing fiber input (Eccles et al., 1964). Climbing fibers form very large synapses on Purkinje cells, with each individual synapse having around 500 release sites (Silver et al. 1998). Complex spikes occur relatively infrequent (0.2–10 Hz) with an average around 1 Hz. Following a complex spike, a Purkinje cell cannot fire a simple spike during a period of about 20 ms (Bell and Grimm, 1969; Granit and Phillips, 1956; Simpson et al., 1996). The duration of this so-called climbing fiber pause can even be prolonged by optogenetic stimulation of the climbing fibers due to their impact on the molecular layer interneurons (Mathews et al., 2012), and dependent on the network properties as well as the intrinsic properties of the Purkinje cell involved, it can also be followed by a period of increased simple spike firing (Simpson et al., 1996). Thus, input from the IO does not only evoke complex spikes in Purkinje cells but also modulates simple spike firing (Badura et al., 2013; De Zeeuw et al., 2011).

Because of the exceptionally strong synaptic coupling between climbing fibers and Purkinje cells, complex spike firing follows in part the oscillations observed in the IO (Armstrong, 1974; Bell and Kawasaki, 1972; Blenkinsop and Lang, 2006; Khosrovani et al., 2007; Lang et al., 1996; Llinás and Sasaki, 1989; Marshall et al., 2007; Van Der Giessen et al., 2008). The subthreshold oscillations of the IO neurons may affect both the rate and the absolute timing of the complex spikes for short durations (Devor and Yarom, 2002a; Lampl and Yarom, 1993; Van Der Giessen et al., 2008). Input to the IO can reset the phase of the subthreshold oscillations (Khosrovani et al., 2007; Leznik et al., 2002; Van Der Giessen et al., 2008). Consequently, the complex spike

pattern could be “restarted” following a strong, unexpected sensory input, thus triggering a new motor program (Llinás, 2009). In addition to these acute effects of IO oscillations, they may also facilitate long-term plasticity by affecting the number of spikelets per complex spike, which in turn could modulate heterosynaptic plasticity at the parallel fiber to Purkinje cell synapse (Bazzigaluppi et al., 2012a; Mathy et al., 2009; Van Der Giessen et al., 2008).

In addition to the temporal patterning, climbing fiber input also organizes the spatial extent of complex spike firing. Because of the strong electrotonic coupling within the glomeruli, groups of IO neurons fire in synchrony (De Zeeuw et al., 2003; Long et al., 2002; Sotelo et al., 1974). The divergence of climbing fibers ensures that the synchrony within the IO is transmitted to large areas of the cerebellar cortex (Blenkinsop and Lang, 2006; Bosman et al., 2010; De Zeeuw et al., 1997b; Marshall et al., 2007; Ozden et al., 2009; Sasaki et al., 1989; Van Der Giessen et al., 2008). Coherent complex spike firing, which we define as co-occurrences during bins of 3–10 ms, can occur across larger parts of the cerebellar cortex (Fig. 8) (Bell and Kawasaki, 1972; Bosman et al., 2010; De Zeeuw et al., 1996; Kros et al., 2017; Welsh et al., 1995). Well-timed complex synchrony, occurring within 2 ms bins, is usually restricted to parasagittal zones (up to ca. 500 µm wide) that are defined by the pattern of climbing fiber innervation (Fig. 9) (Bosman et al., 2010; Lang et al., 1999; Llinás and Sasaki, 1989; Mukamel et al., 2009; Ozden et al., 2009; Schultz et al., 2009; Sugihara et al., 1993, 2007; Wylie et al., 1995). Two-photon Ca^{2+} imaging of Purkinje cell dendrites showed that the highest degree of complex spike synchrony is found in parasagittal “microzones,” which are 3–19 Purkinje cells wide (Mukamel et al., 2009; Ozden et al., 2009; Schultz et al., 2009). Microzones can act as ensembles of Purkinje cells encoding sensorimotor and cognitive processes (Mukamel et al., 2009; Ozden et al., 2012; Schultz et al., 2009; De Zeeuw 2021). Furthermore, two types of Purkinje cell microzones can be recognized based on changes in simple spike frequency during the initial stages of learning: ‘upbound’ and ‘downbound’ microzones. Purkinje cells of upbound microzones exhibit low frequency spontaneous simple spike firing, which can be increased upon learning, whereas Purkinje cells of downbound microzones show high frequency spontaneous simple spike firing, which can be decreased upon learning. These opposing changes in the activity exhibited by both types of microzones might allow them to operate in a complementary manner or a particular sequence during learning (De Zeeuw, 2021). Differences observed in simple spike firing frequency among these two groups have mainly been attributed to different expression patterns of proteins involved in controlling the membrane potential and cellular excitability (Perkins et al., 2018; Wu et al., 2019). However, it has been shown that the inferior olive, via climbing fiber activity, may also affect the baseline of the simple spike frequency. Specifically, climbing fiber terminals present in downbound

microzones exhibit a larger pool of vesicles ready to be released, increased multivesicular release, and larger synaptic glutamate transients. This results in longer-duration complex spikes containing an increased number of spikelets (Paukert et al., 2010), which would cause a drop in simple spike firing frequency by temporarily prolonging their interval (De Zeeuw, 2021).

The finding that complex spike synchrony is not restricted to microzones may reflect IO projections to different zones (Bosman et al., 2010; De Zeeuw et al., 1998; Welsh, 2002; Welsh et al., 1995). In addition, the extent of electrotonic coupling may be modified by afferent input to the IO (De Zeeuw et al., 1998; Llinás and Sasaki, 1989; Van Der Giessen et al., 2008; Welsh et al., 1995). Thus, complex spikes occur in specific spatiotemporal patterns, dictated by input to the IO, and dynamic regulation of the olivocerebellar pathway can have acute and long-term effects on the spiking pattern of the Purkinje cells and thereby on the output of the cerebellar cortex. Considering these facts, it would be very interesting to investigate the spatiotemporal footprints of complex spikes underlying different behaviors and how they change as motor learning occurs.

1.6.2 Behavioral consequences

Alterations in climbing fiber activity affect motor behavior. A number of studies have indicated that normal activity of the IO is essential for motor performance, motor learning, and memory. Moreover, recent studies are challenging the idea that the inferior olive is purely involved in motor functions. Indeed, it has been shown that complex spike activity is able to encode non-motor tasks such as reward expectation, delivery, and omission (Kostadinov et al., 2019). In these experiments, it was observed that complex activity was spatially and temporally heterogeneous, because while some cerebellar microzones show an increased complex activity upon reward delivery, other adjacent microzones show an inhibited complex spike activity. Furthermore, ramp-like activity was observed in some microzones previous to the reward delivery. Complex spike activity was also inversely scaled with reward predictability and enhanced when the reward was omitted. Finally, complex spike activity scales with reward size (Larry et al., 2019). Complex spike activity has also been associated with decision-making in that complex spike firing is increased when a wrong decision is made in a decision-making task (Deverett et al., 2018). Finally, the olivo-cerebellar loop has been involved in motor planning (Gao et al., 2018). In this latter study, ramping activity was observed seconds before the onset of the movement in the frontal cortex and the cerebellar nuclei (fastigial nucleus). Transient perturbations of this cerebellar region resulted in erroneous subsequent correct responses without affecting the motor performance.

The inferior olive must play a crucial role in this non-motor task, since it has a strong reciprocal connection with the cerebellar nuclei (Ruigrok and Voogd, 1990, 2000).

Lesions and (acute) inactivation of the IO result in a large variety of altered motor behaviors, including deficits in both acute motor performance and motor learning (McCormick et al., 1985; Rondi-Reig et al., 1997; Turker and Miles, 1986; Voneida et al., 1990; Welsh and Harvey, 1998; Yeo et al., 1986). Experiments that hyperactivate the IO, either by electrical or optogenetic means, also reveal interesting effects; under these conditions acute motor activity can be triggered, and motor learning can be either blocked or enhanced, dependent on the timing of the climbing fiber activity with respect to that of the mossy fiber system (Harvey and Romano, 1993; Kesner et al., 1995; Luebke and Robinson, 1994; Turker and Miles, 1984; Welsh, 1998). Under non-pathological conditions, the majority of climbing fibers are considered to signal general disturbances of the body (Gibson et al., 2004) or errors in motor performance (Simpson et al., 1996). The body disturbances relayed by the IO might provide the cerebellum with a representation of an unconditioned stimulus that can be used during associative motor learning, and together with conditioned stimuli, it enables the animal to (re) organize their motor behavior (Gibson et al., 2004). In order to process and correct errors in motor performance, the firing frequency of single climbing fibers is too low to evaluate and control fast motor movements. To accomplish motor control at this level, population coding is required. Synchronization of the climbing fibers signals will then be essential for the temporal organization of the population in order to establish an appropriate control of movement (Ten Brinke et al., 2017). Accordingly, simultaneous electrophysiological recordings of ensembles of Purkinje cells (located in parasagittal zones) have revealed correlated changes in complex spike synchrony in specific spatial domains during motor tasks (Lang et al., 2006; Welsh et al., 1995) as well as during sensory stimulation (Wise et al., 2010; Wylie et al., 1995). Moreover, these synchronizing effects of motor and sensory signals have also been confirmed by optical imaging in both wild-type animals and mouse mutants (Mukamel et al., 2009; Ozden et al., 2009, 2012).

Desynchronization of the climbing fiber signal can be accomplished genetically (Marshall et al. 2007) as well as pharmacologically (Blenkinsop and Lang, 2006; Ozden et al., 2009) by removing or blocking the Cx36 protein in the IO. Genetically altered mice that lack Cx36 have subtle, but significant, deficits in motor performance (Kistler et al., 2002), as well as more prominent problems during associative motor learning tasks that require timing (Van Der Giessen et al., 2008).

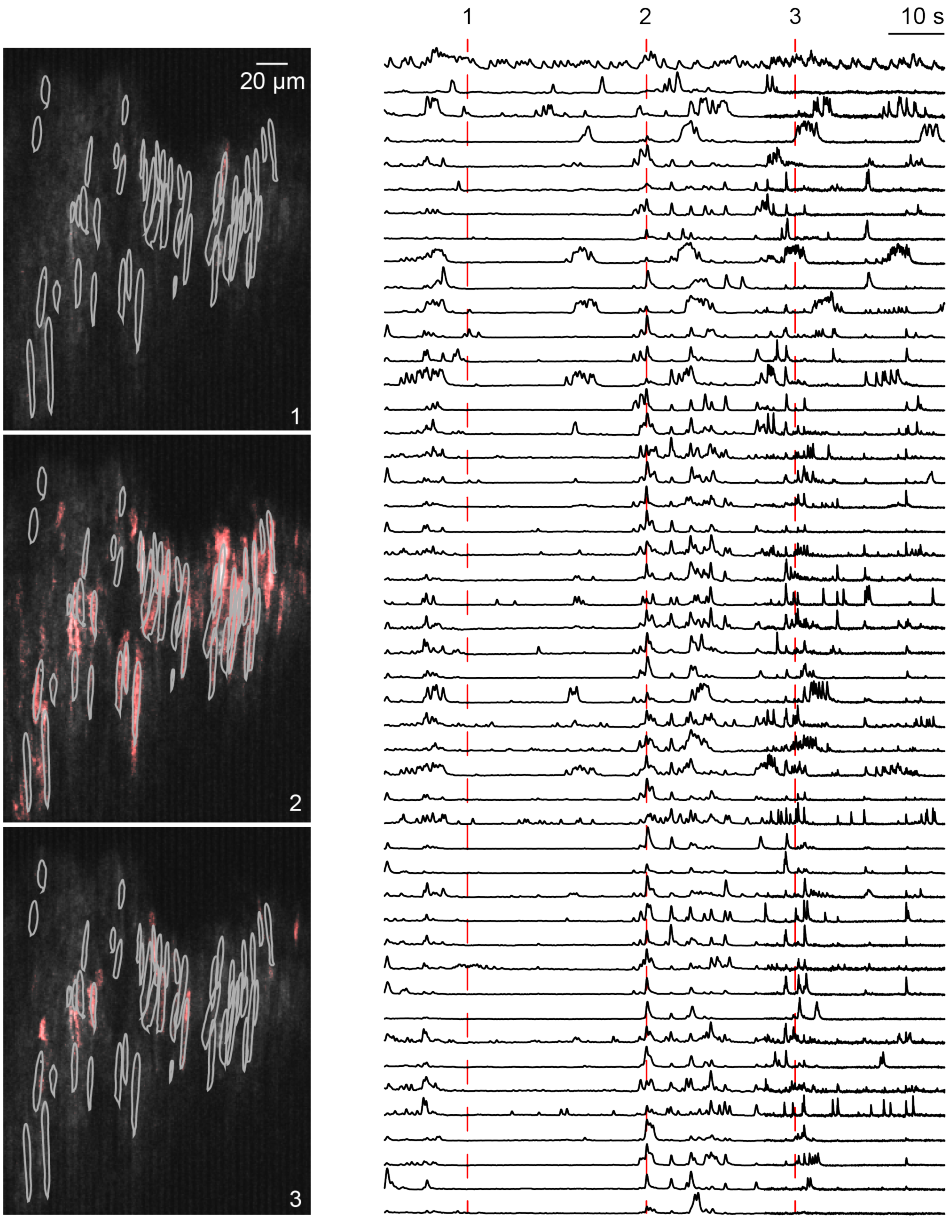

Fig. 8 Coherent complex spike firing. Two-photon Ca^{2+} imaging of ensembles of Purkinje cells in an awake mouse expressing GCaMP6f. Purkinje cells show dynamic complex spike coherence in awake animals. At times large numbers of complex spike-triggered Ca^{2+} transients are seen in many Purkinje cell dendrites (1), sometimes only a few cells are responsive (2), or a subset of cells that also participated during large-scale coherence (3). This suggests that the coherence of IO neurons is dynamically regulated. In the images responding PC dendrites are shown in red pseudo-color. All detected PC dendrites are shown as gray outlines.

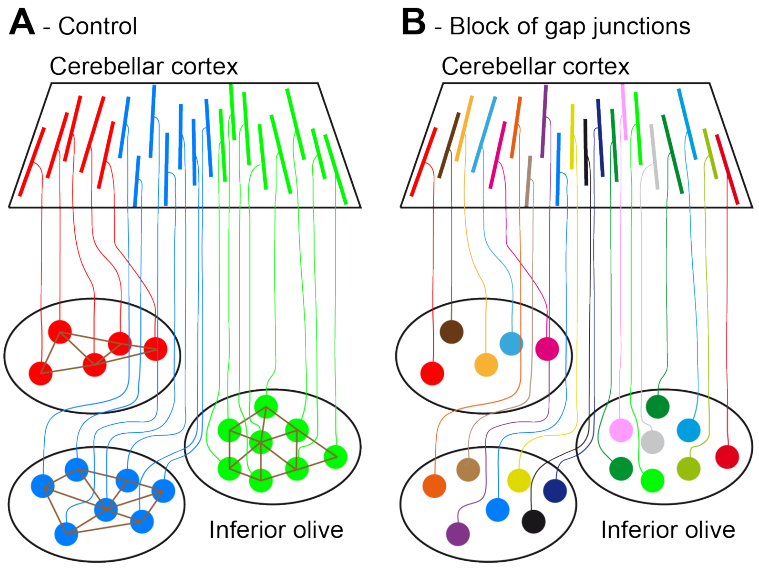

Fig. 9 Spatial patterns of complex spike synchrony. A – In normal animals, the neurons of the IO are organized in glomeruli, in which they are functionally coupled by dendrodendritic gap junctions (brown lines). Due to their electrotonic coupling, the neurons within a glomerulus have an increased tendency to fire synchronously. Because of the strict anatomical organization of the climbing fiber projections, each glomerulus projects to a parasagittal band of Purkinje cells in the cerebellar cortex. The upper part shows a schematic section through the molecular layer parallel to the surface. Each Purkinje cell forms a line, the transected dendritic tree. The synchrony in the glomeruli results in increased complex spike synchrony within "microbands." B – Disruption of the electrotonic coupling of the neurons in the IO abolishes synchrony within the glomeruli of the IO and thus also of complex spike firing by Purkinje cells. Each Purkinje cell now follows its own firing pattern, symbolized by different colors.

Indeed, eyeblink conditioning experiments revealed abnormal timing of the conditioned eyeblink responses in Cx36 / mice (Fig. 10a–b). The abnormal timing in these Cx36 -/- mice is probably due to an increased variety in the timing of climbing fiber responses, which in turn is probably the result of the desynchronization of the subthreshold oscillations in the IO (Van Der Giessen et al., 2008). In fact, this process will not only affect climbing fiber activity mediating the unconditioned stimulus but as the learning progresses also that of the conditioned stimuli (Ohmae and Medina 2015; Ten Brinke et al., 2015, 2017, 2019). Similar results in aberrant conditioned responses can be obtained when Cx36 gap junctions are pharmacologically blocked by mefloquine (Ozden et al., 2009). Interestingly, this impaired associative motor learning can also be observed in humans who use mefloquine as prophylaxis of malaria (van Essen et al., 2010). In silico simulations of the olivocerebellar module support the idea that unsynchronized climbing fiber feedback to Purkinje cells affects the plasticity of the parallel fiber – Purkinje cell synapse (Fig. 10c–d) – which ultimately results in an impaired timing of the conditioned behavior (see also De Zeeuw et al. 2011; Ten Brinke et al., 2015, 2017).

The IO receives feedback signals from the cerebellar and vestibular nuclei in the hindbrain. The inhibitory nucleo-olivary pathway gates the information relayed by the IO. Bengtsson et al.

(2007) showed, using eyeblink conditioning, that blocking the unconditioned stimuli by activating the nucleo-olivary pathway results in extinction of the conditioned blink response. Along the same line, blocking the inhibitory transmission of the nucleo-olivary pathway prevented the extinction of the conditioned response (Medina et al., 2002). Therefore, the inhibitory nucleo-olivary pathway might serve as a negative feedback loop to control motor learning (Bengtsson et al., 2007). In short, the behavioral data indicate that the output of the IO forms a population signal that contains a temporal code, which is able to adapt or reorganize the active motor system according to its needs and which can be controlled by feedback inputs from the hindbrain (De Zeeuw and Ten Brinke, 2015).

1.7 Functional models of the olivocerebellar system

1.7.1 Marr-Albus-Ito learning models

Important pioneering work on the theory of cerebellar function was made by Marr, Albus, and Ito (Albus 1971; Ito, 1984; Marr, 1969). Their theories combined are now widely known as the Marr-Albus-Ito hypothesis. Based on anatomical data, Marr initially put forward the idea of parallel fiber to Purkinje cell synapses as the main site of plasticity in the cerebellar cortex (Marr, 1969). Although plasticity was first proposed to potentiate synaptic transmission, it was Albus who proposed the oppo- site. From his point of view, climbing fiber activation served to signal an error that is able to cause depression of the synaptic transmission (Albus, 1971). Subsequently, Ito provided evidence that climbing fiber activation can indeed induce long-term depression at the parallel fiber to Purkinje cell synapse when it is conjunctively applied with parallel fiber activation (Ito and Kano, 1982; Ito et al. 1982). The size of such effects may even be graded, dependent on the duration of the burst in the IO axon involved (Mathy et al., 2009; Najafi and Medina, 2013).

The occurrence of a complex spike often correlates with some sort of unexpected event that can serve as an error signal. These include, for example, retinal slip signals during adaptation of the vestibulo-ocular reflex (Stone and Lisberger, 1986), sensory cornea signals during classical or Bayesian eyeblink conditioning with an air puff as an unconditioned stimulus (Anderson and Steinmetz, 1994), skin signals while triggering limb reflexes during locomotion (Armstrong et al., 1968; Ekerot and Jörntell, 2001), or whisker stimulation during a discrimination task (Bosman et al., 2010; Rahmati et al., 2014). All these conditions can be readily incorporated in the Marr-Albus-

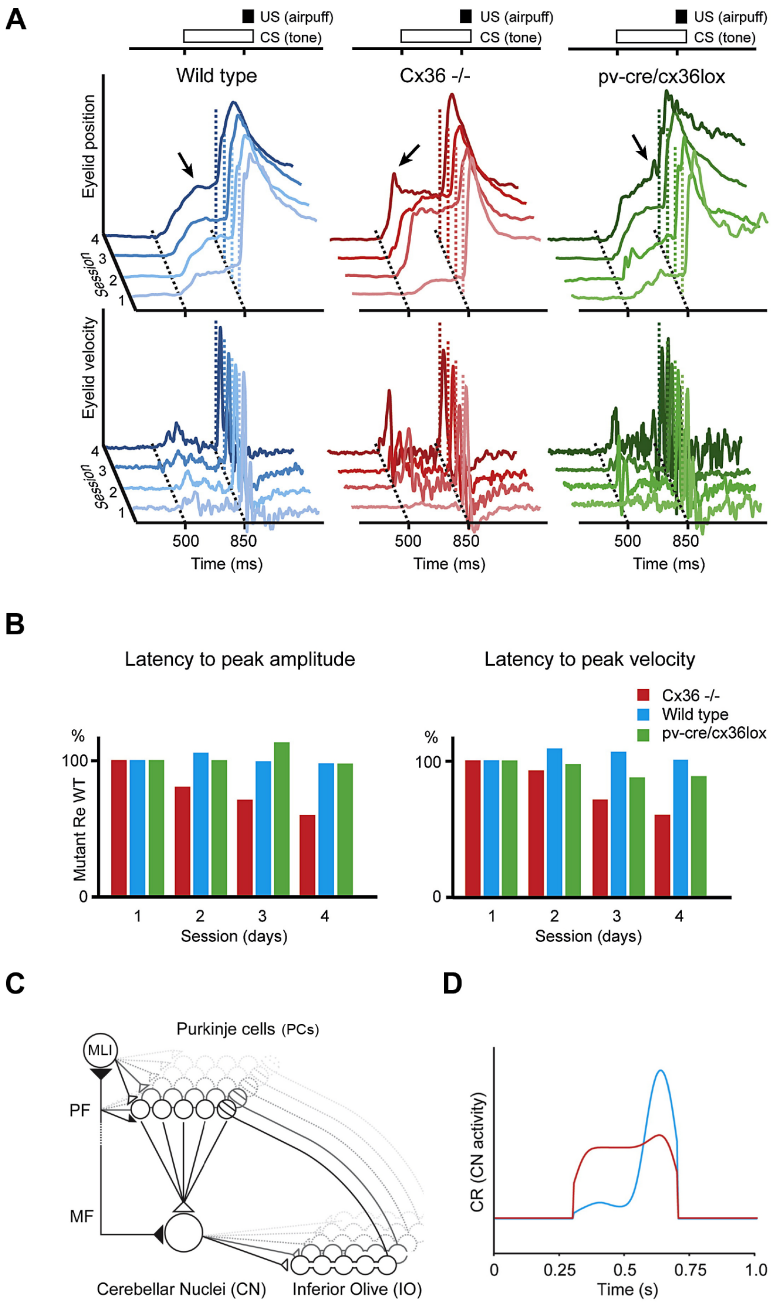

Fig. 10 Inferior olivary gap junctions are essential for proper timing in eyeblink conditioning task. A – Representative examples of eyeblink traces in a wild type (blue), global Cx36 / mutant (red), and Cx36 del(LacZ)/flox(CFP): parvalbumin-Cre control mouse (green). They all show conditioned eyeblink responses after four training sessions using a tone as the conditioned stimulus (CS) and an air puff as the unconditioned stimulus (US). However, while the timing of the learned response in wild-type and floxed-Cre control mice improves over the sessions, that in the global Cx36 / mutants gets worse (see arrows). B – While the latency to peak amplitude (left panel) in the global knockouts of Cx36 (red) got worse during the training sessions, that in the parvalbumin- Cre control mouse (green) was indistinguishable from that in their unaffected littermates (blue). Similarly, the average latency to peak velocity (right panel) in the mutants was also significantly reduced ($p < 0.01$; t test). C – A mathematical network simulation was used to analyze the impact of altered IO coupling on eyeblink conditioning. Panel C shows the schematic representation of the olivocerebellar model that is used for our network simulation. Purkinje cells (PK), neurons of the cerebellar nuclei (CN), and neurons of the IO (IO) form a close loop. A key feature is the strong convergence of Purkinje cells onto CN neurons. MF, PF, and BS indicate mossy fibers, parallel fibers, and basket/stellate cells, respectively. D – Conditioned eyeblink responses of wild types (blue) and Cx36 / mutants (red) resulting from the network simulation. More details can be found in Van der Giessen et al. (2008). (Reprinted with permission of Van der Giessen et al. 2008).

Ito hypothesis, as it states that learning takes place at the parallel fiber to Purkinje cell synapses when climbing fiber activation signals undesired events. Due to the simplicity and elegance of this hypothesis and its similarity to the simple neural networks used in the field of machine learning (e.g., perceptrons), many models simulating the olivocerebellar system have been built using the Marr- Albus-Ito framework (Albus, 1975; Fujita, 1982; Medina et al., 2000; Porrill et al., 2004; Schweighofer et al., 1998; Spoelstra et al., 2000; Van Der Giessen et al., 2008). Often, these models consist of an expansion filter for the input layer (granular layer), one layer of learning units (Purkinje cell layer), a layer to interpret the output (cerebellar nuclei), and a source for providing a corrective signal to guide learning (IO). The Golgi cells usually serve to prevent saturation and to ensure sparseness of encoding in the input layer, but under physiological circumstances, granule cells appear to be activated at relatively high numbers during sensorimotor learning (Badura and De Zeeuw, 2017; Giovannucci et al., 2017).

More recently, the Marr-Albus-Ito hypothesis has expanded into the concept of distributed synergistic plasticity (Gao et al., 2012). It involves three extra steps, all of which built upon the original theory. First, it is not only the presence of climbing fiber activity (i.e., complex spikes) but also the absence of it that can mediate motor learning. Indeed, parallel fiber activation without climbing fiber activation generates long-term potentiation (LTP) of the parallel fiber to Purkinje cell synapse (Coesmans et al., 2004), and this type of postsynaptic plasticity appears to be relevant, if not essential, for particular forms of motor learning, such as adaptation of the vestibulo- ocular reflex (Gutierrez-Castellanos et al., 2017; Schonewille et al., 2010; Voges et al., 2017) and reflex adaptation (Romano et al., 2018). Possibly, this form of plasticity is particularly relevant when the Purkinje cells involved fire their simple spikes at a relatively low baseline firing frequency, i.e., those of the zebrin-positive modules (De Zeeuw and Ten Brinke, 2015; Zhou et al., 2014). This is in contrast to the zebrin-negative modules, which fire at a high baseline firing frequency and which show decreases during other forms of motor learning, such as eyeblink conditioning (Halverson et al., 2015; Jirenhed et al., 2007; Ten Brinke et al., 2015). Second, climbing fibers facilitate and suppress many forms of plasticity, including both post- and presynaptic forms of plasticity at not only the parallel fiber to Purkinje cell Synapse, but also the parallel fiber to molecular layer interneuron synapses and the molecular layer interneuron to Purkinje Cell synapses (for review, see Gao et al., 2012; Boele et al., 2018). However, these synapses are not

Modified in a random fashion; the climbing fibers make sure that they influence them in a synergistic manner. For example, enhanced climbing fiber activity will induce long-term depression (LTD) at the parallel fiber to Purkinje cell synapse but potentiation at the parallel fiber to molecular layer interneuron synapse and the molecular layer interneuron to Purkinje cell

synapse, ultimately all leading to a reduced simple spike activity of the Purkinje cells. Likewise, absent or reduced climbing fiber activity will not only result in LTP at the parallel fiber to Purkinje cell synapse but also to depression at the parallel fiber to molecular layer interneuron synapse and the molecular layer interneuron to Purkinje cell synapse, ultimately increasing the simple spike activity. Third, the climbing fibers do not only influence activity in the output layer, but by modifying the parallel fiber to Golgi cell synapse, they may also influence activity in the input layer, further strengthening the synergy in a distributed fashion (Gao et al. 2012).

1.7.2 Motor timing models

An increasing amount of evidence indicates that the IO serves to signal errors and consequently guide the process of motor learning. The question that remains is: how can a heterogeneously electrotonically coupled network of IO neurons, with all the properties described above, consistently convey errors in such a way that it is well- suited for motor learning? So far, there have been only a few large-scale learning models that take the specific quirks of the IO into account (e.g., Van Der Giessen et al., 2008), as it is computationally demanding. As a result, it remains as of yet rather unclear how such properties may or may not contribute to providing an error and/or teaching signal.

The outcome may well be that the IO is not just a “teaching structure.” In theory, if the IO only flags errors or body disturbances, learning could take a long time due to the low incidence of spikes. Attempts to solve this problem by increasing the amount by which synaptic weights are modified would lead to inaccurate or even unstable learning. The low-firing rate of IO neurons, the oscillatory properties of the IO, and the immediate short-term effect of climbing fiber activations on the cerebellar cortex led to alternative hypotheses and models, in which the IO is a timing device necessary for accurate motor execution or timing-dependent motor learning.

One such theory highlights the role that recurrent connections in the olivocerebellar system may have (Kistler and De Zeeuw, 2002). The IO receives direct inhibitory input from the cerebellar nuclei and excitatory input from the mesodiencephalic junction, which in turn receives excitatory input from the cerebellar nuclei (De Zeeuw et al., 1998). Since cerebellar nuclei neurons have a tendency to show rebound activity several tens of ms after inhibition by Purkinje cells (Aizenman and Linden 1999; Aizenman et al. 1998; Czubayko et al. 2001; Jahnsen 1986; Llinás and Mühlethaler 1988; Ruigrok 1997), and this inhibition is likely to be most pronounced as a result of complex spikes (Hoebeek et al., 2010; Ten Brinke et al., 2017; Witter et al., 2013), the input from cerebellar nuclei neurons to the IO can be interpreted as a representation of IO activity tens of

ms earlier. Using simulations with a randomly distributed connectivity of the cerebellar nuclei neurons to the IO, it has been suggested that the reverberating loops present in the system may produce particular olivary firing patterns at subsequent firing windows, effectively rendering the IO capable of representing past events (Kistler and De Zeeuw, 2002).

Rodolfo Llinás, Yosef Yarom, John Welsh, and Eric Lang are advocates of a more IO-centric view of the olivocerebellar system (Welsh et al., 1995; Tang et al., 2019). Their hypotheses are focused on IO subthreshold oscillations and their possibilities to impose temporal control on dynamically shaped and coupled IO networks. In their models, the mossy fiber pathway may function to communicate a requested pattern, upon which the cerebellum primes the IO by splitting up the network into functional ensembles. These ensembles may in turn fire a temporal pattern determined by the phase differences in oscillations between cell ensembles, in theory allowing the system to use finer timing than just the 10 Hz dictated by IO subthreshold oscillations and to adjust the speed of motor control without affecting the sequence (Jacobson et al., 2008a). Indeed, the temporal patterns of IO activity may drive the beat of motor activity, similar to what can be seen following application of the tremorgenic drug harmaline (Llinás and Volkind, 1973). Similar motor-related activity can also be seen under more natural circumstances, such as at the onset of compensatory eye movements or of conditioned responses (Frens et al. 2001; Sato et al. 1993). Interestingly, the complex spikes and rebound activity highlighted above following eyeblink conditioning both emerge most prominently at the onset of these movements when the learning is fully completed (Ten Brinke et al., 2017).

A model based on the timing framework has been put forward as a working universal control system (Kazantsev et al., 2003). The system utilizes a hardware implementation of IO neurons and is reminiscent of the olivocerebellar system in architecture. In this model, oscillating units (i.e., IO cells) are connected by means of resistors (i.e., gap junctions) that can be altered by a controller (i.e., parts of the cerebellar nuclei and/or cerebellar cortex). The input consists of motor intention patterns sent to the coupling controller and the oscillators and external feedback sent to the oscillators only. The output of the oscillators is used to drive an actuator system and is also sent to the coupling controller for internal feedback. Despite some simplifications of the anatomy of the olivocerebellar system, it does show that alternative interpretations of the olivocerebellar system may be viable. Thus, most classical theories like the one propagated by Marr-Albus-Ito fail to fully explain some of the cellular features of the cerebellar nuclei and the IO, whereas the IO-centric motor timing theories leave questions to be answered about the necessity and abundance of parallel fibers. As is often the case when theories are not mutually exclusive, the actual truth is likely to be found in the combination of them (De Zeeuw et al., 2011).

1.8 Pahology of the inferior olive

Dysfunction of the IO may contribute to diseases including essential tremor, palatomyoclonus, and dystonia, as well as more rarely to disorders like some forms of ataxia, sudden infant death syndrome and other respiratory disorders, and autism spectrum disorders. Essential tremor is a common action tremor, starting most often in the arms, but it may also emerge in other parts of the body like the head, trunk, or vocal muscles (Deuschl and Elble, 2009; Louis and Ferreira, 2010). Patients with essential tremor share several symptoms with typical cerebellar patients, including overshoot and intention tremor during voluntary movements (Deuschl et al. 2000; Köster et al. 2002), impaired eyeblink conditioning (Kronenbuerger et al., 2007), and abnormal rhythm generation (Avanzino et al., 2009; Farkas et al., 2006). The characteristics of the 8–10 Hz tremor can be mimicked by application of harmaline, which hyperpolarizes neurons of the IO and presumably leads to burst firing by de-inactivating calcium currents (Bernard et al., 1984; Llinás and Volkind, 1973, 1986; Long et al., 2002; Louis et al., 2002; Martin et al., 2005). Indeed, blocking T-type Ca^{2+} channels in the IO abolishes a harmaline-induced tremor (Handforth et al. 2010; Park et al., 2010). Interestingly, silencing the synaptic output of the IO can also induce a tremor with a frequency of about 10 Hz (White and Sillitoe, 2017), which highlights the possibility that the rhythms in the IO are partly generated to dampen some of the oscillations that may occur within the motor system under natural circumstances. Thus, both abnormalities that overactivate the olivary output and those that inactivate it can cause, or contribute to, essential tremor, highlighting the importance of fine-regulating the olivary oscillations.

Other types of tremor have also been described in combination with IO pathology. Hypertrophy of the IO, which typically occurs following a stroke affecting the dentato-olivary pathway (Koeppen et al., 1980), can lead to contralateral palatomyoclonus, which is an involuntary tremor of the soft palate (Deuschl et al., 1994; Lim and Lim, 2009). Palatomyoclonus occurs relatively often, but not always, together with pendular nystagmus (Deuschl et al., 1994; Liao et al., 2008; Lim and Lim, 2009). Hypertrophy of the principal olive and rostral medial accessory olive, both of which receive input from the mesodiencephalic junction (see section “Inputs and Origin”), can be mimicked in cats following lesions of the brachium conjunctivum or its source in the cerebellar nuclei (De Zeeuw et al., 1990d; Ruigrok et al., 1990). The hypertrophic cells are characterized by extensive dendritic and somatic coupling as well as relatively many long-latency responses following stimulation from mesodiencephalic junction. Possibly, the extensive coupling at the proximal level of the IO cells allows them to survive and generate

prominent oscillations at relatively low-firing frequency (De Zeeuw et al., 1990d; Ruigrok et al., 1990).

In addition, a tremor induced by abnormal olivary activity can be part of a larger syndrome, such as dystonia, which is characterized by symptoms like early-onset twisting and stiff limbs. Indeed, in some patients suffering from basal ganglia- independent dystonia, the IO is infiltrated by microglia and macrophages and shows metabolic defects (Raike et al., 2005; Simonyan et al., 2010; Zhao et al., 2011). Likewise, olivary lesions and/or reduced olivary activity may also contribute to dystonic postures in animals (LeDoux, 2011; Llinás et al., 1975). But then again, in other rodent models, the dystonic symptoms can be rescued by inactivation of the IO (Hisatsune et al., 2013). Thus, here too it appears to be critical to fine-regulate IO activity in a well-balanced way to avoid symptoms of dystonia.

Finally, the IO is infrequently also implicated in specific disorders that are associated with general movement deficits, like spinocerebellar ataxia (SCA) type 6, 7, and 23 (Holmberg et al., 1998; Verbeek, 2009; Wang et al., 2010a, b), in specific disorders that are associated with inhalation or speech issues, like fatal insomnia (Ayuso Blanco et al., 2006; Montagna et al., 2003), Wolfram syndrome (Hilson et al., 2009), semantic dementia (Davies et al. 2005), acute respiratory defects (Harper et al., 2000; Matschke and Laas, 2007), or forms of sudden infant death syndrome that result from abnormalities in substance P neurokinin-1 receptor binding (Bright et al., 2017), or in more general disorders with both motor and cognitive dysfunctions, like fetal alcohol syndrome (Dikranian et al., 2005; Jacobson et al., 2008b; Swayze et al., 1997) and autism spectrum disorders (Bailey et al., 1998; Prandota, 2010; Welsh et al., 2005).

1.9 Inferior Olive and Sleep

Sleep is one of the most important, ubiquitous but still unknown animal behavior. It is crucial for cognition, memory, decision making, immnunity and health in general (Scammel et al., 2017; Canto et al., 2017). Based on electroencephalogram (EEG) and electromyogram recordings (EMG) sleep can be divided in 4 stages: 1 stage of rapid eye movement (REM) and 3 stages of Non-REM (NREM 1, 2 and 3). As its name indicates, REM sleep is chactacterized by fast saccadic eye movement and cortical EEG recordings showing low amplitude waves in the theta range (4-7 Hz). The REM theta activity, which arises mostly from the dorsal hippocampus, is more abundant in rodents than in humans. In this sleep stage muscle activity is suppressed to avoid dream-enacting; indeed it is in this period during which one can experience vivid dreams or story-like dreams (Scammel et al., 2017).

Unlike REM sleep, during NREM sleep the animal is mainly unconscious or has bland thoughts and eyes movements are rather roving. NREM 1 and 2 are the light phases of sleep, which means that during these stages an animal can be awakened more easily. NREM1 is the lightest phase of sleep and shows theta activity and a loss of alpha activity (8 to 13 Hz), which was present previously during the drowsy wakefulness state (Carley and Farabi. 2016). NREM2 sleep is characterized by the presence of single slow waves called K-complexes, whereas NREM3 or slow-wave sleep shows high amplitude waves with a peak frequency of less than 1 Hz (Canto et al., 2017). These latter slow waves are probably generated by the cortical activity and reflect the synchronous hyperpolarization and depolarization with irregular firing of a big neuronal ensemble (Steriade and Amizca, 1993). These stages may be crucial for memory consolidation (Klinzing et al., 2019). NREM2 and NREM3 share in common the presence of spindles, short burst of activity in the range of 10 to 15 Hz, which may well facilitate memory formation and learning (Piantoni et al., 2016; Ulrich, 2016). They probably reflect the interaction between Gabaergic cells located in the reticular nucleus of the thalamus and glutamatergic thalamocortical cells (Piantoni et al., 2016).

Most of the sleep research has only focused on the interaction between cerebral cortex and subcortical structures ignoring the contribution of the olivo-cerebellar circuit. This is surprising, because there is a strong connectivity between the cerebellum and the cerebral cortex via the thalamus, the inferior olive (IO), mesodiencephalic junction - one of the main excitatory inputs of the IO - and the pons (De Zeeuw et al., 2008). Moreover, changes in the cerebellar structure such as decreased gray matter volume are related to chronic insomnia (Del Rosso and Hoque., 2014) and spinocerebellar ataxia can lead to sleep disorders (Pedroso at al., 2011; Sonni et al., 2014). Furthermore, cerebellar cortex activity of cats has also shown to be modulated by different sleep stages where simple and complex spikes activity are enhanced during NREM sleep and decreased during REM sleep (Hobson and McCarley., 1972). Similar observations apply to the ceberellar nuclei where firing frequency is increased during NREM sleep (Palmer, 1979). However, it is not known how spatiotemporal patterns of complex and simple spike activity in the cerebellar cortex change across the various sleep stages.

1.10 Conclusions

The inferior olive has evolved as a unique nucleus in the brain with neurons that show extensive electrotonic coupling and a propensity to oscillate. Most, if not all, their dendritic spines receive a combined excitatory and inhibitory input, by which the spatial configuration of ensembles of activated olivary neurons can be shaped and by which the onset of the oscillatory activity can be determined and reset. Through its climbing fibers, the inferior olive exerts a prominent impact on cerebellar output and thereby on motor behavior; it does so both acutely by pacing the motor commands and more long-term by modifying the weights of many different types of synapses in the cerebellar cortex in a synergistic fashion. As a consequence, deficits in olivary function can contribute to a plethora of syndromes, varying from simple tremors up to complex disorders like dystonia and autism.

1.11 Scopes of the thesis

In this thesis I investigate several aspects of the inferior olive (IO) that are crucial to understand how this brainstem structure processes information and controls motor learning. The topics studied in this thesis are the anatomical organization of the IO network, the temporal interactions of postsynaptic responses to excitatory and inhibitory inputs and their impact on subthreshold oscillations, spike output and motor learning, as well as the changes in the spatiotemporal patterns of complex spikes during sleep.

Previous studies have proposed that IO neurons can be divided into two types based on their dendritic morphology: straight neurons, with long dendrites that radiate away from the soma, and curly neurons, with dendrites coiling back to the soma with the appearance of spirals (Ruigrok et at.1990). These two types are supposed to be functionally distinct and spatially segregated in different IO subnuclei (Urbano et al., 2006). However, this classification is based on historical observations of a limited number of cells, making it difficult to judge if IO neurons really exist as two morphological cell types or whether perhaps there is a smooth continuum of morphologies. In Chapter 2, I study if the latter hypothesis holds by making 3D reconstructions of an extensive data set of labeled IO neurons spanning several IO subnuclei to obtain detailed and quantitative measures of IO dendrite morphology. One of these parameters, the directionality of their dendrites allow us to address a topic that is still under debate, i.e. whether IO neurons are grouped into anatomical clusters.

As a result of the close proximity of inhibitory and excitatory synaptic inputs on electrically coupled dendritic spines of IO neurons, their local temporal interaction is critical in affecting how IO neurons generate output (De Zeeuw et al., 1995; Segev and Parnas, 1983). A majority of IO neurons display subthreshold oscillations (STOs) that are modulated by both excitatory or inhibitory synaptic inputs (Turecek et al., 2014; Leefler et al., 2013). A subset of IO neurons do not generate STOs, but some of them, the so-called 'condtional oscillators' still respond to input with transient STOs following injection of a hyperpolarizing current pulse (Bazzigaluppi et al., 2016). Despite the unique features exhibited by IO neurons, there are no studies that have addressed how the presentation of the inhibitory and excitatory inputs they receive interact. For this reason, in Chapter 3 I investigate how inhibitory and excitatory inputs presented at different intervals affect the amplitude and phase of the STOs as well as the spike probability of IO neurons. Likewise, I investigate the impact of excitatory and inhibitory inputs on conditional oscillators. I use electrophysiological recordings in vitro along with optogenetic stimulation in order to selectively stimulate inhibitory and excitatory afferents coming from the CN and MDJ, respectively. Furthermore, I show how stimulating CN and MDJ afferents to the IO at specific intervals can have great consequences for motor learning using a paradigm of reflexive whisker protraction (Romano et al., 2018).

Despite the fact that the cerebellum and cerebral cortex are reciprocally connected (De Zeeuw et al., 2008) and that cerebellar loss-of-function can cause sleep disorders (Pedroso at al., 2011; Sonni et al., 2014), relatively little is known about the engagement of the olivo-cerebellar circuit during sleep. For this reason, in Chapter 4 I focus on the role of the inferior olive during sleep. By using miniscope recordings along with EEG and EMG recordings, I describe sleep stage specific modulation of complex spike activity in ensembles spanning many neighboring Purkinje cells.

1.13 References

Acampora D, Mazan S, Lallemand Y, Avantaggiato V, Maury M, Simeone A, Brûlet P (1995) Forebrain and midbrain regions are deleted in Otx2-/- mutants due to a defective anterior neuroectoderm specification during gastrulation. Development 121:3279–3290

Adams KA, Maida JM, Golden JA, Riddle RD (2000) The transcription factor Lmx1b maintains Wnt1 expression within the isthmic organizer. Development 127:1857–1867

Aizenman CD, Linden DJ (1999) Regulation of the rebound depolarization and spontaneous firing patterns of deep nuclear neurons in slices of rat cerebellum. J Neurophysiol 82:1697–1709.

Aizenman CD, Manis PB, Linden DJ (1998) Polarity of long-term synaptic gain change is related to postsynaptic spike firing at a cerebellar inhibitory synapse. Neuron 21:827–835

Albus JS (1971) A theory of cerebellar function. Math Biosci 10:25–61

Albus JS (1975) New approach to manipulator control: the cerebellar model articulation controller (CMAC). Trans ASME J Dyn Syst Meas Control 97:220–227

Alexander T, Nolte C, Krumlauf R (2009) Hox genes and segmentation of the hindbrain and axial skeleton. Annu Rev Cell Dev Biol 25:431–456. Altman J (1972) Postnatal development of the cerebellar cortex in the rat. II. Phases in the maturation of Purkinje cells and of the molecular layer. J Comp Neurol 145:399–463.

Altman J, Anderson WJ (1972) Experimental reorganization of the cerebellar cortex.

I. Morphological effects of elimination of all microneurons with prolonged x-irradiation started at birth. J Comp Neurol 146:355–406.

Altman J, Bayer SA (1978a) Prenatal development of the cerebellar system in the rat. I. Cytogenesis and histogenesis of the deep nuclei and the cortex of the cerebellum. J Comp Neurol 179:23–48.

Altman J, Bayer SA (1978b) Prenatal development of the cerebellar system in the rat.

II. Cytogenesis and histogenesis of the inferior olive, pontine gray, and the precerebellar reticular nuclei. J Comp Neurol 179:49–75.

Altman J, Bayer SA (1987) Development of the precerebellar nuclei in the rat: II. The intramural olivary migratory stream and the neurogenetic organization of the inferior olive. J Comp Neurol 257:490–512.

Ambrosiani J, Armengol JA, Martinez S, Puelles L (1996) The avian inferior olive derives from the alar neuroepithelium of the rhombomeres 7 and 8: an analysis by using chick-quail chimeric embryos. Neuroreport 7:1285–1288.

Amoyel M, Cheng YC, Jiang YJ, Wilkinson DG (2005) Wnt1 regulates neurogenesis and mediates lateral inhibition of boundary cell specification in the zebrafish hindbrain. Development 132:775–785.

Anderson BJ, Steinmetz JE (1994) Cerebellar and brainstem circuits involved in classical eyeblink conditioning. Rev Neurosci 5:251–273.

Apps R and Hawkes R (2009) Cerebellar cortical organization: a one-map hypothesis. Nat Rev Neurosci. 10(9): 670-681.

Aragón F et al (2005) vHnf1 regulates specification of caudal rhombomere identity in the chick hindbrain. Dev Dyn 234:567–576.

Armstrong DM (1974) Functional significance of connections of the inferior olive. Physiol Rev 54:358–417.

Armstrong DM, Eccles JC, Harvey RJ, Matthews PBC (1968) Responses in the dorsal accessory olive of the cat to stimulation of hind limb afferents. J Physiol 194:125–145.

Avanzino L, Bove M, Tacchino A, Ruggeri P, Giannini A, Trompetto C, Abbruzzese G (2009) Cerebellar involvement in timing accuracy of rhythmic finger movements in essential tremor. Eur J Neurosci 30:1971–1979.

Ayuso Blanco T, Urriza Mena J, Caballero Martinez C, Iriarte Franco J, Munoz R, Garcia-Bragado F (2006) Insomnio letal familiar: Estudio clínico, neurofisiológico e histopatológico de dos casos. Neurologia 21:414–420.

Badura A, De Zeeuw CI (2017) Cerebellar granule cells: dense, rich and evolving representations. Curr Biol 27:R415–R418.

Badura A et al (2013) Climbing fiber input shapes reciprocity of Purkinje cell firing. Neuron 78:700–713.

Bailey A et al (1998) A clinicopathological study of autism. Brain 121:889–905.

Bal T, McCormick DA (1997) Synchronized oscillations in the inferior olive are controlled by the hyperpolarization-activated cation current I(h). J Neurophysiol 77:3145–3156.

Barragan LA, Galindo-Morales JA, Delhaye-Bouchaud N (1983) The microiontophoretic sensitivity of the inferior olivary nucleus to serotonin and related drugs. Proc West Pharmacol Soc 26:151–154.

Bazzigaluppi P, De Gruijl JR, van der Giessen RS, Khosrovani S, De Zeeuw CI, de Jeu MTG (2012a) Olivary subthreshold oscillations and burst activity revisited. Front Neural Circuits 6:91.

Bazzigaluppi P, de Jeu MTG (2016) Heterogeneous expression of T-type Ca^{2+} channels defines different neuronal populations in the inferior olive of the mouse. Front Cell Neurosci 10:192.

Bazzigaluppi P, Isenia SC, Haasdijk ED, Elgersma Y, De Zeeuw CI, van der Giessen RS, de Jeu MTG (2017) Modulation of murine olivary connexin 36 gap junctions by PKA and CaMKII. Front Cell Neurosci 11:397.

Bazzigaluppi P, Ruigrok T, Saisan P, De Zeeuw CI, de Jeu M (2012b) Properties of the nucleo-olivary pathway: an in vivo whole-cell patch clamp study. PLoS One 7:e46360.

Becker N et al (1994) Several receptor tyrosine kinase genes of the Eph family are segmentally expressed in the developing hindbrain. Mech Dev 47:3–17.

Bell CC, Grimm RJ (1969) Discharge properties of Purkinje cells recorded on single and double microelectrodes. J Neurophysiol 32:1044–1055.

Bell CC, Kawasaki T (1972) Relations among climbing fiber responses of nearby Purkinje cells.

J Neurophysiol 35:155–169.

Benardo LS, Foster RE (1986) Oscillatory behavior in inferior olive neurons: mechanism, modulation, cell aggregates. Brain Res Bull 17:773–784.

Bengtsson F, Jirenhed DA, Svensson P, Hesslow G (2007) Extinction of conditioned blink responses by cerebello-olivary pathway stimulation. Neuroreport 18:1479–1482.

Berkley KJ, Worden IG (1978) Projections to the inferior olive of the cat. I. Comparisons of input from the dorsal column nuclei, the lateral cervical nucleus, the spino-olivary pathways, the cerebral cortex and the cerebellum. J Comp Neurol 180(2):237-51.

Bergemann AD, Cheng HJ, Brambilla R, Klein R, Flanagan JG (1995) ELF-2, a new member of the Eph ligand family, is segmentally expressed in mouse embryos in the region of the hindbrain and newly forming somites. Mol Cell Biol 15:4921–4929.

Bernard JF, Buisseret-Delmas C, Compoint C, Laplante S (1984) Harmaline induced tremor. III. A combined simple units, horseradish peroxidase, and 2-deoxyglucose study of the olivocerebellar system in the rat. Exp Brain Res 57:128–137.

Bishop GA, Ho RH (1984) Substance P and serotonin immunoreactivity in the rat inferior olive. Brain Res Bull 12:105–113.

Bleasel AF, Pettigrew AG (1992) Development and properties of spontaneous oscillations of the membrane potential in inferior olivary neurons in the rat. Brain Res Dev Brain Res 65:43–50.

Bleckert A, Wong ROL (2011) Identifying roles for neurotransmission in circuit assembly: insights gained from multiple model systems and experimental approaches. BioEssays 33:61–72.

Blenkinsop TA, Lang EJ (2006) Block of inferior olive gap junctional coupling decreases Purkinje cell complex spike synchrony and rhythmicity. J Neurosci 26:1739–1748.

Bloch-Gallego E, Ezan F, Tessier-Lavigne M, Sotelo C (1999) Floor plate and netrin-1 are involved in the migration and survival of inferior olivary neurons. J Neurosci 19:4407–4420.

Boele HJ, Peter S, Ten Brinke MM, Verdonschot L, IJpelaar ACH, Rizopoulos D, Gao Z, Koekkoek SKE, Zeeuw CID (2018) Impact of parallel fiber to Purkinje cell long-term depression is unmasked in absence of inhibitory input Science Advances, vol 4, no 10.

Boesten AJ, Voogd J (1975) Projections of the dorsal column nuclei and the spinal cord on the inferior olive in the cat. J Comp Neurol 161(2):215-37.

Bosman LWJ, Hartmann J, Barski JJ, Lepier A, Noll-Hussong M, Reichardt LF, Konnerth A (2006) Requirement of TrkB for synapse elimination in developing cerebellar Purkinje cells. Brain Cell Biol 35:87–101.

Bosman LWJ et al (2010) Encoding of whisker input by cerebellar Purkinje cells. J Physiol 588:3757–3783.

Bosman LWJ, Konnerth A (2009) Activity-dependent plasticity of developing climbing fiber-Purkinje cell synapses. Neuroscience 162:612–623.

Bosman LWJ, Takechi H, Hartmann J, Eilers J, Konnerth A (2008) Homosynaptic LTP of the "winner" climbing fiber synapse in developing Purkinje cells. J Neurosci 28:798–807

Bourrat F, Sotelo C (1988) Migratory pathways and neuritic differentiation of inferior olivary neurons in the rat embryo. Axonal tracing study using the in vitro slab technique. Brain Res Dev Brain Res 39:19–37.

Bowman JP, Sladek JR Jr (1973) Morphology of the inferior olivary complex of the rhesus monkey (Macaca mulatta). J Comp Neurol 152:299–316.

Bright FM, Vink R, Byard RW, Duncan JR, Krous HF, Paterson DS (2017) Abnormalities in substance P neurokinin-1 receptor binding in key brainstem nuclei in sudden infant death syndrome related to prematurity and sex. PLoS One 12:e0184958.

Broccoli V, Boncinelli E, Wurst W (1999) The caudal limit of Otx2 expression positions the isthmic organizer. Nature 401:164–168.

Bull MS, Mitchell SK, Berkley KJ (1990) Convergent inputs to the inferior olive from the dorsal column nuclei and pretectum in the cat. Brain Res. 525(1):1-10.

Canto CB, Onuki Y, Bruinsma B, van der Werfm De Zeeuw CI (2017). The sleeping cerebellum. Trends Neurosci. 40(5): 309-323.

Carley DW and Farabi SS (2016). Physiology of sleep. Diabetes Spect 29(1):5-9.

Carpenter EM, Goddard JM, Chisaka O, Manley NR, Capecchi MR (1993) Loss of Hox-A1 (Hox-1.6) function results in the reorganization of the murine hindbrain. Development 118:1063–1075

Cesa R, Morando L, Strata P (2005) Purkinje cell spinogenesis during architectural rewiring in the mature cerebellum. Eur J Neurosci 22:579–586.

Cesa R, Scelfo B, Strata P (2007) Activity-dependent presynaptic and postsynaptic structural plasticity in the mature cerebellum. J Neurosci 27:4603–4611.

Chan-Palay V, Palay SL (1971) Tendril and glomerular collaterals of climbing fibers in the granular layer of the rat's cerebellar cortex. Z Anat Entwicklungsgesch 133:247–273.

Chédotal A, Sotelo C (1992) Early development of olivocerebellar projections in the fetal rat ssing CGRP immunocytochemistry. Eur J Neurosci 4:1159–1179.

Chédotal A, Sotelo C (1993) The 'creeper stage' in cerebellar climbing fiber synaptogenesis precedes the 'pericellular nest'–ultrastructural evidence with parvalbumin immunocytochemis- try. Brain Res Dev Brain Res 76:207–220.

Chi CL, Martinez S, Wurst W, Martin GR (2003) The isthmic organizer signal FGF8 is required for cell survival in the prospective midbrain and cerebellum. Development 130:2633–2644.

Chizhikov VV et al (2010) Lmx1a regulates fates and location of cells originating from the cerebellar rhombic lip and telencephalic cortical hem. Proc Natl Acad Sci U S A 107:10725–10730.

Choi S, Yu E, Kim D, Urbano FJ, Makarenko V, Shin HS, Llinás RR (2010) Subthreshold membrane potential oscillations in inferior olive neurons are dynamically regulated by P/Q- and T-type calcium channels: a study in mutant mice. J Physiol 588:3031–3043.

Choo M et al (2017) Retrograde BDNF to TrkB signaling promotes synapse elimination in the developing cerebellum. Nat Commun 8:195.

Ciani L, Salinas PC (2005) WNTs in the vertebrate nervous system: from patterning to neuronal connectivity. Nat Rev Neurosci 6:351–U317.

Coesmans M, Weber JT, De Zeeuw CI, Hansel C (2004) Bidirectional parallel fiber plasticity in the cerebellum under climbing fiber control. Neuron 44:691–700.

Condorelli DF, Parenti R, Spinella F, Trovato Salinaro A, Belluardo N, Cardile V, Cicirata F (1998) Cloning of a new gap junction gene (Cx36) highly expressed in mammalian brain neurons. Eur J Neurosci 10:1202–1208.

Cozzi B, Huggenberger S, Oelschläger H (2016) Anatomy of dolphins. Academic Press, London

Crepel F (1971) Maturation of climbing fiber responses in the rat. Brain Res 35:272–276.

Crepel F (1982) Regression of functional synapses in the immature mammalian cerebellum. Trends Neurosci 5:266–269.

Crepel F, Delhaye-Bouchaud N, Dupont JL (1981) Fate of the multiple innervation of cerebellar Purkinje cells by climbing fibers in immature control, x-irradiated and hypothyroid rats. Brain Res Dev Brain Res 1:59–71.

Crill WE (1970) Unitary multiple-spiked responses in cat inferior olive nucleus. J Neurophysiol 33:199–209.

Crill WE, Kennedy TT (1967) Inferior olive of the cat: intracellular recording. Science (New York, NY) 157:716–718.

Cunningham TJ, Duester G (2015) Mechanisms of retinoic acid signalling and its roles in organ and limb development. Nature Reviews Molecular and Cellular Biology 16:110–123.

Czubayko U, Sultan F, Thier P, Schwarz C (2001) Two types of neurons in the rat cerebellar nuclei as distinguished by membrane potentials and intracellular fillings. J Neurophysiol 85:2017–2029.

Dahmann C, Oates AC, Brand M (2011) Boundary formation and maintenance in tissue development. Nat Rev Genet 12:43–55.

Davies RR, Hodges JR, Kril JJ, Patterson K, Halliday GM, Xuereb JH (2005) The pathological basis of semantic dementia. Brain 128:1984–1995.

De Groot A, Den Boom BJG, Van Genderen RM, Coppens J, Van Veldhuijzen J, Bos G, Hoedemaker H, Negrello M, Willuhn I, De Zeeuw CI, Hoogland TM (2020) NINscope: a versatile miniscopes for multi-region circuit investigations. eLife 9: e49987.

De Gruijl J, Sokol P, Negrello M, De Zeeuw CI (2016) Calcium dependent gap junction plasticity: modulation of electrotonic coupling in the inferior olive glomerulus. bioRxiv:072041.

De Gruijl JR, Bazzigaluppi P, de Jeu MTG, De Zeeuw CI (2012) Climbing fiber burst size and olivary sub-threshold oscillations in a network setting. PLoS Comput Biol 8:e1002814.

De Gruijl JR, Hoogland TM, De Zeeuw CI (2014a) Behavioral correlates of complex spike synchrony in cerebellar microzones. J Neurosci 34:8937–8944.

De Gruijl JR, Sokol PA, Negrello M, De Zeeuw CI (2014b) Modulation of electrotonic coupling in the inferior olive by inhibitory and excitatory inputs: integration in the glomerulus. Neuron 81:1215–1217

DelRosso LM and Hoque R (2014). The cerebellum and sleep. Neur. ol Clin 32(4):893-900.

De Zeeuw CI (2021). Bidirectional learning in upbound and downbound microzones of the cerebellum. Nat Rev Neurosci.

De Zeeuw C (1990) Ultrastructure of the cat inferior olive. Erasmus, Rotterdam.

De Zeeuw CI et al (2003) Deformation of network connectivity in the inferior olive of connexin 36-deficient mice is compensated by morphological and electrophysiological changes at the single neuron level. J Neurosci 23:4700–4711.

De Zeeuw CI, Gerrits NM, Voogd J, Leonard CS, Simpson JI (1994) The rostral dorsal cap and ventrolateral outgrowth of the rabbit inferior olive receive a GABAergic input from dorsal group Y and the ventral dentate nucleus. J Comp Neurol 341:420–432.

De Zeeuw CI, Hertzberg EL, Mugnaini E (1995) The dendritic lamellar body: a new neuronal organelle putatively associated with dendrodendritic gap junctions. J Neurosci 15:1587–1604.

De Zeeuw CI, Hoebeek FE, Bosman LWJ, Schonewille M, Witter L, Koekkoek SK (2011) Spatiotemporal firing patterns in the cerebellum. Nat Rev Neurosci 12:327–344.

De Zeeuw CI, Holstege JC, Calkoen F, Ruigrok TJ, Voogd J (1988) A new combination of WGA-HRP anterograde tracing and GABA immunocytochemistry applied to afferents of the cat inferior olive at the ultrastructural level. Brain Res 447:369–375.

De Zeeuw CI, Holstege JC, Ruigrok TJ, Voogd J (1989a) Ultrastructural study of the GABAergic, cerebellar, and mesodiencephalic innervation of the cat medial accessory olive: anterograde tracing combined with immunocytochemistry. J Comp Neurol 284:12–35.

De Zeeuw CI, Holstege JC, Ruigrok TJH, Voogd J (1989b) The cerebellar, mesodiencephalic and GABAergic innervation of the glomeruli in the cat inferior olive. A comparison at the ultra-structural level. In: Strata P (ed) The olivocerebellar system in motor control, Experimental brain research series, vol 17. Springer, Berlin/Heidelberg.

De Zeeuw CI, Holstege JC, Ruigrok TJH, Voogd J (1990a) Mesodiencephalic and cerebellar terminals terminate upon the same dendritic spines in the glomeruli of the cat and rat inferior olive: an ultrastructural study using a combination of [3H]leucine and wheat germ agglutinin coupled horseradish peroxidase anterograde tracing. Neuroscience 34:645–655.

De Zeeuw CI, Hoogenraad CC, Goedknegt E, Hertzberg E, Neubauer A, Grosveld F, Galjart N (1997a) CLIP-115, a novel brain-specific cytoplasmic linker protein, mediates the localization of dendritic lamellar bodies. Neuron 19:1187–1199.

De Zeeuw CI, Hoebeek FE, Schonewille M (2008). Causes and consequences of oscillations in the cerebellar cortex. Neuron 58(5): 655-658.

De Zeeuw CI, Koekkoek SKE, Wylie DRW, Simpson JI (1997b) Association between dendritic lamellar bodies and complex spike synchrony in the olivocerebellar system. J Neurophysiol 77:1747–1758.

De Zeeuw CI, Lang EJ, Sugihara I, Ruigrok TJH, Eisenman LM, Mugnaini E, Llinás R (1996) Morphological correlates of bilateral synchrony in the rat cerebellar cortex. J Neurosci 16:3412–3426.

De Zeeuw CI, Ruigrok TJ (1994) Olivary projecting neurons in the nucleus of Darkschewitsch in the cat receive excitatory monosynaptic input from the cerebellar nuclei. Brain Res 653:345–350

De Zeeuw CI, Ruigrok TJH, Holstege JC, Jansen HG, Voogd J (1990b) Intracellular labeling of neurons in the medial accessory olive of the cat: II. Ultrastructure of dendritic spines and their GABAergic innervation. J Comp Neurol 300:478–494.

De Zeeuw CI, Ruigrok TJH, Holstege JC, Schalekamp MPA, Voogd J (1990c) Intracellular labeling of neurons in the medial accessory olive of the cat: III. Ultrastructure of axon hillock and initial segment and their GABAergic innervation. J Comp Neurol 300:495–510.

De Zeeuw CI, Ruigrok TJH, Schalekamp MPA, Boesten AJ, Voogd J (1990d) Ultrastructural study of the cat hypertrophic inferior olive following anterograde tracing, immunocytochemistry, and intracellular labeling. Eur J Morphol 28:240–255.

De Zeeuw CI, Simpson JI, Hoogenraad CC, Galjart N, Koekkoek SKE, Ruigrok TJH (1998) Microcircuitry and function of the inferior olive. Trends Neurosci 21:391–400.

De Zeeuw CI, Ten Brinke MM (2015) Motor learning and the cerebellum. Cold Spring Harb Perspect Biol 7:a021683.

De Zeeuw CI, Wentzel P, Mugnaini E (1993) Fine structure of the dorsal cap of the inferior olive and its GABAergic and non-GABAergic input from the nucleus prepositus hypoglossi in rat and rabbit. J Comp Neurol 327:63–82.

Deuschl G, Elble R (2009) Essential tremor–neurodegenerative or nondegenerative disease towards a working definition of ET. Mov Disord 24:2033–2041.

Deuschl G, Toro C, Valls-Solé J, Zeffiro T, Zee DS, Hallett M (1994) Symptomatic and essential palatal tremor. 1. Clinical, physiological and MRI analysis. Brain 117:775–788.

Deuschl G, Wenzelburger R, Löffler K, Raethjen J, Stolze H (2000) Essential tremor and cerebellar dysfunction clinical and kinematic analysis of intention tremor. Brain 123:1568–1580.

Deverett B, Koay SA, Oostland M, Wang SS (2018) Cerebellar involvement in an evidence-accumulation decision-making task. Elife 7:e36781.

Devor A, Yarom Y (2002a) Electrotonic coupling in the inferior olivary nucleus revealed by simultaneous double patch recordings. J Neurophysiol 87:3048–3058.

Devor A, Yarom Y (2002b) Generation and propagation of subthreshold waves in a network of inferior olivary neurons. J Neurophysiol 87:3059–3069.

Di Meglio T, Nguyen-Ba-Charvet KT, Tessier-Lavigne M, Sotelo C, Chédotal A (2008) Molecular mechanisms controlling midline crossing by precerebellar neurons. J Neurosci 28:6285–6294.

Dikranian K, Qin YQ, Labruyere J, Nemmers B, Olney JW (2005) Ethanol-induced neuroapoptosis in the developing rodent cerebellum and related brain stem structures. Brain Res Dev Brain Res 155:1–13.

Duester G (2007) Retinoic acid regulation of the somitogenesis clock. Birth Defects Res C Embryo Today 81:84–92.

Duggan AW, Lodge D, Headley PM, Biscoe TJ (1973) Effects of excitants on neurones and cerebellar-evoked field potentials in the inferior olivary complex of the rat. Brain Res 64:397–401

Eccles J, Llinás R, Sasaki K (1964) Excitation of cerebellar Purkinje cells by the climbing fibres. Nature 203:245–246.

Egea J, Klein R (2007) Bidirectional Ephephrin signaling during axon guidance. Trends Cell Biol 17:230–238.

Eilers J, Plant TD, Marandi N, Konnerth A (2001) GABA-mediated Ca^{2+} signalling in developing rat cerebellar Purkinje neurones. J Physiol 536:429–437.

Ekerot CF, Jörntell H (2001) Parallel fibre receptive fields of Purkinje cells and interneurons are climbing fibre-specific. Eur J Neurosci 13:1303–1310.

Ellenberger C Jr, Hanaway J, Netsky MG (1969) Embryogenesis of the inferior olivary nucleus in the rat: a radioautographic study and a re-evaluation of the rhombic lip. J Comp Neurol 137:71–79.

Essick CR (1912) The development of the nuclei pontis and the nucleus arcuatus in man. Am J Anat 13:25–54.

Farkas Z, Szirmai I, Kamondi A (2006) Impaired rhythm generation in essential tremor. Mov Disord 21:1196–1199.

Foster RE, Peterson BE (1986) The inferior olivary complex of Guinea pig: cytoarchitecture and cellular morphology. Brain Res Bull 17:785–800.

Fraser S, Keynes R, Lumsden A (1990) Segmentation in the chick embryo hindbrain is defined by cell lineage restrictions. Nature 344:431–435.

Frens MA, Mathoera AL, van der Steen J (2001) Floccular complex spike response to transparent retinal slip. Neuron 30:795–801.

Frohman MA, Martin GR, Cordes SP, Halamek LP, Barsh GS (1993) Altered rhombomere-specific gene expression and hyoid bone differentiation in the mouse segmentation mutant, kreisler (kr). Development 117:925–936.

Fujita M (1982) Adaptive filter model of the cerebellum. Biol Cybern 45:195–206.

Gao Z, Davis C, Thomas AM, Economo MN, Abrego AM, Svoboda K, De Zeeuw CI, Li N (2018) A cortico-cerebellar loop for motor planning. Nature 563(7729):113-116.

Gao Z, Van Beugen BJ, De Zeeuw CI (2012) Distributed synergistic plasticity and cerebellar learning. Nat Rev Neurosci 13:619–635.

Garcia-Dominguez M, Gilardi-Hebenstreit P, Charnay P (2006) PIASxb acts as an activator of Hoxb1 and is antagonized by Krox20 during hindbrain segmentation. EMBO J 25:2432–2442.

Garden DLF, Rinaldi A, Nolan MF (2017) Active integration of glutamatergic input to the inferior olive generates bidirectional postsynaptic potentials. J Physiol 595:1239–1251.

Gibson AR, Horn KM, Pong M (2004) Activation of climbing fibers. Cerebellum 3:212–221

Giovannucci A et al (2017) Cerebellar granule cells acquire a widespread predictive feedback signal during motor learning. Nat Neurosci 20:727–734.

Glickstein M, Oberdick J, Voogd J (2007) Evolution of the cerebellum. In: Kaas JH (ed) Evolution of nervous systems, 1st edn. Academic, pp 413–442.

Granit R, Phillips CG (1956) Excitatory and inhibitory processes acting upon individual Purkinje cells of the cerebellum in cats. J Physiol 133:520–547.

Guo C et al (2007) Lmx1b is essential for Fgf8 and Wnt1 expression in the isthmic organizer during tectum and cerebellum development in mice. Development 134:317–325.

Gutierrez-Castellanos N et al (2017) Motor learning requires Purkinje cell synaptic potentiation through activation of AMPA-receptor subunit GluA3. Neuron 93:409–424.

Gwyn DG, Nicholson GP, Flumerfelt BA (1977) The inferior olivary nucleus of the rat: a light and electron microscopic study. J Comp Neurol 174:489–520.

Halverson HE, Khilkevich A, Mauk MD (2015) Relating cerebellar Purkinje cell activity to the timing and amplitude of conditioned eyelid responses. J Neurosci 35:7813–7832.

Hámori J, Szentágothai J (1966) Identification under the electron microscope of climbing fibers and their synaptic contacts. Exp Brain Res 1:65–81

Hámori J, Szentágothai J (1980) Lack of evidence of synaptic contacts by climbing fibre collaterals to basket and stellate cells in developing rat cerebellar cortex. Brain Res 186:454–457.

Handforth A et al (2010) T-type calcium channel antagonists suppress tremor in two mouse models of essential tremor. Neuropharmacology 59:380–387.

Hansel C (2009) Reading the clock: how Purkinje cells decode the phase of olivary oscillations. Neuron 62:308–309.

Harkmark W (1954) Cell migrations from the rhombic lip to the inferior olive, the nucleus raphe and the pons; a morphological and experimental investigation on chick embryos. J Comp Neurol 100:115–209.

Harper RM, Woo MA, Alger JR (2000) Visualization of sleep influences on cerebellar and brainstem cardiac and respiratory control mechanisms. Brain Res Bull 53:125–131. Harvey JA, Romano AG (1993) Harmaline-induced impairment of Pavlovian conditioning in the rabbit. J Neurosci 13:1616–1623.

Hashimoto K, Ichikawa R, Kitamura K, Watanabe M, Kano M (2009a) Translocation of a “winner” climbing fiber to the Purkinje cell dendrite and subsequent elimination of “losers” from the soma in developing cerebellum. Neuron 63:106–118.

Hashimoto K et al (2001) Roles of glutamate receptor d2 subunit (GluRd2) and metabotropic glutamate receptor subtype 1 (mGluR1) in climbing fiber synapse elimination during postnatal cerebellar development. J Neurosci 21:9701–9712.

Hashimoto K, Kano M (2003) Functional differentiation of multiple climbing fiber inputs during synapse elimination in the developing cerebellum. Neuron 38:785–796.

Hashimoto K, Kano M (2005) Postnatal development and synapse elimination of climbing fiber to Purkinje cell projection in the cerebellum. Neurosci Res 53:221–228.

Hashimoto K, Yoshida T, Sakimura K, Mishina M, Watanabe M, Kano M (2009b) Influence of parallel fiber-Purkinje cell synapse formation on postnatal development of climbing fiber- Purkinje cell synapses in the cerebellum. Neuroscience 162:601–611.

Häusser M, Clark BA (1997) Tonic synaptic inhibition modulates neuronal output pattern and spatiotemporal synaptic integration. Neuron 19:665–678.

Hernandez-Miranda LR, Müller T, Birchmeier C (2017) The dorsal spinal cord and hindbrain: from developmental mechanisms to functional circuits. Dev Biol 432:34–42.

Hernandez RE, Rikhof HA, Bachmann R, Moens CB (2004) vhnf1 integrates global RA patterning and local FGF signals to direct posterior hindbrain development in zebrafish. Development 131:4511–4520.

Hidalgo-Sánchez M, Millet S, Bloch-Gallego E, Alvarado-Mallart RM (2005) Specification of the meso-isthmo-cerebellar region: the Otx2/Gbx2 boundary. Brain Res Brain Res Rev 49:134–149.

Hidalgo-Sánchez M, Millet S, Simeone A, Alvarado-Mallart RM (1999) Comparative analysis of Otx2, Gbx2, Pax2, Fgf8 and Wnt1 gene expressions during the formation of the chick midbrain/ hindbrain domain. Mech Dev 81:175–178.

Hilson JB, Merchant SN, Adams JC, Joseph JT (2009) Wolfram syndrome: a clinicopathologic correlation. Acta Neuropathol 118:415–428.

Hirai H et al (2005) Cbln1 is essential for synaptic integrity and plasticity in the cerebellum. Nat Neurosci 8:1534–1541.

His W (1891) Die Entwicklung des menschlichen Rautenhirns vom Ende des ersten bis zum Beginn des dritten Monats. Abhandlungen der mathematisch-physischen Classe der Königlichen Sachsischen Gesellschaft der Wissenschaften 17:1–74.

Hisatsune C et al (2013) IP3R1 deficiency in the cerebellum/brainstem causes basal ganglia-independent dystonia by triggering tonic Purkinje cell firings in mice. Front Neural Circuits 7:156.

Hobson JA, McCarley RW (1972). Spontaneous discharge rates of cat cerebellar Purkinje cells in sleep and waking. Electroencephalogr Clin Neurophysiol 33(5): 457-469.

Hoebeek FE, Witter L, Ruigrok TJH, De Zeeuw CI (2010) Differential olivo-cerebellar cortical control of rebound activity in the cerebellar nuclei. Proc Natl Acad Sci U S A 107:8410–8415.

Hoge GJ, Davidson KGV, Yasumura T, Castillo PE, Rash JE, Pereda AE (2011) The extent and strength of electrical coupling between inferior olivary neurons is heterogeneous. J Neurophysiol 105:1089–1101.

Holmberg M et al (1998) Spinocerebellar ataxia type 7 (SCA7): a neurodegenerative disorder with neuronal intranuclear inclusions. Hum Mol Genet 7:913–918.

Hoogland TM, De Gruijl JR, Witter L, Canto CB, De Zeeuw CI (2015) Role of synchronous activation of cerebellar Purkinje cell ensembles in multi-joint movement control. Curr Biol 25:1157–1165.

Horn KM, Deep A, Gibson AR (2013) Progressive limb ataxia following inferior olive lesions. J Physiol 591:5475–5489.

Horn KM, Pong M, Gibson AR (2010) Functional relations of cerebellar modules of the cat. J Neurosci 30:9411–9423.

Ichikawa R et al (2002) Distal extension of climbing fiber territory and multiple innervation caused by aberrant wiring to adjacent spiny branchlets in cerebellar Purkinje cells lacking glutamate receptor d2. J Neurosci 22:8487–8503.

Iskusnykh IY, Steshina EY, Chizhikov VV (2016) Loss of Ptf1a leads to a widespread cell-fate misspecification in the brainstem, affecting the development of somatosensory and viscerosensory nuclei. J Neurosci 36:2691–2710.

Ito M (1984) The cerebellum and neural control. Raven Press, New York

Ito M, Kano M (1982) Long-lasting depression of parallel fiber-Purkinje cell transmission induced by conjunctive stimulation of parallel fibers and climbing fibers in the cerebellar cortex. Neurosci Lett 33:253–258.

Ito M, Sakurai M, Tongroach P (1982) Climbing fibre induced depression of both mossy fibre responsiveness and glutamate sensitivity of cerebellar Purkinje cells. J Physiol 324:113–134

Izhikevic EM (2007) Dynamical systems in neuroscience: the geometry of excitability and bursting. MIT Press, Cambridge.

Jacobson GA, Rokni D, Yarom Y (2008a) A model of the olivo-cerebellar system as a temporal pattern generator. Trends Neurosci 31:617–625.

Jacobson SW et al (2008b) Impaired eyeblink conditioning in children with fetal alcohol syndrome. Alcohol Clin Exp Res 32:365–372.

Jahnsen H (1986) Electrophysiological characteristics of neurones in the Guinea-pig deep cerebellar nuclei in vitro. J Physiol Lond 372:129–147.

Jirenhed DA, Bengtsson F, Hesslow G (2007) Acquisition, extinction, and reacquisition of a cerebellar cortical memory trace. J Neurosci 27:2493–2502.

Joyner AL, Liu A, Millet S (2000) Otx2, Gbx2 and Fgf8 interact to position and maintain a mid-hindbrain organizer. Curr Opin Cell Biol 12:736–741.

Kakizawa S, Miyazaki T, Yanagihara D, Iino M, Watanabe M, Kano M (2005) Maintenance of presynaptic function by AMPA receptor-mediated excitatory postsynaptic activity in adult brain. Proc Natl Acad Sci U S A 102:19180–19185.

Kamei I et al (1981) Comparative anatomy of the distribution of catecholamines within the inferior olivary complex from teleosts to primates. J Comp Neurol 202:125–133.

Kania A, Klein R (2016) Mechanisms of ephrin-Eph signalling in development, physiology and disease. Nature Reviews Molecular and Cellular Biology 17:240–256.

Kano M, Hashimoto K (2009) Synapse elimination in the central nervous system. Curr Opin Neurobiol 19:154–161.

Katz LC, Shatz CJ (1996) Synaptic activity and the construction of cortical circuits. Science 274:1133–1138.

Kawamura Y, Nakayama H, Hashimoto K, Sakimura K, Kitamura K, Kano M (2013) Spike timing-dependent selective strengthening of single climbing fibre inputs to Purkinje cells during cerebellar development. Nat Commun 4:2732.

Kazantsev VB, Nekorkin VI, Makarenko VI, Llinás R (2003) Olivo-cerebellar cluster-based universal control system. Proc Natl Acad Sci U S A 100:13064–13068.

Kemp HA, Cooke JE, Moens CB (2009) EphA4 and EfnB2a maintain rhombomere coherence by independently regulating intercalation of progenitor cells in the zebrafish neural keel. Dev Biol 327:313–326.

Kesner RP, Jackson-Smith P, Henry C, Amann K (1995) Effects of ibogaine on sensory-motor function, activity, and spatial learning in rats. Pharmacol Biochem Behav 51:103–109.

Khosrovani S, Van Der Giessen RS, De Zeeuw CI, De Jeu MTG (2007) In vivo mouse inferior olive neurons exhibit heterogeneous subthreshold oscillations and spiking patterns. Proc Natl Acad Sci U S A 104:15911–15916.

Kikuta H, Kanai M, Ito Y, Yamasu K (2003) gbx2 Homeobox gene is required for the maintenance of the isthmic region in the zebrafish embryonic brain. Dev Dyn 228:433–450.

Kim FA, Sing IA, Kaneko T, Bieman M, Stallwood N, Sadl VS, Cordes SP (2005) The vHNF1 homeodomain protein establishes early rhombomere identity by direct regulation of Kreisler expression. Mech Dev 122:1300–1309.

Kistler WM et al (2002) Analysis of Cx36 knockout does not support tenet that olivary gap junctions are required for complex spike synchronization and normal motor performance. Ann N Y Acad Sci 978:391–404.

Kistler WM, De Zeeuw CI (2002) Dynamical working memory and timed responses: the role of reverberating loops in the olivo-cerebellar system. Neural Comput 14:2597–2626.

Klaus A, Birchmeier W (2008) Wnt signalling and its impact on development and cancer. Nat Rev Cancer 8:387–398.

Klinzing JG, Niethard N, Born K (2019). Mechanisms of systems memory consolidation during sleep. Nat Neurosci 22(10): 1598-1610.

Koeppen AH, Barron KD, Dentinger MP (1980) Olivary hypertrophy: histochemical demonstration of hydrolytic enzymes. Neurology 30:471–480.

Kooy FH (1917) The inferior olive in vertebrates. Folia Neurobiol 10:205–369.

Kostadinov D, Beau M, Blanco-Pozo M, Häusser M (2019) Predictive and reactive reward signals coveyed by climbing fiber input to cerebellar Purkinje cells. Nat Neurosci 22(6): 950-962.

Köster B, Deuschl G, Lauk M, Timmer J, Guschlbauer B, Lücking CH (2002) Essential tremor and cerebellar dysfunction: abnormal ballistic movements. J Neurol Neurosurg Psychiatry 73:400–405.

Kronenbuerger M, Gerwig M, Brol B, Block F, Timmann D (2007) Eyeblink conditioning is impaired in subjects with essential tremor. Brain 130:1538–1551.

Kros L et al (2017) Synchronicity and rhythmicity of Purkinje cell firing during generalized spike-and-wave discharges in a natural mouse model of absence epilepsy. Front Cell Neurosci 11:346.

Lampl I, Yarom Y (1993) Subthreshold oscillations of the membrane potential: a functional synchronizing and timing device. J Neurophysiol 70:2181–2186.

Lampl I, Yarom Y (1997) Subthreshold oscillations and resonant behavior: two manifestations of the same mechanism. Neuroscience 78:325–341.

Landsberg RL, Awatramani RB, Hunter NL, Farago AF, DiPietrantonio HJ, Rodriguez CI, Dymecki SM (2005) Hindbrain rhombic lip is comprised of discrete progenitor cell populations allocated by Pax6. Neuron 48:933–947.

Lang EJ (2001) Organization of olivocerebellar activity in the absence of excitatory glutamatergic input. J Neurosci 21:1663–1675.

Lang EJ (2002) GABAergic and glutamatergic modulation of spontaneous and motor-cortex-evoked complex spike activity. J Neurophysiol 87:1993–2008.

Lang EJ, Sugihara I, Llinás R (1996) GABAergic modulation of complex spike activity by the cerebellar nucleoolivary pathway in rat. J Neurophysiol 76:255–275.

Lang EJ, Sugihara I, Llinás R (2006) Olivocerebellar modulation of motor cortex ability to generate vibrissal movements in rat. J Physiol 571:101–120.

Lang EJ, Sugihara I, Welsh JP, Llinás R (1999) Patterns of spontaneous Purkinje cell complex spike activity in the awake rat. J Neurosci 19:2728–2739.

Larry N, Yarkoni M, Lixenberg A, Joshua M (2019) Cerebellar climbing fibers encode expected reward size. Elife 8: e46870.

Larsell O (1947) The development of the cerebellum in man in relation to its comparative anatomy. J Comp Neurol 87:85–129.

Latorre R, Aguirre C, Rabinovich MI, Varona P (2013) Transient dynamics and rhythm coordination of inferior olive spatio-temporal patterns. Front Neural Circuits 7:138.

Lecaudey V, Anselme I, Rosa F, Schneider-Maunoury S (2004) The zebrafish Iroquois gene iro7 positions the r4/r5 boundary and controls neurogenesis in the rostral hindbrain. Development 131:3121–3131.

LeDoux MS (2011) Animal models of dystonia: lessons from a mutant rat. Neurobiol Dis 42:152–161.

Lee SMK, Danielian PS, Fritzsch B, McMahon AP (1997) Evidence that FGF8 signalling from the midbrain-hindbrain junction regulates growth and polarity in the developing midbrain. Development 124:959–969.

Lefler Y, Torben-Nielsen B, Yarom Y (2013) Oscillatory activity, phase differences, and phase resetting in the inferior olivary nucleus. Front Syst Neurosci 7:22.

Lefler Y, Yarom Y, Uusisaari MY (2014) Cerebellar inhibitory input to the inferior olive decreases electrical coupling and blocks subthreshold oscillations. Neuron 81:1389–1400.

Leto K et al (2016) Consensus paper: cerebellar development. Cerebellum 15:789–828.

Leznik E, Llinás R (2005) Role of gap junctions in synchronized neuronal oscillations in the inferior olive. J Neurophysiol 94:2447–2456.

Leznik E, Makarenko V, Llinás R (2002) Electrotonically mediated oscillatory patterns in neuronal ensembles: an in vitro voltage-dependent dye-imaging study in the inferior olive. J Neurosci 22:2804–2815.

Liao K, Hong S, Zee DS, Optican LM, Leigh RJ (2008) Impulsive head rotation resets oculopalatal tremor: examination of a model. Prog Brain Res 171:227–234.

Lim CCT, Lim SA (2009) Pendular nystagmus and palatomyoclonus from hypertrophic olivary degeneration. New Engl J Med 360:e12.

Liu Z et al (2008) Control of precerebellar neuron development by Olig3 bHLH transcription factor. J Neurosci 28:10124–10133.

Llano I, DiPolo R, Marty A (1994) Calcium-induced calcium release in cerebellar Purkinje cells. Neuron 12:663–673.

Llinás R, Baker R, Sotelo C (1974) Electrotonic coupling between neurons in cat inferior olive. J Neurophysiol 37:560–571.

Llinás R, Mühlethaler M (1988) Electrophysiology of Guinea-pig cerebellar nuclear cells in the in vitro brain stem-cerebellar preparation. J Physiol 404:241–258.

Llinás R, Sasaki K (1989) The functional organization of the olivo-cerebellar system as examined by multiple Purkinje cell recordings. Eur J Neurosci 1:587–602.

Llinás R, Sugimori M (1980) Electrophysiological properties of in vitro Purkinje cell somata in mammalian cerebellar slices. J Physiol 305:171–195.

Llinás R, Sugimori M, Lin JW, Cherksey B (1989) Blocking and isolation of a calcium channel from neurons in mammals and cephalopods utilizing a toxin fraction (FTX) from funnel-web spider poison. Proc Natl Acad Sci U S A 86:1689–1693.

Llinás R, Volkind RA (1973) The olivo-cerebellar system: functional properties as revealed by harmaline-induced tremor. Exp Brain Res 18:69–87.

Llinás R, Walton K, Hillman DE, Sotelo C (1975) Inferior olive: its role in motor learning. Science 190:1230–1231.

Llinás R, Yarom Y (1981a) Electrophysiology of mammalian inferior olivary neurones in vitro. Different types of voltage-dependent ionic conductances. J Physiol 315:549–567.

Llinás R, Yarom Y (1981b) Properties and distribution of ionic conductances generating electro-responsiveness of mammalian inferior olivary neurones in vitro. J Physiol 315:569–584.

Llinás R, Yarom Y (1986) Oscillatory properties of Guinea-pig inferior olivary neurones and their pharmacological modulation: an in vitro study. J Physiol 376:163–182.

Llinás RR (2009) Inferior olive oscillation as the temporal basis for motricity and oscillatory reset as the basis for motor error correction. Neuroscience 162:797–804.

Long MA, Deans MR, Paul DL, Connors BW (2002) Rhythmicity without synchrony in the electrically uncoupled inferior olive. J Neurosci 22:10898–10905.

Louis ED, Ferreira JJ (2010) How common is the most common adult movement disorder? Update on the worldwide prevalence of essential tremor. Mov Disord 25:534–541.

Louis ED, Zheng W, Jurewicz EC, Watner D, Chen J, Factor-Litvak P, Parides M (2002) Elevation of blood b-carboline alkaloids in essential tremor. Neurology 59:1940–1944.

Luebke AE, Robinson DA (1994) Gain changes of the cat's vestibulo-ocular reflex after flocculus deactivation. Experimental brain research Experimentelle Hirnforschung 98:379–390.

Lumsden A, Krumlauf R (1996) Patterning the vertebrate neuraxis. Science 274:1109–1115.

Mahmood R, Mason IJ, Morriss-Kay GM (1996) Expression of Fgf-3 in relation to hindbrain segmentation, otic pit position and pharyngeal arch morphology in normal and retinoic acid-exposed mouse embryos. Anat Embryol (Berl) 194:13–22.

Manor Y, Rinzel J, Segev I, Yarom Y (1997) Low-amplitude oscillations in the inferior olive: a model based on electrical coupling of neurons with heterogeneous channel densities. J Neurophysiol 77:2736–2752.

Manzanares M, Cordes S, Ariza-McNaughton L, Sadl V, Maruthainar K, Barsh G, Krumlauf R (1999) Conserved and distinct roles of kreisler in regulation of the paralogous Hoxa3 and Hoxb3 genes. Development 126:759–769.

Manzanares M, Cordes S, Kwan CT, Sham MH, Barsh GS, Krumlauf R (1997) Segmental regulation of Hoxb-3 by kreisler. Nature 387:191–195.

Maqbool A, Batten TFC, Berry PA, McWilliam PN (1993) Distribution of dopamine-containing neurons and fibres in the feline medulla oblongata: a comparative study using catecholamine-synthesizing enzyme and dopamine immunohistochemistry. Neuroscience 53:717–733

Marcos S, Backer S, Causeret F, Tessier-Lavigne M, Bloch-Gallego E (2009) Differential roles of Netrin-1 and its receptor DCC in inferior olivary neuron migration. Mol Cell Neurosci 41:429–439.

Mariani J, Changeux JP (1981) Ontogenesis of olivocerebellar relationships I. Studies by intracellular recordings of the multiple innervation of Purkinje cells by climbing fibers in the developing rat cerebellum. J Neurosci 1:696–702.

Marillat V, Sabatier C, Failli V, Matsunaga E, Sotelo C, Tessier-Lavigne M, Chédotal A (2004) The slit receptor Rig-1/Robo3 controls midline crossing by hindbrain precerebellar neurons and axons. Neuron 43:69–79.

Marin F, Charnay P (2000) Hindbrain patterning: FGFs regulate Krox20 and mafB/kr expression in the otic/preotic region. Development 127:4925–4935.

Mark M et al (1993) Two rhombomeres are altered in Hoxa-1 mutant mice. Development 119:319–338.

Marr D (1969) A theory of cerebellar cortex. J Physiol 202:437–470.

Marshall SP, van der Giessen RS, de Zeeuw CI, Lang EJ (2007) Altered olivocerebellar activity patterns in the connexin36 knockout mouse. Cerebellum (London, England):1–13.

Martin FC, Thu Le A, Handforth A (2005) Harmaline-induced tremor as a potential preclinical screening method for essential tremor medications. Mov Disord 20:298–305.

Martin GF, Dom R, King JS, RoBards M, Watson CRR (1975) The inferior olivary nucleus of the opossum (Didelphis marsupialis virginiana), its organization and connections. J Comp Neurol 160:507–533.

Martinez S, Andreu A, Mecklenburg N, Echevarria D (2013) Cellular and molecular basis of cerebellar development. Front Neuroanat 7:18.

Maruta J, Hensbroek RA, Simpson JI (2007) Intraburst and interburst signaling by climbing fibers. J Neurosci 27:11263–11270.

Mason CA, Christakos S, Catalano SM (1990) Early climbing fiber interactions with Purkinje cells in the postnatal mouse cerebellum. J Comp Neurol 297:77–90.

Mastick GS, Fan CM, Tessier-Lavigne M, Serbedzija GN, McMahon AP, Easter SS Jr (1996) Early deletion of neuromeres in Wnt-1-/- mutant mice: evaluation by morphological and molecular markers. J Comp Neurol 374:246–258.

Mathews PJ, Lee KH, Peng Z, Houser CR, Otis TS (2012) Effects of climbing fiber driven inhibition on Purkinje neuron spiking. J Neurosci 32:17988–17997.

Mathy A, Clark BA, Häusser M (2014) Synaptically induced long-term modulation of electrical coupling in the inferior olive. Neuron 81:1290–1296.

Mathy A, Ho SSN, Davie JT, Duguid IC, Clark BA, Häusser M (2009) Encoding of oscillations by axonal bursts in inferior olive neurons. Neuron 62:388–399.

Matschke J, Laas R (2007) Sudden death due to central alveolar hypoventilation syndrome (Ondine's curse) in a 39-year-old woman with heterotopia of the inferior olive. Am J Forensic Med Pathol 28:141–144.

Matsumoto-Makidono Yet al (2016) Ionic basis for membrane potential resonance in neurons of the inferior olive. Cell Rep 16:994–1004.

Maves L, Jackman W, Kimmel CB (2002) FGF3 and FGF8 mediate a rhombomere 4 signaling activity in the zebrafish hindbrain. Development 129:3825–3837.

McCormick DA, Steinmetz JE, Thompson RF (1985) Lesions of the inferior olivary complex cause extinction of the classically conditioned eyeblink response. Brain Res 359:120–130.

McKay BE, Turner RW (2005) Physiological and morphological development of the rat cerebellar Purkinje cell. J Physiol 567:829–850.

Mcmahon AP, Bradley A (1990) The Wnt-1 (Int-1) Protooncogene is required for development of a large region of the mouse-brain. Cell 62:1073–1085.

Medina JF, Garcia KS, Nores WL, Taylor NM, Mauk MD (2000) Timing mechanisms in the cerebellum: testing predictions of a large-scale computer simulation. J Neurosci 20:5516–5525.

Medina JF, Nores WL, Mauk MD (2002) Inhibition of climbing fibres is a signal for the extinction of conditioned eyelid responses. Nature 416:330–333.

Mikuni T, Uesaka N, Okuno H, Hirai H, Deisseroth K, Bito H, Kano M (2013) Arc/Arg3.1 is a postsynaptic mediator of activity-dependent synapse elimination in the developing cerebellum. Neuron 78:1024–1035.

Millet S, Bloch-Gallego E, Simeone A, Alvarado-Mallart RM (1996) The caudal limit of Otx2 gene expression as a marker of the midbrain/hindbrain boundary: a study using in situ hybridisation and chick/quail homotopic grafts. Development 122:3785–3797.

Millet S, Campbell K, Epstein DJ, Losos K, Harris E, Joyner AL (1999) A role for Gbx2 in repression of Otx2 and positioning the mid/hindbrain organizer. Nature 401:161–164.

Miyashita Y, Nagao S (1984) Contribution of cerebellar intracortical inhibition to Purkinje cell response during vestibulo-ocular reflex of alert rabbits. J Physiol 351:251–262.

Miyazaki T, Hashimoto K, Shin HS, Kano M, Watanabe M (2004) P/Q-type Ca^{2+} channel α1A regulates synaptic competition on developing cerebellar Purkinje cells. J Neurosci 24:1734–1743.

Miyazaki T, Yamasaki M, Takeuchi T, Sakimura K, Mishina M, Watanabe M (2010) Ablation of glutamate receptor GluRd2 in adult Purkinje cells causes multiple innervation of climbing fibers by inducing aberrant invasion to parallel fiber innervation territory. J Neurosci 30:15196–15209.

Montagna P, Gambetti P, Cortelli P, Lugaresi E (2003) Familial and sporadic fatal insomnia. Lancet Neurol 2:167–176.

Morara S, van der Want JJL, de Weerd H, Provini L, Rosina A (2001) Ultrastructural analysis of climbing fiber-Purkinje cell synaptogenesis in the rat cerebellum. Neuroscience 108:655–671.

Mukamel EA, Nimmerjahn A, Schnitzer MJ (2009) Automated analysis of cellular signals from large-scale calcium imaging data. Neuron 63:747–760.

Najafi F, Giovannucci A, Wang SSH, Medina JF (2014) Coding of stimulus strength via analog calcium signals in Purkinje cell dendrites of awake mice. elife 3:e03663.

Najafi F, Medina JF (2013) Beyond “all-or-nothing” climbing fibers: graded representation of teaching signals in Purkinje cells. Front Neural Circuits 7:115.

Nelson BJ, Mugnaini E (1988) The rat inferior olive as seen with immunostaining for glutamate decarboxylase. Anat Embryol (Berl) 179:109–127.

Nemecek S, Wolff J (1969) Light and electron microscopic evidence of complex synapses (glomeruli) in Oliva inferior (cat). Experientia 25:634–635.

Nishida K, Hoshino M, Kawaguchi Y, Murakami F (2010) Ptf1a directly controls expression of immunoglobulin superfamily molecules Nephrin and Neph3 in the developing central nervous system. J Biol Chem 285:373–380.

Nonchev S et al (1996) Segmental expression of Hoxa-2 in the hindbrain is directly regulated by Krox-20. Development 122:543–554.

O’Leary JL, Inukai J, Smith JM (1971) Histogenesis of the cerebellar climbing fiber in the rat. J Comp Neurol 142:377–391.

Ohmae S, Medina JF (2015) Climbing fibers encode a temporal-difference prediction error during cerebellar learning in mice. Nat Neurosci 18:1798–1803.

Ohtsuki G, Hirano T (2008) Bidirectional plasticity at developing climbing fiber-Purkinje neuron synapses. Eur J Neurosci 28:2393–2400.

Ohtsuki G, Kawaguchi SY, Mishina M, Hirano T (2004) Enhanced inhibitory synaptic transmission in the cerebellar molecular layer of the GluRd2 knock-out mouse. J Neurosci 24:10900–10907.

Onodera S (1984) Olivary projections from the mesodiencephalic structures in the cat studied by means of axonal transport of horseradish peroxidase and tritiated amino acids. J Comp Neurol. 227(1):37-49.

Onodera S, Hicks TP (1995) Patterns of transmitter labelling and connectivity of the cat's nucleus of Darkschewitsch: a wheat germ agglutinin-horseradish peroxidase and immunocytochemical study at light and electron microscopical levels. J Comp Neurol 361:553–573.

Osumi-Yamashita N, Ninomiya Y, Doi H, Eto K (1996) Rhombomere formation and hind-brain crest cell migration from prorhombomeric origins in mouse embryos. Develop Growth Differ 38:107–118.

Oxtoby E, Jowett T (1993) Cloning of the zebrafish krox-20 gene (krx-20) and its expression during hindbrain development. Nucleic Acids Res 21:1087–1095.

Ozden I, Dombeck DA, Hoogland TM, Tank DW, Wang SS (2012) Widespread state-dependent shifts in cerebellar activity in locomoting mice. PLoS One 7:e42650.

Ozden I, Sullivan MR, Lee HM, Wang SSH (2009) Reliable coding emerges from coactivation of climbing fibers in microbands of cerebellar Purkinje neurons. J Neurosci 29:10463–10473.

Packer AI, Crotty DA, Elwell VA, Wolgemuth DJ (1998) Expression of the murine Hoxa4 gene requires both autoregulation and a conserved retinoic acid response element. Development 125:1991–1998.

Palmer C (1979). Interpositus and fastigial unit activity during sleep and waking in the cat. Electroencephalogr Clin Neurophysiol 46(4): 357-370.

Paré M, Descarries L, Wiklund L (1987) Innervation and reinnervation of rat inferior olive by neurons containing serotonin and substance P: an immunohistochemical study after 5,6-dihydroxytryptamine lesioning. J Neurocytol 16:155–167.

Park YG et al (2010) Ca(V)3.1 is a tremor rhythm pacemaker in the inferior olive. Proc Natl Acad Sci U S A 107:10731–10736.

Pedroso JL, Braga-Neto P, Felício AC, Aquino CC, Prado LB, Prado GF, Barsottini OG (2011). Sleep disorders in cerebellar ataxia. Arq Neuropsiquiatr 69(2A): 253-257.

Perkins EM, Clarkson YL, Suminaite D, Lyndon AR, Tanaka K, Rothstein JD, Skehel PA, Wyllie DJA, Jackson M (2018) Loss of cerebellar glutamate transporters EAAT4 and GLAST differentially affects the spontaneous firing pattern and survival of Purkinje cells. Hum Mol Genet. 27(15):2614-2627.

Piantoni G, Halgren E, Cash SS (2016) The contribution of thalamocortical core and matrix pathways to sleep spindles. Neural Plast. 2016: 3024342.

Placantonakis D, Welsh J (2001) Two distinct oscillatory states determined by the NMDA receptor in rat inferior olive. J Physiol 534:123–140.

Placantonakis DG, Schwarz C, Welsh JP (2000) Serotonin suppresses subthreshold and supra-threshold oscillatory activity of rat inferior olivary neurones in vitro. J Physiol 524 (Pt 3):833–851.

Porrill J, Dean P, Stone JV (2004) Recurrent cerebellar architecture solves the motor-error problem.Proc Biol Sci 271:789–796.

Powers RE, O'Connor DT, Price DL (1990) Noradrenergic innervation of human inferior olivary complex. Brain Res 523:151–155.

Prandota J (2010) Neuropathological changes and clinical features of autism spectrum disorder participants are similar to that reported in congenital and chronic cerebral toxoplasmosis in humans and mice. Res Autism Spectrum Disord 4:103–118.

Purves D, Lichtman JW (1980) Elimination of synapses in the developing nervous system. Science 210:153–157.

Rahmati N et al (2014) Cerebellar potentiation and learning a whisker-based object localization task with a time response window. J Neurosci 34:1949–1962.

Raike RS, Jinnah HA, Hess EJ (2005) Animal models of generalized dystonia. NeuroRx 2:504–512.

Raman IM, Bean BP (1999) Ionic currents underlying spontaneous action potentials in isolated cerebellar Purkinje neurons. J Neurosci 19:1663–1674 Ramón y Cajal S (1911) Histologie du système nerveux de l'homme et des vertébrés, vol 2. Maloine,Paris.

Ray RS, Dymecki SM (2009) Rautenlippe redux – toward a unified view of the precerebellar rhombic lip. Curr Opin Cell Biol 21:741–747.

Renier N et al (2010) Genetic dissection of the function of hindbrain axonal commissures. PLoS Biol 8:e1000325.

Robain O, Bideau I, Farkas E (1981) Developmental changes of synapses in the cerebellar cortex of the rat. A quantitative analysis. Brain Res 206:1–8.

Romano V, De Propris L, Bosman LWJ, Warnaar P, ten Brinke MM, Lindeman S, Ju C, Velauthapillai A, Spanke JK, Guerra EM, Hoogland TM, Negrello M, D'Angelo E, De Zeeuw CI (2018) Potentiation of cerebellar Purkinje cells facilitates whisker reflex adaptation through increased simple spike activity. eLife 2018;7:e38852.

Rondi-Reig L, Delhaye-Bouchaud N, Mariani J, Caston J (1997) Role of the inferior olivary complex in motor skills and motor learning in the adult rat. Neuroscience 77:955–963.

Rossel M, Capecchi MR (1999) Mice mutant for both Hoxa1 and Hoxb1 show extensive remodeling of the hindbrain and defects in craniofacial development. Development 126:5027–5040.

Rubenstein JLR, Martinez S, Shimamura K, Puelles L (1994) The embryonic vertebrate forebrain: the prosomeric model. Science 266:578–580.

Ruigrok TJ, Voogd J (1990) Cerebellar nucleo-olivary projections in the rat: an anterograde tracing study with Phaseolus vulgaris-leucoagglutinin (PHA-L). J Comp Neurol 298(3):315-33.

Ruigrok TJ, Voogd J (2000) Organization of projections from the inferior olive to the cerebellar nuclei in the rat. J Comp Neurol 426:209–228.

Ruigrok TJH (1997) Cerebellar nuclei: the olivary connection. Prog Brain Res 114:167–192.

Ruigrok TJH, de Zeeuw CI, van der Burg J, Voogd J (1990) Intracellular labeling of neurons in the medial accessory olive of the cat: I. Physiology and light microscopy. J Comp Neurol 300:462–477.

Scammell TE, Arrigoni E, Lipton JO (2017). Neural circuitry of wakefulness and sleep. Neuron 93(4): 747-765.

Sakurai Y, Kurokawa D, Kiyonari H, Kajikawa E, Suda Y, Aizawa S (2010) Otx2 and Otx1 protect diencephalon and mesencephalon from caudalization into metencephalon during early brain regionalization. Dev Biol 347:392–403.

Sasaki K, Bower JM, Llinás R (1989) Multiple Purkinje cell recording in rodent cerebellar cortex. Eur J Neurosci 1:572–586.

Sato Y, Miura A, Fushiki H, Kawasaki T, Watanabe Y (1993) Complex spike responses of cerebellar Purkinje cells to constant velocity optokinetic stimuli in the cat flocculus. Acta Otolaryngol Suppl 504:13–16.

Scelfo B, Strata P (2005) Correlation between multiple climbing fibre regression and parallel fibre response development in the postnatal mouse cerebellum. Eur J Neurosci 21:971–978.

Scelfo B, Strata P, Knöpfel T (2003) Sodium imaging of climbing fiber innervation fields in developing mouse Purkinje cells. J Neurophysiol 89:2555–2563.

Scheibel ME, Scheibel AB (1954) Observations on the intracortical relations of the climbing fibers of the cerebellum; a Golgi study. J Comp Neurol 101:733–763.

Scheibel ME, Scheibel AB (1955) The inferior olive; a Golgi study. J Comp Neurol 102:77–131

Schonewille M et al (2010) Purkinje cell-specific knockout of the protein phosphatase PP2B.

impairs potentiation and cerebellar motor learning. Neuron 67:618–628 Schulman JA, Bloom FE (1981) Golgi cells of the cerebellum are inhibited by inferior olive activity. Brain Res 210:350–355.

Schultz SR, Kitamura K, Post-Uiterweer A, Krupic J, Häusser M (2009) Spatial pattern coding of sensory information by climbing fiber-evoked calcium signals in networks of neighboring cerebellar Purkinje cells. J Neurosci 29:8005–8015.

Schweighofer N, Doya K, Fukai H, Chiron JV, Furukawa T, Kawato M (2004) Chaos may enhance information transmission in the inferior olive. Proc Natl Acad Sci U S A 101:4655–4660.

Schweighofer N, Doya K, Kawato M (1999) Electrophysiological properties of inferior olive neurons: a compartmental model. J Neurophysiol 82:804–817.

Schweighofer N, Spoelstra J, Arbib MA, Kawato M (1998) Role of the cerebellum in reaching movements in humans. II. A neural model of the intermediate cerebellum. Eur J Neurosci 10:95–105.

Sham MH et al (1993) The zinc finger gene Krox20 regulates HoxB2 (Hox2.8) during hindbrain segmentation. Cell 72:183–196.

Shimozono S, Iimura T, Kitaguchi T, Higashijima S, Miyawaki A (2013) Visualization of an endogenous retinoic acid gradient across embryonic development. Nature 496:363–366.

Silver RA, Momiyama A, Cull-Candy SG (1998) Locus of frequency-dependent depression identified with multiple-probability fluctuation analysis at rat climbing fibre-Purkinje cell synapses. J Physiol 510:881–902.

Simeone A (2000) Positioning the isthmic organizer where Otx2 and Gbx2 meet. Trends Genet 16:237–240.

Simeone A, Acampora D, Gulisano M, Stornaiuolo A, Boncinelli E (1992) Nested expression domains of four homeobox genes in developing rostral brain. Nature 358:687–690.

Simonyan K, Ludlow CL, Vortmeyer AO (2010) Brainstem pathology in spasmodic dysphonia. Laryngoscope 120:121–124.

Simpson JI, Wylie DR, De Zeeuw CI (1996) On climbing fiber signals and their consequence(s). BehBrain Sciences 19:380–394.

Sladek JR Jr, Bowman JP (1975) The distribution of catecholamines within the inferior olivary complex of the cat and rhesus monkey. J Comp Neurol 163:203–213.

Sladek JR Jr, Hoffman GE (1980) Monoaminergic innervation of the mammalian inferior olivary complex. In: Courville J, de Montigny C, Lamarre Y (eds) The inferior olivary nucleus. Raven Press, New York.

Smirnow AE (1897) Ueber eine besondere Art von Nervenzellen der Molecularschicht des Kleinhirns bei erwachsenen Saugetieren und beim Menschen. Anat Anz 13:636–642.

Sonni A, Kurdziel LB, Baran B, Spencer RMC (2014). The effects of sleep dysfunction on cognition, affect, and quality of life in individuals with cerebellar ataxia. J Clin Sleep Med 10(5): 535-543.

Sotelo C, Chédotal A (2005) Development of the olivocerebellar system: migration and formation of cerebellar maps. Prog Brain Res 148:1–20.

Sotelo C, Hillman DE, Zamora AJ, Llinás R (1975) Climbing fiber deafferentation: its action on Purkinje cell dendritic spines. Brain Res 98:574–581.

Sotelo C, Llinás R, Baker R (1974) Structural study of inferior olivary nucleus of the cat: morphological correlates of electrotonic coupling. J Neurophysiol 37:541–559.

Spoelstra J, Schweighofer N, Arbib MA (2000) Cerebellar learning of accurate predictive control for fast-reaching movements. Biol Cybern 82:321–333.

Srinivas M et al (1999) Functional properties of channels formed by the neuronal gap junction protein connexin36. J Neurosci 19:9848–9855.

Steriade M, Nuñez A, amzica F. A novel slow (<1 Hz) oscillation of neocortical neurons in vivo: depolarizing and hyperpolarizing components (1993). J Neurosci 13(8): 3252-3265.

Stone LS, Lisberger SG (1986) Detection of tracking errors by visual climbing fiber inputs to monkey cerebellar flocculus during pursuit eye movements. Neurosci Lett 72:163–168.

Storm R et al (2009) The bHLH transcription factor Olig3 marks the dorsal neuroepithelium of the hindbrain and is essential for the development of brainstem nuclei. Development 136:295–305.

Strata P (ed) (1989) The olivocerebellar system in motor control, vol 17, 1st edn. Springer, Berlin

Studer M, Gavalas A, Marshall H, Ariza-McNaughton L, Rijli FM, Chambon P, Krumlauf R (1998) Genetic interactions between Hoxa1 and Hoxb1 reveal new roles in regulation of early hindbrain patterning. Development 125:1025–1036.

Sugihara I (2005) Microzonal projection and climbing fiber remodeling in single olivocerebellar axons of newborn rats at postnatal days 4-7. J Comp Neurol 487:93–106.

Sugihara I (2006) Organization and remodeling of the olivocerebellar climbing fiber projection. Cerebellum 5:15–22.

Sugihara I, Lang EJ, Llinás R (1993) Uniform olivocerebellar conduction time underlies Purkinje cell complex spike synchronicity in the rat cerebellum. J Physiol 470:243–271.

Sugihara I, Marshall SP, Lang EJ (2007) Relationship of complex spike synchrony bands and climbing fiber projection determined by reference to aldolase. C compartments in crus IIa of the rat cerebellar cortex. J Comp Neurol 501:13–29.

Sugihara I, Wu H, Shinoda Y (1999) Morphology of single olivocerebellar axons labeled with biotinylated dextran amine in the rat. J Comp Neurol 414:131–148.

Sugihara I, Wu HS, Shinoda Y (2001) The entire trajectories of single olivocerebellar axons in the cerebellar cortex and their contribution to cerebellar compartmentalization. J Neurosci 21:7715–7723.

Sun Z, Hopkins N (2001) vhnf1, the MODY5 and familial GCKD-associated gene, regulates regional specification of the zebrafish gut, pronephros, and hindbrain. Genes Dev 15:3217–3229.

Swayze VW, Johnson VP et al (1997) Magnetic resonance imaging of brain anomalies in fetal alcohol syndrome. Pediatrics 99:232–240.

Swenson C (1983) The afferent connections of the inferior olivary complex in rats. An anterograde study using autoradiographic and axonal degeneration techniques. Neuroscience 8:259–275

Szapiro G, Barbour B (2007) Multiple climbing fibers signal to molecular layer interneurons exclusively via glutamate spillover. Nat Neurosci 10:735–742.

Takebayashi H et al (2002) Non-overlapping expression of Olig3 and Olig2 in the embryonic neural tube. Mech Dev 113:169–174.

Tang T, Blenkinsop TA, Lang EJ (2019) Complex spike synchrony dependent modulation of rat deep cerebellar nuclear activity. Elife. vol 9 no 8, e40101.

Ten Brinke MM, Boele HJ, De Zeeuw CI (2019) Conditioned climbing fiber responses in cerebellar cortex and nuclei. Neurosci Lett 688:26–36.

Ten Brinke MM et al (2015) Evolving models of Pavlovian conditioning: cerebellar cortical dynamics in awake behaving mice. Cell Rep 13:1977–1988.

Ten Brinke MM et al (2017) Dynamic modulation of activity in cerebellar nuclei neurons during Pavlovian eyeblink conditioning in mice. Elife 6.

ten Donkelaar HJ, Lammens M (2009) Development of the human cerebellum and its disorders. Clin Perinatol 36:513–530.

Toonen M et al (1998) Light microscopic and ultrastructural investigation of the dopaminergic innervation of the ventrolateral outgrowth of the rat inferior olive. Brain Res 802:267–273

Tümpel S, Wiedemann LM, Krumlauf R (2009) Hox genes and segmentation of the vertebrate hindbrain. Curr Top Dev Biol 88:103–137.

Turecek J, Han VZ, Cuzon Carlson VC, Grant KA, Welsh JP (2016) Electrical coupling and synchronized subthreshold oscillations in the inferior olive of the rhesus macaque. J Neurosci 36:6497–6502.

Turecek J, Yuen GS, Han VZ, Zeng XH, Beyer KU, Welsh JP (2014) NMDA receptor activation strengthens weak electrical coupling in mammalian brain. Neuron 81:1375–1388.

Turker KS, Miles TS (1984) Harmaline disrupts acquisition of conditioned nictitating membrane responses. Brain Res Bull 13:229–233.

Turker KS, Miles TS (1986) Climbing fiber lesions disrupt conditioning of the nictitating membrane response in the rabbit. Brain Res 363:376–378.

Uesaka N et al (2014) Retrograde semaphorin signaling regulates synapse elimination in the developing mouse brain. Science 344:1020–1023.

Ulloa F, Martí E (2010) Wnt won the war: antagonistic role of Wnt over Shh controls dorso-ventral patterning of the vertebrate neural tube. Dev Dyn 239:69–76.

Ulrich D (2016). Sleep spindles as facilitators of memory formation and learning. Neural Plast 2016: 1796715.

Urbano FJ, Simpson JI, Llinás RR (2006) Somatomotor and oculomotor inferior olivary neurons have distinct electrophysiological phenotypes. Proc Natl Acad Sci U S A 103:16550–16555.

Vaage S (1969) The segmentation of the primitive neural tube in chick embryos (Gallus domesticus). A morphological, histochemical and autoradiographical investigation. Ergeb Anat Entwicklungsgesch 41:3–87.

Van Der Giessen RS et al (2008) Role of olivary electrical coupling in cerebellar motor learning. Neuron 58:599–612.

Van der Want JJL, Wiklund L, Guegan M, Ruigrok T, Voogd J (1989) Anterograde tracing of the rat olivocerebellar system with Phaseolus vulgaris leucoagglutinin (PHA-L). Demonstration of climbing fiber collateral innervation of the cerebellar nuclei. J Comp Neurol 288:1–18.

van Essen TA et al (2010) Anti-malaria drug mefloquine induces motor learning deficits in humans.Front Neurosci 4:191.

Velarde MG, Nekorkin VI, Kazantsev VB, Makarenko VI, Llinás R (2002) Modeling inferior olive neuron dynamics. Neural Netw 15:5–10.

Verbeek DS (2009) Spinocerebellar ataxia type 23: a genetic update. Cerebellum 8:104–107.

Voges K, Wu B, Post L, Schonewille M, De Zeeuw CI (2017) Mechanisms underlying vestibulo-cerebellar motor learning in mice depend on movement direction. J Physiol 595:5301–5326.

Voneida TJ, Christie D, Bogdanski R, Chopko B (1990) Changes in instrumentally and classically conditioned limb-flexion responses following inferior olivary lesions and olivocerebellar tractotomy in the cat. J Neurosci 10:3583–3593.

Voogd J, Pardoe J, Ruigrok TJH, Apps R (2003) The distribution of climbing and mossy fiber collateral branches from the copula pyramidis and the paramedian lobule: congruence of climbing fiber cortical zones and the pattern of zebrin banding within the rat cerebellum. J Neurosci 23:4645–4656.

Vrieler N, Loyola S, Yarden-Rabinowitz Y, Hoogendorp J, Medvedev N, Hoogland TM, De Zeeuw CI, Schutter ED, Yarom Y, Negrello M, Torben-Nielsen B, Uusisaari MY (2019) Variability and

directionality of inferior olive neuron dendrites revealed by detailed 3D characterization of an extensive morphological library. Brain Structure and Function. In Press.

Wada N, Kishimoto Y, Watanabe D, Kano M, Hirano T, Funabiki K, Nakanishi S (2007) Conditioned eyeblink learning is formed and stored without cerebellar granule cell transmission. Proc Natl Acad Sci U S A 104:16690–16695.

Walberg F, Ottersen OP (1989) Demonstration of GABA immunoreactive cells in the inferior olive of baboons (Papio papio and Papio anubis). Neurosci Lett 101:149–155.

Walshe J, Maroon H, McGonnell IM, Dickson C, Mason I (2002) Establishment of hindbrain segmental identity requires signaling by FGF3 and FGF8. Curr Biol 12:1117–1123.

Wang HL, Chou AH, Lin AC, Chen SY, Weng YH, Yeh TH (2010a) Polyglutamine-expanded ataxin-7 upregulates Bax expression by activating p53 in cerebellar and inferior olivary neurons. Exp Neurol 224:486–494.

Wang VY, Rose MF, Zoghbi HY (2005) Math1 expression redefines the rhombic lip derivatives and reveals novel lineages within the brainstem and cerebellum. Neuron 48:31–43.

Wang X et al (2010b) Spinocerebellar ataxia type 6: systematic patho-anatomical study reveals different phylogenetically defined regions of the cerebellum and neural pathways undergo different evolutions of the degenerative process. Neuropathology 30:501–514.

Wassarman KM, Lewandoski M, Campbell K, Joyner AL, Rubenstein JLR, Martinez S, Martin GR (1997) Specification of the anterior hindbrain and establishment of a normal mid/hindbrain organizer is dependent on Gbx2 gene function. Development 124:2923–2934.

Wassef M, Chédotal A, Cholley B, Thomasset M, Heizmann CW, Sotelo C (1992) Development of the olivocerebellar projection in the rat: I. Transient biochemical compartmentation of the inferior olive. J Comp Neurol 323:519–536.

Watanabe M (2008) Molecular mechanisms governing competitive synaptic wiring in cerebellar Purkinje cells. Tohoku J Exp Med 214:175–190.

Weickert S, Ray A, Zoidl G, Dermietzel R (2005) Expression of neural connexins and pannexin1 in the hippocampus and inferior olive: a quantitative approach. Brain Res Mol Brain Res 133:102–109.

Welsh JP (1998) Systemic harmaline blocks associative and motor learning by the actions of the inferior olive. Eur J Neurosci 10:3307–3320.

Welsh JP (2002) Functional significance of climbing-fiber synchrony: a popu–lation coding and behavioral analysis. Ann N Y Acad Sci 978:188–204.

Welsh JP, Ahn ES, Placantonakis DG (2005) Is autism due to brain desynchronization? Int J Dev Neurosci 23:253–263.

Welsh JP, Harvey JA (1998) Acute inactivation of the inferior olive blocks associative learning. Eur J Neurosci 10:3321–3332.

Welsh JP, Lang EJ, Suglhara I, Llinás R (1995) Dynamic organization of motor control within the olivocerebellar system. Nature 374:453–457.

White JJ, Sillitoe RV (2017) Genetic silencing of olivocerebellar synapses causes dystonia-like behaviour in mice. Nat Commun 8:14912.

White RJ, Schilling TF (2008) How degrading: Cyp26s in hindbrain development. Dev Dyn 237:2775–2790.

Wiellette EL, Sive H (2003) vhnf1 and Fgf signals synergize to specify rhombomere identity in the zebrafish hindbrain. Development 130:3821–3829.

Wiklund L, Björklund A, Sjölund B (1977) The indolaminergic innervation of the inferior olive.
1. Convergence with the direct spinal afferents in the areas projecting to the cerebellar anterior lobe. Brain Res 131:1–21.

Wiklund L, Toggenburger G, Cuénod M (1984) Selective retrograde labelling of the rat olivocerebellar climbing fiber system with D-[3H]aspartate. Neuroscience 13:441–468.

Wilkinson DG, Bhatt S, Cook M, Boncinelli E, Krumlauf R (1989) Segmental expression of Hox-2 homoeobox-containing genes in the developing mouse hindbrain. Nature 341:405–409. Wise AK, Cerminara NL, Marple-Horvat DE, Apps R (2010) Mechanisms of synchronous activity in cerebellar Purkinje cells. J Physiol 588:2373–2390.

Witter L, Canto CB, Hoogland TM, De Gruijl JR, De Zeeuw CI (2013) Strength and timing of motor responses mediated by rebound firing in the cerebellar nuclei after Purkinje cell activation. Front Neural Circuits 7:133.

Woodward DJ, Hoffer BJ, Siggins GR, Bloom FE (1971) The ontogenetic development of synaptic junctions, synaptic activation and responsiveness to neurotransmitter substances in rat cerebellar Purkinje cells. Brain Res 34:73–97.

Wu B, Blot FG, Wong AB, Osório C, Adolfs Y, Pasterkamp RJ, Hartmann J, Becker EB, Boele HJ, De Zeeuw CI, Schonewille M (2019) TRPC3 is a major contributor to functional heterogeneity of cerebellar Purkinje cells. Elife 8:e45590.

Wulff P et al (2009) Synaptic inhibition of Purkinje cells mediates consolidation of vestibulo-cerebellar motor learning. Nat Neurosci 12:1042–1049.

Wylie DR, De Zeeuw CI, Simpson JI (1995) Temporal relations of the complex spike activity of Purkinje cell pairs in the vestibulocerebellum of rabbits. J Neurosci 15:2875–2887.

Xu W, Edgley SA (2008) Climbing fibre-dependent changes in Golgi cell responses to peripheral stimulation. J Physiol 586:4951–4959.

Yamada M, Terao M, Terashima T, Fujiyama T, Kawaguchi Y, Nabeshima Y, Hoshino M (2007) Origin of climbing fiber neurons and their developmental dependence on Ptf1a. J Neurosci 27:10924–10934.

Yamamoto M, Fujinuma M, Hirano S, Hayakawa Y, Clagett-Dame M, Zhang J, McCaffery P (2005) Retinoic acid influences the development of the inferior olivary nucleus in the rodent. Dev Biol 280:421–433.

Yarden-Rabinowitz Y, Yarom Y (2019) Delayed Complex Spike Response Evoked by Conditioned Stimulus Encodes Movement Onset Time and Is Determined by Intrinsic Inferior Olive Properties. Front Syst Neurosci 13:50.

Ye WL et al (2001) Distinct regulators control the expression of the mid-hindbrain organizer signal FGF8. Nat Neurosci 4:1175–1181.

Yee KT, Simon HH, Tessier-Lavigne M, O'Leary DDM (1999) Extension of long leading processes and neuronal migration in the mammalian brain directed by the chemoattractant netrin-1. Neuron 24:607–622.

Yeo CH, Hardiman MJ, Glickstein M (1986) Classical conditioning of the nictitating membrane response of the rabbit. IV. Lesions of the inferior olive experimental brain research. Experimentelle Hirnforschung 63:81–92.

Ypsilanti AR, Zagar Y, Chedotal A (2010) Moving away from the midline: new developments for Slit and Robo. Development 137:1939–1952.

Zervas M, Millet S, Ahn S, Joyner AL (2004) Cell behaviors and genetic lineages of the mesenceph- alon and rhombomere 1. Neuron 43:345–357.

Zhang Y et al (2017) Inferior olivary TMEM16B mediates cerebellar motor learning. Neuron 95:1103–1111 e1104.

Zhao Y, Sharma N, LeDoux MS (2011) The DYT1 carrier state increases energy demand in the olivocerebellar network. Neuroscience 177:183–194.

Zhou H et al (2014) Cerebellar modules operate at different frequencies. elife 3:e02536.

Chapter 2

Variability and directionality of inferior olive neuron dendrites revealed by detailed 3D characterization of an extensive morphological library

Brain Structure and Function (2019) 224:1677–1695

Nora Vrieler, Sebastián Loyola, Yasmin Yarden-Rabinowitz, Jesse Hoogendorp, Nikolay Medvedev, Tycho Hoogland, Chris De Zeeuw, Erik De Schutter, Yosef Yarom, Mario Negrello, Ben Torben-Nielsen, Marylka Yoe Uusisaari

Abstract

The inferior olive (IO) is an evolutionarily conserved brain stem structure and its output activity plays a major role in the cerebellar computation necessary for controlling the temporal accuracy of motor behavior. The precise timing and synchronization of IO network activity has been attributed to the dendro-dendritic gap junctions mediating electrical coupling within the IO nucleus. Thus, the dendritic morphology and spatial arrangement of IO neurons governs how synchronized activity emerges in this nucleus. To date, IO neuron structural properties have been characterized in few studies and with small numbers of neurons; these investigations have described IO neurons as belonging to two morphologically distinct types, “curly” and “straight”. In this work we collect a large number of individual IO neuron morphologies visualized using different labeling techniques and present a thorough examination of their morphological properties and spatial arrangement within the olivary neuropil. Our results show that the extensive heterogeneity in IO neuron dendritic morphologies occupies a continuous range between the classically described “curly” and “straight” types, and that this continuum is well represented by a relatively simple measure of “straightness”. Furthermore, we find that IO neuron dendritic trees are often directionally oriented. Combined with an examination of cell body density distributions and dendritic orientation of adjacent IO neurons, our results suggest that the IO network may be organized into groups of densely coupled neurons interspersed with areas of weaker coupling.

Introduction

The inferior olive (IO) provides the sole source of climbing fibers that evoke potent complex spikes in cerebellar Purkinje neurons (PNs), and thereby plays a critical role in controlling cerebellar function (Azizi, 2007; Jacobson et al., 2008; Ito, 2013; Llinás, 2014; Ten Brinke et al., 2018; Streng et al., 2018). The neurons within the IO are exclusively interconnected by dendro-dendritic gap-junctions (GJs; Sotelo et al., 1974; De Zeeuw et al., 1989; Placantonakis et al., 2004). The GJ-mediated signaling shapes sub- threshold oscillations (STOs) and spike timing among coupled IO neurons (De Zeeuw et al., 1998, 2003; Long et al., 2002; Blenkinsop and Lang, 2006; Jacobson et al., 2009; Kitazawa and Wolpert, 2005; Welsh et al., 1995; Lampl and Yarom 1997; Loewenstein et al., 2001; Manor et al., 1997; Placantonakis et al., 2006; Torben-Nielsen et al., 2012). Thus, the dendritic layout which determines connectivity within the nucleus is at the core of the spatiotemporal patterning of IO network activity.

Morphologically, IO neurons have historically been classified into “curly” and “straight” types (Ramón y Cajal, 1995; Scheibel and Scheibel, 1955; Foster and Peterson, 1986). The “curly” type is characterized by complex curled dendritic trees that branch and bend profusely within a very small volume of the neuropil around the soma. In contrast, the “straight” neurons have dendrites sparsely occupying a much larger volume. As GJs are overwhelmingly located on the IO neuron’s dendrites, the different dendritic shapes must lead to different connectivity profiles. Nevertheless, relatively little is known about the structural properties of IO neurons, and quantitative descriptions of different IO neuron morphologies are lacking. One reason for this is that anatomical investigations have long been limited to the examination of two-dimensional projections of neuronal structures. Using more advanced labeling techniques and detailed confocal imaging, we can now fully reconstruct and accurately quantify complex dendritic morphologies in 3D.

In this work we constructed an extensive library of IO neuron morphologies and give a detailed quantitative description of the variability in their morphological properties and the spatial arrangement of their dendritic arbors. Our results reveal that dendritic tree shapes span a continuum between the classically described “curly” and “straight” IO neuron morphologies and that dendritic trees are often directional. These findings have important implications for our understanding of connectivity in the IO network.

Materials and Methods

All animal experimental procedures were approved by the Hebrew University's Animal Care and Use Committee, and the animal experiment committee of the Royal Netherlands Academy of Arts and Sciences (DEC-KNAW) which follows the European guidelines for the care and use of laboratory animals (Council Directive 86/6009/EEC).

Single neuron labeling

Sparse viral labeling of neurons was achieved by injecting a cre-dependent fluorophore-expressing virus mixed with a highly diluted cre-expression virus into the IO of juvenile or adult mice (6 weeks to 4 months old; all animals were at least 10 weeks old after the viral transfection period). The Cre-expression virus (AAV9.CamKIIa.cre, Penn Vector Core) was diluted (1:3000, 1:3500 or 1:4000) with saline in multiple steps, taking care to mix well at each step. The diluted viral suspension was then mixed 1:1 with a loxed GFP-expression virus (AAV9.CAG.flex.eGFP.bGH, Penn Vector Core). Mice were anaesthetized using a mixture of ketamine and xylazine (100 mg/kg and 20 mg/kg) and head-fixed into a stereotaxic device. The skull over the IO was exposed through a single incision into the skin and scraping away some of the soft tissue covering the area. A single craniotomy, ~ 2 mm wide was then drilled in the skull, centered around the midline just behind the posterior suture. ~500 nL of the mixture of Cre and lox viruses was then slowly injected at 6.5 mm depth, bilaterally to the midline using air pressure. After 4–6 weeks incubation time, mice were deeply anesthetized with pentobarbital and fixed through transcardiac perfusion with 4% para- formaldehyde (PFA) in phosphate-buffered saline (PBS), and brains were post-fixed overnight in the same solution. The brains were then washed in PBS and the brain stem cut into 150 µm-thick sections in coronal or sagittal plane using a Leica VT1000S or Leica VT1200S vibratome (Leica Biosystems, Germany) and subsequently mounted with prolong gold antifade mounting medium (RI 1.47; Thermo Fisher Scientific, MA) under #1.5 coverslip glass (Thermo Fisher).

Dye-filling of IO neurons was achieved during in vitro patch-clamp experiments on acute brainstem slices (performed by N.V. or S.L., for the purpose of other projects). Alexa-labeling of IO neurons was done in 200 µm-thick coronal brainstem slices prepared following the "hot" procedure (Huang and Uusisaari 2013; Ankri et al. 2014); in brief, adult mice (3–12 months old) of either sex were deeply anesthetized with pentobarbital, decapitated and their brain stem extracted from the skull while continuously kept in oxygenated artificial cerebrospinal fluid (ACSF) warmed

to a temperature of 30–35 °C. The ACSF was composed of (in mM) 126 NaCl, 3 KCl, 1.2 kH2PO4, 26 NaHCO3, 10 glucose, 2.4 CaCl2, 1.3 MgSO4 and continuously bubbled with carbogen (95% O2/5% CO2). Slices were then incubated at 35 °C for at least half an hour and then at room temperature. Fluorescent labeling of IO neurons was achieved by adding 20–50 μM Alexa-594 or Alexa-488 Hydrazide (Thermo Fisher Scientific, MA) to a patch pipette solution containing (in mM) 4 NaCl, 140 K-gluconate, 10 HEPES, 0.01 EGTA, 0.001 CaCl2 and 4 Mg-ATP (pH adjusted with KOH to 7.2–7.3, osmolality 290–310 mOsm) during whole-cell recordings performed at room temperature. Whole-cell configuration was maintained for at least half an hour and slices were incubated for an additional half hour after recordings were termi- nated to allow dye to spread through dendrites. Slices were subsequently preserved by fixation in 0.1 M PBS contain- ing 1% PFA for 30 min and then washed and stored in PBS until mounted with Vectashield (RI 1.45; Vector laborato- ries, CA) and coverslipped. The biocytin-labeling experiments differed on several points: juvenile (4–8-week-old) mice of either sex were anesthetized with isoflurane, and their brain stem extracted and sliced in ice-cold ACSF. Slices were cut sagittally and then incubated at 35 °C for half an hour and at room temperature for at least half an hour, before being transferred into a recording chamber maintained at ~ 32 °C. The ACSF had the same composition as used in the Alexa-labeling experiments, as was the patch pipette solution except in that it contained 5 EGTA and 0.5 CaCl2, and 0.1–0.5% (w/v) biocytin (Sigma) was added. After recordings were completed, slices containing biocytin-filled neurons were fixed in 0.1 M PBS containing 4% PFA overnight at 4 °C. Slices were then washed three times (0.1 M PBS, 10 min at 4 °C), incubated with Alexa Fluor 594-conjugated streptavidin (Life technologies, 2 mg/ml) and 0.6% Triton X-100 (Sigma) in 0.1 M PBS (4 h at 4 °C), washed three times (0.1 M PBS, 10 min at 4 °C), mounted with Dako glycergel fluorescence mounting medium (RI 1.47–1.50; Dako) and coverslipped.

In our examinations of hundreds of IO neurons in both sagittal and coronal brain stem slices we noted no overt differences in the morphologies' orientations relative to the confocal z-axis, or any tendency for "curlier" or "straighter" neurons to be more prevalent in juvenile or adult mice; regardless of the experimental conditions, labeled morphologies exhibited extensive heterogeneity covering the full range from "curly" to "straight". We therefore chose to consider all the available material together and select only the most complete morphologies (see below) for inclusion in our library.

Recovery and reconstruction of morphologies

The labelled material was examined and imaged using confocal microscopy (Leica SP5 and SP8, Leica Microsystems, Germany; Zeiss LSM 510, 710, 780 and 880, Zeiss, Germany). Each mounted section was first scanned with low magnification (10×) and a maximal projection of the slice was created to record the position of the neurons within the IO volume and select candidates for high-resolution stack acquisition.

High-magnification confocal image stacks were obtained with either 40 or 63× plan-Apochromat objectives (NA 1.25–1.3) as were available at each confocal system, so that resolution ranged from 0.11 to 0.38 μm/pixel in XY plane. The sections were oversampled in z-dimension (ranging 0.1–0.3 μm/z-step) to support correction of the z-axis values due to shrinkage factor. The morphologies were manually reconstructed using the Vaa3D software (Peng et al., 2010), taking care that the reconstructions end up as sorted trees with a single root. The shrinkage was estimated from the thickness of the mounted section (as measured by confocal visualization) relative to the fresh section and the final reconstructions were expanded in z-dimension to account for the shrinkage (ranging 1.5–3×).

To ensure that the overall dendritic shape of the morphologies in our library was not distorted, morphologies were carefully selected for inclusion based on the completeness of their 3D reconstruction. Morphologies that appeared skewed, due to optical or physical distortions, were discarded from analysis. Distal and/or very thin dendrites were occasionally difficult to reconstruct in entirety due to decreasing signal/noise ratio, and reconstructions were discarded if multiple disconnected fine branches could be observed around a reconstruction's dendrite tips in the confocal image stack. We also kept track of the number dendrite tips occurring at the slice surface counting these as "cut tips" and discarded any morphologies that had more than half of tips cut, or that had one or more proximal dendrites cut at < 50 μm path length. Out of the hundreds of neurons examined in confocal image stacks, ~ 150 morphologies were reconstructed, and a total of 36, 27 and 29 morphologies were selected for the viral, Alexa- and biocytin-labeled datasets, respectively. The selected morphologies will be submitted to NeuroMorpho.org.

Quantification of morphological properties

The included morphologies were first inspected by the authors and subjectively labeled as being either "straight", "curly" or "ambiguous" (18, 44 and 30 out of 92 morphologies, respectively). Subsequently, the 25 parameters, covering both "within-tree" and "whole-tree" variables (Uylings

and van Pelt, 2002) were obtained as extracted by Vaa3D or by custom scripts in MatLab and btmorph (Torben-Nielsen, 2014). The complete list of measurements, together with their definition, is provided in Table 1.

Three of the measures obtained by custom scripts were defined as follows. Soma-border distance was defined as the shortest distance of the reconstruction root node to the extrapolated convex hull of the full reconstruction. Soma- center of mass distance was defined as the distance of the root node to the average location of all the nodes of the reconstruction. Stem directionality was defined as the length of the vector obtained by sum of all vectors formed from reconstruction root node to the first nodes of each dendrite, normalized by the number of stem vectors; in this way, a soma with one dendrite would have a directionality value of 1, whereas a soma with dendrites stemming evenly around the cell body would approach directionality of 0.

Statistical analyses

Statistical analyses were performed in R (R Core Team, 2018; Wickam et al., 2017, 2018; Fox and Weisberg, 2011; Wickam, 2016; Revelle, 2018; Ogle, 2018; Peterson and Carl, 2018; Kassambara and Mundt, 2017; Venables and Ripley, 2002), unless stated otherwise. The assumption that data are sampled from a normal distribution was rejected for almost all measures based on the Shapiro–Wilk normality test ($p < 0.1$ in each data set for all measures except number of stems and average local bifurcation angle). Therefore, correlation estimates and p values were calcu- lated using Spearman's rank correlation test, and group- level comparisons in mean and variance were calculated using Welch's ANOVA and Levene's test for equality of variance, respectively.

For performing PCA on the morphometric data per dataset, the values of all morphometric features were scaled and centered to have zero mean and unit variance. We then applied K-means clustering into two clusters to the data as represented along the first three components of the decomposition (which resulted in nearly identical clustering as applying K-means clustering to the data represented along the first two PCs only).

On individual morphologies, PCA was performed in MatLab and applied to the x-, y-, z-coordinates of each point on the reconstruction without re-scaling the data since variance has the same units in each dimension of 3D space.

Table 1 The morphometric measures used in the study

Measure #	Name	Description
1	Number of stems	Number of primary dendrites
2	Stem diameter—mean	Average diameter of dendrite stems (μm)
3	Stem diameter—sum	Sum of the diameter of all dendrite stems (μm)
4	Stem diameter—maximum	Maximal diameter of dendrite stems (μm)
5	Stem directionality	Directionality of dendrite stems; for definition see "Methods"
6	Dendrites—total length	The summed length of all of a neuron's dendrites (μm)
7	Dendrite diameter—mean	Average diameter of the dendrites (μm)
8	Dendrites—longest single path length	Longest soma-to-tip dendrite path length (μm)
9	Number of bifurcations	Number of bifurcation points on the dendritic tree
10	Local bifurcation angle—mean	Angle formed at the vertex of a bifurcation, averaged over all bifurcations
11	Remote bifurcation angle—mean	Angle to the tips of two daughter branches of a bifurcation, averaged over all bifurcations
12	Number of branches	Number of segments (between two branch points or between a branch point and a tip)
13	Branch order—maximum	The number of branches coming off the most-branching dendrite on the tree
14	Number of tips	Number of dendrite terminal points within the imaged slice
15	Number of cut tips	Number of dendrites running out of the imaged slice
16	Number of tips—total	Total number of dendrite terminal points on the reconstructed morphology
17	Soma area	Area of the 2D projection of the soma
18	Hull volume	Volume of the convex hull containing all of the neuron's dendrites (μm^3)
19	Soma-to-hull distance	Smallest distance between the soma and the hull containing all of the neuron's dendrites (μm)
20	Soma-to-center of gravity distance	Distance between the soma and the average of all points of the reconstructed morphology (μm)
21	Reach—maximum	Furthest reach of the dendritic tree away from the soma (μm)
22	Straightness	Maximal reach divided by maximal path length
23	Mean contraction	Furthest reach divided by longest path length of each tree arising from the primary den- drites, averaged over the number of primary dendrites
24	Hausdorff dimension	Measure of fractal dimension (Mizrahi et al. 2000)
25	Mean fragmentation	Number of compartments that form a branch between two bifurcation points, or between a bifurcation and a terminal tip

Numbers in the first column are used to reference to the measures in Fig. 3c. "Compartment" refers to the variable-length nodes of reconstruction within which the dendrite thickness and shape is uniform.

Reconstruction and analysis of IO soma distribution

For analyzing the spatial distribution and clustering of IO somata, we used two mice obtained from a PDX-cre (Song et al. 2010) X Ai9 (Madisen et al. 2010) mating, resulting in strong expression of tdTomato in IO neurons. The mice were perfusion-fixed and their brains sectioned and mounted as described above, and all somata on one hemisphere in both animals were reconstructed manually for each subnucleus using Fiji software (Schindelin et al. 2012).

The density distribution of IO somata was estimated by 3D binning the somata in voxels of 10 μm3, and subsequently applying an isotropic 3D-gaussian kernel to account for binning artifacts. The standard deviation parameter utilized for the 3D kernel was 4. To test the null-hypothesis that

the density of somata was isotropic, the distribution of voxel densities of the data was compared to a volume bootstrapping the somata densities assuming a uniform density. Thus, the bootstrap was constructed by drawing somata counts from a uniform distribution within the bounded volume formed by the non-zero somata voxels. The density per voxel in the uniform distribution is simply the total somata count in the actual subnucleus divided by the total volume included in non-zero voxels. A two-sample Kolmogorov–Smirnov test was used to compare the distributions.

Presence of local soma clusters was examined using the DBSCAN algorithm (Ram et al. 2010) implemented in MatLab. This algorithm assigns cluster membership to any group of at least N somata where any one soma within the cluster is at most D μm removed from another cluster member. Clustering was explored for values of D ranging from 15 to 100 μm and values of N ranging from 3 to 20.

Results

Variability of IO dendritic morphology

We used a sparse viral labeling technique to induce strong fluorescent labeling in a small number of neurons in a given IO (Fig. 1a, b) as well as IO neurons that were labeled using either Alexa (488 or 594) or Biocytin during in vitro patch- clamp experiments (see “Methods”). Confocal image stacks were acquired from the labeled tissue and a total of 90 manually reconstructed morphologies were analyzed (see “Methods”). Except for two neurons from the dorsal cap of Kooy (DCK)-subnucleus (which has been shown to be phenotypically distinct from the main IO subnuclei; Urbano et al., 2006), neurons from all IO subnuclei were included in our analyses. The different methods of neuronal labeling lead to some variability in the quality of the confocal image stacks; specifically, the viral-labeled material was of higher quality regarding the ratio between signal strength and background noise. Nonetheless, qualitative differences between morphologies reconstructed from the differently labeled materials were not immediately apparent (see Fig. 1c–f). To exemplify morphologies from each of the three data sets, Fig. 1c–e show maximal Z-projections of confocal stacks from viral-, Alexa- and biocytin-labeled data, respectively; the corresponding reconstructed morphologies are shown in the left column in Fig. 1f. Additional examples of morphologies reconstructed from the three datasets are shown in the middle and right columns of Fig. 1f, indicating a progression from “very curly” (left column) to “very straight” (right column) morphologies in each of the three data sets.

Examining the full morphological library, both “clearly curly” (30 out of 90; Fig. 1f, left column) and “clearly straight” morphologies (16 out of 90; Fig. 1f, right column) could be subjectively identified. However, categorical distinction was ambiguous, as a significant portion of the morphologies could not be easily classified (44 out of 90; examples are shown in Fig. 1f, middle column).

It has been previously considered that IO neurons with subjectively straight and curly appearance would be anatomically segregated into different parts of the olivary nucleus (Scheibel and Scheibel 1955; Ruigrok et al. 1990). However, we found that “curly” and “straight” neurons could be found within each of the main IO subnuclei. This is demonstrated in Fig. 1g, where morphologies from different sources are shown at their anatomical locations approximated at two different levels of the anterio-posterior axis (see “Methods”). These results demonstrate extensive morphological heterogeneity in IO neuron dendritic morphologies across all subdivisions of the nucleus.

Quantitative analyses reveal a continuum in neuronal morphology

While the ambiguity of dendritic morphologies seemed to rule out clear classification, we investigated whether features distinguishing between IO cell classes could be revealed using a quantitative approach. To this end we measured 25 morphometric parameters from each of the reconstructed neurons (see Table 1 and “Methods” for measurement definitions). The measured parameters included basic ones such as the number of dendrite stems, number of branches, dendritic path length and maximal reach (see Fig. 2a). We also measured a number of parameters aimed at describing the overall shape of the dendritic trees; most prominent among these (as explained below) is “straightness”, which was defined as maximal reach divided by the longest single dendrite path length.

Examining the distributions of morphological parameter values, we noted that there are some differences between the three groups of neurons reconstructed from material obtained using different labeling methods. The outcome of statistical tests performed to assess differences across groups are summarized in Table 2 and show that group means were significantly different on almost all measures. Thus, we performed quantitative analyses of morphometric measures on each of the three data sets separately.

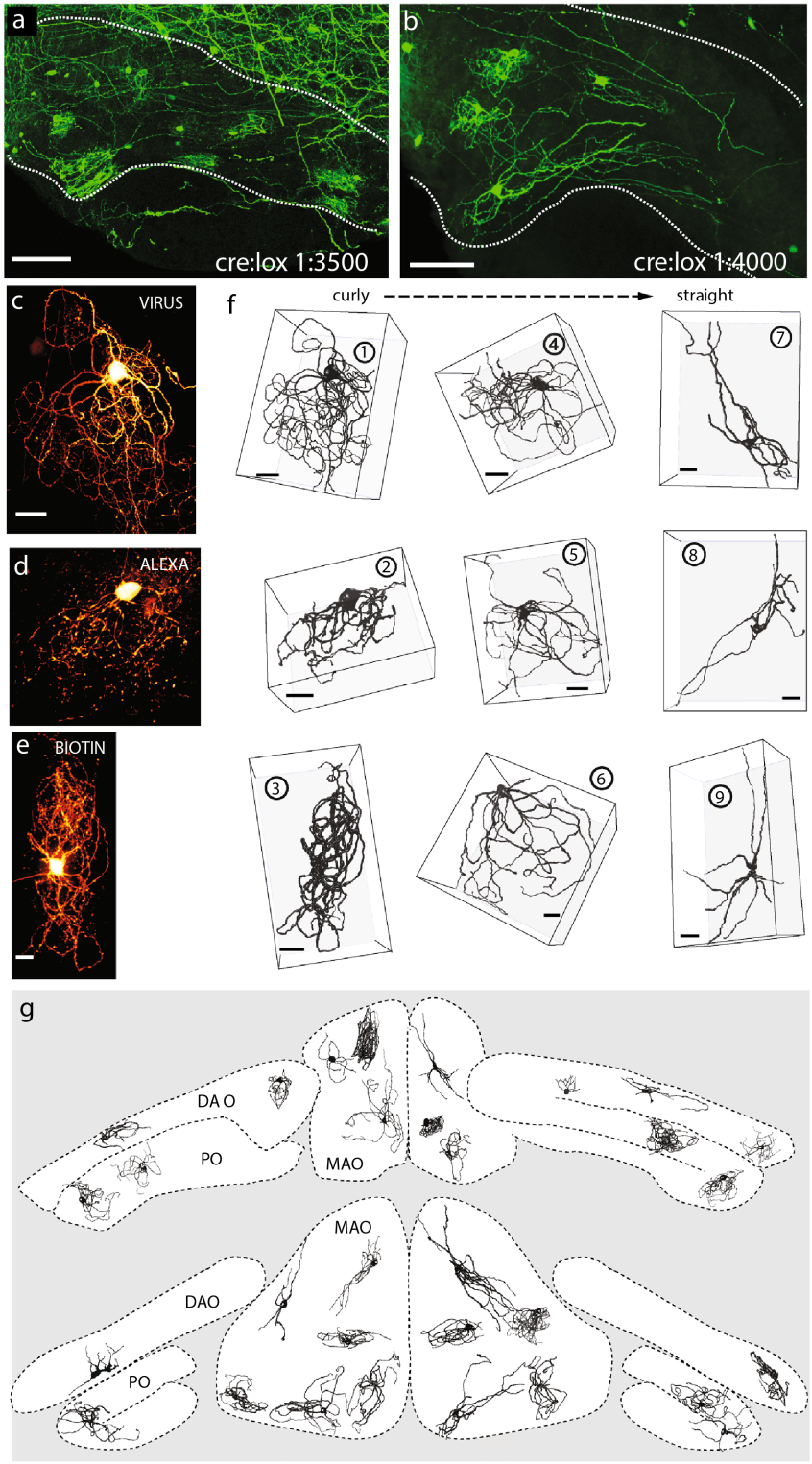

Fig. 1 Fluorescent labeling of IO neurons reveals complex projection of a 100 µm-thick confocal image stack of a coronal brain stem slice labeled sparsely by viral transfection (1:3500 dilution of cre-expression virus). IO borders are marked with a white dotted line. Scale bar 100 µm. b as in a, but with 1:4000 dilution. exemplifying "very curly" IO c), Alexa-594 (d) or biocytin (e) staining. Scale bar 20 µm. f Examples of reconstructed morphologies from the three data sets (as in c–e) ranging from "very curly" (left column, same examples as shown in c–e) to "straight" (rightmost column). Note that the scale varies between subpanels and perspective; scale bars represent 20 µm in the xy plane. Encircled numbers denote reconstruction IDs as referred to in the text. g A composite drawing showing the shape and orientation of a selection of the morphologies within the volume of the IO. Note the presence of curly and straight neurons in all subnuclei (abbreviations: PO principal olive, DAO dorsal accessory olive, MAO medial accessory olive).

In an ideal and simple case, a distinction between groups is implied by a clear bi- or multimodal distribution in one or more features. However, we observed no immediately apparent groupings in the distributions of any of the measured parameters. To exemplify the variability in morphological parameter distributions, histograms of maximal reach, number of stems, number of branches, total dendrite length and straightness are shown in Fig. 2b–e for each data set as indicated in the legend, demonstrating that there are no clear multimodal distributions in any of the data sets. Nonetheless, it was evident that IO neurons do not form a single population with normally distributed inter-individual variability: as shown in Table 3, we found that in each data set, the null-hypothesis that data are sampled from a single normal distribution should be rejected for almost all measures except number of stems and local bifurcation angle. To enumerate the distributions of the measured morphological parameters, Table 4 displays the minimal, mean, median and maximal values of each parameter distribution in each data set. Taken together, while we should conclude that the observed morphological heterogeneity is unlikely to result from normally distributed inter-individual variability in a single neuronal population, we did not find any single morphometric parameter that would clearly distinguish between morphologically different classes of neurons.

We then asked which of the objectively defined morphological parameters could best be used to describe the subjectively perceived range of variability from “curly” to “straight” by calculating the Spearman correlation between the subjectively assigned categories (curly, ambiguous and straight) and each of the measured parameters (Table 5, left side). Of all the different measures describing dendritic tree shape, straightness best corresponded to our subjective categorization across all three datasets; therefore, we chose this measure as an objective representation of a neuron’s position along the curly–straight continuum. Notably, besides measures directly aimed at describing the dendritic tree shape we found that in each data set at least one other measure was also correlated with the subjectively assigned classes (see Table 5); for example, in all three datasets the number of dendrite tips was significantly correlated with subjective class such that the “straight” neurons had the fewest tips. Similarly, these correlations could be found with the straightness-parameter instead of subjective class; for example, the number of stems and branches are strongly correlated both to subjective class and straightness in the viral- and Alexa-labeled datasets (see Table 5). Correlation statistics between straightness and all other morphometric parameters are reported on the right side in Table 5, and as examples, correlations of straightness to the number of stems, branches and total length are shown in Fig. 2f–h for the data obtained from viral-labeled morphologies; correlations between these parameters in the other two data sets follow the same trends and are shown in Supplementary Fig. 1.

Taking another approach to assessing which properties might best distinguish “curly” from “straight” morphologies we performed principal component analysis (PCA) and K-means clustering on the quantified morphological data (see “Methods”). If distinct morphological classes could be defined based on a combination of parameters, then dimensionality reduction of the data through PCA would result in a gap between groups of data points belonging to different classes. Due to the previously mentioned quantitative differences between the three data sets, the PCA-decomposition and K-means clustering results also vary quantitatively across data sets; nonetheless, the obtained results were qualitatively similar in each case, and are shown for viral-labeled data in Fig. 3 while the results of the same analyses performed on the patch-filled data sets are provided in Supplementary Fig. 2.

As shown in Fig. 3a, we found that a clear gap between groups of data points did not become apparent in the distribution of the data along the first two principal components (PC1 and PC2) of the PCA-decomposed morphometric data. groups was defined almost exclusively along PC1; this is shown in Fig. 3a by the almost vertical grey dashed line marking the border between the two clusters. More than that, PC1 appeared to follow our subjective classification of the IO neuron morphological types; this is apparent in Fig. 3a in that most morphologies that were subjectively classified as being “curly” are found on the left side, while subjectively “straight” morphologies are all found on the right and “ambiguous” morphologies are mostly in between. Thus, it seems that PC1 closely follows the curly- to-straight continuum, and that “curly” and “straight” are indeed relevant descriptors of the morphological variability among IO neurons, i.e., a classification based on features unrelated to morphological “straightness” was not found. This idea was also reflected in the strong and significant correlation between PC1 and straightness (Fig. 3b, $Rho = 0.84$, $p < 0.0001$).

Our quantified morphometric data set contains multiple parameters aimed at describing the overall shape of dendritic trees; such parameters are correlated with each other by definition, and this may artificially cause the main principal component to follow measures of dendritic tree shape. However, as depicted in Fig. 3c where the relative contribution of each measure to the first two PCs is displayed on a scale from 0 to 1 for the viral-labeled morphologies, measures such as the number of stems and branches also contributed strongly to the separation along PC1. This shows that properties not directly describing dendritic tree shape also vary systematically with the measured straightness of the morphologies, and further strengthens our confidence that the curly–straight axis is the most relevant descriptor of morphological variability in the IO neuron population.

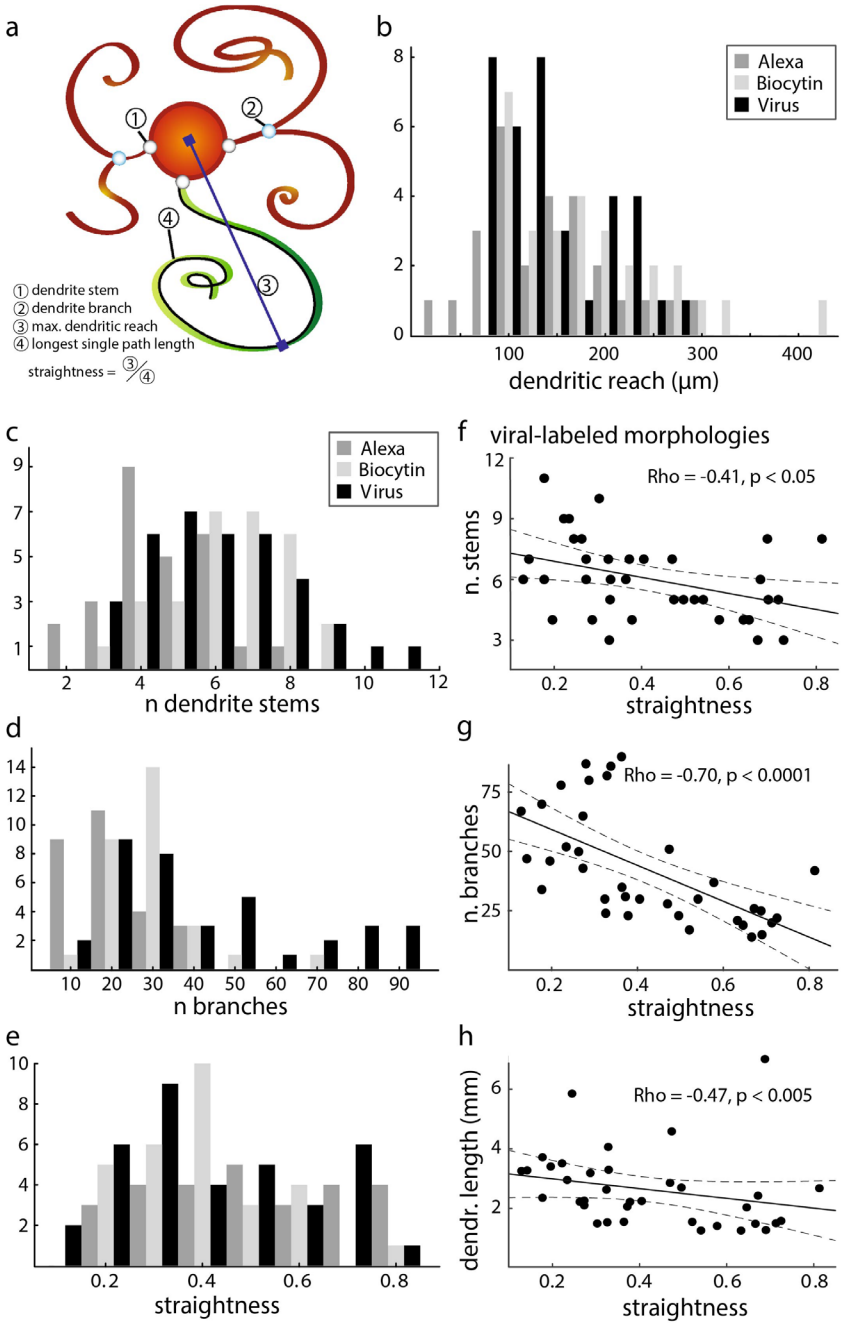

Fig. 2 Morphological properties of IO neurons quantified. a Schematic illustration of some of the basic morphological parameters used to characterize the dendritic morphologies. Maximal dendritic reach is defined as the furthest reach of the dendritic tree away from the soma; the longest single path length is defined as the longest soma-to-tip path length on a dendritic tree; and straightness is defined as the maximal dendritic reach divided by the longest single dendrite path length. For a list of all morphometric parameters and their definitions, see Table 1. Distributions of maximal dendritic reach (b), number of dendrite stems emerging from the soma (c), number of branch points on the dendritic trees (d) and straightness (e) in each of the three data sets; shadings refer to morphologies recovered using different labeling method as indicated. Distributions of number of dendrite stems (f), number of branch points (g) and total dendritic length (h) with respect to straightness in the viral-labeled data; the same distributions in the Alexa- and biotin-labeled data sets are displayed in Supplementary Fig. 1. Reported correlation statistics represent the strength and direction (Rho) and significance level (p) calculated using Spearman's rank correlation test (see "Methods"). Correlations between straightness and all other morphological measuresare reported in the right halfof Table 2 for each of the three data sets.

Table 2 significance of group level differences in mean (left column) and variance (right column)

Measure names	Welch's ANOVA	Levene's test for equality of variance
Number of stems	< **0.0001**	0.2562
Stem diameter—mean	**0.0129**	0.7094
Stem diameter—sum	< **0.0001**	**0.0071**
Stem diameter—maximum	**0.0004**	0.4644
Stem directionality	0.5522	0.8356
Dendrites—total length	< 0.0001	0.0743
Dendrite diameter—mean	**0.0005**	0.6540
Dendrites—longest single path length	< **0.0001**	0.3177
Number of bifurcations	< **0.0001**	< **0.0001**
Local bifurcation angle—mean	0.2153	0.1322
Remote bifurcation angle—mean	0.7173	0.1410
Number of branches	< **0.0001**	< **0.0001**
Branch order—maximum	**0.0002**	**0.0295**
Number of tips	**0.0065**	**0.0460**
Number of cut tips	**0.0006**	0.1199
Number of tips—total	< **0.0001**	**0.0332**
Soma area	< **0.0001**	**0.0279**
Hull volume	**0.0152**	0.3412
Soma-to-hull distance	**0.0076**	0.0862
Soma-to-center of gravity distance	**0.0138**	0.2072
Reach—maximum	0.0522	0.3715
Straightness	0.0543	0.0755
Mean contraction	< **0.0001**	0.2088
Hausdorff dimension	**0.0002**	**0.0123**
Mean fragmentation	**0.0016**	0.3353

Values reflect p levels calculated using Welch's ANOVA (left) and Levene's test (right), for each of the morphological parameters as indicated in each row. Values highlighted in bold indicate measures on which morphological parameter distributions across the three data sets were significantly different in their mean/ variance, respectively.

Taken together, the results described so far do not support the idea that IO neurons could or should be classified into subtypes based on their morphological appearance. Furthermore, these results indicate that a description of the morphological variability based on the simple straightness-measure is as informative as a description based on a decomposition of the quantified data.

Table 3 Likelihoods of normality

Measure names	Viral-labeled	Alexa-labeled	Biotin-labeled
Number of stems	0.1355	0.1881	0.1440
Stem diameter—mean	0.1712	**0.0078**	**0.0366**
Stem diameter—sum	0.8794	0.5099	**0.0007**
Stem diameter—maximum	**0.0068**	**0.0097**	**0.0298**
Stem directionality	0.1491	*0.0814*	0.6311
Dendrites—total length	**0.0003**	*0.0689*	0.1586
Dendrite diameter—mean	0.2036	0.6204	**0.0056**
Dendrites—longest single path length	**0.0010**	0.2313	**0.0009**
Number of bifurcations	**0.0012**	0.1020	**0.0007**
Local bifurcation angle—mean	0.2128	0.7908	0.5166
Remote bifurcation angle—mean	0.2437	*0.0913*	0.7735
Number of branches	**0.0015**	0.1663	**0.0010**
Branch order—maximum	*0.0812*	0.0066	**0.0052**
Number of tips	*0.0892*	0.0368	**0.0040**
Number of cut tips	*0.0826*	0.2140	**0.0004**
Number of tips—total	**0.0144**	0.1568	**0.0003**
Soma area	0.8722	**0.0006**	**0.0408**
Hull volume	< **0.0001**	**0.0059**	< **0.0001**
Soma-to-hull distance	**0.0043**	**0.0039**	**0.0011**
Soma-to-center of gravity distance	< **0.0001**	< **0.0001**	*0.0613*
Reach—maximum	**0.0019**	0.2754	**0.0099**
Straightness	**0.0349**	0.3158	*0.0946*
Mean contraction	**0.0453**	*0.0892*	0.1451
Hausdorff dimension	*0.0545*	0.5955	0.1031
Mean fragmentation	**0.0101**	0.6274	**0.0132**

Values reflect p levels calculated using the Shapiro–Wilk normality test for each measure as indicated in each row, for each of the three data sets as indicated on the top of each column. Distributions that are unlikely to reflect a normal distribution are highlighted in italics ($p < 0.1$) and bold ($p < 0.05$).

Table 4 Minimal, median, mean, and maximal values of each morphological parameter distribution as indicated in each row, for each of the three data sets as indicated above the columns.

Subjective class	Virus				Alexa				Biocytin			
	Min	Median	Mean	Max	Min	Median	Mean	Max	Min	Median	Mean	Max
Number of stems	3	6	6.03	11	2	4	4.63	8	3	7	6.45	9
Stem diameter—mean	0.68	2.16	2.17	3.22	1.17	1.75	1.97	3.88	1.67	2.5	2.49	3.95
Stem diameter—sum	6.11	12.7	12.55	18.93	4.6	8.6	8.94	15.5	10.2	15.13	16.98	32.6
Stem diameter—maximum	1.46	3.5	3.32	4.67	1.6	2.5	2.66	5.1	2.2	3.33	3.62	5.1
Stem directionality	0.12	0.3665	0.41	0.865	0.127	0.384	0.42	0.749	0.131	0.458	0.46	0.881
Dendrites—total length	1260	2311	2634.67	7006	372	1328	1423.93	3458	860	2974	3098.48	5764
Dendrite diameter—mean	0.81	2.045	2.05	3.45	1.1	2.5	2.46	4.1	1.53	2.83	2.98	5.87
Dendrites—longest single path length	170	330	367.69	906	92	268	295.56	523	257	436	468.52	1076
Number of bifurcations	6	16.5	20.22	43	3	8	9.11	17	3	12	12.48	31
Local bifurcation angle—mean	61.4	74.95	74.96	89.4	41.8	65.8	70.11	97.7	48	73	73.10	98.3
Remote bifurcation angle—mean	58.5	84.2	84.04	107.8	26.2	87.6	84.00	114.9	49.6	90.3	86.82	122.3
Number of branches	14	34.5	42.78	90	8	20	21.11	40	8	28	29.62	68
Branch order—maximum	3	6	6.81	13	2	4	4.67	9	3	4	4.72	9
Number of tips	1	10.5	11.94	33	0	7	8.04	19	3	12	12.66	31
Number of cut tips	0	7	6.08	11	0	4	3.59	9	1	3	3.76	13
Number of tips—total	9	16.5	18.03	38	5	11	11.63	23	6	16	16.41	35
Soma area	112	188	195.04	304	97	124	131.19	242	150	246	252.69	444
Hull volume (10^4 μm^3)	13.99	49.00	121.050	2062.27	6.930	49.24	60.25	160.1	23.53	115.07	192.64	1293.8
Soma-to-hull distance	0	11.621	14.55	51.332	0	6.218	6.64	24.62	0	7.258	10.54	37.675
Soma-to-center of gravity distance	8.445	30.697	37.67	133.65	8.912	30.76	52.69	201.5	7.417	51.762	59.69	131.57
Reach—maximum	65	121	139.53	265	35	154	145.56	298	95	165	183.62	420
Straightness	0.129	0.368	0.42	0.813	0.19	0.49	0.51	0.81	0.21	0.39	0.40	0.79
Mean contraction	0.59	0.695	0.71	0.83	0.53	0.68	0.69	0.79	0.5	0.6	0.61	0.8
Hausdorff dimension	1.05	1.18	1.20	1.47	1	1.1	1.11	1.28	1.06	1.14	1.16	1.3
Mean fragmentation	43.8	86.75	92.12	173.6	43.5	73.5	76.04	115	54	96.6	97.60	184.1

Table 5 Correlations between morphometric measures and subjective classification (left) and straightness (right)

Measure names	Correlations to subjective classification						Correlations to straightness					
	Viral-labeled		Alexa-labeled		Biotin-labeled		Viral-labeled		Alexa-labeled		Biotin-labeled	
	Rho	p	Rho	p	Rho	p	Rho	p	Rho	p	Rho	p
Subjective class							− 0.71	< 0.0001	− 0.83	< 0.0001	− 0.50	0.005
Number of stems	0.31	0.067	0.51	0.007	0.36	0.055	− 0.41	0.013	− 0.60	0.001	− 0.12	0.536
Stem diameter—mean	− 0.30	0.080	− 0.35	0.075	− 0.32	0.089	0.58	0.000	0.42	0.030	0.15	0.428
Stem diameter—sum	− 0.08	0.661	0.23	0.254	− 0.35	0.067	0.14	0.411	− 0.10	0.608	0.31	0.104
Stem diameter—maximum	− 0.22	0.210	− 0.32	0.103	− 0.18	0.361	0.24	0.158	0.37	0.058	0.11	0.567
Stem directionality	0.37	0.027	0.00	0.996	0.11	0.563	− 0.11	0.538	− 0.09	0.664	− 0.13	0.492
Dendrites—total length	0.52	0.001	0.32	0.106	− 0.02	0.915	− 0.47	0.004	− 0.25	0.212	0.12	0.544
Dendrite diameter—mean	− 0.41	0.014	− 0.69	< 0.0001	− 0.28	0.145	0.53	0.001	0.52	0.005	0.47	0.011
Dendrites—longest single path length	0.33	0.051	− 0.09	0.660	− 0.16	0.399	− 0.53	0.001	0.02	0.906	− 0.19	0.328
Number of bifurcations	0.60	< 0.0001	0.50	0.008	0.33	0.085	− 0.69	< 0.0001	− 0.31	0.112	− 0.25	0.192
Local bifurcation angle—mean	− 0.07	0.702	− 0.26	0.194	− 0.29	0.132	− 0.13	0.459	0.50	0.008	− 0.11	0.554
Remote bifurcation angle—mean	0.28	0.095	0.33	0.096	0.05	0.815	− 0.26	0.119	− 0.41	0.034	− 0.14	0.466
Number of branches	0.62	< 0.0001	0.54	0.004	0.36	0.052	− 0.70	< 0.0001	− 0.38	0.051	− 0.19	0.334
Branch order—maximum	0.51	0.002	0.19	0.345	0.10	0.592	− 0.74	< 0.0001	0.01	0.972	− 0.43	0.020
Number of tips	0.73	< 0.0001	0.69	< 0.0001	0.48	0.008	− 0.67	< 0.0001	− 0.54	0.004	− 0.42	0.025
Number of cut tips	− 0.40	0.017	− 0.30	0.125	− 0.22	0.254	0.40	0.015	0.21	0.298	0.39	0.036
Number of tips—total	0.65	< 0.0001	0.68	< 0.0001	0.32	0.091	− 0.63	< 0.0001	− 0.54	0.003	− 0.26	0.173
Soma area	0.15	0.391	0.04	0.855	− 0.15	0.426	− 0.04	0.816	0.05	0.806	0.29	0.131
Hull volume	− 0.42	0.010	− 0.43	0.024	− 0.48	0.008	0.50	0.002	0.45	0.017	0.49	0.007
Soma-to-hull distance	− 0.02	0.910	0.24	0.225	− 0.07	0.713	− 0.12	0.504	− 0.23	0.249	0.09	0.649
Soma-to-center of gravity distance	− 0.47	0.004	− 0.63	< 0.0001	− 0.41	0.026	0.48	0.003	0.67	< 0.0001	0.40	0.034
Reach—maximum	− 0.54	0.001	− 0.72	< 0.0001	− 0.52	0.004	0.71	< 0.0001	0.80	< 0.0001	0.68	< 0.0001
Straightness	− 0.71	< 0.0001	− 0.83	< 0.0001	− 0.50	0.005						
Mean contraction	− 0.60	< 0.0001	− 0.79	< 0.0001	− 0.58	0.001	0.57	< 0.0001	0.77	< 0.0001	0.44	0.016
Hausdorff dimension	0.58	< 0.0001	0.43	0.026	0.36	0.058	− 0.69	< 0.0001	− 0.44	0.021	− 0.19	0.334
Mean fragmentation	0.05	0.778	0.57	0.002	− 0.01	0.974	− 0.12	0.491	− 0.56	0.002	− 0.08	0.691

Values reflect Spearman correlation statistics with each of the morphological parameters as indicated in each row, for each data set as indicated at the top of each column. Rho reflects the strength and direction of the correlation; p values highlighted in bold indicate measures that were significantly correlated with the subjective classification/straightness, respectively.

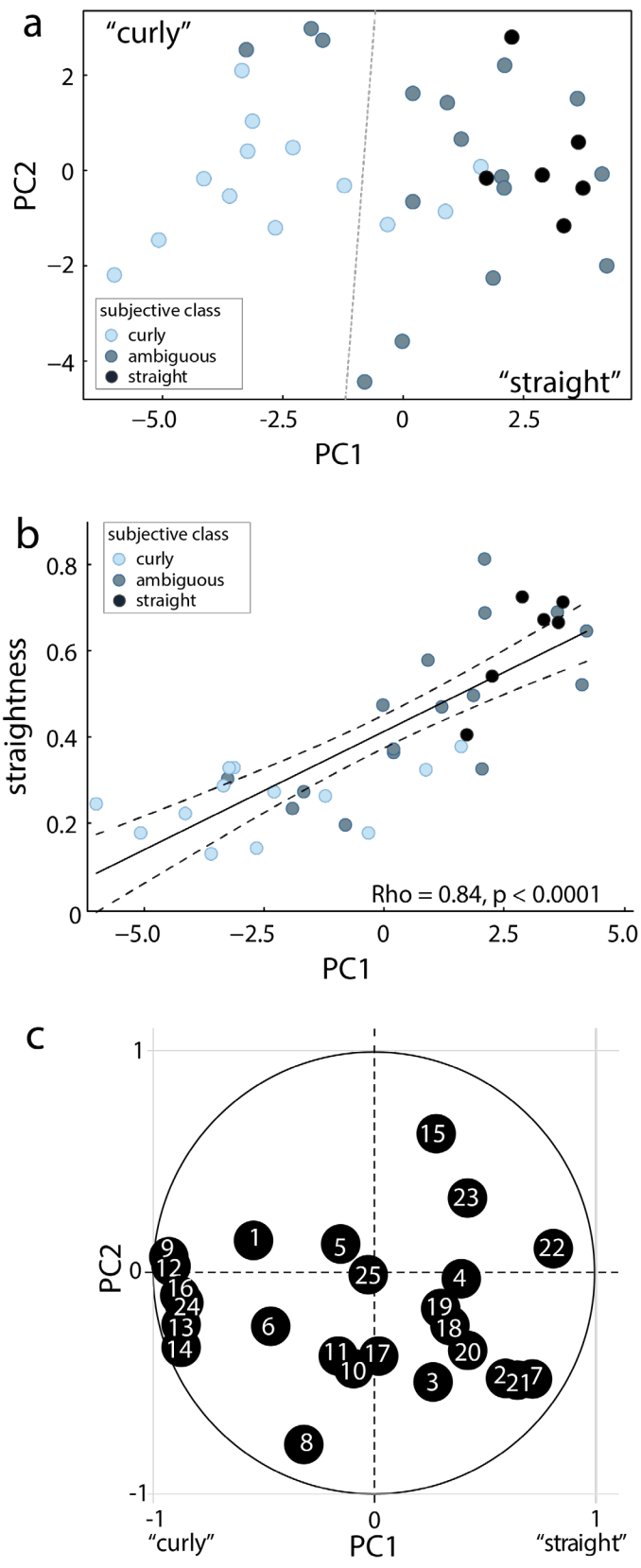

Fig. 3 Algorithmic classification does not reveal clearly separated ▸clusters. a Algorithmic classification shown as a scatter along the first two principal components (PCs) of separation for the viral-labeled data set. The grey dashed line marks the division into "curly" and "straight" groups as determined by a K-means algorithm; fill color represents subjective classification, as indicated. Note that the separation along the first principal component (PC1) appears to correspond to the subjective classification into morphological subtypes: subjectively "straight" neurons occupy the far-right side of the distribution while "ambiguous" and "curly" neurons are found in the middle and to the left. The slight mismatch between the subjective and algorithmic classification into "curly" and "straight" morphological types is another indication that seeking a quantitative justification for the subjective typification is futile. b Correlation of the main axis of separation to "straightness" in the viral-labeled data set; fill color represents subjective classification as indicated. c Relative contributions of the 25 morphometric parameters to the principal component separation in the viral-labeled data set. Numbers in circles correspond to the measures as listed in Table 1. The closer a parameter is to 1, the more it contributed to the separation in the PC space, in the direction indicated by its position within the unit circle; a parameter located at the origin did not contribute to the PC separation.

Non-isomorphic IO dendrite fields

Non-isomorphic, or “pyriform” IO neuron dendritic fields have been described as early as the anatomical work of Ramón y Cajal (first published between 1905 and 1911); however, it has been assumed that such directionality arises only in the proximity of borders of the IO or its different subnuclei and that IO neurons residing within the main IO volume have roughly spherical shapes with somata surrounded by dendrites on all sides (Ramón y Cajal, 1995; Scheibel and Scheibel, 1955). Contrary to this description we found that neurons with directionally extended den- dritic trees were also regularly encountered at distances far (> 75 µm) removed from boundaries of IO subnuclei (see Fig. 1a, g). In the following paragraphs we present two descriptors of dendritic directionality in IO neurons, one pertaining to the distribution of dendrites within the 3D volume occupied by the neuron (Fig. 4a), and one pertaining to the location of the soma within the dendritic volume (Fig. 4b). As no more correlation statistics will be presented, data acquired using different labeling methods are shown overlaid in the same panel, using different symbols to mark the different data sets as indicated.

There are two distinct ways in which the dendritic arrangement of an individual IO neuron can be non-homogeneous. First, the neuron’s dendrites are not distributed evenly within a spherical volume. We quantified this by performing PCA on the x-, y-, z-coordinates of the dendritic tree of each individual morphology. The relative proportions of variance explained along each of the three principal components (PCs) of a decomposed morphology represent the “stretchedness” of the dendritic tree along the axes of 3D space; if dendrites are distributed evenly within a spherical volume, each PC would explain 33% of the variance. Figure 4a shows that a large portion of neurons occupy a highly uneven volume with the first PC explaining more than 60% of their ‘variance in space’, whereas very few neurons are even roughly spherically shaped. As the examples shown in Fig. 4d illustrate, there is a continuum of dendritic tree shapes ranging from spherical (orange, red, and pink examples) to ellipsoid (green) to conical (blue) and even flat (cyan) morphologies. Notably, while the “straightest” morphologies were almost always highly elongated (see positions of examples 7–9 from Fig. 1 and the examples marked with blue and cyan in Fig. 4d), very “curly” morphologies also tended to have elongated shapes (see Fig. 1, example 3 and the example marked with green in Fig. 4d).

Second, IO neuron somata are usually not located in the center of mass (CoM) of the dendrites; instead, we found that in more than 90% of all neurons the shortest distance between the soma and the border of the volume they occupy(soma-border (SB) distance) is smaller than the soma-CoM distance (Fig. 4b). This means that IO neuron dendrites do not uniformly occupy the space around the soma, but instead extend into a preferred direction. In contrast to the

directionality of the overall dendritic mass, the directionality in the positioning of dendrite stems on the soma is distributed randomly (Fig. 4c), so that directionality arises because dendrites take a sharp turn as they emerge from the soma and branch profusely only in the main direction.

Taken together, these results show that IO neuron dendritic trees are directional and indicate that this directionality is a relevant feature of the network's architecture.

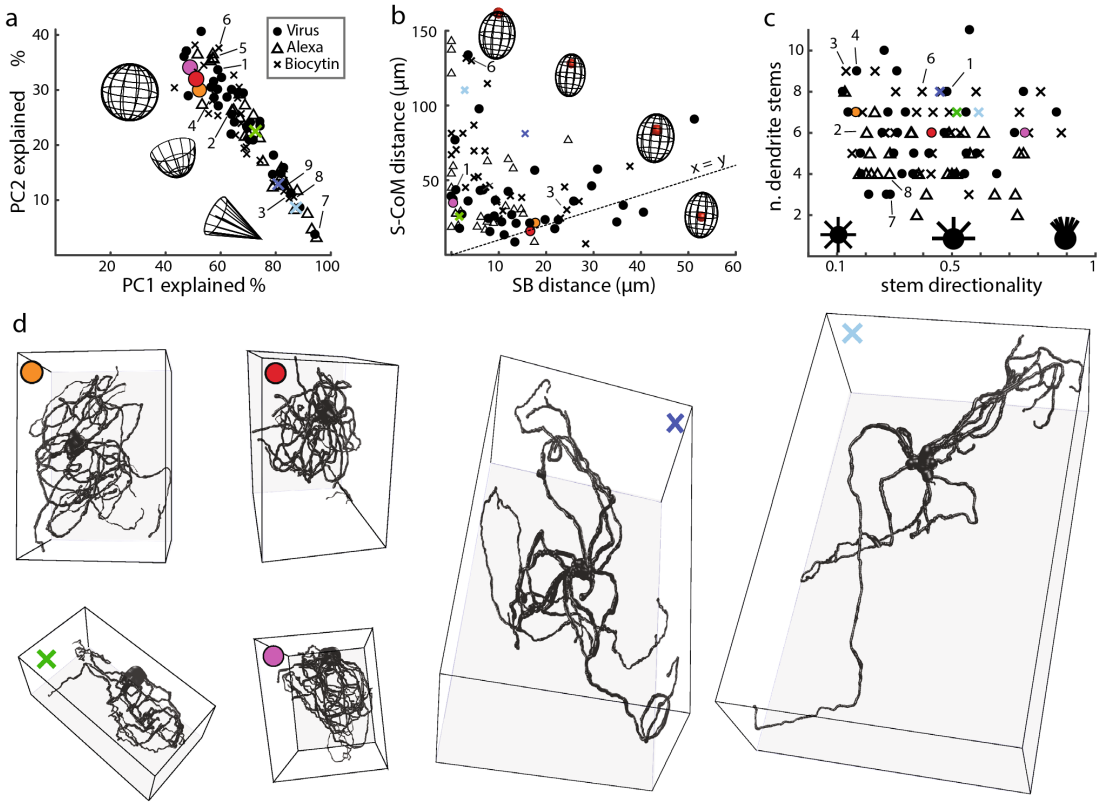

Fig. 4 IO neuron morphologies with spherical dendritic fields and somata in the center are rare. a Scatter plot showing the percentage of variance explained by the first two principal components of the decomposition of IO neuron morphologies. The schematic line drawing insets in the plot illustrate the transition from "spherical" to "directional" dendritic field shapes. Colored points correspond to examples shown in panel d, while numbered points refer to examples shown in Fig. 1f. Symbols correspond to morphologies from the three datasets as indicated. b Scatter plot showing the distance from the soma to the extrapolated border of the neuron's dendritic field (soma- border (SB) distance) relative to the distance from the soma to the center of mass of the dendritic arbor (S-CoM distance). Schematic line drawings illustrate the transition from "eccentric" to "centered" somata within an idealized, ovaloid dendritic field shape. Dotted line depicts unity, highlighting that the majority of neurons have somata much closer to the border than to the center of the volume they occupy. Numbers, symbols and colors used as in a. c Distribution of dendritic stem directionality with respect to number of stems. Insets in the plot schematically depict the variation from isomorphic (left) to directional (right). Note that the morphologies shown as examples in Figs. 1f and 4d have mostly isomorphically extending dendrite stems. Numbers, symbols and colors used as in a. d Additional examples of IO neuron morphologies. Colored circles denote morphologies from the viral-labeled data set; colored x's denote morphologies from the biotin-labeled data. The orange and red morphologies are the only two examples in our library in which dendrites densely surround the soma on all sides. The morphologies marked with green and pink exemplify extreme (though not infrequent) examples of soma eccentricity. The morphologies marked with blue and cyan are examples of extremely extensive IO neuron morphologies with dendritic trees spreading far and wide in almost every direction around the soma. Note that the scale in the reconstructions varies according to viewing angle; somata are 15–18 µm in diameter.

Influence of dendrite directionality on network connectivity

As a final step in this anatomical investigation, we examined how the morphological variability and dendritic directionality might interplay in determining connectivity in the IO network. To this end, we first examined the distribution of IO neuron somata within the volume of the nucleus by manually reconstructing all 11,800 somata from one side of an entire rostro-caudal extent of an IO (Fig. 5a, “Methods”). While we found that the distribution of IO neuron somata is less homogeneous than would be expected if they were distributed uniformly within the IO volume (Fig. 5b), the inhomogeneities in the somata distribution were too weak to define anatomically segregated groups of neurons based on inter-soma distances alone. In fact, distance-based algorithmic clustering of somata showed that anatomically, somata are all grouped together into a single large cluster for inter-soma distances as small as 40 µm (Fig. 5c). Since all reconstructed morphologies have a reach of at least 35 µm, and the majority reach beyond 100 µm (see Fig. 2b), this result would indicate that IO neurons form a single, large interconnected mesh network. However, this assessment does not take into consideration that IO neuron dendritic trees can be strongly directional, as described in the previous paragraphs.

What connectivity properties may be bestowed on the IO network by the directionality in dendritic trees? We obtained data indicative of an answer to this question in experiments where labeling was less sparse than described so far, allowing us to occasionally visualize pairs or groups of neighboring neurons. In this material we observed that pairs of neighboring, directional morphologies were arranged such that their dendritic fields either expressly overlapped (Fig. 6a) or avoided each other nearly entirely (Fig. 6b). Furthermore, in rare cases where many nearby neurons could be reconstructed, their dendrites extensively overlapped and somata were located at the outer rim of the group of neurons (Fig. 6c). Thus, an attractive possibility is that the directionality of IO neuron dendritic trees, as well as their varying dendritic tree shapes, delineate anatomically segregated areas of mostly dense or more sparse connectivity.

Discusion

In this study we provide a detailed, quantitative description of the morphological properties of a large sample of individual IO neurons and show that the heterogeneity in dendritic tree shapes spans a continuum between the “curly” and “straight” morphological types, defying this classical categorization. Furthermore, we find that IO neuron dendritic arbors are often clearly directional. In combination with our examination of their spatial distribution within the IO volume and their

orientation relative to each other this leads to new ideas regarding the layout of connectivity within the IO network.

In the following paragraphs, we will first discuss some issues related to the description and classification of IO neuron morphologies, before delving into questions related to the significance of our findings for IO network architecture.

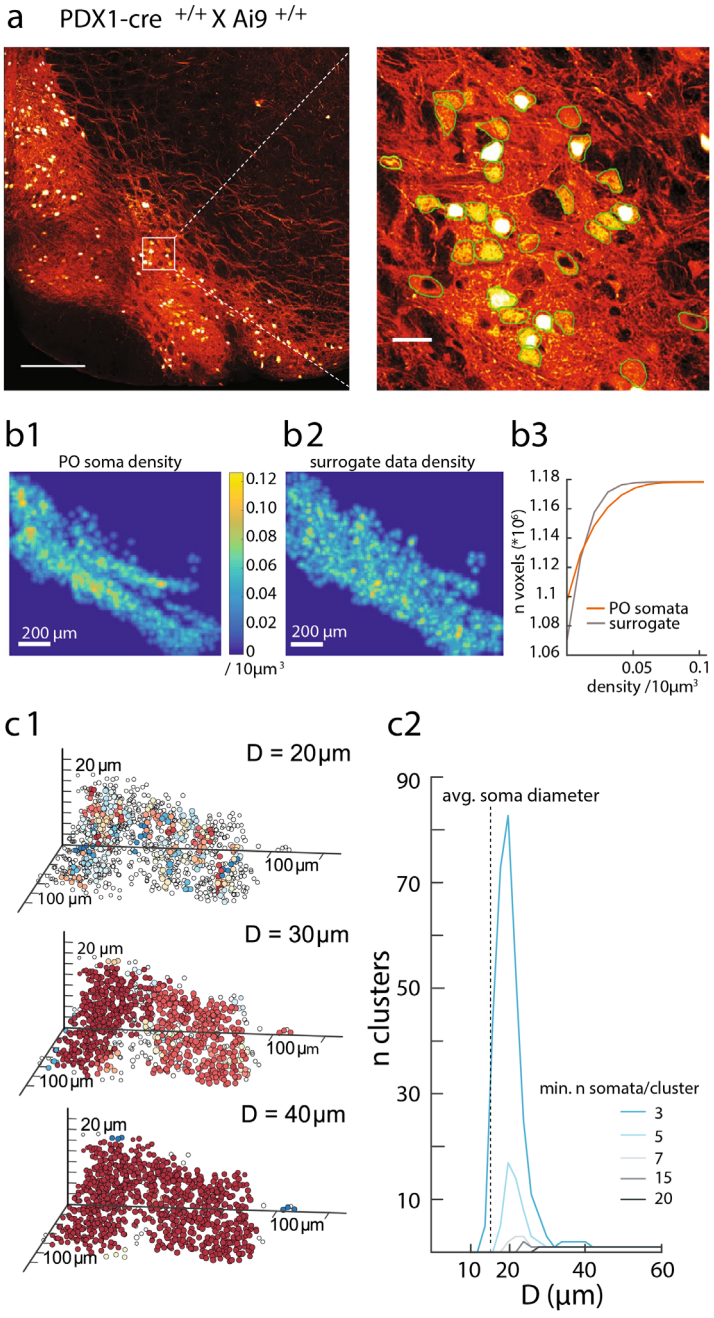

Fig. 5 Anatomical clusters cannot be detected in the distribution of IO neuron somata. a Fluorescent labeling of all IO neuron somata. Left panel: coronal cross-section showing a full hemi-olive (scale bar 200 µm); right panel: magnification of the area delineated with a white square on the left (scale bar 25 µm). Detected somata are outlined in thin green lines; black holes are blood vessels. b Density distribution of somata. b1 Soma density shown in a caudal view projection for the principal olive (PO). b2 Same as b1 but for shuffled surrogate data. b3 Comparison of soma densities per 10µm3 voxel. Note that while the PO data has more high-density "hotspots" as well as "empty" regions (see "Methods"), density gradients are too weak to delineate anatomical clusters of somata. c Detection of clusters using the DBSCAN clustering algorithm (see "Methods"), in which cluster membership is defined as a group of points where each point is at most D µm removed from another point in the cluster. c1 3D-representation of clustering in the medial accessory olive (MAO) for different values of D as indicated (the minimal number of somata per cluster was set to 3). c2 Total number of distinct clusters for different minimal cluster sizes as indicated by color-code. Dashed line represents average soma diameter. Note that multiple clusters are only detected at very short (< 20 µm) inter-soma distances, while the entire IO becomes a single cluster at inter-soma distance as short as 40 µm.

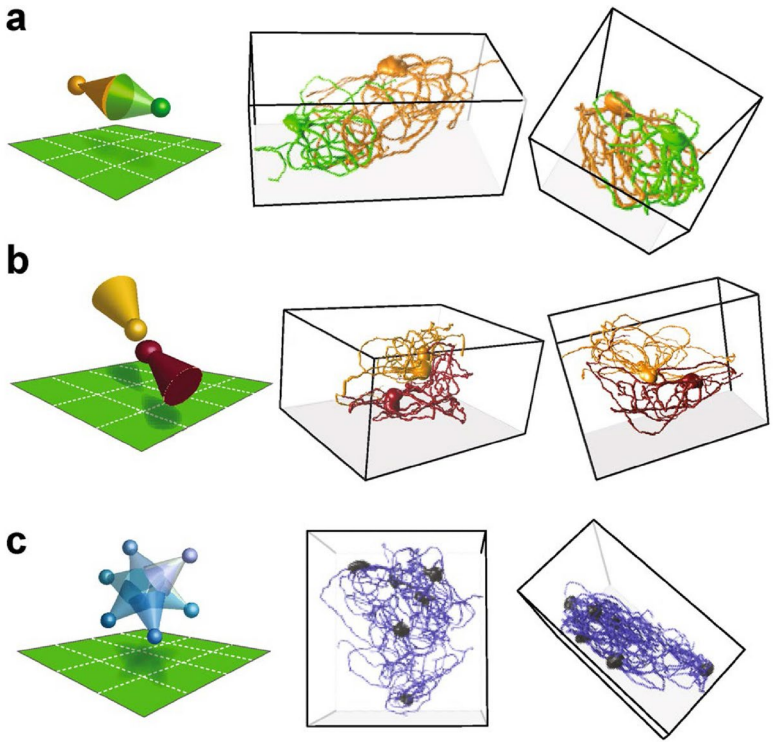

Fig. 6 IO neuron dendritic tree arrangements relative to their neigh- bors suggest anatomical clustering of dendro-dendritic connectivity in the network. Schematic illustrations of dendritic field positioning are shown on the left, while the two right panels show reconstructed morphologies from two different viewing angles (a–c). a A pair of neurons with overlapping, directional dendritic trees. b A pair of neurons with proximally placed somata, but non-overlapping dendritic fields. c A group of neurons with somata residing at the outer rim of their overlapping dendritic fields.

Morphological characterization of IO neurons

Defining cell types has always been a major undertaking in neuroscience, as the layout of neuronal structures is of direct consequence to the connectivity, and thereby the function, of neuronal systems (Mukamel and Ngai, 2018). Neurons in the IO network have classically been described as belonging either to the “curly” or “straight” subtype; however, this classification has always been subjective, and generalizable quantitative definitions of the classes are lacking. In this study, we give a detailed quantitative description of IO neuron morphological properties and find that the inter-individual variability is best described as encompassing a continuum along the curly-to-straight axis. To our knowledge, the included 90 morphologies form the most extensive collection of IO neuron reconstructions to date. Nonetheless, there are several issues pertaining to the labeling, sampling and statistical analysis of our library of IO neuron morphologies that need to be addressed.

First, it should be noted that the different methods for staining individual IO neurons lead to slightly differing data sets. Sparse viral transfection with fluorescent reporter proteins effectively reveals full individual neurons with minimal staining in the background; thus, even the most

densely twisting, extremely “curly” morphologies could be reconstructed in fine detail. In contrast, reconstructions made of neurons patch-filled with either Alexa or biocytin may often underestimate the full extent of the dendritic arborizations, as incomplete penetration of the dye can leave parts of dendrites invisible. In our library, this is reflected in the overall lower number of branches in both patch-filled data sets, and the relatively short over- all length of Alexa-filled morphologies (see Fig. 2b–e; Table 2). Furthermore, the different sample preparation methods used for viral-labeled and patch-filled cells may result in geometrical inconsistencies due to tissue shrinking and/or deformation during the experiment. Nevertheless, the general similarity of measurement distributions across the three datasets strongly suggests that even somewhat incomplete and deformed morphologies provide reliable information on the extent of a neuron’s “curliness”.

Another point requiring consideration is that we selected neuron morphologies for reconstruction based on the completeness of their being contained within the slice (see “Methods”); and since “curlier” neurons tend to occupy smaller volumes, they were less likely than their “straighter” counterparts to be excluded based on having multiple dendrites cut off at the slice surface. This issue is particularly prominent in the neurons labeled with biocytin which were often very close to the slice surface and selected for reconstruction only if their dendrites could be seen to extend down into the slice, while being much less apparent in the Alexa-labeled data because care was taken to patch neurons residing deeper (> 40 μm) in the slice. In addition, and in contrast to the more homogenous tissue sample set obtained from perfusion-fixed brains, the shape of post-fixed acute slices is affected by details of the in vitro experiment, making it difficult to ascertain uniform geometry especially in z-dimension.

Given the extensive morphological heterogeneity and the fact that the morphologies in our library were selected for inclusion based on the completeness of the reconstruction, it should be noted that our sample encompassing 90 morphologies does not necessarily reflect the distribution of morphological properties in the IO neuron population in an accurate and statistically representative manner. It is possible that overlapping, yet distinct morphological categories could be characterized in the full population encompassing more than 20,000 neurons in a single mouse IO (see Fig. 5). The reasons enumerated above also preclude us from making any claims about the relative proportions of “curlier” and “straighter” morphologies in the IO neuron population based on the samples included in our library. Nevertheless, as our investigation uncovered the same trend of continuity in morphological properties in each of three independently acquired data sets, we can confidently state that if a categorization of IO neuron types does exist, the type of an individual IO neuron cannot be deduced with certainty from its morphological properties alone.

Significance of morphological variability and directionality for network architecture

The IO network is often implicitly considered as a homogeneously coupled mesh of neurons. However, such an organization would be computationally inefficient, and possibilities for delineating functional neuronal subgroups through modulation of GJ coupling between IO neurons have been examined through theoretical and experimental approaches alike (Benardo and Foster, 1986; De Zeeuw et al., 1998; Tokuda et al., 2013; Pereda et al., 2013; Kazantsev et al., 2003; Blenkinsop and Lang, 2006; Chaumont et al., 2013; De Zeeuw et al., 2011). For example, functional sub- groups could be defined by inhibitory inputs shunting GJ currents between IO neurons, thereby effectively decoupling them (Llinás, 1974; Lefler et al., 2014). The results presented in this paper are relevant to our understanding of the mechanisms generating synchronized activity in groups of IO neurons because they suggest that alongside the dynamic modulation of electrical coupling, the layout of coupling in the IO network is also defined in the variable density of dendro-dendritic overlap between neighboring IO neurons. Specifically, our results show that IO neuron morphologies have directional shapes (see Fig. 4a) and that somata are most often found at an eccentric location within the dendritic volume (see Fig. 4b). Importantly, such directionality occurs regardless of the distance between an IO neuron's soma and the border of the subnucleus it resides in (see Fig. 1a, g). Thus, it is evident that the distribution of IO neuron somata (see Fig. 5) by itself is not directly indicative of the layout of functional connectivity between individual IO neurons.

Further evidence for a structured layout of electrical coupling in the IO network comes from examining the orientation of IO neuron dendritic trees relative to those of their neighbors. Examples where nearby directional neurons are labeled imply that IO neurons with closely situated somata need not necessarily form electrical connections (see Fig. 6b), and that dendritic directionality can delineate small subsets of IO neurons whose dendrites overlap with each other (see Fig. 6c). Thus, it is likely that the dendritic directionality delineates boundaries between groups of neurons, such that neurons residing within the same group are coupled to each other more tightly than to other neurons in the network. A network architecture like this has been previously proposed (Torben-Nielsen et al., 2012) as a mechanistic explanation for experimental observations of synchronized activity in groups of nearby IO neurons and propagating waves of oscillatory activity in slices (Leznik et al., 2002; Rekling et al., 2012; Kølvraa et al., 2014). Furthermore, experiments using tracer-diffusion as a measure of GJ-connectivity between IO neurons have shown that the extent and strength of coupling is heterogeneous and that coupled neurons usually reside within the dendritic field of the primary labeled neuron (Hoge et al., 2011),

which is in line with the idea that there exist anatomical boundaries between groups of neurons in the IO network.

In the same way that dendritic directionality likely underlies functional clustering of IO neurons, dendritic curliness is likely to be the structural correlate of especially extensive dendro-dendritic coupling. Considering this, we propose that the straighter and less-directional neurons may function to provide weaker electrical coupling across different clusters in the network, effectively forming “bridges” between them. In this scenario, “cluster neurons” and “bridge neurons” form functionally distinct IO neuron subtypes whose morphological appearance may coarsely correspond to the “curly” and “straight” morphological subtypes. However, variability in the cluster sizes and in the strength and remoteness of bridge-connections results in considerable variability in “cluster” and “bridge” neuron shapes, giving rise to a continuum of morphological properties rather than clearly defined classes.

A tantalizing example in line with such “cluster-bridge connectivity” is shown in Fig. 7. In this sample, a single patched neuron (Fig. 7b, reconstructed in orange) is accompanied by a number of densely overlapping dendritic arbors forming a compact cluster of neurons in a volume spanning the extent of the primary neurons’ dendritic field. Additionally, two neurons located further away from the primary labeled cell (indicated by blue arrows in Fig. 7c)

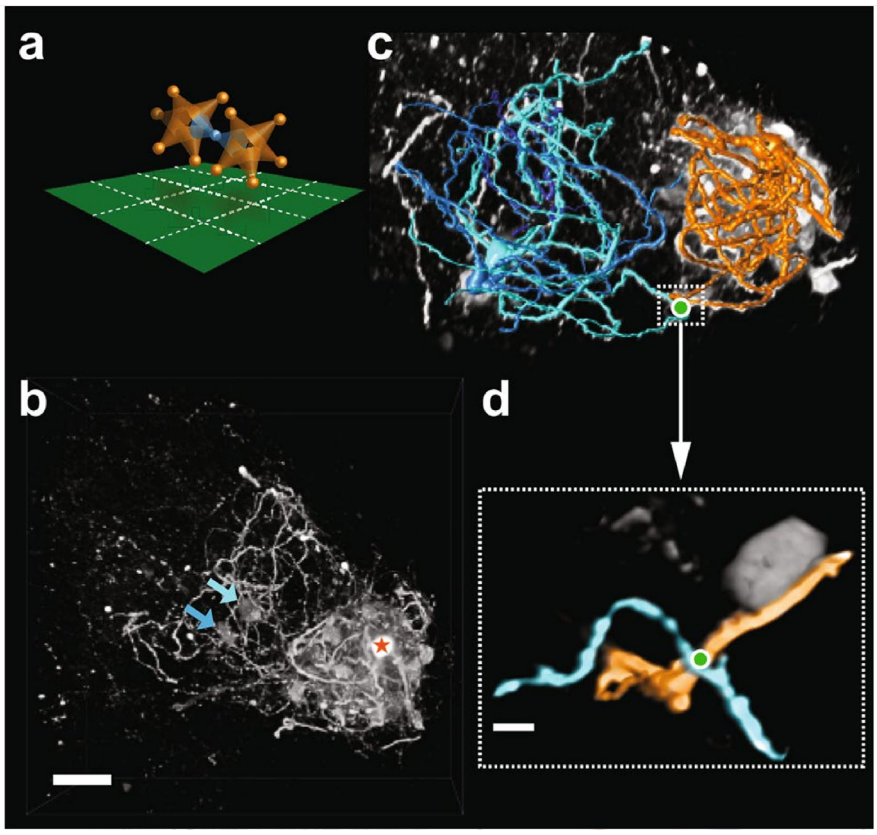

Fig. 7 Example suggesting tight within-cluster coupling and weak inter-cluster coupling. a Schematic illustration of a “bridge neuron” (blue) providing weak coupling between two clusters (orange). b Confocal image stack z-projection showing a single directly labeled IO neuron (marked with an orange star) and a dense cluster of indirectly labeled neighbors, as well as two indirectly labeled neurons with somata residing outside the cluster (marked with blue and cyan arrows). Scale bar 50 µm. c Reconstructions of the neurons marked in b, revealing a point of close proximity between their dendrites. d High-magnification confocal z-stack image showing the area marked with a white box in c. Green dot marks a putative GJ-connection between the primary labeled neuron (orange-colored dendrite) and a “bridge neuron” (blue-colored dendrite). Scale bar 5 µm.

were also labeled and could be resolved well enough to be partially reconstructed (blue and cyan reconstructions in Fig. 7d), revealing a location where a dendrite passes close by that of the directly labeled neuron (marked with a green dot in Fig. 7c, d). This raises the possibility of GJ-mediated coupling between the dense cluster and the “bridge neurons”.

In summary, our anatomical investigation of IO neurons showed that a binary classification into the classically described “curly” and “straight” morphological types is not justified as morphological heterogeneity is better described as varying along a continuous straightness-axis. In addition, the prevalence of directional over isomorphic dendritic fields implies that connectivity in the IO network is structured to support functional clustering. We propose that borders between anatomical clusters are delineated in the dense electrical coupling within groups of “cluster neurons”, and that coupling across such clusters is mediated by dedicated “bridge neurons”. The specific morphology of individual neurons forming clusters and bridges can both vary considerably, resulting in an apparent continuum of morphological properties.

However, the density of IO neuropil and the limitations of the present random-sampling approach preclude strong conclusions to be drawn from anatomical evidence alone, and further electrophysiological and imaging experiments detailing the relationship between the structure and activity of IO neurons will be required to confirm and refine any hypothesis about the hard-wired connectivity of the IO network.

References

Ankri L, Yarom Y, Uusisaari MY (2014) Slice it hot: acute adult brain slicing in physiological temperature. J Vis Exp 92:e52068.

Ausim Azizi S (2007) And the olive said to the cerebellum: organiza- tion and functional significance of the olivo-cerebellar system. Neuroscientist 13:616–625.

Benardo LS, Foster RE (1986) Oscillatory behavior in inferior olive neurons: mechanism, modulation, cell aggregates. Brain Res Bull 17:773–784.

Blenkinsop TA, Lang EJ (2006) Block of inferior olive gap junctional coupling decreases Purkinje cell complex spike synchrony and rhythmicity. J Neurosci 26:1739–1748.

Chaumont J, Guyon N, Valera AM et al (2013) Clusters of cerebellar Purkinje cells control their afferent climbing fiber discharge. Proc Natl Acad Sci 110:16223–16228.

De Zeeuw CI, Holstege JC, Ruigrok TJ, Voogd J (1989) Ultrastructural study of the GABAergic, cerebellar, and mesodiencephalic innervation of the cat medial accessory olive: anterograde tracing combined with immunocytochemistry. J Comp Neurol 284:12–35.

De Zeeuw CI, Hoogenraad CC, Koekkoek SKE et al (1998) Micro- circuitry and function of the inferior olive. Trends Neurosci 21:391–400.

De Zeeuw CI, Chorev E, Devor A, Manor Y, Van Der Giessen RS, De Jeu MT, Hoogenraad CC, Bijman J, Ruigrok TJ, French P, Jaarsma D, Kistler WM, Meier C, Petrasch-Parwez E, Dermietzel R, Sohl G, Gueldenagel M, Willecke K. Yarom Y (2003) Deformation of network connectivity in the inferior olive of connexin 36-deficient mice is compensated by morphological and electrophysiological changes at the single neuron level. J Neurosci 23:4700–4711.

De Zeeuw CI, Hoebeek FE, Bosman LWJ, Schonewille M, Witter L, Koekkoek SK (2011) Spatiotemporal firing patterns in the cerebellum. Nat Rev Neurosci 12:327–344.

Foster RE, Peterson BE (1986) The inferior olivary complex of guinea pig: cytoarchitecture and cellular morphology. Brain Res Bull 17:785–800.

Fox J, Weisberg S (2011) An {R} companion to applied regression, 2d edn. Sage, Thousand Oaks.

Hoge GJ, Davidson KGV, Yasumura T et al (2011) The extent and strength of electrical coupling between inferior olivary neurons is heterogeneous. J Neurophysiol 105:1089–1101.

Huang S, Uusisaari MY (2013) Physiological temperature during brain slicing enhances the quality of acute slice preparations. Front Cell Neurosci 7:48.

Ito M (2013) Error detection and representation in the olivo-cerebellar system. Front Neural Circuits 7:1.

Jacobson GA, Rokni D, Yarom Y (2008) A model of the olivo-cerebellar system as a temporal pattern generator. Trends Neurosci 31:617–625.

Jacobson GA, Lev I, Yarom Y, Cohen D (2009) Invariant phase structure of olivo-cerebellar oscillations and its putative role in temporal pattern generation. Proc Natl Acad Sci 106:3579–3584.

Kassambara A, Mundt F (2017) factoextra: extract and visualize the results of multivariate data analyses. R package version 1.0.5.

Kazantsev VB, Nekorkin VI, Makarenko VI, Llinás R (2003) Olivo-cerebellar cluster-based universal control system. Proc Natl Acad Sci USA 100:13064–13068.

Kitazawa S, Wolpert DM (2005) Rhythmicity, randomness and synchrony in climbing fiber signals. Trends Neurosci 28:611–619.

Kølvraa M, Müller FC, Jahnsen H, Rekling JC (2014) Mechanisms contributing to cluster formation in the inferior olivary nucleus in brainstem slices from postnatal mice. J Physiol 592:33–47.

Lampl I, Yarom Y (1997) Subthreshold oscillations and resonant behavior: two manifestations of the same mechanism. Neuroscience 78:325–341

Lefler Y, Yarom Y, Uusisaari M (2014) Cerebellar inhibitory input to the inferior olive decreases electrical coupling and blocks subthreshold oscillations. Neuron 81:1389–1400.

Leznik E, Makarenko V, Llinás R (2002) Electrotonically mediated oscillatory patterns in neuronal ensembles: an in vitro voltage- dependent dye-imaging study in the inferior olive. J Neurosci 22:2804–2815.

Llinás R (1974) Eighteenth Bowditch lecture. Motor aspects of cerebellar control. Physiologist 17:19–46.

Llinás R (2014) The olivo-cerebellar system: a key to understanding the functional significance of intrinsic oscillatory brain properties. Front Neural Circuits 7:1–13.

Loewenstein Y, Yarom Y, Sompolinsky H (2001) The generation of oscillations in networks of electrically coupled cells. Proc Natl Acad Sci 98:8095–8100.

Long MA, Deans MR, Paul DL, Connors BW (2002) Rhythmicity without synchrony in the electrically uncoupled inferior olive. J Neurosci 22:10898–10905.

Madisen L, Zwingman TA, Sunkin SM, Oh SW, Zariwala HA, Gu H, Ng LL et al (2010) A robust and high-throughput Cre reporting and characterization system for the whole mouse brain. Nat Neurosci 13:133–140

Manor Y, Rinzel J, Segev I, Yarom Y (1997) Low-amplitude oscillations in the inferior olive: a model based on electrical coupling of neurons with heterogeneous channel densities. J Neurophysiol 77:2736–2752.

Mizrahi A, Ben-Ner E, Katz M, Kedem K, Glusman G, Libersat F (2000) Comparative analysis of dendritic architecture of identified neurons using the Hausdorff distance metric. J Comp Neurol 422:415–428.

Mukamel E, Ngai J (2018) Perspectives on defining cell types in the brain. Curr Opin Neurobiol 56:61–68.

Ogle DH (2018) FSA: fisheries stock analysis. R package version 0.8.20

Peng H, Ruan Z, Long F et al (2010) V3D enables real-time 3D visualization and quantitative analysis of large-scale biological image data sets. Nat Biotechnol 28:348–353.

Pereda AE, Curti S, Hoge G et al (2013) Gap junction-mediated electrical transmission: regulatory mechanisms and plasticity. Biochim Biophys Acta - Biomembr 1828:134–146.

Peterson BG, Carl P (2018) Performance analytics: econometric tools for performance and risk analysis. R package version 1.5.2.

Placantonakis DG, Bukovsky AA, Zeng X-H, Kiem H-P, Welsh JP (2004) Fundamental role of inferior olive connexin 36 in muscle coherence during tremor. Proc Natl Acad Sci USA 101:7164–7169.

Placantonakis DG, Bukovsky AA, Aicher SA, Kiem H-P, Welsh JP (2006) Continuous electrical oscillations emerge from a coupled network: a study of the inferior olive using lentiviral knockdown of connexin36. J Neurosci 26:5008–5016.

R Core Team (2018) R: a language and environment for statistical computing. R Foundation for Statistical Computing, Vienna.

Ram A, Jalal S, Jalal AS, Kumar M (2010) A density based algorithm for discovering density varied clusters in large spatial databases. Int J Comput Appl 3:1–4.

Ramón y Cajal S (1995) Histology of the nervous system of man and vertebrates. Oxford University Press, Oxford

Rekling JC, Jensen KHR, Jahnsen H (2012) Spontaneous cluster activity in the inferior olivary nucleus in brainstem slices from post- natal mice. J Physiol 5907:1547–1562.

Revelle W (2018) psych: procedures for personality and psychological research. Northwestern University, Evanston.

Ruigrok TJH, de Zeeuw CI, van der Burg J, Voogd J (1990) Intracellular labeling of neurons in the medial accessory olive of the cat: I. Physiology and light microscopy. J Comp Neurol 300:462–477.

Scheibel ME, Scheibel AB (1955) The inferior olive: a Golgi study. J Comp Neurol 102:77–131.

Schindelin J, Arganda-Carreras I, Frise E et al (2012) Fiji: an open source platform for biological image analysis. Nat Methods 9:676–682.

Song J, Xu Y, Hu X, Choi B, Tong Q (2010) Brain expression of Cre recombinase driven by pancreas-specific promoters. Genesis 48:628–634.

Sotelo C, Llinás R, Baker R (1974) Structural study of inferior olivary nucleus of the cat: morphological correlates of electrotonic coupling. J Neurophysiol 37:541–559.

Streng ML, Popa LS, Ebner TJ (2018) Complex spike wars: a new hope. Cerebellum 17:735.

Ten Brinke MM, Boele HK, de Zeeuw CI (2019) Conditioned climbing fiber responses in cerebellar cortex and nuclei. Neurosci Lett 688:26–36.

Tokuda I, Hoang H, Schweighofer N, Kawato M (2013) Adaptive coupling of inferior olive neurons in cerebellar learning. Neural Netw 47:42–50.

Torben-Nielsen B (2014) An efficient and extendable python library to analyze neuronal morphologies. Neuroinformatics 12:619–622.

Torben-Nielsen B, Segev I, Yarom Y (2012) The generation of phase differences and frequency changes in a network model of inferior Olive subthreshold oscillations. PLoS Comput Biol 8:e1002580.

Urbano FJ, Simpson JI, Llinás RR (2006) Somatomotor and oculo- motor inferior olivary neurons have distinct electrophysiological phenotypes. Proc Natl Acad Sci USA 103:16550–16555.

Uylings HBM, van Pelt J (2002) Measures for quantifying dendritic arborizations. Netw Comput Neural Syst 13:397–414.

Venables WN, Ripley BD (2002) Modern applied statistics with S, 4th edn. Springer, New York. ISBN 0-387-95457-0

Welsh JP, Lang EJ, Sugihara I, Llinás R (1995) Dynamic organization of motor control within the olivocerebellar system. Nature 374:453–457.

Wickham H (2016) ggplot2: elegant graphics for data analysis. Springer, New York.

Wickham H, Hester J, Francois R (2017) readr: read rectangular text data. R package, version 1.1.1.

Wickham H, François R, Henry L, Müller K (2018) dplyr: a grammar of data manipulation. R package version 0.7.6.

Supplementary Figures

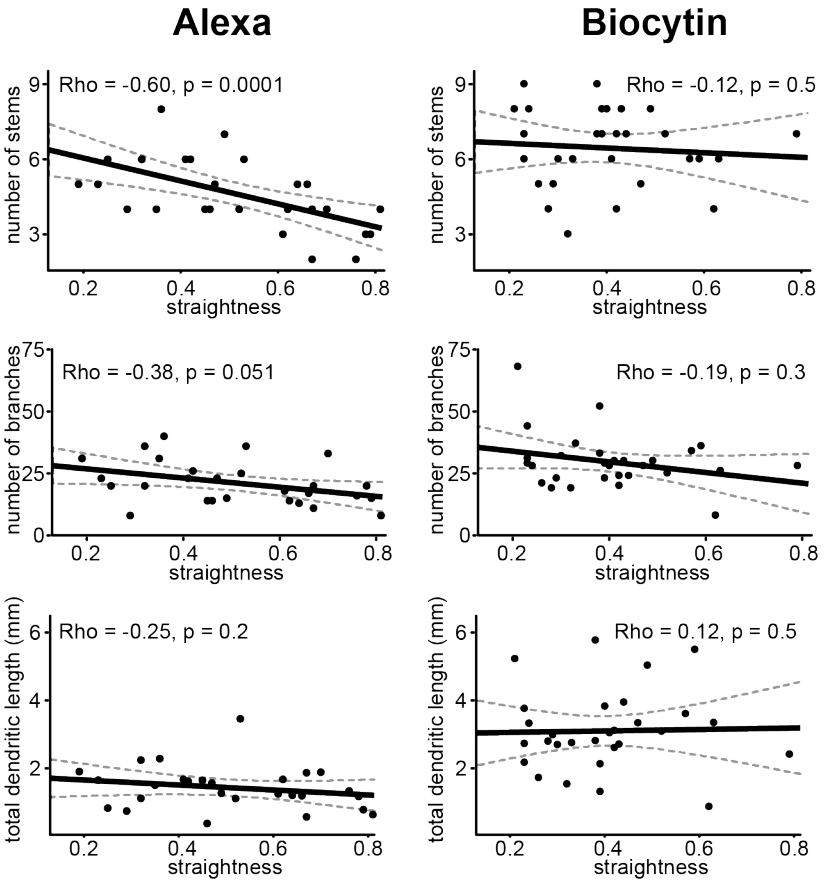

Supplementary Figure 1 (supplement to Figure 2). Morphological parameter correlations to straightness in the patch labeled data sets. Distributions of number of dendrite stems (top), number of branch points (middle) and total dendritic length (bottom) with respect to straightness in the Alexa-labeled data (left column) and the Biocytin-labeled data (right column); the same distributions in the viral-labeled data set are displayed in Fig. 2f–h. Reported correlation statistics represent the strength and direction (Rho) and significance level (*p*) calculated using Spearman's rank correlation test (see "Methods"). Correlations between straightness and all other morphological measures are reported in the right half of Table 2 for each of the three data sets.

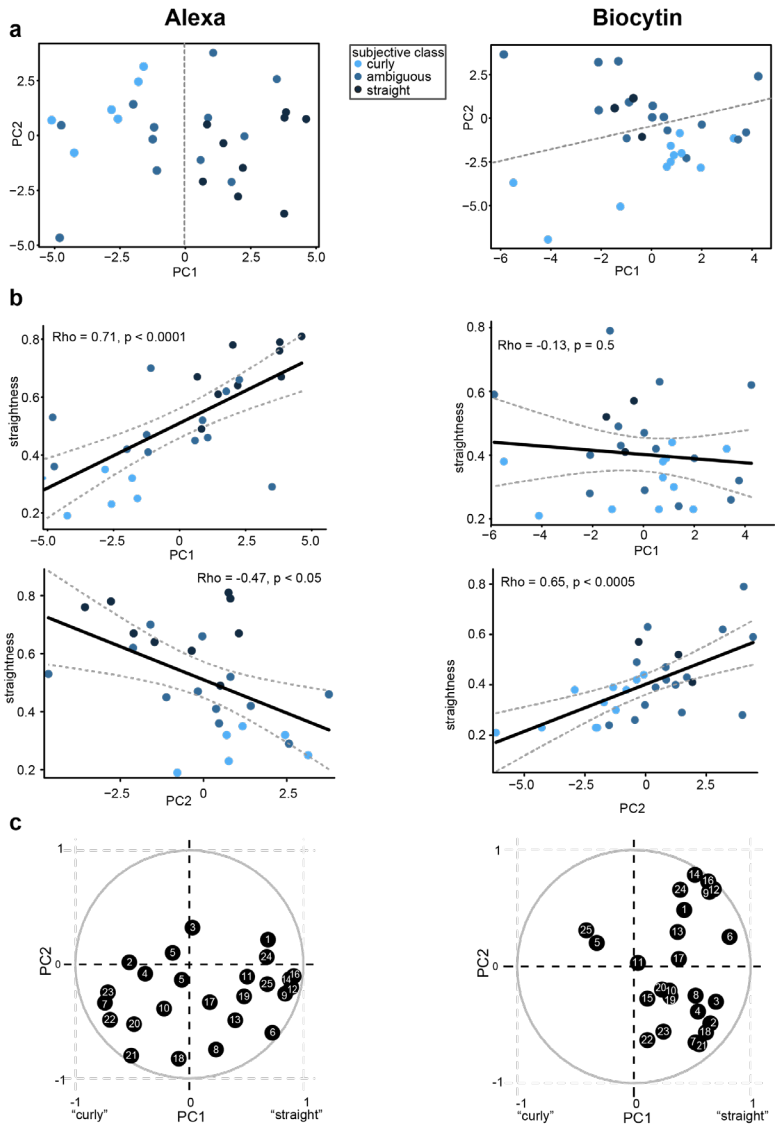

Suppplementary Figure 2 (supplement to Figure 3). Algorithmic classification does not reveal clearly separated clusters in two data sets of patch-filled morphologies. a Algorithmic classification shown as a scatter along the first two principal components (PCs) of separation for the Alexa-labeled (left) and Biocytin-labeled (right) data sets. The grey dashed line marks the algorithmically forced *K*-means grouping into "curly" and "straight"; fill color represents subjective classification, as indicated. In the Alexa-labeled data, as in the viral-labeled data, the separation into distinct groups (as determined by the *K*-means algorithm) spreads along PC1, whereas in the Biocytin-labeled data, the distinction is better represented along PC2. b Correlation between "straightness" and the first (top panel) and second (bottom panel) principal component of separation for the Alexa-labeled (left) and Biocytin-labeled (right) data sets. In the Alexa-labeled data the first two principal components of separation are both correlated with straightness. In contrast, only PC2 is significantly correlated with straightness in the Biocytin-labeled data. Nonetheless, the classification results are qualitatively similar in all three data sets in that the grouping assigned by the *K*-means algorithm draws a distinguishing line almost perpendicular to the principal component most strongly correlated to straightness. c Relative contributions of the 25 morphometric parameters to the principal component separation in the Alexa-labeled (left) and Biocytin-labeled (right) data sets. Numbers in circles correspond to the measures as listed in Table 1. The closer a parameter is to 1, the more it contributed to the separation in the PC space, in the direction indicated by its position within the unit circle; a parameter located at the origin did not contribute to the PC separation. Notably, the distribution of parameters contributing strongly to the separation along PC2 in the Biocytin-labeled data set is similar to the distribution of parameters contributing strongly to PC1 in the Alexa-labeled and viral-labeled data (see Fig. 3c).

Chapter 3

The impact of excitatory and inhibitory inputs on sub- and suprathreshold activity of inferior olivary neurons and motor learning

Sebastián Loyola, Tycho Hoogland, Vincenzo Romano, Hugo Hoedemaker, Roberta Mazza, Farnaz Nassirinia, Mario Negrello, Chris De Zeeuw

Abstract

The inferior olive nucleus is a brainstem structure in the medulla oblongata, which through its climbing fiber axons, generates strong excitatory responses in Purkinje cells called complex spikes. Complex spikes contribute to online motor control and their timing is equally important in driving plasticity and motor learning. Inferior olive neurons exhibit unique features that set specific boundaries on when a complex spike can fire. One of their hallmark features is that they display subthreshold oscillations that are synchronized by dendro-dendritic gap junctions. Dendritic spines of olivary neurons are contacted by both inhibitory and excitatory afferents arising from the cerebellar nuclei and mesodiencephalic junction, respectively. Due to this unusual synaptic arrangement, it has been suggested that specific intervals of olivary inhibition and excitation control the output gain of the inferior olive. Here, we use dual color optogenetic stimulation to demonstrate how such intervals affect the subthreshold and suprathreshold response in both non-oscillating and oscillating inferior olive neurons. We find that inhibition and excitation can both drive transient oscillations in a subset of non-oscillating neurons. We reveal that the two inputs by themselves have distinct effects on the amplitude and phase of oscillations in spontaneously oscillating inferior olive neurons and that specific intervals of these inputs in combination are permissive for spike generation. We apply this knowledge to investigate how motor learning is affected by optimally tuning the inputs to the inferior olive using a whisker reflex learning paradigm and show this can indeed affect the direction of behavioral adaptation.

Introduction

The inferior olive nucleus (IO) is a brainstem structure in the medulla oblongata, which, by way of its climbing fiber axons elicits strong synaptic responses or complex spikes in Purkinje cells of the cerebellum. The timing of complex spikes is crucial for motor adaptation and learning in the cerebellum, yet it remains unclear how mid- and hindbrain inputs are integrated in the inferior olive to shape it (De Zeeuw et at., 1998). During perturbations, synchronized complex spikes elicit transient simple spike pauses in Purkinje cells that directly affect motor output by disinhibiting the cerebellar nuclei (Heiney et al., 2014). Complex spikes contribute to long-term plasticity changes and motor learning through their timing relative to that of parallel fiber input to Purkinje cells and molecular layer interneurons (Ito and Kano, 1982; Raymond and Lisberger, 1998; Wang et al., 2000; Safo and Regher, 2008; Gao et al., 2012; Ten Brinke at al., 2015). To understand short- and long-term cerebellar learning, it is therefore critical to understand how higher brain areas and the cerebellum itself control the timing of inferior olive output.

A distinguishing feature of IO neurons is their electrical coupling through dendro-dendritic gap junctions and their intrinsic subthreshold oscillations (STOs) (Llinás and Yarom, 1986). STOs emerge spontaneously from an interplay of somatic and dendritic membrane conductances (Llinás and Yarom, 1981) and are synchronized through gap junctional coupling. STOs modulate the probability and timing of complex spikes (Negrello et al., 2019), and thereby their rhythmic activity during rhythmic behaviors (Welsh et al., 1995).

The efficacy of motor adaptation and learning depends on the timing of complex spikes, which raises the question of how the phase and amplitude of STOs can be modulated. Intrinsic properties of IO neurons including membrane voltage and capacitance modulate STO amplitude and frequency, respectively (Choi et al., 2010; Turecek et al., 2016). Synaptic potentials also have a direct impact on both the phase and amplitude of STOs. Hindbrain GABAergic inputs originating in the cerebellar nuclei (CN) can transiently suppress STOs in vitro (Lefler et al., 2014) and in vivo (Bazzigaluppi et al., 2012a), facilitating the resetting of the oscillations. Descending glutamatergic inputs originating in the mesodiencephalic junction (MDJ) - a midbrain region that comprises the nucleus of Darkschewitch, nucleus of Bechterew, nucleus interstitialis of Cajal, red nucleus, tegmental field of forel, zona incerta, subparafasciularis nucleus and the prerubral reticular formation (De Zeeuw et al., 1998) - can probably also modulate the STOs, as pharmacological activation of NMDA receptors in IO spines have been shown to increase STO amplitude and synchrony (Turecek et al., 2014). Moreover, suprathreshold responses triggered by excitatory inputs reset the phase of STOs when triggered near the peak of an oscillation (Leznik et al., 2002;

Khosrovani et al., 2007; Van der Giessen et al., 2008). So far, it has not been shown how inhibitory CN and excitatory MDJ inputs, which have overlapping axon terminations in the rostral medial accessory olive (MAO) and principal olive (PO), evoke responses within the same IO neurons, nor how these inputs interact to affect their phase response properties and spike probability.

IO neurons display multi-phasic synaptic responses when activated by inhibitory and excitatory afferents. Inhibitory synaptic responses consist of a $GABA_AR$ mediated hyperpolarization ($V_{hyp.}$) followed by a rebound depolarization ($V_{reb.}$), which relies on low voltage-gated T-type calcium channels and I_h channels (Bal and McCormick, 1997; Choi et al., 2010). Synaptic responses to excitatory input are composed of a depolarization ($V_{dep.}$) mediated by AMPA and NMDA receptors, followed by a hyperpolarization ($V_{hyp.}$), mediated by both I_h and SK channels (Garden et al., 2017; Garden et al., 2018), that if sufficiently large also drives a rebound depolarization ($V_{reb.}$) mediated by I_h and T-type calcium channels which in turn could drive rebound spikes.

Whereas most IO neurons display STOs in vitro or under anesthesia in vivo, a significant fraction is silent (Khosrovani et al., 2007; Turecceck et al., 2014). A subset of neurons within this silent group can be induced to oscillate and are referred to as ‘conditional oscillators’ (Khosrovani et al., 2007; Leznik et al., 2002; Bazzigaluppi et al., 2016). Neither the function nor the mechanism behind the initiation of STOs in this group of cells is clear. Recent studies in awake animals have shown that sensory stimulation can boost the probability of IO neurons to display transient periodic firing of complex spikes suggesting a strong dependency of STOs on input (Negrello et al., 2019). However, to what extent and how excitatory and inhibitory inputs contribute to such transient oscillations is unknown.

Excitatory and inhibitory terminals are spatially arranged in a glomerulus in close proximity to coupled dendritic spines of IO neurons (De Zeeuw et al., 1990a). Due to this unique synaptic configuration, the temporal interplay of excitatory and inhibitory responses has a big impact on the output of an olivary neuron (Segev and Parnas, 1983). In this work we address how these interactions affect STO amplitude, phase, and spike probability and motor learning.

We show that inhibitory sub- and suprathreshold synaptic responses triggered by CN afferents and suprathreshold excitatory activity triggered by MDJ afferent stimulation both boost STO amplitude and reset their phase. By contrast, subthreshold excitatory synaptic responses evoke smaller post-stimulus amplitude changes, as well as weaker phase resetting and its persistence across trials (‘phase-locking’). Moreover, we demonstrate that stimulation of either CN or MDJ afferents is able to elicit transient STOs in a subset of non-oscillating neurons, and that the amplitude and phase of these induced oscillations are determined by the hyperpolarizing

component of the synaptic response. When MDJ and CN stimulation are combined, specific stimulus time intervals have differential effects on oscillation amplitude, phase resetting, phase-locking, and spike probability. For example, excitatory MDJ input presented 150 ms after the onset of inhibitory CN input (+150 ms) is associated both with a strong resetting of the phase and increased probability to generate complex spikes. On the other hand, presentation of MDJ excitation 50 ms after inhibition (+50 ms) suppresses complex spikes and only weakly phase-locked the IO STOs. Finally, we wanted to test the impact of this temporal interplay on motor learning. To assess that, we used a whisker reflex learning paradigm in which whisker protraction is enhanced and mediated by LTP of Paralel fiber to Purkine Cell synapses induced by puff stimulation at 4 Hz for 20 seconds (Romano et al., 2018). Preliminary data shows that when we combined time interval stimulation of +50 ms in conjunction with puff stimulation we observed that the absolute amplitude of whisker movement was larger than observed when +150 ms stimulation was used. This suggests that temporal interplay would have an impact on motor learning.

In conclusion, our data support the notion that the interaction of MDJ and CN inputs in the IO helps setting specific time windows to facilitate or suppress complex spike output, and thereby would modulate the timing of complex spikes, dictating the permissive time windows for learning and motor adaptation.

Results

Physiological properties of IO neurons

Prior to investigating how IO neurons integrate synaptic inputs, we characterized their overall physiological properties in sagittal sections of the brainstem (Figure 1A. Recordings were obtained from cells in the rostral part of the medial accessory olive (rMAO) and principal olive (PO) using whole-cell patch-clamp recordings (Figure 1 panels A, B and C). One of the hallmarks of the IO is the presence of dendro-dendritic electrical coupling via connexin 36 containing gap junctions (De Zeeuw et al.,1989; Van der Giessen et al., 2006), which allows the synchronization of membrane potentials across connected IO neurons (Figure 1D). To determine the number of coupled neurons we included biocytin (0.5%) in our patch pipette, a molecule sufficiently small to cross the connexin 36 containing gap junctions. Using this approach, we obtained an average of 7.6 ± 7.21 dye-coupled neurons (range: 0 – 27, n = 13), which lies within the range of previous in vitro studies (Turececk et al., 2014; Placantonakis et al., 2006).

Across all recordings 69.6% of IO neurons recorded (71/102 cells, N = 45, Figure 1E) displayed STOs with a mean amplitude of 9.27 ± 5.52 mV (range: 0.34 - 21.14 mV, figure 1F) and

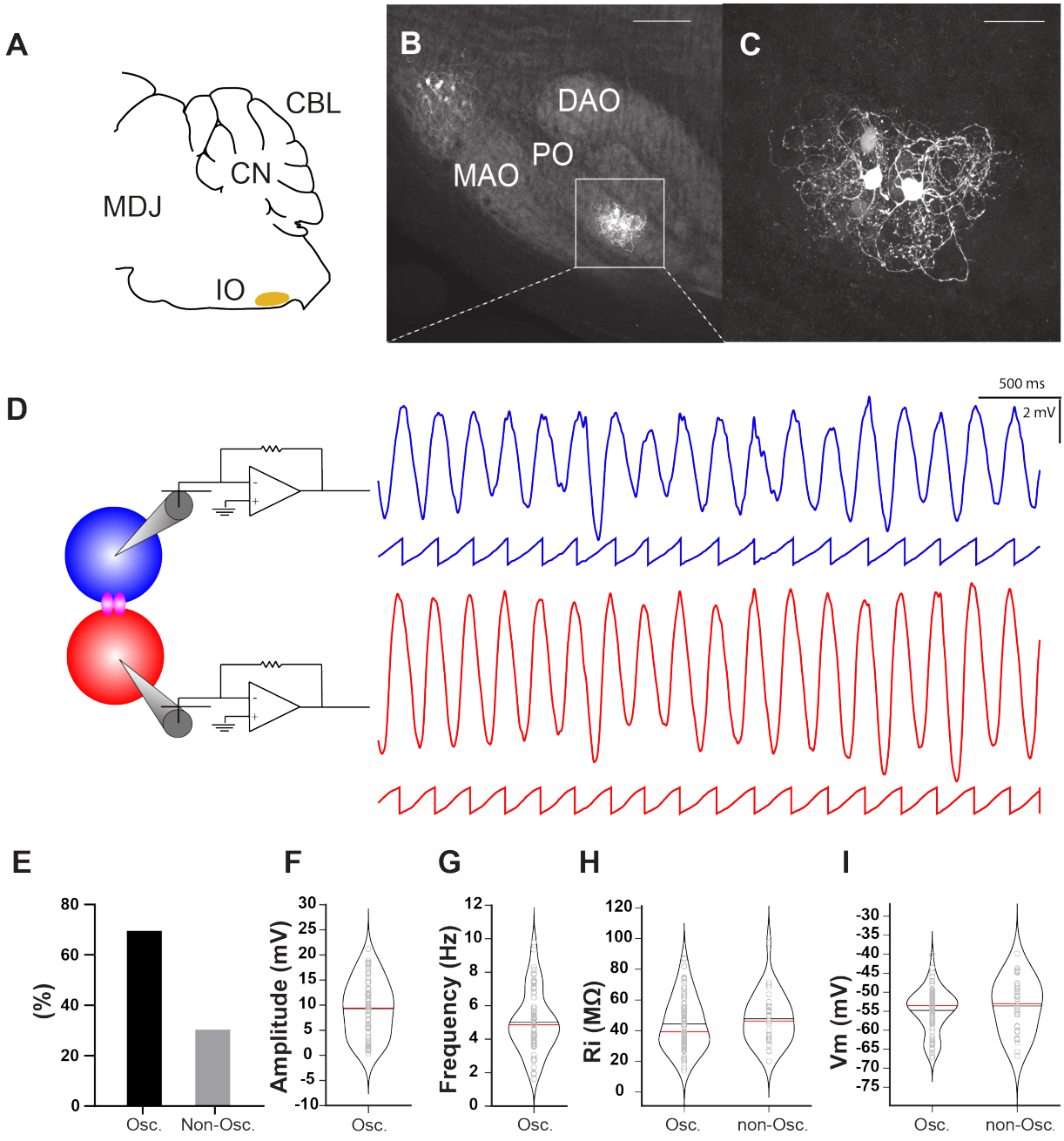

Figure 1. In vitro whole-cell patch clamp recordings of oscillating and non-oscillating inferior olive neurons. A, Schematic of a sagittal section of the mouse brain showing the inferior olive (IO) in relation to the cerebellar cortex (CBL), cerebellar nuclei (CN) and mesodiencephalic junction (MDJ). B, Sagittal brain stem sections were cut to perform whole-cell patch-clamp recordings from IO neurons in the medial and principal accessory olive subnuclei. C, Dye-coupling between electrically coupled IO neurons was visualized by performing immunostainings on neurons dialyzed with biocytin. Dye-coupled cells are visible in C, a close up of the boxed region in B. D, Left: Schematic illustrating dual whole-cell patch-clamp recording of gap junction coupled IO neurons. Right: Example traces of two coupled IO neurons displaying synchronized STOs and their corresponding phases underneath. E, Bar plot showing the proportion (in %) of IO neurons displaying subthreshold oscillations (STOs) and non-oscillating activity. Violin plots: F, STO amplitude. G, STO frequency. H, input resistance (R_{in}) of oscillating and non-oscillating neurons. I, V_m of oscillating and non-oscillating neurons. Each open gray circle represents one cell. Red lines represent median and black lines indicate mean values.

an average frequency of 5 ± 1.84 Hz (range: 1.63 – 9.77 Hz, Figure 1G); the 30.4% of cells that did not oscillate (31/102 cells, N = 25) formed an identifiable different category based on their oscillating properties. Next, we determined to what extent these two groups differed in their passive membrane properties. Input resistance (oscillating: 44.3 ± 17.7 MΩ, range: 13.8 – 87.09 MΩ, non-oscillating: 47.6 ± 16.6 MΩ, range: 20.2 – 97.5 MΩ, p = 0.3771, unpaired t-test, Figure 1H) and resting membrane potential (oscillating: -54.8 ± 5.8 mV, range: -67.3 - -40.2 mV; non-oscillating: -53.6 ± 7.1 mV, range: -66.86 - -39.8 mV, p = 0.3874, unpaired t-test, Figure 1I) did not differ significantly. We therefore characterized evoked postsynaptic potentials in non-oscillating neurons.

Impact of subthreshold CN input on IO neurons

The cerebellar nuclei are the main source of inhibitory input to the principal olive (PO), medial accessory olive and dorsal accessory olive (Lefler et al., 2014; De Zeeuw et al., 1989; Ruigrok and Voogd, 1990; Apps and Hawkes, 2009). To selectively stimulate inhibitory inputs, we used two approaches to stimulate CN afferents optogenetically (Supplemental Figure 1A): a transgenic line, consisting of a cross between a Gad2-IRES-Cre and Ai32(RCL-ChR2(H134R)/EYFP) to obtain GABAergic neurons expressing the ChR2 opsin (Fink et al., 2014; Berndt et al., 2011) and C57BL/6 mice in which the CN was virally transduced with the Chrimson-tdTomato opsin-fusion protein (Kaploetke et al., 2014). Using our viral-based approach CN fibers could be most clearly discerned throughout the IO (Supplemental Figure 1B). Using both approaches, optogenetic stimulation evoked biphasic responses consisting of a hyperpolarizing ($V_{hyp.}$) and a rebound component ($V_{reb.}$, Supplemental Figure 1C), which, if reaches spike threshold, can elicit spikes at its peak (This spike is referred to as 'CN suprathreshold synaptic response' or 'CN spike'). The half-widths of V_{hyp} and V_{reb} were not significantly different in transgenic mice expressing ChR2, or in mice virally transduced with Chrimson (V_{hyp}: p = 0.29, unpaired t-test. Supplemental table 1). Onset latencies of the synaptic responses were shorter for stimulation of Chrimson relative to ChR2(H134R) transgenic mice (p < 0.0001, Mann-Whitney U test, Supplemental table 2). Synaptic responses evoked by CN afferent stimulation were significantly reduced by the $GABA_A$ receptor antagonist picrotoxin (amplitude change relative to baseline (in %), $V_{hyp.}$: 7.8 ± 12.2% p < 0.0001, n = 5 ,$V_{reb.}$ = 1.6 ± 3.7%, p < 0.0001, n = 5, paired t-test), suggesting that the inhibitory response is largely mediated by $GABA_A$ receptors (Supplemental Figure 1 panels J,K,L).

In vivo hyperpolarizing current steps can induce transient oscillations in a subset of non-oscillating cells (39%, Bazzigaluppi et al., 2016). However, it is unclear whether STOs are also

induced following transient activation of synaptic inputs. Here we show in vitro that CN afferent stimulation can indeed elicit transient STOs (STOs duration: 1.8 ± 0.65 s, n = 5 cells, Supplemental Figure 3A) in a similar subset of IO neurons (37.5%) that exhibit $V_{hyp.}$ amplitude of at least 1.14 mV. On average, we find that the amplitude of the first cycle following stimulation scales with the amplitude of $V_{hyp.}$ (first cycle: R^2 = 0.95, n = 5, Figure 2B), with V_{hyp} having less impact on the amplitude of the second (R^2 = 0.53, n = 5, Supplemental Figure 3C) and third cycle (R^2 = 0.49, n = 5, Supplemental Figure 4D). Latencies to the peak of the rebound component and rebound slope fell into two categories, including responses with a short latency independent of $V_{hyp.}$ amplitude and responses where the latency showed a dependency on V_{hyp} (Figure 2C and figure 2D). Our data are in line with previous studies that identified two types of synaptic responses in IO neurons to transient and focal GABA application: a slow desensitizing somatic response and a fast dendritic desensitizing response, mediated by $GABA_A$ receptors with different subunit composition (Devor et al., 2001). Together, these findings reveal that the amplitude of the hyperpolarizing component of the CN synaptic response determines the amplitude and timing of the upcoming cycles in conditional oscillators.

The majority of IO neurons in our recordings had STOs and we determined their phase responses (phase change, $\Delta\varphi$) by stimulating CN afferents at different phases (φ) of the STO cycle (Phase Response Curve also referred to as 'PRC', appendix 1). From each PRC curve we extracted two parameters, including the slope and Y-intercept. The slope defines how sensitive the changes of the phase responses are to the phases at which the synaptic input hits the STOs and the Y-intercept, or ΔΦ-intercept, determines whether the phase changes caused by the synaptic responses consist of only phase delays (negative intercept) or phase delays and advances (positive intercept).

CN afferent stimulation eliciting subthreshold synaptic responses acted as a strongly resetting stimulus for oscillating IO neurons and introduced a phase delay for each phase of the cycle that a stimulus was presented (slope = -0.52, ΔΦ-intercept = 0.07, R^2 = 0.86, n = 5, Figure 3B).

To get an indication for the persistence of phase resetting across trials - or phase locking -, we calculated the phase lags across three oscillation cycles before and after inhibitory stimulation and compared the standard deviations of pre- and post-stimulus phase lags. Across trials, phase lags were significantly reduced after stimulation ($SD_{pre\text{-}stim}$ = 59.51 ms, $SD_{post\text{-}stim}$ = 20.35 ms,n = 15, $p < 0.0001$. F test, Figure 3C), indicating that the stimulus induced transient phase-locking (Bazzigaluppi et al., 2012a). To determine to what extent subthreshold inhibitory stimulation affected STO amplitude, we next quantified the increase in STO amplitude of four post-stimulus cycles relative to a pre-stimulus baseline (average of four pre-stimulus cycles). Inhibitory synaptic

responses could significantly boost STO amplitude (ΔSTO amplitude first cycle: 4.8 ± 3.7 mV, p < 0.0001, second cycle: 1.0 ± 1.7 mV, p < 0.0001, third cycle: 0.57 ± 1.7 mV, p < 0.0001, fourth cycle: 0.4 ± 1.3 mV, n = 23, p = 0.0002, Friedman test, Figure 3D).

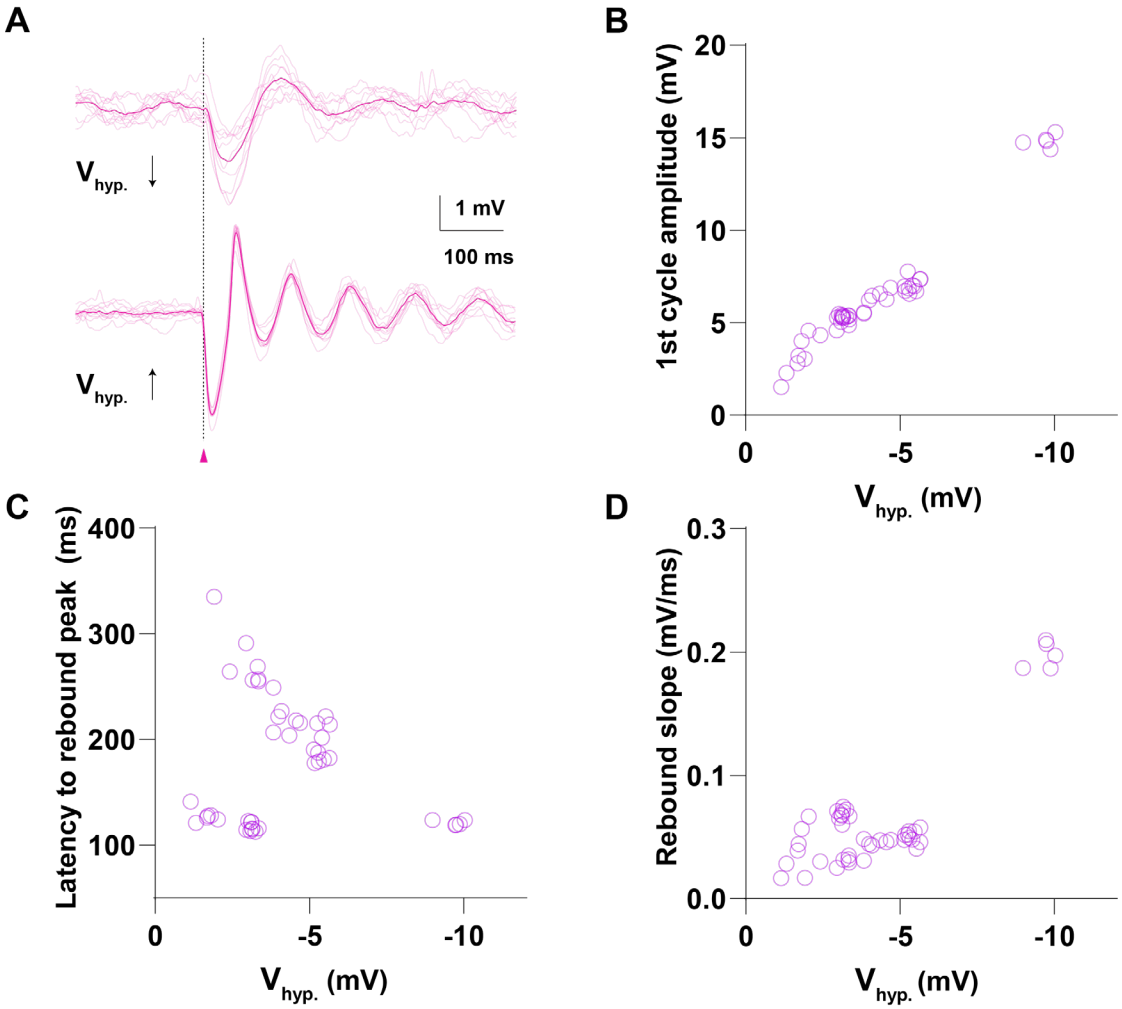

Figure 2. CN afferent stimulation induces STOs in a subset of silent IO neurons. A, Whole-cell patch-clamp recording of an IO neuron in which a weak stimulus with a corresponding small V_{hyp} triggered weak oscillations, while a strong stimulus presented in the same neuron caused a large V_{hyp} associated with a more pronounced transient oscillation (individual trials: light purple, average response: dark purple). B, Amplitude of the 1st STO cycle (rebound peak) following stimulation as a function of the amplitude of the hyperpolarizing component ($V_{hyp.}$). C, Latency to the peak of the rebound component ($V_{reb.}$) as a function of $V_{hyp.}$ D, Rebound slope as a function of $V_{hyp.}$ Open purple circies represent individual trials.

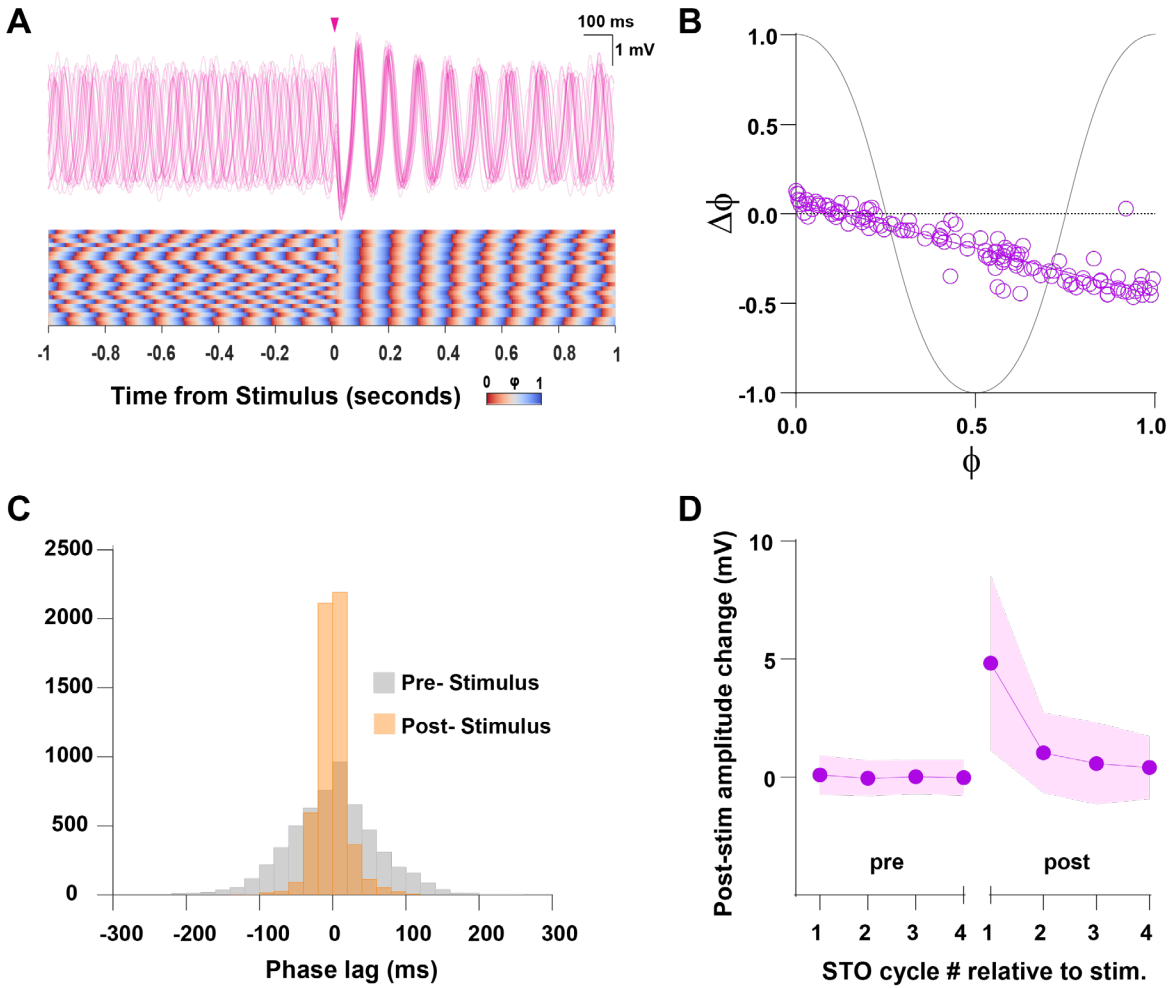

Figure 3. Response properties of IO neurons to subthreshold CN afferent stimulation. A, CN inhibitory afferent stimulation (triangle denotes stimulus onset) in an oscillating IO neuron (top: superimposed recording trials, bottom: phase plot of all trials). B, The phase response curve (PRC) for subthreshold CN inhibitory stimulation. Open purple circles represent individual trials. C, Histogram showing the distribution of phase lags calculated across trials for three cycles before (pre-stimulus) or after (post-stimulus) stimulation. D, Changes in peak STO oscillation amplitude following stimulation (for each cycle the average over four pre-stimulus cycles was subtracted, shaded area represent SD).

Impact of suprathreshold CN input on STOs

In awake animals, spontaneous complex spikes are clearly apparent and complex spike firing is stably maintained at roughly 1 Hz (Ju et al., 2019). However, in our reduced preparation 57.1 % of cells analyzed (32 out of 56 neurons) showed spontaneous spikes at a significantly lower frequency (Range: 0.0017-0.34 Hz, average: 0.095 ± 0.0958 Hz). This frequency depended on the membrane potential (Supplemental Figure 5).

Due to the presence of a rebound component in the CN synaptic response, it is possible to elicit spikes by stimulating these afferents. In one instance we observed that at resting membrane potential the rebound depolarization induced by inhibitory CN afferent stimulation could even

trigger a complex spike without concomitant depolarizing current injections (1 out of 7 neurons, V_m = -56.25 ± 0.52 mV) (Figure 4A, top panel). However, in all other cells a depolarizing step current was required to elicit spikes (6 out of 7, current injected = 580.1 ± 293.94 pA, V_m -40.24 ± 9.52 mV, n = 6). Spikes driven by CN input exhibited PRCs with a slope similar to CN synaptic subthreshold responses (slope: -0.54, R^2 = 0.78, n = 8, p = 0.68, Ancova, Figure 4B), but with different ΔΦ-intercepts (ΔΦ-intercept = 0.1597, p < 0.0001, Ancova, Figure 4B), which resulted in CN spikes causing phase advances besides phase delays. Phase-locking induced by spikes triggered by CN inputs ($SD_{pre\text{-}stim}$ = 61.05 ms, $SD_{post\text{-}stim}$ = 38.1 ms, p < 0.0001, F test, n = 7, Figure 4C) was weaker than that induced by subthreshold stimuli ($\Delta SD_{pre\text{-}post\text{-}CN\_sub}$ = 39.16 ms, $\Delta SD_{pre\text{-}post\text{-}CN\_supra}$ = 22.95, supplemental Figure 7). Moreover, CN suprathreshold responses increased the post-stimulus STO amplitude (ΔSTO amplitude first cycle: 4.04 ±3.19 mV, p < 0.0001, second cycle: 2.89 ± 2.79 mV, p < 0.0001, third cycle: 2.72 ± 3.04 mV, p < 0.0001, fourth cycle: 2.5 ± 2.93 mV, p < 0.0001, n = 6, Friedman test, Figure 4D). The 1st cycle following suprathreshold CN stimulation, which corresponds to the amplitude of the rebound following the spike after-hyperpolarizing component, showed comparable boost with respect to the boost of the 1st cycle following CN subthreshold stimulation, which is the rebound component following the hyperpolarizing component of the CN subthreshold synaptic response. However, this was not the case for the three subsequent cycles following stimulation (cycles 2nd, 3rd , and 4th), where CN suprathreshold synaptic responses caused a larger boost than those caused by subthreshold synaptic responses (ΔSTO amplitude following stimulation of CN_{supra} vs $CN_{sub.}$ 1st cycle: p < 0.0001, 2nd cycle: p < 0.0001, 3rd cycle: p < 0.0001, 4th cycle: p < 0.0001, Mann-Whitney U test). This means that suprathreshold synaptic responses elicited by CN input caused a longer lasting increase of oscillation amplitude than in the case of subthreshold CN stimulation.

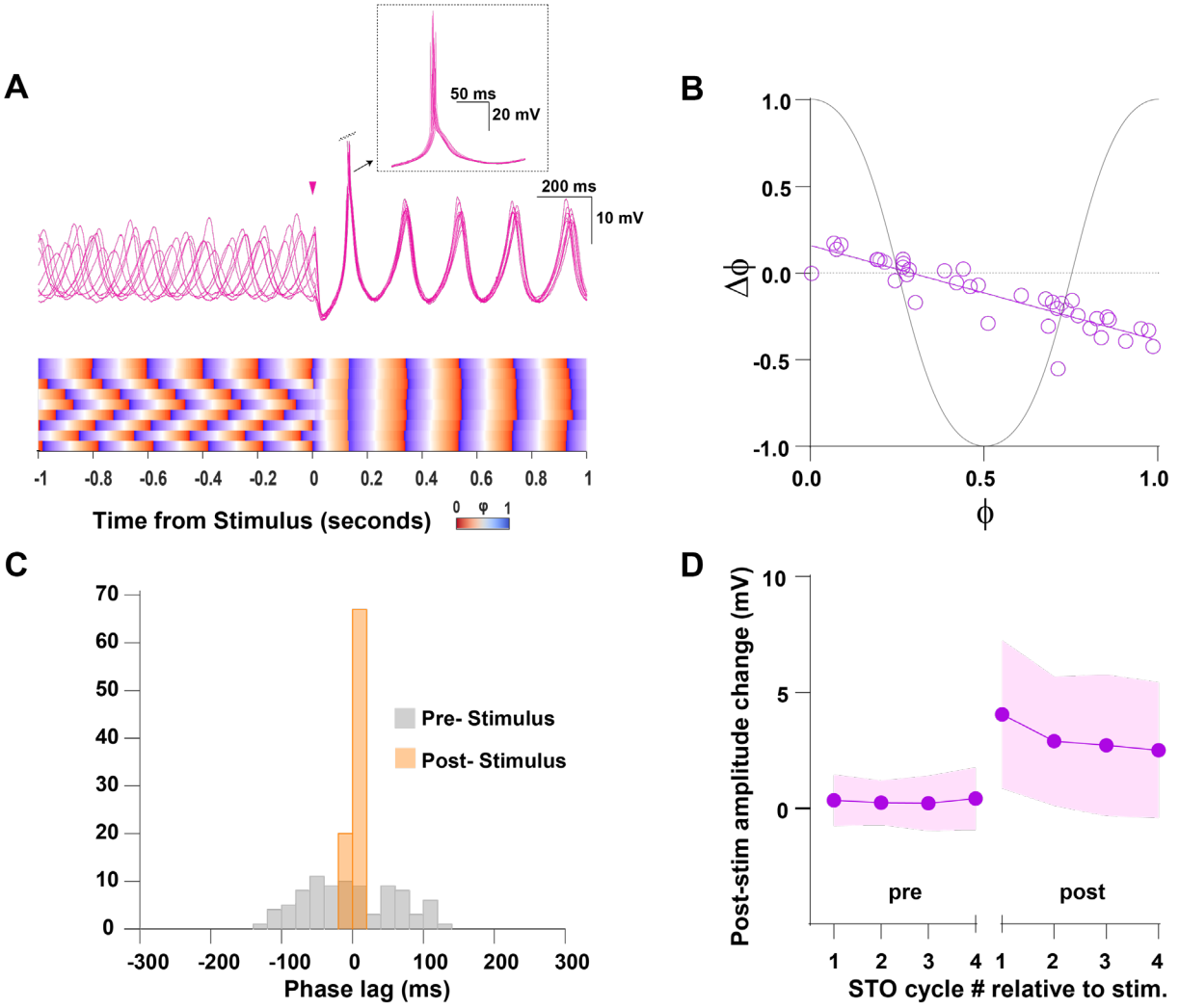

Figure 4. Response properties of oscillating IO neurons to CN suprathreshold synaptic responses. A, Inhibitory stimulation (triangle denotes stimulus onset) in an oscillating IO neuron (top: superimposed recording trials, bottom: phase plot of all trials). B Phase response curve of phase changes (ΔΦ) at different phases (Φ) of stimulation. Open purple cicles represent individual trials. C, Histogram showing the distribution of phase lags calculated across trials for three cycles before (pre-stimulus or after (post-stimulus) stimulation. D, Changes in peak STO oscillation amplitude following stimulation. The mean amplitude before stimulation of the CN afferents was subtracted from four individual cycles before and after stimulation (shaded area represents the standard deviation).

Impact of subthreshold MDJ input on IO neurons

The mesodiencephalic junction (MDJ) in the midbrain is a major source of excitatory input to the medial accessory olive (MAO) and principal olive nucleus (PO) (De Zeeuw et al., 1989; De Zeeuw et al., 1994). We stimulated this input both electrically and ontogenetically. In the case of electrical stimulation, a bipolar stimulation electrode was placed in the medial tegmental tract, which contains descending fibers from the MDJ to MAO and PO (Ruigrok and Voogd, 1995); responses

were evoked with 100 µs pulses (0.1-1.2 mA). For optogenetic stimulation, AAV-Syn-Chronos (Kaploetke et al., 2014) was injected in the MDJ. Optogenetic stimulation commenced at least 4 weeks post-transduction when MAO and PO showed clear innervation of excitatory afferents from MDJ, whereas dorsal accessory olive (DAO) was largely devoid of innervation (Supplemental Figure 2B). Synaptic responses were evoked using 1 ms light pulses (0.6-1.7 mW/mm^2). Optogenetic stimulation ensured selective afferent stimulation at the termination site in the IO and acted as a control for the specificity of electrical stimulation (Supplemental Figure 2A).

The relationship between stimulus strength and response amplitude as well as the time course of evoked excitatory synaptic potentials were compared for electrical and optogenetic stimulation. In both instances, MDJ afferents elicited tri-phasic synaptic potentials (Supplemental Figure 2C), consisting of a depolarization (V_{dep}), hyperpolarization (V_{hyp}), and rebound depolarization (V_{reb}). The rebound depolarization scaled with the size of the preceding hyperpolarization (Supplemental Figure 1 panels D,H, I). The amplitude of V_{dep} scaled linearly with stimulus strength (Supplemental figure 2 panels E and I) while V_{hyp} and V_{reb} scaled with stimulation strength in a non-linear manner (Supplemental Figure 2 panels F,G,J,K). The half-width of these three components was comparable (V_{dep}: $p = 0.84$, V_{hyp}: $p = 0.62$, V_{reb}: $p = 0.085$, unpaired t-test, Supplemental table 3). As expected, synaptic potentials evoked by electrical stimulation had shorter latency onsets than those evoked by light stimulation (Mann-Whitney U test, $p < 0.0001$, Supplemental table 4).
To demonstrate that MDJ stimulation evoked indeed purely glutamatergic responses, ruling out recruitment of GABAergic fibers, we performed a set of pharmacological experiments. V_{hyp} and V_{reb} were not affected by the $GABA_A$ receptor antagonist picrotoxin (amplitude change relative to baseline, V_{hyp}: 138.1 ± 66.6%, $p = 0.1493$, $n = 8$, $V_{reb.}$= 103.7 ± 36.5%, $p = 0.7852$, $n = 8$, paired t-test), whereas V_{dep} increased (V_{dep} = 122.7 ± 13.92 % $n = 8$, $p = 0.0024$ paired t-test). When AMPA receptors were blocked with CNQX all three components were significantly reduced (V_{dep}=22.9 ± 12.18 %, $p < 0.0001$ $n = 8$; $V_{hyp.}$= 21.2 ± 19.7%, $p < 0.0001$ $n = 8$; V_{reb}: 10.8 ± 12.6%, $p < 0.0001$ $n = 8$, paired t-test). The NDMA receptor antagonist APV caused a further reduction ($V_{dep.}$= 7.0 ± 9.7%, $p = 0.001$ $n = 4$, paired t-test; $V_{hyp.}$ = 13.8 ± 17.4%, $p = 0.0022$ $n = 4$,$V_{reb.}$= 7.2 ± 14.4 $n = 4$, $p = 0.001$, paired t-test; Supplemental Figure 2 panels L, M, N and O). Thus, we conclude that stimulation of MDJ afferents resulted in synaptic potentials that were predominantly mediated by glutamate receptors.

As shown during stimulation of CN afferents and in line with previous findings that showed that pharmacological activation of NMDA receptors can result in induction of STOs in a subset of silent IO neurons (Turecek et al. 2014), STOs could also be triggered in a subset of silent IO neurons when the MDJ synaptic potential had a large hyperpolarizing component ($V_{hyp} \geq 2.93$ mV).

As for oscillations induced by CN afferent stimulation, MDJ induced oscillations were transient, but had shorter durations (1.3 ± 0.64 s, n = 6, p = 0.005, unpaired t-test, Supplemental Figure 3). Here too, amplitudes of the elicited oscillations scaled with V_{hyp} (first cycle: $R^2 = 0.92$, n = 8, Figure 2B; second cycle: $R^2 = 0.26$, n = 8, third cycle: $R^2 = 0.04$, n = 8, Supplemental Figure 4 panels A and B) and their timing was modulated by its amplitude, which was reflected in the exponential decay of the latency to peak of the rebound component with increasing V_{hyp} (Figure 5C) while the rebound slope scaled linearly ($R^2 = 0.93$, n = 8) (figure 5D).

Thus, under certain conditions, in particular when the synaptic potential is associated with a large hyperpolarizing component, MDJ input can elicit transient oscillatory behavior in IO neurons that are normally silent. However, we were not able to fully resolve whether IO neurons in the awake state display persistent oscillatory behavior or only briefly resonate in response to salient sensory input.

Subthreshold MDJ stimuli acted as a weakly resetting stimulus (Figure 6B, n = 7). Phase-locking was significantly reduced ($SD_{pre\text{-}stim}$ = 56.47 ms, $SD_{post\text{-}stim}$ = 44.97 ms, p < 0.0001, F test, n = 15, Figure 6C) although smaller than seen with subthreshold (or suprathreshold) inhibitory CN afferent stimulation ($\Delta SD_{pre\text{-}post\text{-}MDJ\_sub}$ = 11.49 ms, Supplemental Figure 7). Moreover, MDJ subthreshold synaptic responses induced a weak, but significant, increase of the amplitude of the post-stimulus oscillation cycles (ΔSTO amplitude first cycle: 1.52 ± 3.0 mV, p < 0.0001, second cycle: 0.60 ± 2.0 mV, p < 0.0001, third cycle: 0.37 ± 1.7 mV,p = 0.0101, fourth cycle: 0.5 ± 3.69 mV, p = 0.0119, Friedman test, n = 26, Figure 6D). MDJ afferent stimulation also induced relative increases in oscillation amplitude that were significantly lower than for subthreshold inhibitory (1^{st} cycle: p < 0.0001, 2^{nd} cycle: p < 0.0001, 3^{rd} cycle: p < 0.0001, 4^{th} cycle: p < 0.0001, Mann-Whitney U test) and suprathreshold inhibitory inputs (1^{st} cycle: p < 0.0001 , 2^{nd} cycle: p < 0.0001, 3^{rd} cycle: p < 0.0001, 4^{th} cycle: p = 0.0123, Mann-Whitney U test).

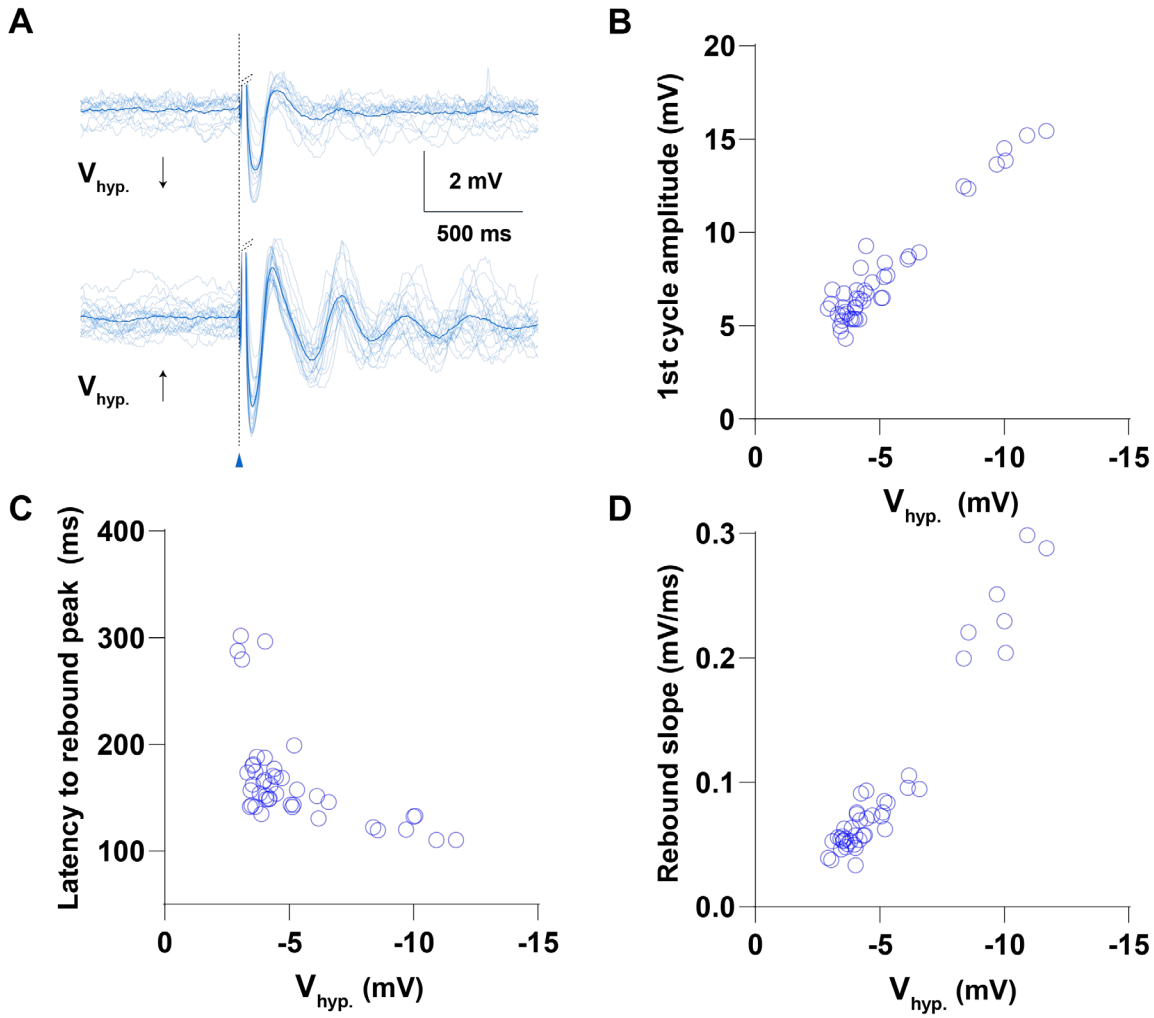

Figure 5. MDJ afferent stimulation induces STOs in a subset of silent IO neurons. A, Whole-cell patch-clamp recording of an IO neuron in which synaptic responses with small V_{hyp} amplitude elicited no oscillations, but larger amplitude did (individual trials: light blue, average response: dark blue. Part of the depolarizing phase of the synaptic potential ($V_{dep.}$) has been omitted for clarity). B, Amplitude of 1st cycle (rebound peak) following stimulation as a function of the amplitude of the hyperpolarizing component ($V_{hyp.}$). C, Latency to the peak of the rebound component ($V_{reb.}$) as a function of $V_{hyp.}$ D, Rebound slope as a function of $V_{hyp.}$ Open blue circles represent individual trials.

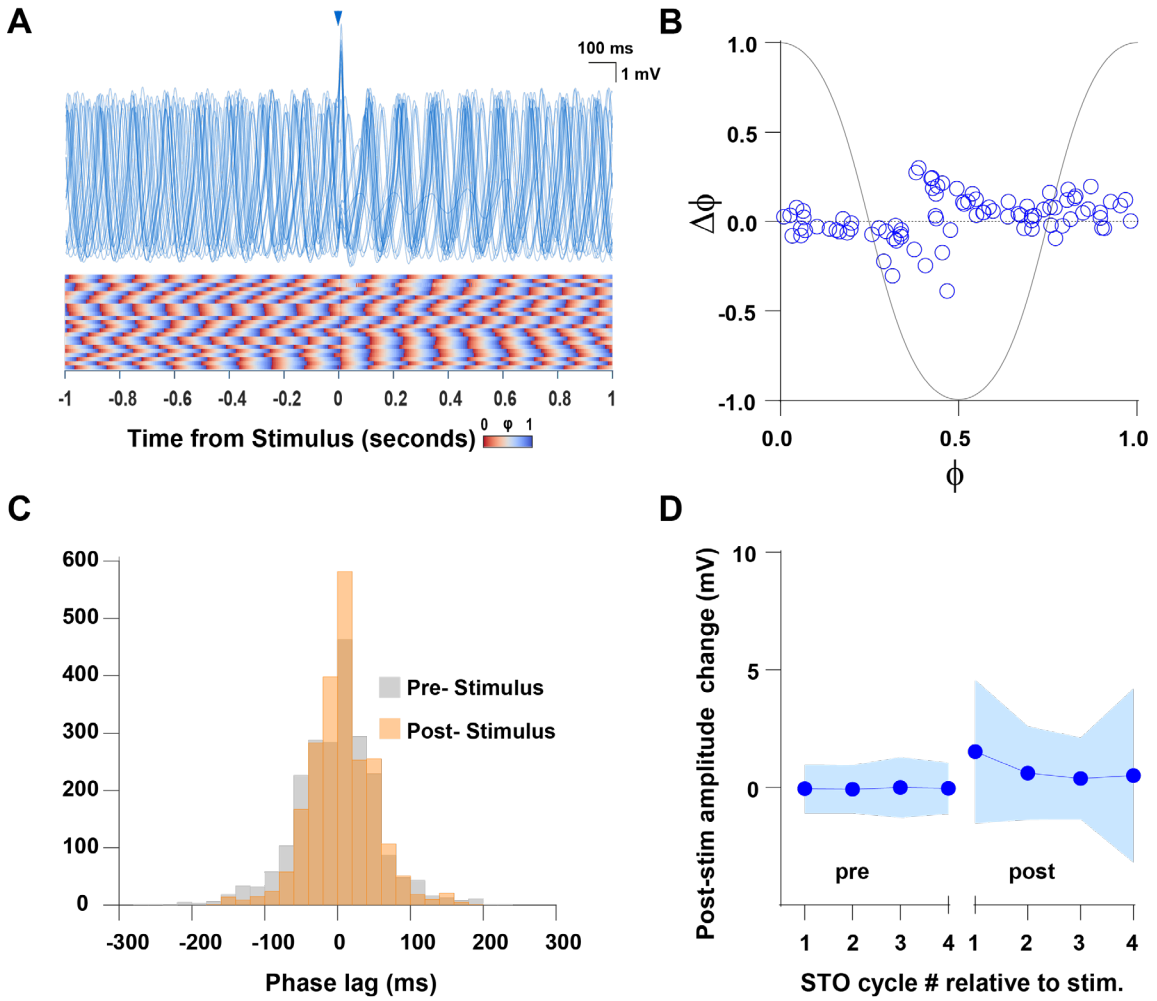

Figure 6. Response properties of oscillating IO neurons to MDJ afferent stimulation that evoke subthreshold responses. A, Excitatory stimulation (triangle indicates stimulus onset) in an oscillating IO neuron (top: superimposed recording trials, bottom: phase plot of all trials). B, Phase response curve of phase changes (ΔΦ) at different phases of stimulation (Φ). Open blue circles represent individual trials. C, Histogram showing the distribution of phase lags calculated for three cycles before (pre-stimulus) and after (post-stimulus) stimulation. D, Changes in peak STO oscillation amplitude following stimulation. The mean amplitude before stimulation of the MDJ afferents was subtracted from four individual cycles before and after stimulation (shaded area represents the standard deviation).

Impact of suprathreshold MDJ input on IO neurons

Unlike subthreshold excitatory responses, suprathreshold spikes driven by MDJ afferent stimulation caused phase delays similar to those induced by CN subthreshold responses, having a similar PRC slope and ΔΦ-intercept (slope = -0.50, p = 0.4127, ΔΦ-intercept = 0.09, n = 5, p = 0.0003, R^2 = 0.82, Ancova, Figure 6B, Supplemental Table 5). When MDJ suprathreshold responses were compared with CN suprathreshold responses a similar PRC slope but lower ΔΦ-intercept was found (P_{slope} = 0.40, $P_{intercept}$ = 0.0093, Ancova). This means that both kinds of suprathreshold responses exhibited similar input phase-phase shift relationships but, unlike CN

spikes, MDJ spikes only caused phase delays and not advances, which means that periods of the cycles containing MDJ spikes cannot be shorter than those previous to stimulation. Therefore, the nature of the suprathreshold MDJ responses determines the repertoire of phase shifts of the STOs, which in turn may have an impact on online motor control and synaptic plasticity.

Spikes triggered by MDJ afferent stimulation occurred around the oscillation as also happened for spontaneously occurring spikes (Bazzigaluppi et al. 2012b). This was also reflected by the PRC (Figure 7B).

Action potentials triggered by MDJ afferent stimulation caused a weak phase-locking across trials ($SD_{pre\text{-}stim}$ = 59.10 ms, $SD_{post\text{-}stim}$ = 36.05 ms, n = 8, $p < 0.0001$, F test, Figure 7C), even weaker than induced by subthreshold MDJ afferent stimulation ($\Delta SD_{pre\text{-}post\text{-}MDJ\_supra}$ = 9.29 ms, Supplemental Figure 7 and Supplemental Table 8). Despite the lack of phase-locking, suprathreshold MDJ afferent stimulation significantly increased the post-stimulus oscillation amplitude (ΔSTO amplitude 1st cycle = 6.75 ± 4.26, $p < 0.0001$, 2nd cycle = 1.76 ± 2.24, $p < 0.0001$, 3rd cycle= 1.15 ± 1.63 mV, $p < 0.0001$, 4th cycle = 0.73 ± 1.59, $p < 0.0001$, Friedman test, n = 10, Figure 7D). The increases in post-stimulus oscillation amplitude were significantly larger than those induced by subthreshold excitatory input (1st cycle, $p < 0.0001$, 2nd cycle, $p < 0.0001$, 3rd cycle, $p < 0.0001$, 4th cycle, $p = 0.0123$, Mann-Whitney U test), CN subthreshold input (1st cycle, $p < 0.0001$, 2nd cycle, $p < 0.0001$, 3rd cycle, $p < 0.0001$, 4th cycle, $p = 0.03$, Mann-Whitney U test) and CN suprathreshold input (1st cycle, $p < 0.001$, 2nd cycle, $p = 0.06$, 3rd cycle, $p = 0.013$, 4th cycle, $p < 0.0001$, Mann-Whitney U test).

Finally, we compared spikes generated by MDJ afferent stimulation with those triggered by CN afferent stimulation. We selected spikes for each condition evoked with the same current pulses (760 ± 106.9 pA, range: 600-900 pA, for both conditions) and comparable membrane voltage previous to stimulation (CN spikes: -36.26 ± 3.75 mV, n = 4, MDJ spikes: -36.92 mV ± 4.86 mV, n = 4, $p = 0.30$, paired t-test). Spikes driven by CN and MDJ input exhibited a comparable half-width (CN spikes: 22.02 ± 5.88 ms n = 4, MDJ spikes: 21.48 ± 4.04 ms n = 4, p = 0.=70, paired t-test, Supplemental Figure 6A). However, 80% of the trials of the spikes elicited by CN input showed an increased number of spikelets with respect to spikes driven by MDJ input, even though this was not significant (CN spike: 3.188 ± 2.32, MDJ spike: 2.06 ± 2.27, $p = 0.09$, paired t-test, Supplemental Figure 6B). Furthermore, CN spikes showed a higher rheobase (CN spikes: 675 ± 50 pA n = 4, MDJ spikes: 287.5 ± 201.6 pA n = 4, $p = 0.0183$, paired t-test, Supplemental Figure 6C). These findings reveal that suprathreshold synaptic responses require different levels of synaptic current to be elicited and that CN spikes show an upward trend in the number of spikelets.

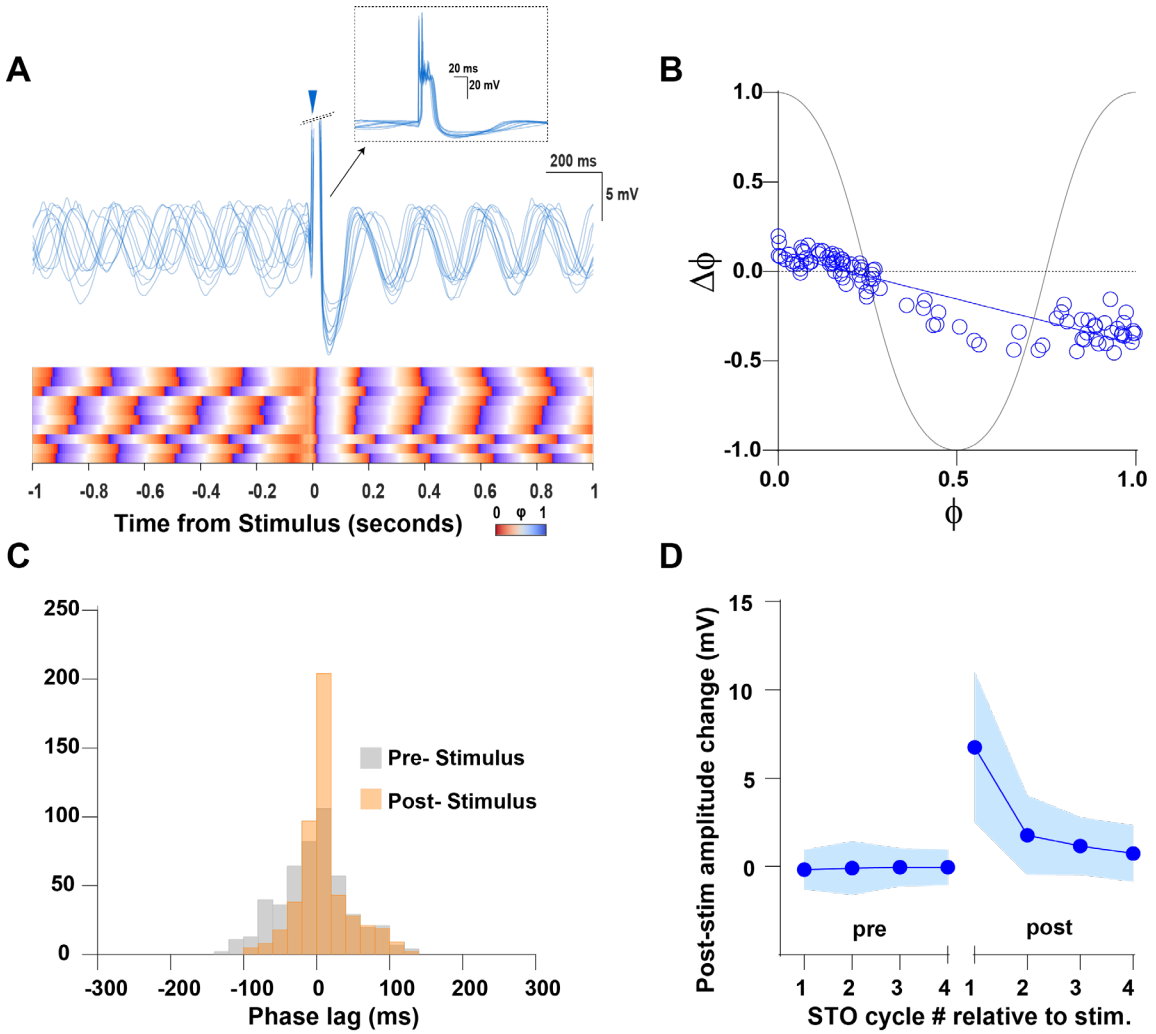

Figure 7. Impact of MDJ suprathreshold synaptic responses on IO oscillating neurons. A, Suprathreshold responses in IO neurons during MDJ afferent stimulation (stimulus onset indicated by a triangle, recording trials in light blue). Action potentials are clipped in order to visualize the induced phase resetting. B, PRC of phase changes (ΔΦ) at different phases of stimulation (Φ). Open blue circles represent individual trials. C, Histogram showing the distribution of phase lags calculated across trials for three cycles before (pre-stimulus or after (post-stimulus stimulation. Spike activity reveals a narrower distribution with increased 0-phase lag following the excitatory stimulus. D, Changes in peak STO oscillation amplitude. The mean amplitude before stimulation of the MDJ afferents was subtracted from four individual cycles before and after stimulation to reveal (shaded area represents the standard deviation).

Interaction of CN and MDJ inputs and their impact on IO neurons

Given the unique synaptic arrangement at IO dendritic spines (De Zeeuw et al.,1990a), the temporal interplay of CN and MDJ inputs is bound to have a big impact on the input-output relationship of IO neurons where inhibition could gate IO output for specific input timing intervals (De Zeeuw et al.,1995; Segev and Parnas, 1983). Gating of complex spikes is observed in vivo during animal locomotion (Lawrenson et al., 2016; Ozden et al., 2012), but little is known about

the temporal intervals of IO inputs that underlie such gating. We therefore combined stimulation of MDJ and CN afferents using optogenetic stimulation of two opsins, Chronos-GFP and Chrimson-tdTomato. AAVs were injected into the MDJ and CN of C57BL/6 mice (Figure 8A upper panel). Slices were obtained after at least four weeks to ensure proper expression of the opsins in their termination zones of the IO. The MAO and PO showed a strong overlap of both MDJ and CN afferents, whereas the DAO showed almost exclusively CN afferent projections (Figure 8B left panel). In addition to using the dual opsin approach, we combined electrical stimulation of the medial tegmental tract, which contains descending fibers from MDJ, with optogenetic stimulation of CN fibers in Gad2-IRES-Cre x Ai32 (RCL-ChR2(H134R)/EYFP) transgenic mice (Figure 8A bottom panel).

For combined input stimulation in IO neurons, we varied intervals between excitatory MDJ and inhibitory CN afferent stimulation ranging from presentation of excitation 100 ms before (-100 ms) to 200 ms after (+200 ms) the onset of inhibition. We subsequently calculated the phase responses, phase-locking, as well as induced changes in STO amplitude and spike probability for a range of intervals. The phase response change-phase input relationships, which is reflected in the slopes of the PRCs, did not differ significantly across a large range of intervals. However, when excitation followed inhibition by +150 ms the PRC slope was significantly steeper (Figure 8G: second panel from top to bottom, Supplemental Table 5 and 6, $P < 0.0001$, One-way ANOVA). This indicates that +150 ms intervals cause larger phase response changes than the other time intervals. Moreover, at this interval the ΔΦ-intercept was more positive (0.35 ± 0.33, n = 7, Figure 8G: first panel from top to bottom, Supplemental Table 7 and 8, $P < 0.0001$, One-way ANOVA), whereas the rest of the intervals showed either ΔΦ-intercept values close to zero (0 ms: 0.08 ± 0.17 ; +30 ms: 0.02 ± 0.16 ; +50 ms: 0.02 ± 0.16 ; +100 ms: 0.09 ± 0.18 ; and +200 ms: 0.08 ± 0.17) or negative (-100 ms: -0.16 ± 0.16; -50 ms: -0.11 ± 0.15). This indicates that +150 ms intervals can either cause phase advances (positive ΔΦ vaues in the PRC curve) or phase delays (negative ΔΦ values in the PRC curve), whereas the rest of time intervals can only cause phase delays.

Across all time intervals, we observed that the weakest phase-locking corresponded to the time interval where excitation followed inhibition by +50 ms, which coincided with presentation of excitation around the trough of inhibitory response. This was reflected by a smaller change in the standard deviation of post-stimulus phase lags relative to pre-stimulus conditions ($\Delta SD_{pre\text{-}post}$ = 28.35 ms, Figure 8 panels D and G: third panel from top to bottom). The interaction of the two stimuli at this time interval appeared to account for the weaker phase-locking, as presentation of inhibition by itself resulted in more pronounced phase-locking. By contrast, when only excitation

was provided phase-locking was weaker, suggesting that inhibition still contributes to phase-locking, but to a lesser degree when combined with excitation at a time interval of + 50 ms (Supplemental Table 8).

For most combinations of inhibition and excitation STO amplitude was increased for the first oscillation cycle after stimulation (Supplemental table 9). When excitation followed inhibition by +50 ms, the amplitude seemed to be most weakly increased (1st cycle: 1.83 ± 3.42 mV, n = 34). The opposite was seen when excitation was presented 150 ms following inhibition (+150ms) which resulted in a large boost (1st cycle: 7.25 ± 3.45, n = 10, Supplemental table 10 and 11). This large boost of the first cycle following stimulation exceeded the observed when independently presenting inhibition or excitation (EPSP: 1.52 ± 3.04 mV, n =7, IPSP: 4.82 ± 3.70, n = 7, Supplemental table 10 and table 11).

Our findings raise the question of how spike probability is affected by the precise timing of inhibition and excitation. As can be expected, spike probability was significantly reduced when excitation followed inhibition at intervals of +50 ms and +70 ms near the trough of the hyperpolarizing component of the inhibitory response (P_{spike} = 0 ± 0 in both cases, +50 ms, n = 9, +70 ms, n = 6), whereas it was largest at an interval of +150 ms around the peak of the rebound component of the inhibitory response (0.57 ± 0.3, n = 9, figure 8G: fifth panel from top to bottom, Supplemental table 12 and 13)**.** The spike probability for the +150 ms interval was higher than that for either single excitatory or inhibitory synaptic responses (EPSP: 0.22 ± 0.28, n =7, IPSP: 0.01 ± 0.03, n = 7, Supplemental table 12 and 13) under the same experimental conditions. STO phase was strongly reset when presenting CN inhibition in conjunction with MDJ excitation 150 ms later, both in the presence and absence of spikes (Supplemental Tables 6 and 8).

Taken together, our data demonstrate that the temporal interaction of excitatory and inhibitory postsynaptic responses in IO neurons dictate the ability of IO neurons to reset and lock the oscillation phase, thereby providing a control mechanism for the timing of spike generation.

Interaction of CN and MDJ inputs and their impact on motor learning

After investigating how specific intervals of CN and MDJ inputs affect IO subthreshold behavior and spike generation we determined to what extent such inputs could be tuned to affect motor learning. To this end, we employed a whisker reflex learning paradigm (Romano et al., 2018) in which 4 Hz air puff stimulation is presented to the whisker pad for 20 seconds to potentiate whisker protraction. This type of learning relies on parallel fiber to Purkinje cell LTP associated with an increased simple spike firing in Purkinje cells of lobules Crus I and Crus II. We used two intervals

that in our in vitro studies suppressed (+50 ms between inhibition and excitation) or facilitated (+150 ms between inhibition and excitation) IO spike generation. In combination with sensory stimulation in the whisker reflex paradigm such stimulation should respectively result in LTD for +150 ms and LTP for + 50 ms intervals. Based on this reasoning, we expected that the + 50 ms interval should result in a potentiation of whisker protraction. In our experiments, a high variability in the amplitude and direction of the whisker reflex (i.e retraction or protraction) was observed. We therefore decided to look at the absolute amplitude of the whisker reflexes rather than protraction alone. In addition, we used histological analysis to confirm whether co-labelling of both opsins was present in the IO. This allowed us to divide mice into two groups: one with and one without co-labelling (Supplemental Figure 9 and Supplemental Table 14). In mice with co-labelling, stimulation with a +50 ms interval induced a larger whisker reflex than during +150 ms stimulation (+150 ms: 2.31 ± 1.1, +50 ms: 4.14 ± 2.1, n = 10, $p = 0.02$ paired t-test, Figure 9A). By contrast, no difference was found in mice without co-labelling (+150 ms: 2.27 ± 2.03, +50 ms: 2.57 ± 2.06, n = 6, $p = 0.54$ paired t-test, Figure 9B). These preliminary data suggest that intervals of inhibitory and excitatory input to the IO that suppress complex spike firing (e.g. +50 ms interval) have the greatest impact on reflexive motor learning. Further studies are required however to confirm and extent these results, possibly in combination with direct read-out of complex spike firing in the cerebellar cortex.

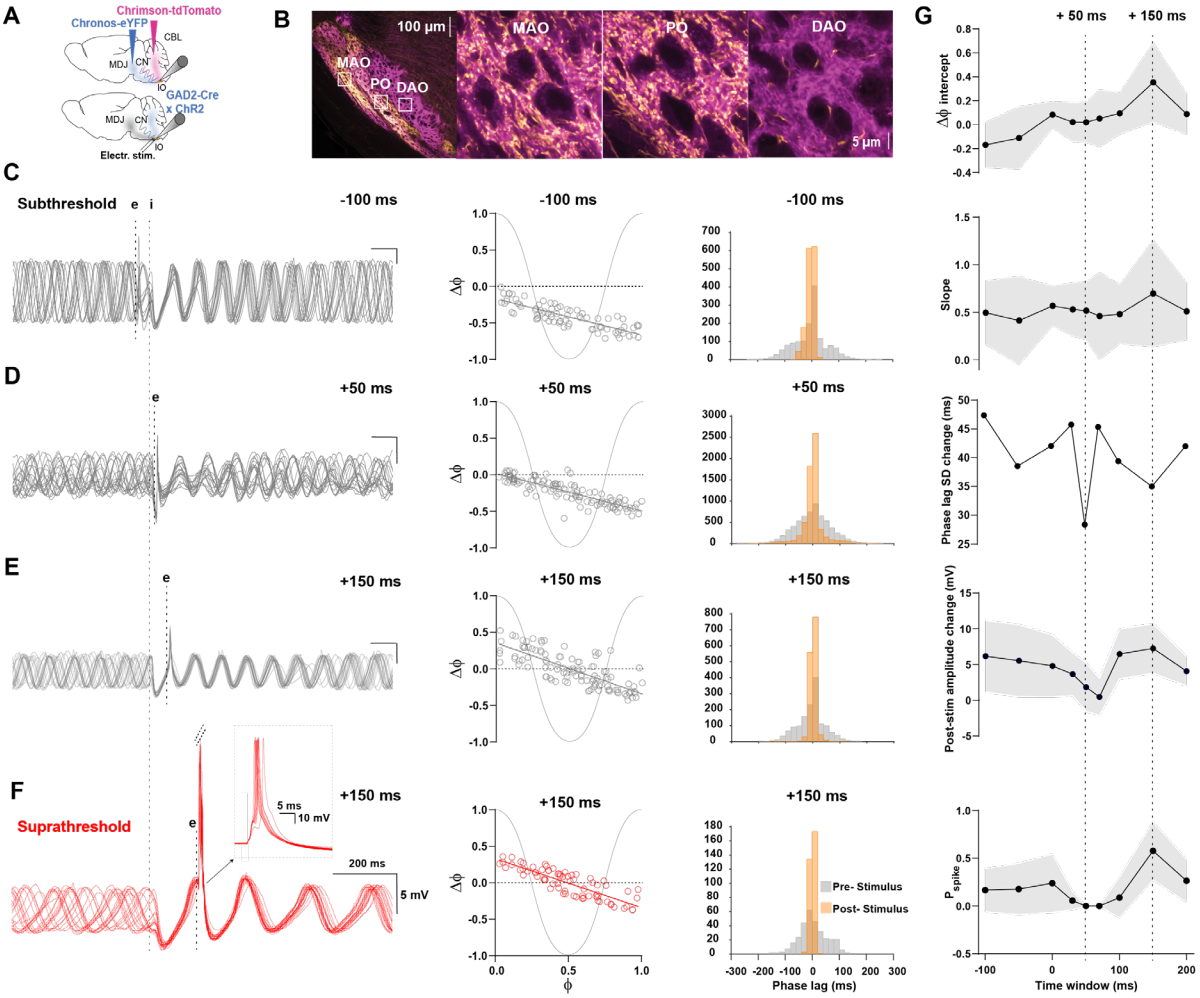

Figure 8. Impact of the timing of CN and MDJ inputs on STOs and output. A, Schematics illustrating the methods used to stimulate excitatory MDJ and inhibitory CN afferents. Top panel: Dual optogenetic approach by transducing opsins with different excitation spectra in C57BL/6 mice: Chronos-GFP and Chrimson-tdTomato in the MDJ and CN, respectively. Bottom panel: Use of Gad2Cre x ChR2-H134R-EYFP transgenic mice where MDJ afferents were stimulated by placing an electrode at the rostral side of the olivary subnuclei in combination with optogenetic stimulation of CN afferents expressing ChR2. B, Sagittal section of the brain stem highlights that MDJ afferents predominantly terminate in the PO and MAO while CN afferents terminate throughout all major nuclei. Higher magnifications of the boxed regions in the left-mostpanel show the innervation to IO subnuclei more clearly. C,D,E, left: trials aligned to stimulus onset for time intervals of -100 ms, +50 ms, +150 ms evoking subthreshold synaptic responses, middle: PRCs for those three time intervals (open gray circles represent individual trials), right: histogram showing the distribution of phase lags calculated across trials for three cycles before (pre-stimulus) or after (post-stimulus) stimulation at those three time intervals. F, left: trials aligned to stimulus onset in IO neurons for time interval of +150 ms in which spikes were evoked, middle: PRCs this time interval (open red circles indicate individual trials), right: histogram of phase pre- and post-stimulus phase lags of this time interval. G, From top to bottom: ΔΦ-intercept of PRC curves, Slope of PRC curves, Change in standard deviation (σ) of phase lags following stimulation (pre-stimulus SD - post-stimulus SD), post-stimulus amplitude change of the 1st cycle following stimulation and spike probability measured at time intervals of -100 ms, -50 ms, 0 ms, +30 ms, +50 ms, +70 ms, +100 ms, +150 ms, and +200 ms. Dash lines indicate +50 ms and +150 ms time intervals.

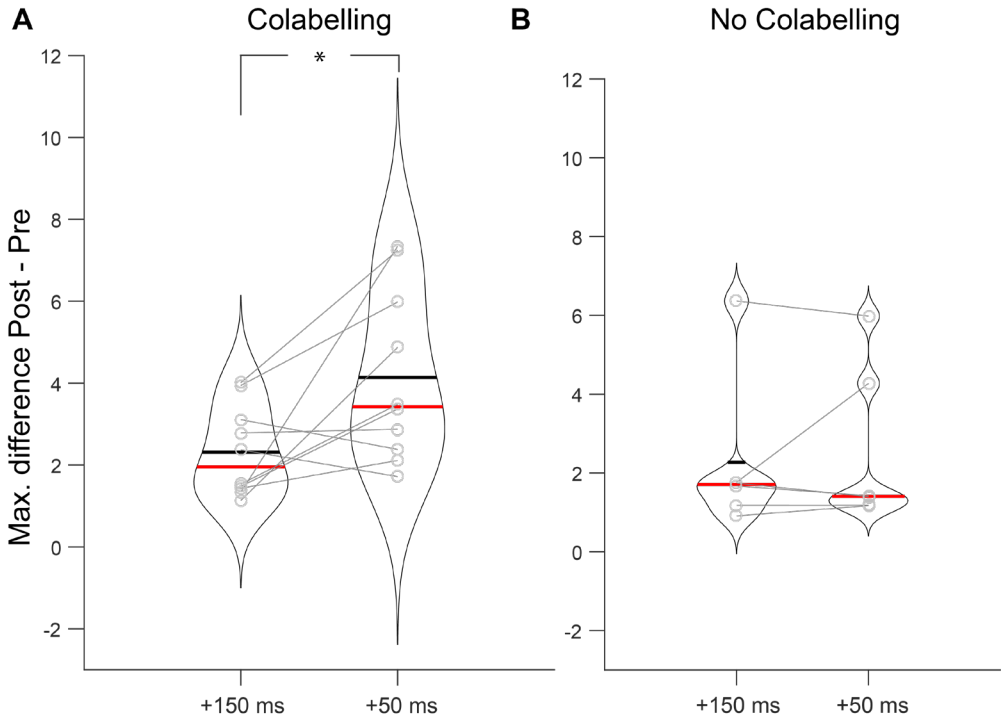

Figure 9. Violin plot showing the Impact of the timing of CN and MDJ inputs on whisker reflex learning. A, Post-Pre stimulation maximum difference of the absolute amplitude of the whisker reflex following +150 ms and + 50 ms stimulation in mice showing IO colabelling of MDJ and CN fibers expressing Chronos and Chrimson, respectively. B, Post-Pre stimulation maximum difference of the absolute amplitude of the whisker reflex following +150 ms and + 50 ms stimulation in mice showing no IO colabelling of MDJ and CN fibers expressing Chronos and Chrimson, respectively. Black line indicates the mean and red line indicates the median (* = p <0.05). Each pair of open gray circles connected by a line represent one animal.

Discussion

We selectively stimulated excitatory afferents from the mesodiencephalic junction and inhibitory afferents from the cerebellar nuclei terminating in the IO and studied how IO neurons respond to these inputs individually or at varying time intervals during joint presentation. Excitatory and inhibitory inputs have a differential impact on STOs in that they either weakly or strongly reset the oscillation phase and differentially affect spike probability. Moreover, together they turn out to provide a control mechanism to determine the timing and probability of the spiking output of olivary neurons; indeed, dependent on the duration of the specific time windows between the excitatory and inhibitory inputs one can predict the generation of olivary action potentials. Thereby, the interaction between both inputs over time appears to have important functional consequences for online motor control and motor learning.

Olivary neurons are composed of two main groups that consist of oscillating and non-oscillating neurons. Both types of subthreshold activity have been reported in reduced and intact

preparations (Bazzigaluppi et al, 2016; Turececk et al., 2014; Khosrovani et al., 2007). The different types of subthreshold activity can be explained at the cellular level by differential expression of Ca_v 3.1 channels (T-type Ca^{+2}) (Bazzigaluppi et al., 2016; Urbano et al., 2006) and at the network level by modulating coupling strength through inhibitory and excitatory synaptic inputs (Lefler et al., 2014; Mathy et al., 2014; Turececk et al., 2014). We show here that within a subset of non-oscillating IO neurons, oscillations can be induced by both MDJ excitatory and CN inhibitory afferent inputs. The hyperpolarizing component present in both the excitatory and inhibitory synaptic potentials affect the magnitude and timing of the induced oscillations. Despite the fact that STOs induced by CN synaptic inputs were induced with lower V_{hyp} amplitudes (CN: -4.29 ± 2.55 mV, n = 5, MDJ: -6.06 ± 2.69 mV, n = 6, p = 0.017, unpaired t-test, supplemental Figure 3B) and that those induced by MDJ input showed a more depolarized resting membrane potential previous to stimulation (CN: -60.55 ± 4.33 mV, n = 5, MDJ: -56.25 ± 6.78 mV, n = 6, p = 0.0072, unpaired t-test, supplemental Figure 3C), the STOs induced by CN input lasted longer than those induced by MDJ inputs. This is probably due to the asynchronous release of GABA by CN terminals in the PO and rMAO (Best and Regehr, 2009; Turececk and Regher, 2019), which can produce a more persistent impact on IO network. The initiation of oscillations in otherwise silent IO neurons has been observed in vitro after hyperpolarizing current injections in IO neurons (Bazzigaluppi et al., 2016), following the bath application of NMDA (Turececk et al., 2014), and indirectly in vivo when transient and rhythmic complex spike activity is evoked after sensory stimulation (Negrello et al., 2019). Thus, it appears that IO neurons are not only able to sustain oscillations, but also to generate resonant activity in response to sensory stimulation.

A relatively minor impact was seen for excitatory subthreshold synaptic responses on STOs as reflected by a weak phase resetting, phase-locking and moderate impact on post-stimulus STO amplitude. This may be due to the fact that subthreshold excitatory synaptic input exhibited a smaller hyperpolarizing component in oscillating than non-oscillating neurons. The hyperpolarizing component triggered by MDJ input is mediated by SK and I_h channels (Garden et al., 2017; Garden et al., 2018), conductances that also sustain STOs (Marshall and Lang, 2004; Bal and McCormick. 1997). Moreover, excitation mediated hyperpolarization also depend on gap-junctional coupling, as the hyperpolarization component of this synaptic response is blocked by gap junction antagonists (Garden et al., 2018). Thus, there are multiple factors that could contribute to the limited impact of MDJ stimulation on $V_{hyp.}$ and STOs.

By contrast, inhibitory subthreshold synaptic responses had a more pronounced effect and resulted in more pronounced phase resetting, phase-locking, and an increase in the post-stimulus STO amplitude. Subthreshold CN synaptic responses presumably cause a long-lasting phase-

locking (Supplemental Figure 7) as a result of the amplitude boost of the rebound component and possibly via a decoupling of IO neurons mediated by asynchronous GABA release (Leefler et al., 2014; Bazzigaluppi et al., 2012a, Best and Regehr., 2009).

Spikes driven by both MDJ and CN input caused phase resetting and low phase-locking. Phase resetting caused by these suprathreshold responses was similar to that caused by subthreshold CN input alone. This may be attributed to the fact that the afterhyperpolarization found in spiking neurons and the hyperpolarizing phase ($V_{hyp.}$) of the CN subthreshold synaptic response are prominent enough to reset the phase efficiently. Mechanisms underlying the low phase-locking caused by suprathreshold responses triggered by MDJ and CN inputs must be different, since spikes driven by CN input induced a low, but stable phase-locking throughout the 3 cycles post-stimulus (Supplemental Figure 8L), whereas MDJ caused a transient phase-locking similar to CN spikes for the first cycle post-stimulus and then decayed for the second and the third cycle (Supplemental Figure 8M). These findings require further investigation to understand the mechanisms underlying these different phenomena.

To our knowledge, we present the first systematic investigation on the effects of combined inhibition and excitation on IO STOs and spike probability. Our findings follow up on the idea that the close proximity of excitatory and inhibitory inputs on electrically coupled olivary dendritic spines endow IO neurons with a gating mechanism that is permissive only for specific temporal combinations of inhibitory and excitatory input (Segev and Parnas, 1983; De Zeeuw, 1990b). Furthermore, as shown here and in previous studies (Lefler et al., 2014; Garden et al., 2018), inhibitory and excitatory synaptic responses have both hyperpolarizing and depolarizing components, which make them suitable to increase or reduce subthreshold and suprathreshold activity when triggered at specific time intervals.

Moreover, this timing is critical in determining the degree of phase reset, phase-locking, and oscillation amplitude as well as the propensity of IO neurons to fire spikes. We show that when excitation follows inhibition by 50 ms and hits the peak of the hyperpolarizing component of the CN synaptic response, the STO amplitude boost is small, which is likely the result of the inactivation of I_h channels induced by depolarization. This conductance is activated at the trough of an oscillation and is crucial to initiate a new STO cycle (Bal and McCormick, 1997). Weak phase-locking induced by 50 ms interval presentation of inhibition and excitation could be caused by the weak boost of the first cycle of the oscillation, which also shows the lowest phase-locking (Supplemental Figure 8E). The most obvious explanation for the reduction in spike probability at the +50 ms interval is that excitatory synaptic responses are further away from spike threshold since excitation hits around the trough of the hyperpolarizing component of the inhibitory response

(Figure 7 panels C, D and E). Conversely, excitation that follows inhibition by 150 ms is permissive to generate spikes as excitation is presented around the peak of the rebound component of the inhibitory response, which further brings the cell to spiking threshold. Irrespective of whether a spike is elicited or not at this time window, phase shifts evoked by the +150 ms interval pairing of inhibition followed by excitation are more sensitive, i.e., cause larger phase shifts, to the phase at which the stimuli are presented, as reflected in the higher slope of the PRC. Furthermore, unlike the rest of the time windows and single input stimulation, which show ΔΦ-intercept values either close to zero or negative - meaning that can only delay the phase of the STOs - PRC at the time interval of +150 ms interval showed a pronounced positive Y-intercept. This indicates that this particular interval is able to cause not only phase delays, but also phase advances, endowing the system with a temporal interval that can work as a fine-tuner for phase shifts in the two directions. Regarding the phase-locking induced by +150 ms interval, we observed that if under this particular stimulus paradigm the cell elicit spikes, the phase-locking is very high (Supplemental Figure 8N), whereas it is lower if no spikes are evoked (Supplemental Figure 8H). This high phase-locking generated by spikes elicited at this time interval could possibly be explained by synergistic mechanisms in which decoupling caused by long lasting inhibition is potentiated by spikes driven my MDJ inputs, which if triggered close to threshold at low firing frequency (1 Hz) can in turn also lead to a decreased coupling strength (Mathy et al., 2014).

We have shown that the temporal order in which inhibitory and excitatory stimuli are presented to IO neurons can strongly influence the oscillation phase, amplitude and spike probability, thereby setting specific conditions during which plasticity can be induced or behavior can be adapted in real-time. In our case, we used a whisker reflex paradigm relying on a gating mechanism of complex spike firing, which is provided in this case by the temporal interplay of inhibitory and excitatory inputs to IO neurons, in combination with contextual information, relayed via the mossy fiber granule cell, are able to cause LTP or LTD of the parallel fiber – Purkinje cell synapses (Romano et al., 2018). The preliminary output of these experiments suggests that in animals showing coexpression of the opsins chronos and chrimson in the IO, injected in the MDJ and CN respectively, +50 ms stimulation caused a larger absolute amplitude of learned whisker reflexes than +150 ms regardless their direction (retraction or protraction). On the other hand, mice showing no coexpression exhibited no difference when the two type of stimulations were presented. This indicate that temporal interaction of excitatory and inhibitory inputs of the IO would modulate motor learning but in a more complex way than we expected. The high variability of amplitude of the movements can be explained by changes in the probability of eliciting complex spikes elicited by both kind of stimulation, whose frequency have been related to the amplitude

of arm movement (Kitazawa et al. 1998). Likewise, their presence in PC activity following puff stimulation enhances whisker protaction (Romano et al. 2018). Regarding the variability of the direction of the reflexes following stimulation across mice, it might be explained by the involvement of specific IO subnuclei when stimulation is presented, which is reflected on the differents patters of expression of both opsins observed in the IO subnuclei (Supplemental Figure 9 and Suplemental Table 14). Therefore, there would be certain combination of synchronized activity of some IO subnuclei that would promote either retraction or protraction. Although, this hypothesis requires have further studies. Another factor that could contribute to the amplitude and polarity of the whisker reflexes is the fact that contra and ipsilateral IO are mediating the whisker reflexes as shown by previous studies in which complex spike frequency is enhanced by ipsilateral and contralateral whisker stimulation (Kubo et al., 2018). Furthermore, whisker reflexes show different kinetics when contralateral or ipsilateral stimulation is used (Romano et al., 2018).

Temporal interplay of excitatory in inhibitory olivary afferents would also be crucial for real-time control of behavior, the tuning of synchronization, and firing of complex spikes are highly relevant to adapt ongoing cognitive or motor programs. In fact, synchronous activation of Purkinje cells, which in turn is driven by synchronous complex spike activity, that results in an increase of simple spikes can cause whole body and tail twitches; and preferred limb sequences when an animal is at rest whereas halting and slowdown of the gait during movement (Hoogland et al., 2015). On the other hand, decreasing the levels of complex spikes synchrony, by modulating the coupling strength of IO neurons which in turn lower the phase-locking of complex spikes across neurons, can enhance the temporal resolution of the error signal (complex spikes) transmission to the Purkinje cells. This optimizes the spatio-temporal aspects of the population coding by Purkinje cells that would result in enhanced learning (Tokuda et al., 2013). Furthermore, a reduction of complex spike activity was observed during gating when self-generated, or predictable, sensory signals are expected to happen. By contrast, an increase in complex activity was observed when unpredictable sensory signals occur (Lawreson et al., 2016).

References

Apps R and Hawkes R (2009) Cerebellar cortical organization: a one-map hypothesis. Nat Rev Neurosci. 10(9): 670-681.

Bazzigaluppi P, de Jeu MTG (2016) Heterogeneous expression of T-type Ca2+ channels defines different neuronal populations in the inferior olive of the mouse. Front Cell Neurosci 10: 192.

Bazzigaluppi P, Ruigrok T, Saisan P, De Zeeuw CI, de Jeu M (2012a) Properties of the nucleo-olivary pathway: an in vivo whole-cell patch-clamp study. PLoS One 7: e46360.

Bazzigaluppi P, De Grujil JR, van der Giessen RS, Khosrovani S, De Zeeuw CI, de Jeu MT (2012b) Olivary subthreshold oscillations and burst activity revisited. Front Neural Circuits 6:91.

Bal T, McCormick DA (1997) Synchronized oscillations in the inferior olive are controlled by the hyperpolarization-activated cation current I(h). J Neurophysiol 77: 3145–3156.

Berndt A, Schoenenberger P, Mattis J, Tye KM, Deisseroth K, Hegemann P, Oertner TG (2011) High-efficiency channelrhodopsins for fast neuronal stimulation at low light levels. Proc Natl Acad Sci U S A 108(18): 7595 – 7600.

Best AR, Regehr WG (2009) Inhibitory regulation of electrically coupled neurons in the inferior olive is mediated by asynchronous release of GABA. Neuron 62(4): 555-565.

Choi S, Yu E, Kim D, Urbano FJ, Makarenko V, Shin HS, Llinás RR (2010) Subthreshold membrane potential oscillations in inferior olive neurons are dynamically regulated by P/Q- and T-type calcium channels: a study in mutant mice. J Physiol 588: 3031–3043.

De Groot A, Den Boom BJG, Van Genderen RM, Coppens J, Van Veldhuijzen J, Bos G, Hoedemaker H, Negrello M, Willuhn I, De Zeeuw CI, Hoogland TM (2020) NINscope: a versatile miniscopes for multi-region circuit investigations. eLife 9: e49987.

De Zeeuw CI, Holstege JC, Ruigrok TJ, Voogd J (1989) Ultrastructural study of the GABAergic, cerebellar, and mesodiencephalic innervation of the cat medial accessory olive: anterograde tracing combined with immunocytochemistry. J Comp Neurol 284: 12–35.

De Zeeuw CI, Holstege JC, Ruigrok TJH, Voogd J (1990a) Mesodiencephalic and cerebellar terminals terminate upon the same dendritic spines in the glomeruli of the cat and rat inferior olive: an ultrastructural study using a combination of [3H]leucine and wheat germ agglutinin coupled horseradish peroxidase anterograde tracing. Neuroscience 34: 645–655.

De Zeeuw (1990b). Ultrastructure of the cat inferior olive. Doctoral thesis. Erasmus, Rotterdam.

De Zeeuw CI, Ruigrok TJ (1994) Olivary projecting neurons in the nucleus of Darkschewitsch in the cat receive excitatory monosynaptic input from the cerebellar nuclei. Brain Res 653: 345–350.

De Zeeuw CI, Simpon J, Hoogenraad C, Galjart N, Koekkoek S.K.E, Ruigrok T (1998). Microcircuitry and function of the inferior olive. Cerebellum 21: 391-400.

Devor A, Fritschy JM, Yarom Y (2001) Spatial distribution and subunit composition of GABA(A) receptors in the inferior olivary nucleus. J Neurophysiol 85: 1686-1696.

Fink AJ, Croce KR, Huang ZJ, Abbott LF, Jessell TM, Azim E (2014) Presynaptic inhibition of spinal sensory feedback ensures smooth movement. Nature 509(7498): 43-48.

Gao Z, van Beugen BJ, De Zeeuw CI (2012) Distributed synergistic plasticity and cerebellar learning. Nat Rev Neurosci. 13(9): 619-635.

Garden DLF, Rinaldi A, Nolan MF (2017) Active integration of glutamatergic input to the inferior olive generates bidirectional postsynaptic potentials. J Physiol 595: 1239–1251.

Garden DLF, Rinaldi A, Nolan MF (2018) Inferior olive HCN1 channels coordinate synaptic integration and complex spike timing. Cell Rep 22: 1722-1733.

Heiney SA, Kim J, Augustine GJ, Medina JF (2014) Precise control of movement kinematics by optogenetic inhibition of Purkinje cell activity. J Neurosci 34(6): 2321-2330.

Hoogland TM, De Gruijl JR, Witter L, Canto CB, De Zeeuw CI (2015) Role of synchronous activation of cerebellar Purkinje cell ensembles in multi-joint movement control. Curr Biol 25: 1157–1165.

Ito M, Kano M (1982) Long-lasting depression of parallel fiber-Purkinje cell transmission induced by conjunctive stimulation of parallel fibers and climbing fibers in the cerebellar cortex. Neurosci Lett 33: 253-258.

Ju C, Bosman LWJ, Hoogland TM, Velauthapillai A, Murugesan P, Warnaar P, van Genderen RM, Negrello M, De Zeeuw CI (2019). Neurons of the inferior olive respond to broad classes of sensory input while subject to homeostatic control. J Physiol 597(9): 2483-2514.

Klapoetke NC, Murata Y, Kim SS, Pulver SR, Birdsey-Benson A et al (2014) Independent optical excitation of distinct neural populations. Nat Methods 11(3): 338-346.

Khosrovani S, Van Der Giessen RS, De Zeeuw CI, De Jeu MTG (2007) In vivo mouse inferior olive neurons exhibit heterogeneous subthreshold oscillations and spiking patterns. Proc Natl Acad Sci U S A 104: 15911–15916.

Kitazawa S, Kimura T, Yin PB (1998) Cerebellar complex spikes encode both destinations and erros in arm movements. Nature 392 (6675): 494-497.

Kubo R, Aiba A, Hashimoto K (2018) The anatomical pathway from the mesodiencephalic junction to the inferior olive relays perioral sensory signals to the cerebellum in the mouse. J Physiol 596(16): 3775-3791.

Lawrenson C, Watson T, Apps R (2016) Transmission of predictable sensory signals to the cerebellum via climbing fiber pathways is gated during exploratory behavior. J Neurosci. 36(30): 7841-7851.

Lefler Y, Yarom Y, Uusisaari MY (2014) Cerebellar inhibitory input to the inferior olive decreases electrical coupling and blocks subthreshold oscillations. Neuron 81: 1389–1400.

Leznik E, Makarenko V, Llinás R (2002). Electrotonically mediated oscillatory patterns in neuronal ensembles: An in vitro voltage-dependent dye-imaging study in the inferior olive. J Neurosci. 22(7): 2804-2815.

Llinás R, Yarom Y (1981) Properties and distribution of ionic conductances generating electro-responsiveness of mammalian inferior olivary neurones in vitro. J Physiol 315: 569–584.

Llinás R, Yarom Y (1986) Oscillatory properties of Guinea-pig inferior olivary neurones and their pharmacological modulation: an in vitro study. J Physiol 376: 163–182.

Marshall SP, Lang EJ (2004) Inferior olive oscillations gate transmission of motor cortical activity to the cerebellum. J Neurosci 24(50): 11356-11367.

Mathy A, Clark BA, Häusser M (2014) Synaptically induced long-term modulation of electrical coupling in the inferior olive. Neuron 81: 1290–1296.

Negrello M, Warmaar P, Romano V, Owens CB, Lindeman S, Lavarone E, et al (2019) Quasiperiodic rhythms of the inferior olive. PloS Comput Biol 15(5): e1006475.

Ozden I, Dombeck DA, Hoogland TM, Tank DW, Wang SS (2012) Widespread state-dependent shifts in cerebellar activity in locomoting mice. PloS One 7(8): 642650.

Placantonakis, D.G., Bukovsky, A.A., Aicher, S.A., Kiem, H.P., and Welsh, J.P. (2006). Continuous electrical oscillations emerge from a coupled network: a study of the inferior olive using lentiviral knockdown of connexin36.J Neurosci 26: 5008–5016.

Raymon J and Lisberger S. Neural learning rules for the vestibulo-ocular reflex (1998) J Neurosci 18(21): 9112–9129.

Romano V, De Propris L, Bosman LWJ, Warnaar P, ten Brinke MM, Lindeman S, Ju C, Velauthapillai A, Spanke JK, Guerra EM, Hoogland TM, Negrello M, D'Angelo E, De Zeeuw CI (2018) Potentiation of cerebellar Purkinje cells facilitates whisker reflex adaptation through increased simple spike activity. eLife 7: e38852.

Ruigrok TJ, Voogd J (1990) Cerebellar nucleo-olivary projections in the rat: an anterograde tracing study with Phaselous vulgaris-leucoagglutinin (PHAL-L). J Comp Neurol 298(3): 315-333

Ruigrok TJ, Voogd J (1995) Cerebellar influence on olivary excitability in the cat. Eur J Neurosci 7: 679-693.

Safo S, Regher WG (2008) Timing dependence of the induction of cerebellar LTD. Neuropharmacology 54(1): 213-218.

Segev I, Parnas I (1983) Theoretical and experimental investigation of temporal postsynaptic interactions between excitatory and inhibitory inputs. Biophys J 41: 41-50.

Ten Brinke MM, Boele HJ, Spanke JK, Potters JW, Ruigrok TJ, Hoebeek FE, De Zeeuw (2015) Evolving models of Pavlovian conditioning: cerebellar cortical dynamics in awake behaving mice. Cell Rep 13: 1977–1988.

Tokuda IT, Hoang H, Schweighofer N, Kawato M (2013) Adaptive coupling of inferior olive neurons in cerebellar learning. Neural Networks 47: 42–50.

Turecek J, Han VZ, Cuzon Carlson VC, Grant KA, Welsh JP (2016) Electrical coupling and synchronized subthreshold oscillations in the inferior olive of the rhesus macaque. J Neurosci 36: 6497–6502.

Turecek J, Regehr WG (2019) Neuronal regulation of fast synaptotagmin isoforms controls the relative contributions of synchronous and asynchronous release. Neuron 101(5): 938-949.

Turecek J, Yuen GS, Han VZ, Zeng XH, Beyer KU, Welsh JP (2014) NMDA receptor activation strengthens weak electrical coupling in mammalian brain. Neuron 81: 1375–1388.

Urbano FJ, Simpson JI, Llinás RR (2006) Somatomotor and oculomotor inferior olivary neurons have distinct electrophysiological phenotypes. Proc Natl Acad Sci U S A 103: 16550–16555.

Van Der Giessen RS, Maxeiner S, French PJ, Willecke K, De Zeeuw CI (2006) Spatiotemporal distribution of connexin 45 in the olivocerebellar system. J Comp Neurol 495(2): 173-184.

Van Der Giessen RS, Koekkoek SK, van Dorp S, De Grujil JR, Cupido A, Khosrovani S, Dortland B, Wellershaus K, Degen J, Deuchars J, Fuchs EC, Monyer H, Willecke K, De Jeu MT, De Zeeuw CI (2008) Role of olivary electrical coupling in cerebellar motor learning. Neuron 58(4): 599–612.

Wang SS, Denk W, Häusser M (2000) Coincidence detection in single dendritic spines mediated by calcium release. Nat Neursci 3(12): 1266-1273.

Welsh JP, Lang EJ, Suglhara I, Llinás R (1995) Dynamic organization of motor control within the olivocerebellar system. Nature 374: 453–457.

Supplementary figures

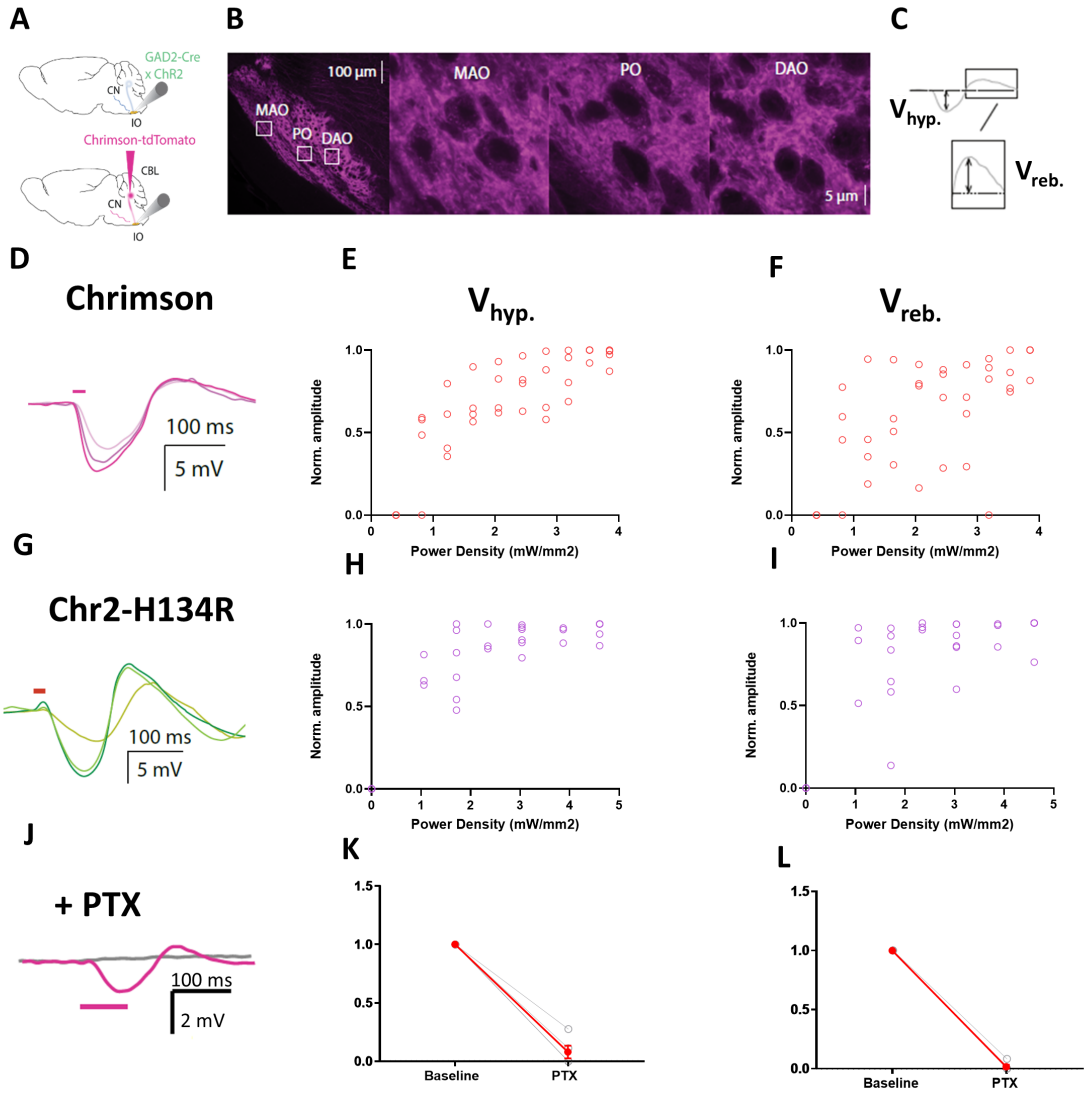

Supplemental Figure 1. CN evoked synaptic responses in the IO. A, Schematics illustrating the methods used to stimulate the inhibitory CN afferents. Top panel: Optogenetic stimulation of inhibitory afferents using GAD2Cre/Chr2-H134R-EYFP transgenic mice. Bottom panel: CN was transduced with Chrimson-tdTomato and their terminals were stimulated optogenetically in the inferior olive. B, left panel: confocal image of a sagittal section of the brain stem showing CN afferent fiber terminations throughout the inferior olive. Right panels: higher magnifications of the boxed regions denoted in the left panel. C, Example of the biphasic response evoked by CN input consisting of a hyperpolarizing component ($V_{hyp.}$) followed by a rebound component ($V_{reb.}$). Arrows denote how the amplitude was measured for each component. D, Synaptic responses to increasing stimulus of optical stimulation of 625nm in wild type mice transduced with Chrimson-tdTomato in the CN. E-F, $V_{hyp.}$ and $V_{reb.}$ (mV) plotted as a function of stimulus intensity at a wavelength of 625nm (mW/mm^2) in WT mice transduced with Chrimson-tdTomato. Open red circles represent individual trials. g, Synaptic responses to increasing stimulus intensities using optical stimulation of 470nm in GAD2Cre/Chr2-H134R-EYFP transgenic mice. H-I, $V_{hyp.}$ and $V_{reb.}$ amplitudes (mV) plotted as a function of stimulus intensity at a wavelength of 470nm (mW/mm^2) in GAD2Cre/Chr2-H134R-EYFP transgenic mice. Open purple circles represent individual trials. j, Example trace of synaptic response to CN inputs before and after the presence of picrotoxin (PTX, 100µM). K-L, $V_{hyp.}$ and $V_{reb.}$ normalized amplitude before and after the presence of PTX. Red lines indicates the mean and light gray lines indicate individual experiments.

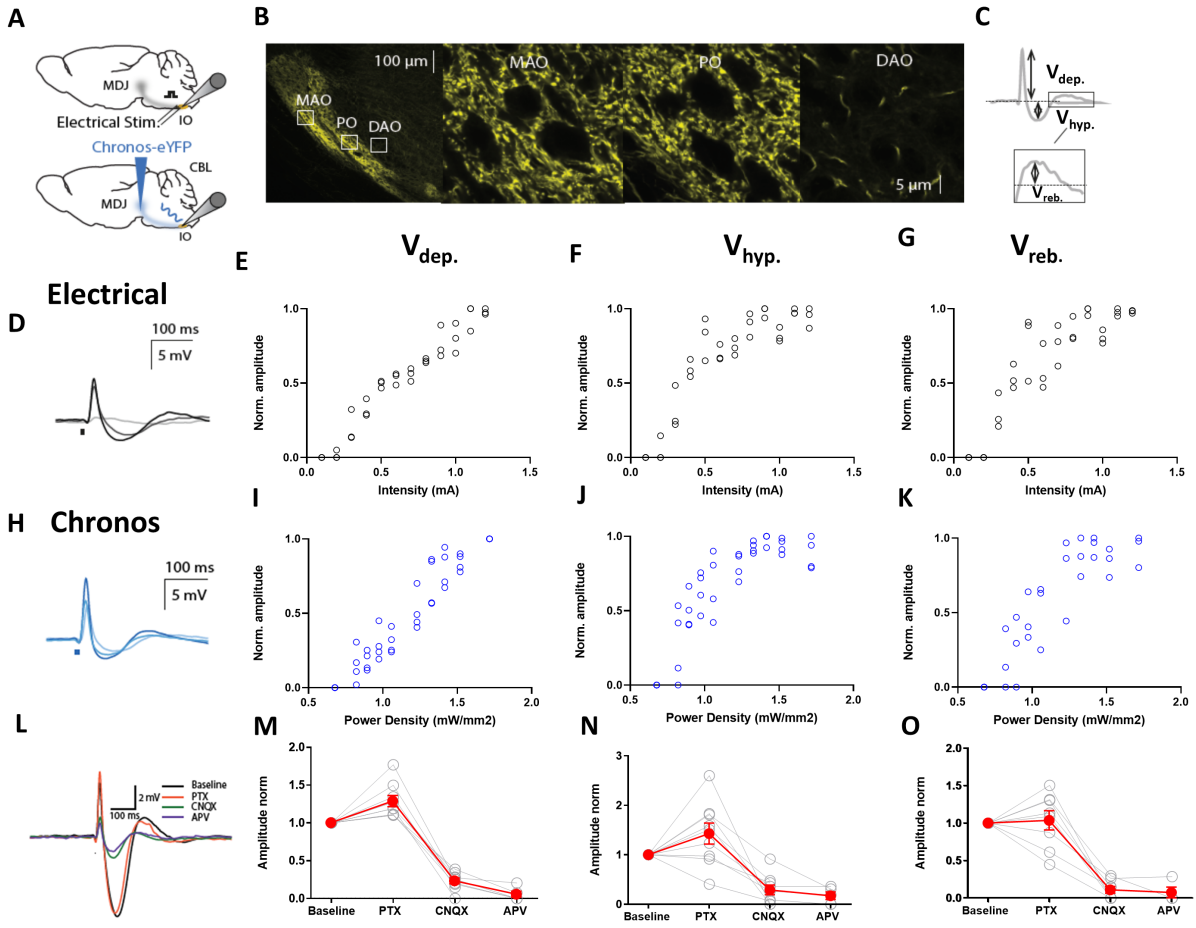

Supplemental Figure 2. Midbrain evoked synaptic responses in the IO. A, Schematics illustrating the methods used to stimulate the excitatory MDJ afferents. Top panel: An electrical stimulation electrode was placed at the rostral side of the olivary subnuclei. Bottom panel: The MDJ was transduced with Chronos-GFP and these terminals were stimulated in the inferior olive. B, left panel: confocal image of a sagittal section of the brain stem showing MDJ afferent fiber terminations in the olivary subnuclei PO and MAO. Right panels: higher magnifications of the boxed regions denoted in the left panel. Note that while PO and MAO show strong labeling whereas the DAO is nearly devoid of MDJ afferents. C, Example of the multi-phasic synaptic response evoked by MDJ input consisting of a depolarizing component ($V_{dep.}$), a hyperpolarizing component ($V_{hyp.}$) and a rebound component ($V_{reb.}$). Arrows denote how the amplitude was measured for each component. D, Synaptic responses to increasing stimulus intensities using electrical stimulation (top). E-G, $V_{dep.}$, $V_{hyp.}$ and $V_{reb.}$ amplitudes (mV) plotted as a function of stimulus intensity during electrical stimulation (mA). Open black circles represent individual trials. H. Synaptic responses to increasing stimulus intensities using optical stimulation. I-K, $V_{dep.}$, $V_{hyp.}$ and $V_{reb.}$ amplitudes (mV) plotted as a function of stimulus intensity during light stimulation. Open blue circles represent individual trials. L, Example trace of synaptic response to MDJ inputs before and after the presence of picrotoxin (PTX, 100µM), CNQX (20 µM) and APV (50 µM). M-O, $V_{dep.}$, $V_{hyp.}$ and $V_{reb.}$ normalized amplitude before and after the presence of CNQX, PTX and APV. Red lines indicates the mean and light gray lines indicate individual experiments.

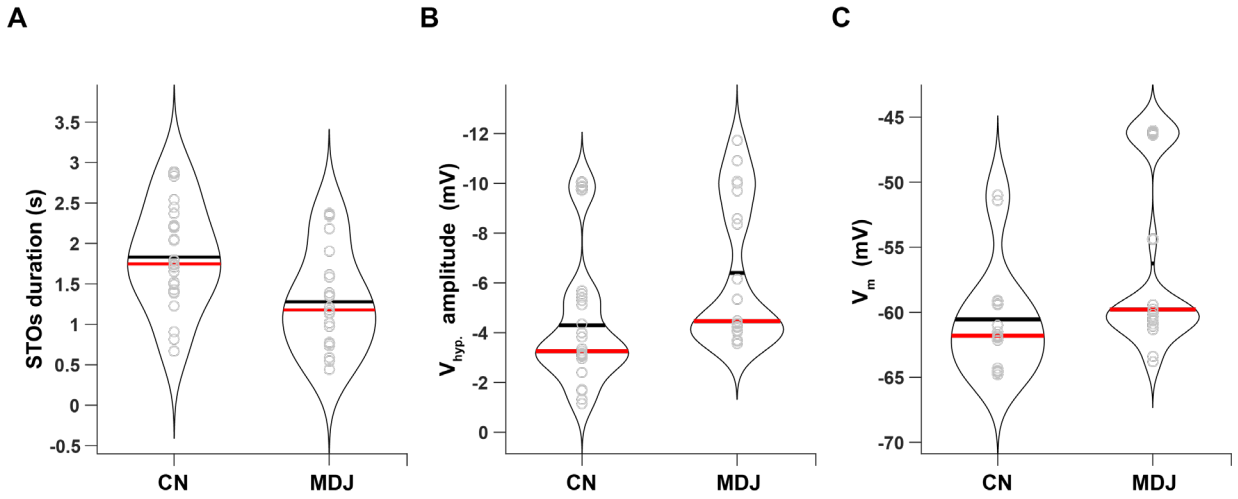

Supplemental Figure 3. A, Violin plot of STOs duration of transient STOs induced by CN subthreshold inhibitory and MDJ excitatory synaptic responses. B, Violin plot of $V_{hyp.}$ amplitude of CN and MDJ synaptic responses that induce transient STOs. C, Violin plot of V_m previous to CN and MDJ synaptic inputs that induce transient STOs. Red lines indicate the median and black lines indicate the mean. Open gray circles represent individual trials.

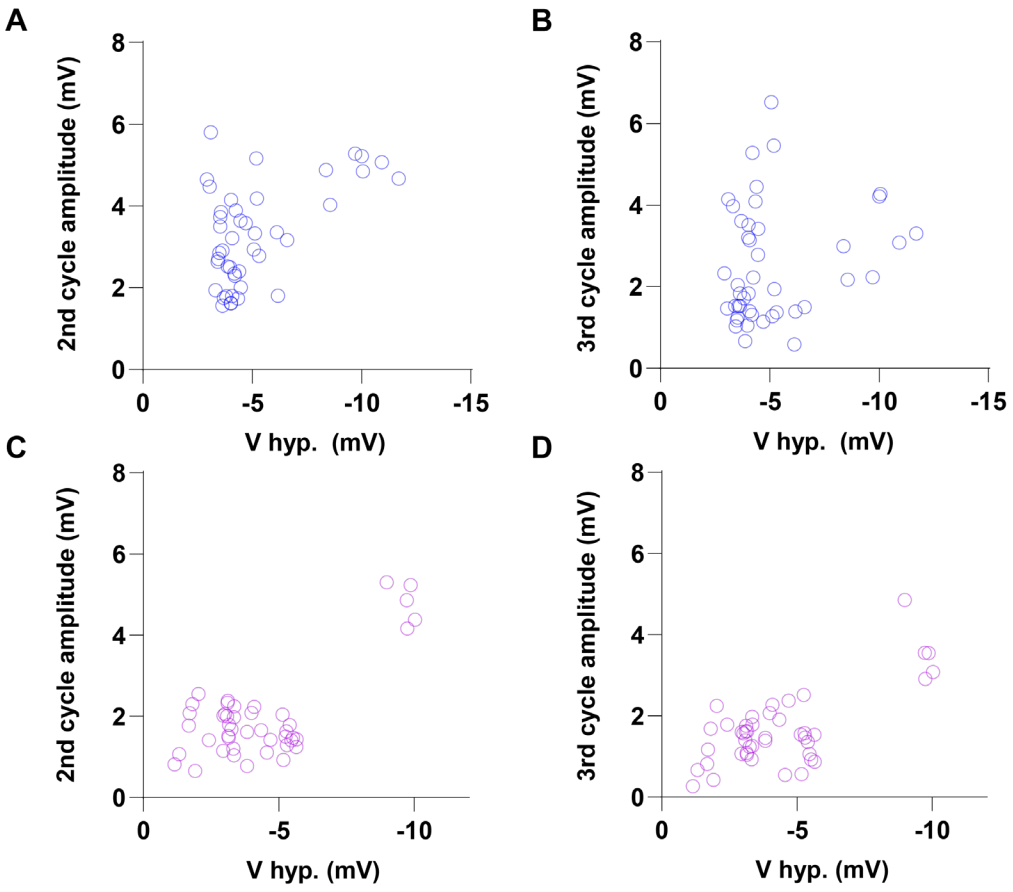

Supplemental Figure 4. Impact of subthreshold synaptic responses on IO conditional oscillators. A, Oscillation amplitudes of 2nd cycle post-stimulus as a function of $V_{hyp.}$ of MDJ synaptic response. B, Oscillation amplitudes of 3rd cycle post-stimulus as a function of $V_{hyp.}$ of MDJ synaptic response. C, Oscillation amplitudes of 2nd cycle post-stimulus as a function of $V_{hyp.}$ of CN synaptic response. D, Oscillation amplitudes of 3rd cycle post-stimulus as a function of $V_{hyp.}$ of CN synaptic response. Open circles represent individual trials.

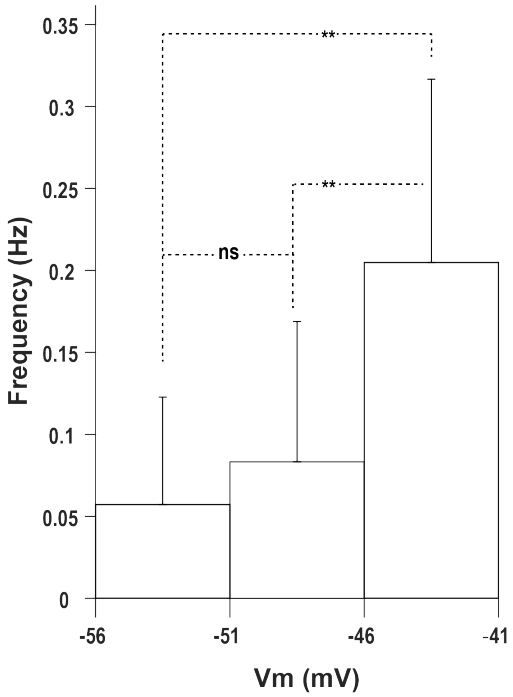

Supplemental Figure 5. Histogram showing the spontaneous spike frequency as a function of membrane voltage (using 5 mV bins). ns = non-significant. ** = p < 0.01. One-way anova test followed by post-hoc Fisher's LSD multiple comparison test.

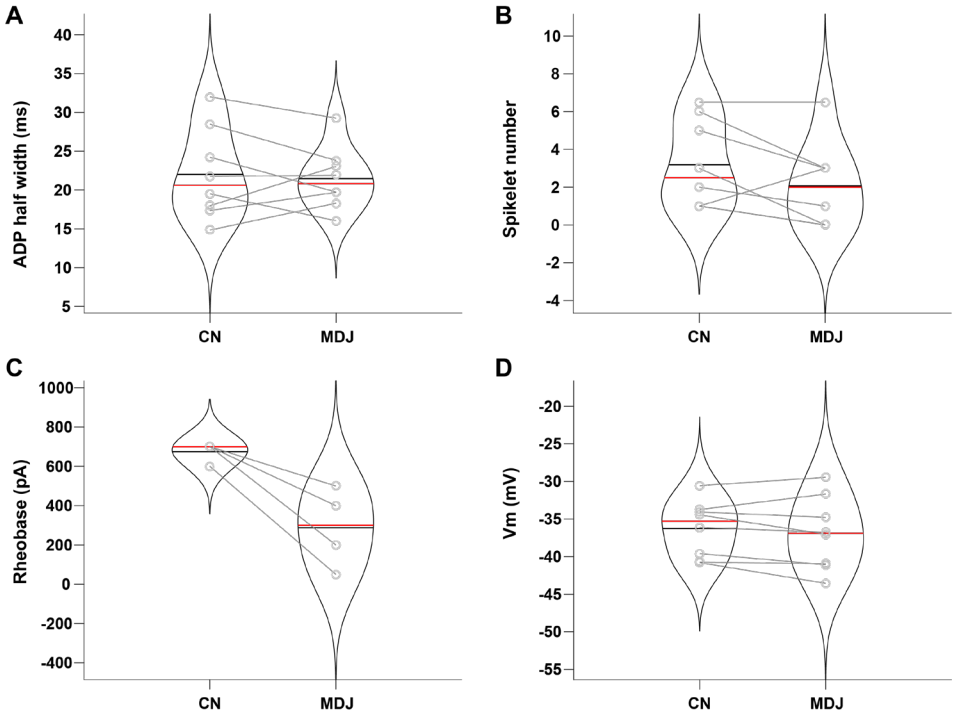

Supplemental Figure 6. Violin plots showing the comparison between suprathreshold responses triggered by CN and MDJ afferent stimulation. A, Half width of the after depolarization component of spikes elicited by IO neurons. B, Spikelet number. C, Rheobase. D, Pre-stimulus membrane voltage of traces used to elicit spikes. Red Line indicates the mean and the red line the median. In A,B and D each pair of open gray circles connected by a line represent trials of a particular neuron in which were used the same amount of current injection whereas in C each pair of open gray circles connected by a line represent one neuron.

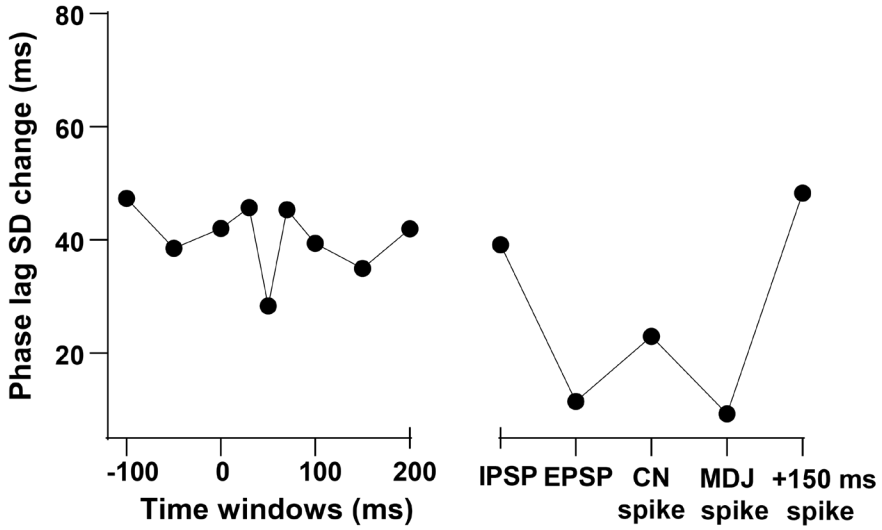

Supplemental Figure 7. Change in standard deviation (SD) of phase lags (pre-stimulus SD - post-stimulus SD of each cycle) corresponding to the first three cycles following different stimulation paradigms.

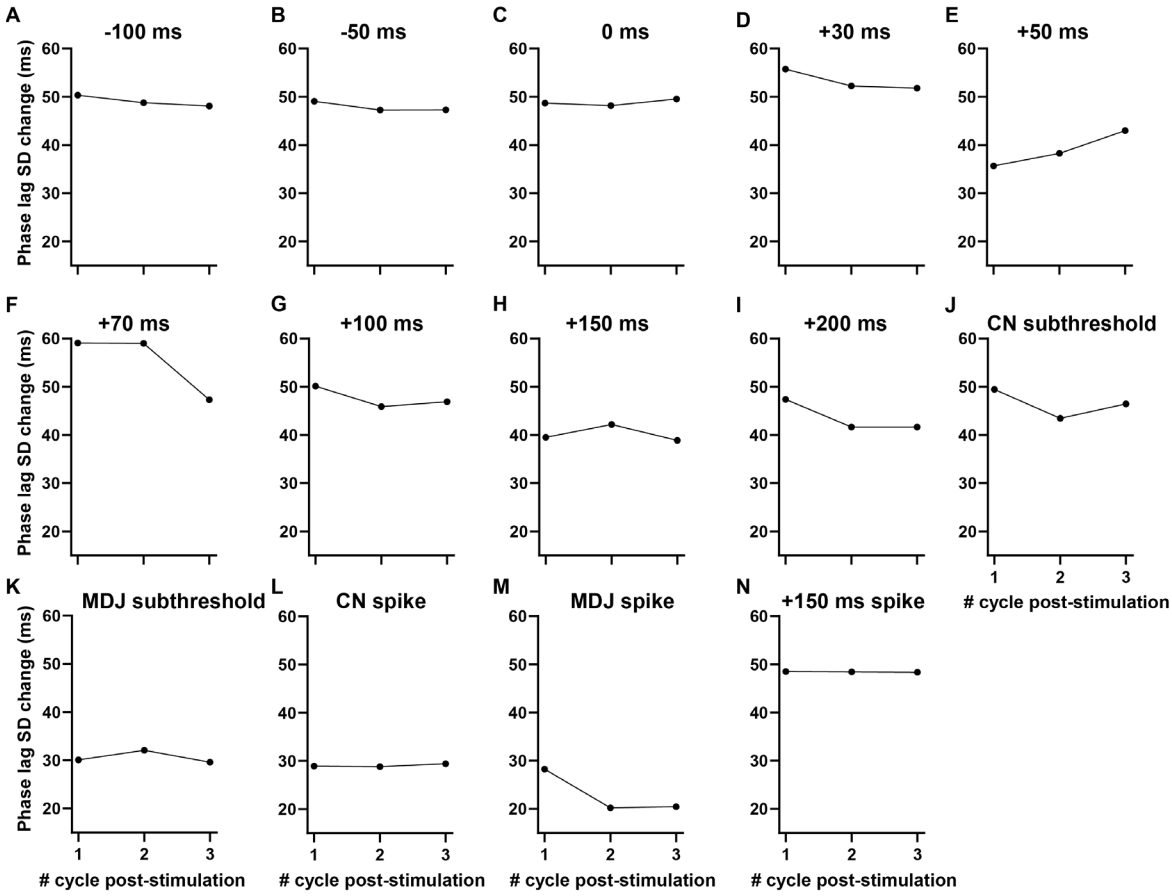

Supplemental Figure 8. Change in standard deviation (SD) of phase lags corresponding to the first three cycles following stimulation (pre-stimulus SD - post-stimulus SD of each cycle). A,-100 ms. B, -50 ms. C, 0 ms. D, +30 ms. E, +50 ms. F, +70 ms. G, +100 ms. H, +150 ms (subthreshold). I, +200 ms. J, CN subthreshold synaptic responses. K, MDJ subthreshold synaptic responses. L, CN Spikes evoked by CN input. M, Spikes evoked by MDJ input. N, Spikes evoked by + 150 ms stimulation.

Mice showing IO colabelling (I Ind: +150 ms, II Ind: +50 ms, III Ind: +150 ms)

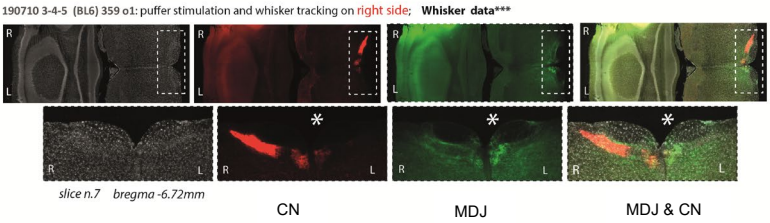

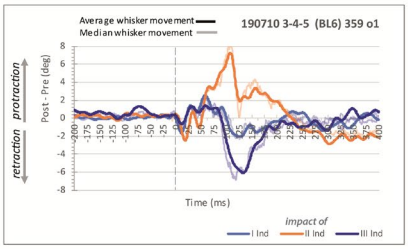

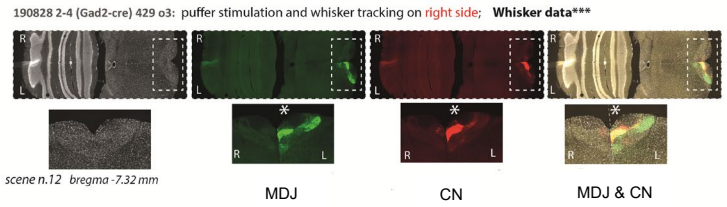

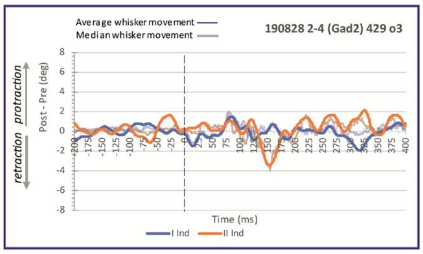

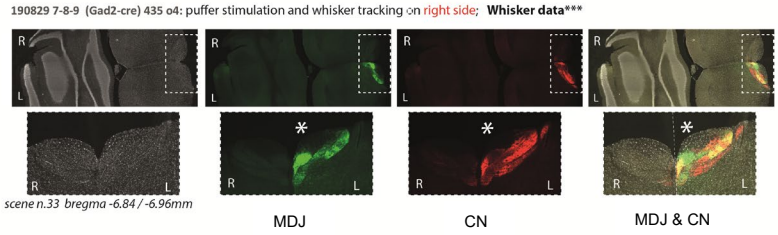

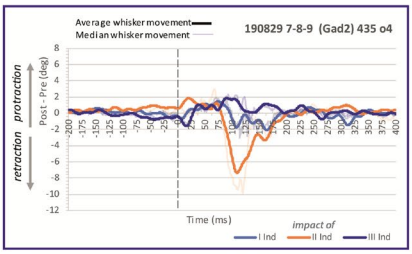

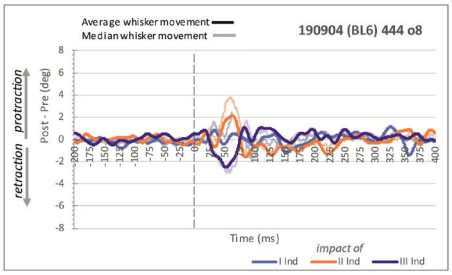

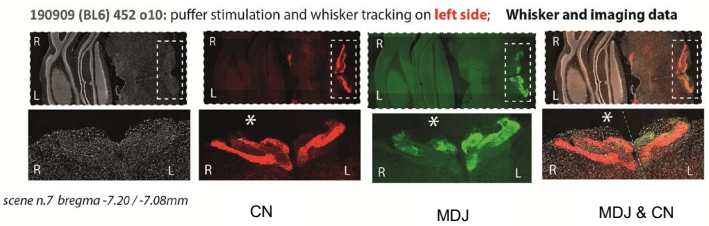

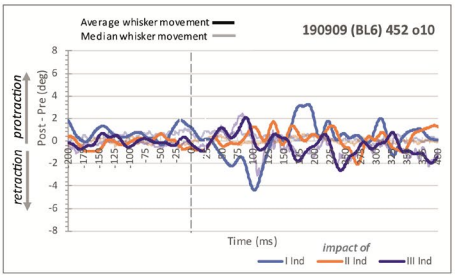

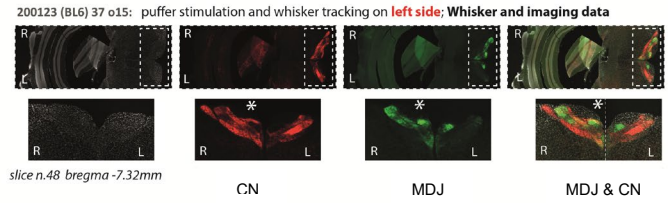

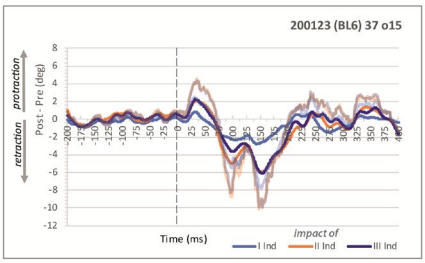

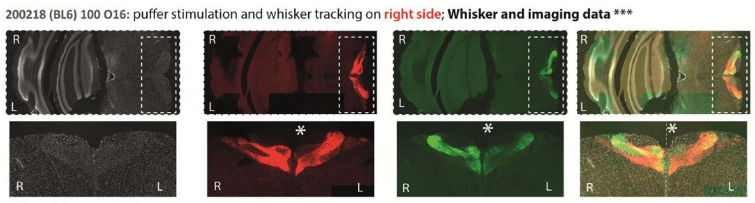

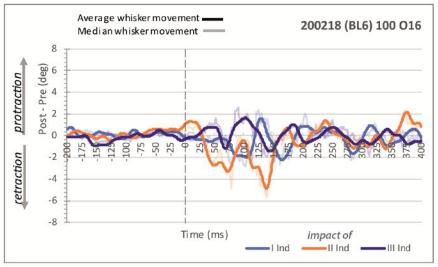

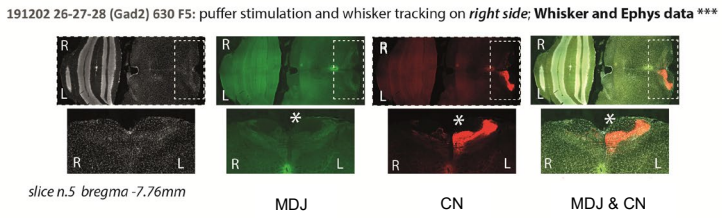

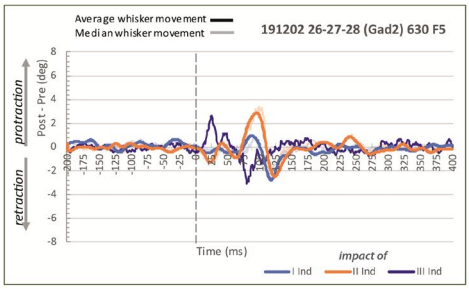

Mice showing IO colabelling (I Ind: +50 ms, II Ind: +150 ms, III Ind: +50 ms)

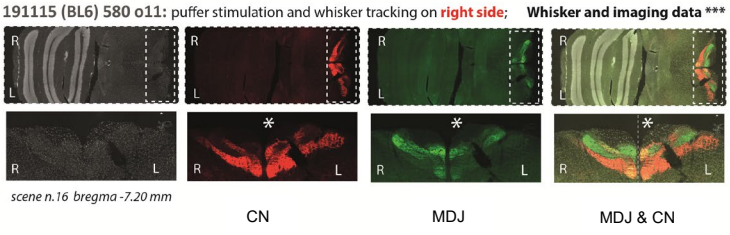

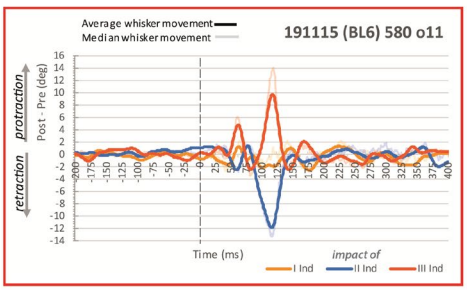

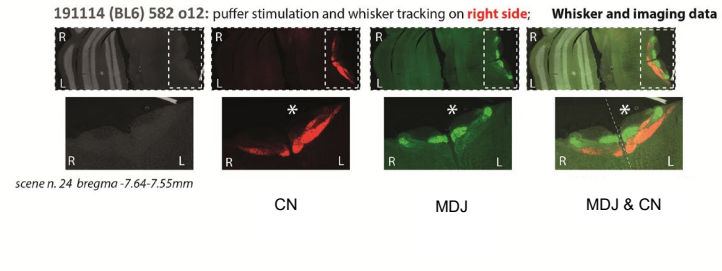

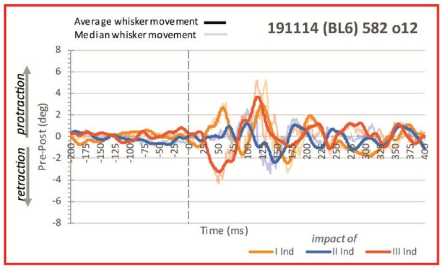

Mice showing no IO colabelling (I Ind: +150 ms, II Ind: +50 ms, III Ind: +150 ms)

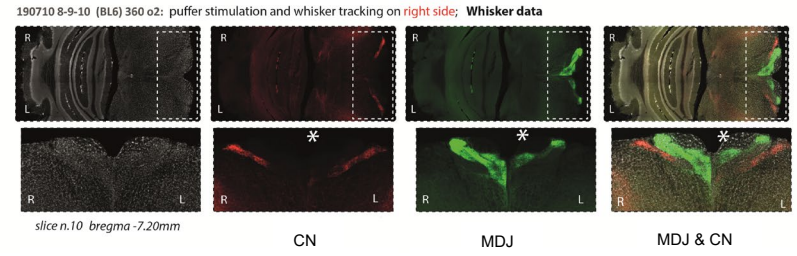

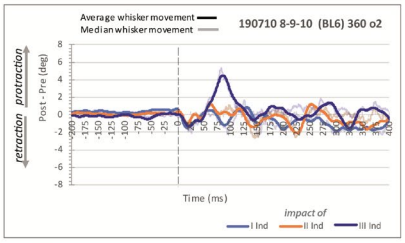

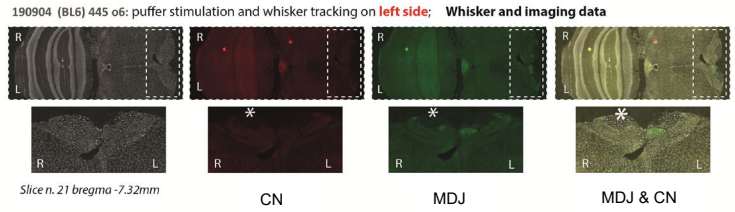

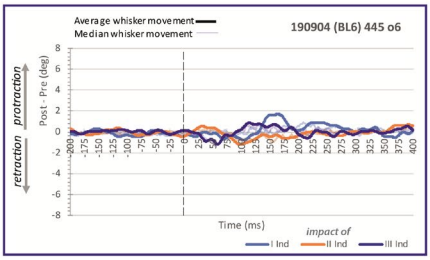

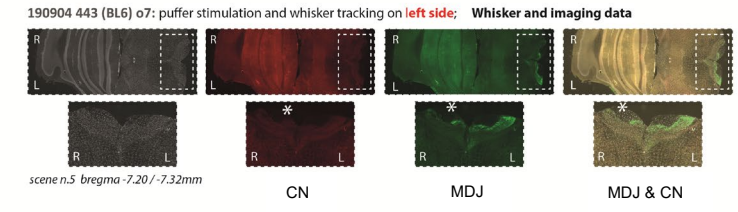

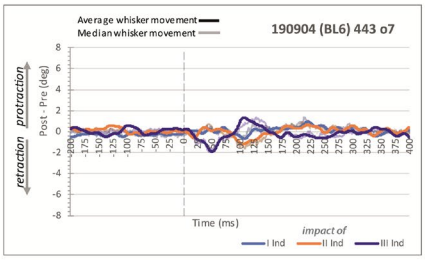

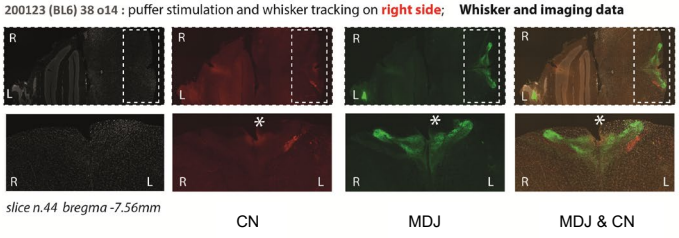

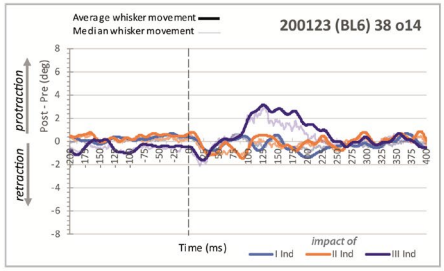

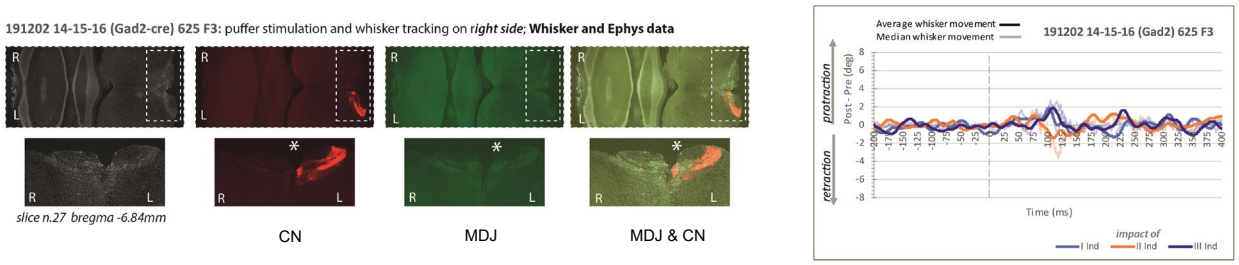

Mice showing no IO colabelling (I Ind: +50 ms, II Ind: +150 ms, III Ind: +50 ms)

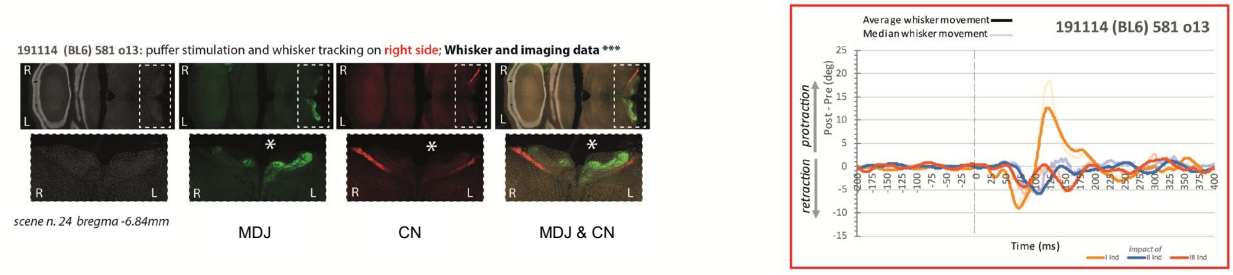

Supplemental figure 9. Histology and behavior obtained from mice subjected to whisker-reflex learning paradigm. Left: Coronal IO sections showing MDJ labelling (Chronos-GFP, green), CN labelling (Chrimson-tdTomato, red) and Colabelling (yellow). Asterisks indicate the contralateral IO side with respect to the puff stimulation and whisker tracking. Right: Plot showing the protraction (positive deflection) or retraction (negative deflection) of the whiskers following double optogenetic stimulation (time zero) at either +150 ms or +50 ms. At the bottom of every subdivision of experiments is indicated the details of the injections, type of labelling observed and sequence of the time intervals used for stimulation. Only animals injected with Channelrhodopsin-2 / GFP in the MDJ were animals Fio3 and Fio5.

Supplementary tables

Half-width (ms)	V hyp.	V reb.
Chrimson Mean ± SD	73.59 ± 14.97	79.74 ± 33.09
GAD2Cre Mean ± SD	77.89 ± 7.49	82.98 ± 17.79

Supplemental Table 1. Half-width of each of the synaptic components of CN synaptic response using mice transduced with Chrimson-tdTomato in the CN and GAD2Cre/Chr2-H134R-EYFP transgenic mice line.

Type of stimulation	Latency (ms)
Chrimson Mean ± SD	14.35 ± 6.74
GAD2Cre Mean ± SD	29.33 ± 10.08

Supplemental Table 2. Latency of CN synaptic response using mice transduced with Chrimson-tdTomato in the CN and GAD2Cre/Chr2-H134R-EYFP transgenic mice line.

Half width (ms)	Vdep	Vhyp	Vreb
Electrical Mean ± SD	12.06 ± 3.06	78.93 ± 11.09	79.16 ± 14.98
Optogenetic Mean ± SD	11.86 ± 5.03	80.90 ± 19.39	86.13 ± 12.96

Supplemental Table 3. Half-width of each of the synaptic components of MDJ synaptic response using electrical and optogenetic stimulation.

Type of stimulation	Latency (ms)
Electrical Mean ± SD	0.57 ± 0.23
Optogenetic Mean ± SD	2.26 ± 0.42

Supplemental Table 4. Latency of MDJ synaptic response using electrical and optogenetic stimulation.

Stimulation	Slope ± Std. Error	Intercept ± Std.Error	R^2	Number of cells
-100 ms	-0.49 ± 0.16	-0.16 ± 0.16	0.69	6
-50 ms	-0.41 ± 0.15	-0.11 ± 0.15	0.44	6
0 ms	-0.56 ± 0.16	0.08 ± 0.16	0.88	5
+30 ms	-0.53 ± 0.16	0.02 ± 0.16	0.78	4
+50 ms	-0.51 ± 0.16	0.02 ± 0.16	0.74	6
+70 ms	-0.45 ± 0.18	0.05 ± 0.18	0.5	5
+100 ms	-0.48 ± 0.18	0.09 ± 0.18	0.71	5
+150 ms	-0.69 ± 0.23	0.35 ± 0.23	0.61	7
+200 ms	-0.51 ± 0.17	0.08 ± 0.17	0.74	4
IPSP	-0.52 ± 0.17	0.07 ± 0.17	0.86	5
MDJ Spike	-0.50 ± 0.19	0.09 ± 0.19	0.82	5
CN spike	-0.54 ± 0.04	0.15 ± 0.02	0.78	8
+150 ms Spike	-0.66 ± 0.19	0.33 ± 0.19	0.72	7

Supplemental Table 5. Slope, Y-intercept, and R^2 of PRCs generated by dual stimulation at different time intervals and single input stimulation.

Fisher's LSD	Mean Diff.	95.00% CI of diff.	Significant?	Summary	Individual P Value
+ 150 ms vs. -100 ms	-0.203	-0.3058 to -0.1002	Yes	***	0.0001
+ 150 ms vs. -50 ms	-0.2849	-0.3877 to -0.1821	Yes	****	<0.0001
+ 150 ms vs. 0 ms	-0.1307	-0.2392 to -0.02220	Yes	*	0.0183
+ 150 ms vs. +30 ms	-0.168	-0.2746 to -0.06144	Yes	**	0.002
+ 150 ms vs. +50 ms	-0.182	-0.2753 to -0.08875	Yes	***	0.0001
+ 150 ms vs. +70 ms	-0.2386	-0.3407 to -0.1365	Yes	****	<0.0001
+ 150 ms vs. +100 ms	-0.2175	-0.3215 to -0.1135	Yes	****	<0.0001
+ 150 ms vs. +200 ms	-0.188	-0.2937 to -0.08234	Yes	***	0.0005
+ 150 ms vs. IPSP	-0.1688	-0.2599 to -0.07774	Yes	***	0.0003
+ 150 ms vs. MDJ spike	-0.1931	-0.2897 to -0.09647	Yes	****	<0.0001
+ 150 ms vs. CN spike	-0.1511	-0.2808 to -0.02137	Yes	*	0.0225
+ 150 ms vs. +150 ms spike	-0.0289	-0.1350 to 0.07720	No	ns	0.5931

Supplemental Table 6. Comparison of PRC slopes between +150 ms and the other time intervals and single sub- and suprathreshold synaptic responses using one-way anova test followed by post-hoc Fisher's LSD multiple comparison test.

Fisher's LSD	Mean Diff.	95.00% CI of diff.	Significant?	Summary	Individual P Value
+ 150 ms vs. -100 ms	0.5216	0.4637 to 0.5795	Yes	****	<0.0001
+ 150 ms vs. -50 ms	0.4647	0.4068 to 0.5226	Yes	****	<0.0001
+ 150 ms vs. 0 ms	0.2699	0.2087 to 0.3310	Yes	****	<0.0001
+ 150 ms vs. +30 ms	0.3317	0.2717 to 0.3917	Yes	****	<0.0001
+ 150 ms vs. +50 ms	0.3324	0.2799 to 0.3849	Yes	****	<0.0001
+ 150 ms vs. +70 ms	0.3021	0.2446 to 0.3596	Yes	****	<0.0001
+ 150 ms vs. +100 ms	0.2582	0.1996 to 0.3167	Yes	****	<0.0001
+ 150 ms vs. +200 ms	0.2648	0.2053 to 0.3243	Yes	****	<0.0001
+ 150 ms vs. IPSP	0.2798	0.2285 to 0.3311	Yes	****	<0.0001
+ 150 ms vs. MDJ spike	0.2551	0.2006 to 0.3095	Yes	****	<0.0001
+ 150 ms vs. CN spike	0.1934	0.1203 to 0.2665	Yes	****	<0.0001
+ 150 ms vs. +150 ms spike	0.0229	-0.03688 to 0.08268	No	ns	0.4524

Supplemental Table 7. Comparison of PRC Y-intercepts between +150 ms and the other time intervals and single sub- and suprathreshold synaptic responses using one-way anova test followed by post-hoc Fisher's LSD multiple comparison test.

Stimulation	SD phase lag pre-stimulus (ms)	SD phase lag post- stimulus (ms)	$\Delta SD_{pre\text{-}post}$	Number of cells
-100 ms	60.84	13.47	47.37	10
-50 ms	58.39	19.86	38.53	13
0 ms	56.87	14.84	42.03	14
+30 ms	62.36	16.61	45.74	17
+50 ms	64.84	36.48	28.35	35
+70 ms	73.352	28	45.34	17
+100 ms	57.51	18.13	39.38	16
+150 ms	49.17	14.88	34.98	10
+200 ms	52.61	10.62	41.99	10
IPSP	59.51	20.35	39.16	15
EPSP	56.47	44.97	11.4989	15
MDJ Spike	51.92	36.05	9.293	8
+150 ms Spike	51.47	3.21	48.2587	7
CN spike	61.05	38.1	22.95	7

Supplemental Table 8. Standard deviation (SD) of phase lags pre- and post-stimulus at different time intervals of stimulation and single input stimulation.

Time interval	Dunn's test	Rank sum diff.	Significant?	Summary	Individual P Value
-100 ms	Δ Pre stim STO average vs. Post stim STO 1st peak	-276	Yes	****	<0.0001
-50 ms	ΔPre stim STO average vs. Post stim STO 1st peak	-346	Yes	****	<0.0001
0 ms	ΔPre stim STO average vs. Post stim STO 1st peak	-396	Yes	****	<0.0001
+30 ms	ΔPre stim STO average vs. Post stim STO 1st peak	-402	Yes	****	<0.0001
+ 50ms	ΔPre stim STO average vs. Post stim STO 1st peak	-452	Yes	****	<0.0001
+70 ms	ΔPre stim STO average vs. Post stim STO 1st peak	-53	No	ns	0.0691
+100 ms	ΔPre stim STO average vs. Post stim STO 1st peak	-440	Yes	****	<0.0001
+150 ms	ΔPre stim STO average vs. Post stim STO 1st peak	-307	Yes	****	<0.0001
+200 ms	ΔPre stim STO average vs. Post stim STO 1st peak	-367	Yes	****	<0.0001

Supplemental Table 9. Comparison between STO amplitude change of the 1st cycle (rebound component) following stimulation at different time intervals and STO amplitude previous to stimulation using Kruskal-Wallis test followed by post-hoc uncorrected Dunn's multiple comparison test.

Stimulation	STO amplitude change of 1st cycle post-stim ± SD (mV)	Number of cells
-100 ms	6.18 ± 4.98	10
-50 ms	5.53 ± 5.03	13
0 ms	4.80 ± 4.32	14
+30 ms	3.66 ± 2.98	16
+50 ms	1.83 ± 3.42	34
+70 ms	0.48 ± 2.59	17
+100 ms	6.48 ± 3.47	16
+150 ms	7.25 ± 3.45	10
+200 ms	4.08 ± 2.05	10
IPSP	4.82 ± 3.70	23
EPSP	1.52 ± 3.04	26
MDJ Spike	6.75 ± 4.26	10
CN spike	4.04 ±3.19	6

Supplemental Table 10. STO amplitude change of the 1st cycle following stimulation (rebound component) at different time intervals and single input stimulation using Kruskal-Wallis test followed by post-hoc uncorrected Dunn's multiple comparison test.

Dunn's test	Mean rank diff.	Significant?	Summary	Individual P Value
+150 ms vs. -100 ms	210.8	Yes	**	0.0056
+150 ms vs. -50 ms	253.8	Yes	***	0.0004
+150 ms vs. 0 ms	322	Yes	****	<0.0001
+150 ms vs. +30 ms	468.3	Yes	****	<0.0001
+150 ms vs. +50 ms	713	Yes	****	<0.0001
+150 ms vs. +70 ms	948.5	Yes	****	<0.0001
+150 ms vs. +100 ms	77.03	No	ns	0.2626
+150 ms vs. +200 ms	371.8	Yes	****	<0.0001
+150 ms vs. EPSP	786.8	Yes	****	<0.0001
+150 ms vs. IPSP	328.8	Yes	****	<0.0001

Suplemental table 11. Comparison of first cycle post-stimulus change between the time interval of +150 ms and the other time intervals and single input stimulation using Kruskal-Wallis test followed by post-hoc uncorrected Dunn's multiple comparison test.

Stimulation	P_{spike} ± SD	Number of cells
-100 ms	0.16 ± 0.22	9
-50 ms	0.17 ± 0.26	9
0 ms	0.23 ± 0.39	7
+30 ms	0.05 ± 0.09	7
+50 ms	0.0 ± 0.0	9
+70 ms	0.0 ± 0.0	6
+100 ms	0.08 ± 0.21	8
+150 ms	0.57 ± 0.30	9
+200 ms	0.26 ± 0.22	7
IPSP	0.01 ± 0.03	7
EPSP	0.22 ± 0.28	7

Supplemental table 12. P_{spike} following dual stimulation at different time intervals and single input stimulation.

Fisher's LSD	Mean Diff.	95.00% CI of diff.	Significant?	Summary	Individual P Value
+150 ms vs. -100 ms	0.4111	0.2059 to 0.6164	Yes	***	0.0002
+150 ms vs. -50 ms	0.4	0.1947 to 0.6053	Yes	***	0.0002
+150 ms vs. 0ms	0.3389	0.1336 to 0.5441	Yes	**	0.0015
+150 ms vs. +30 ms	0.5206	0.3012 to 0.7401	Yes	****	<0.0001
+150 ms vs. +50 ms	0.5778	0.3725 to 0.7830	Yes	****	<0.0001
+150 ms vs. +70 ms	0.5778	0.3483 to 0.8073	Yes	****	<0.0001
+150 ms vs. +100 ms	0.4903	0.2787 to 0.7019	Yes	****	<0.0001
+150 ms vs. +200 ms	0.3135	0.09406 to 0.5329	Yes	**	0.0057
+150 ms vs. EPSPs only	0.3563	0.1369 to 0.5758	Yes	**	0.0018
+150 ms vs. IPSP only	0.5635	0.3441 to 0.7829	Yes	****	<0.0001

Supplemental table 13. Comparison of P_{spike} of time interval of +150 ms and all the other time intervals and CN and MDJ subthreshold synaptic responses (named 'IPSP' and 'EPSP', respectively) using one-way anova test followed by post-hoc Fisher's LSD multiple comparison test.

Animals showing colabelling						
Date	**Mouse**	**IPSI IO subnuclei colabelling**	**Contra IO subnuclei colabelling**	**Behaviour 1st pulse +150ms**	**Behaviour 2nd pulse +50ms**	**Behaviour 3rd Pulse +150 ms**
190710	o1	Dorsal cap of kooy a/b MAO	B-nucleus	**Retraction**	**Protraction**	**Retraction**
190828	o3	No	rMAO vl PO	**None**	**Retraction**	**No stimulus presented**
1908029	o4	No	rMAO dl PO Dorsomedial cell column	**None**	**Retraction**	**None**
190904	o8	Dorsomedial cell column	rMAO dl PO	**None**	**Protraction**	**Retraction**
190909	o10	dl PO Dorsomedial cell column	rMAO	**Retraction**	**None**	**None**
200123	o15	No	rMAO vl PO Dorsomedial cell column	**Retraction**	**Retraction**	**Retraction**
200218	o16	rMAO vl PO Dorsomedial cell column	dl PO	**Small retraction followed by protraction**	**Retraction**	**Small retraction followed by protraction**
191202	Fio5	No	rMAO vl PO dl PO	**Protraction followed by retraction**	**Protraction followed by retraction**	**Protraction followed by retraction**
Date	**Mouse**	**IPSI IO subnuclei colabelling**	**Contra IO subnuclei colabelling**	**Behaviour 1st pulse +50ms**	**Behaviour 2nd pulse +150ms**	**Behaviour 3rd Pulse +50 ms**
191115	o11	vl PO Dorsomedial cell column	rMAO Dorsomedial cell column	**None**	**Retraction**	**Protraction**
191114	o12	No	vl PO dl PO	**protraction**	**retraction followed by protraction**	**delayed retraction**
Animals showing NO colabelling						
Date	**Mouse**	**IPSI IO subnuclei colabelling**	**Contra IO subnuclei colabelling**	**Behaviour 1st pulse +150ms**	**Behaviour 2nd pulse +50ms**	**Behaviour 3rd Pulse +150 ms**
190710	o2	No	No	**small retraction**	**small retraction**	**Retraction followed by protraction**
190904	o6	No	No	**protraction**	**None**	**small retraction followed by small protraction**
190904	o7	No	No	**None**	**None**	**small retraction followed by protraction**
200123	o14	No	No	**None**	**None**	**small retraction followed by protraction**
191202	Fio3	No	No	**small protraction**	**None**	**small protraction**
Date	**Mouse**	**IPSI IO subnuclei colabelling**	**Contra IO subnuclei colabelling**	**Behaviour 1st pulse +50ms**	**Behaviour 2nd pulse +150ms**	**Behaviour 3rd Pulse +50 ms**
191114	o13	No	No	**Retraction followed by protraction**	**Retraction**	**small retraction**

Supplemental Table 14. Sumary of the histology and behavior of the mice used for the whisker-reflex learning paradigm. Group on the the top show mice showing colabelling whereas the group below are mice showing no colabelling. It is also speficied the IO subnuclei in which colabelling were found as well as their side with respect to the whisker stimulation side. In both groups, mice below the orange row were subjected to the stimulation sequence of + 150 ms / + 50 ms / + 150 ms, whereas mice below the blue row were subjected to the stimulation sequence of + 50 ms / + 150 ms / + 50 ms.

Appendix

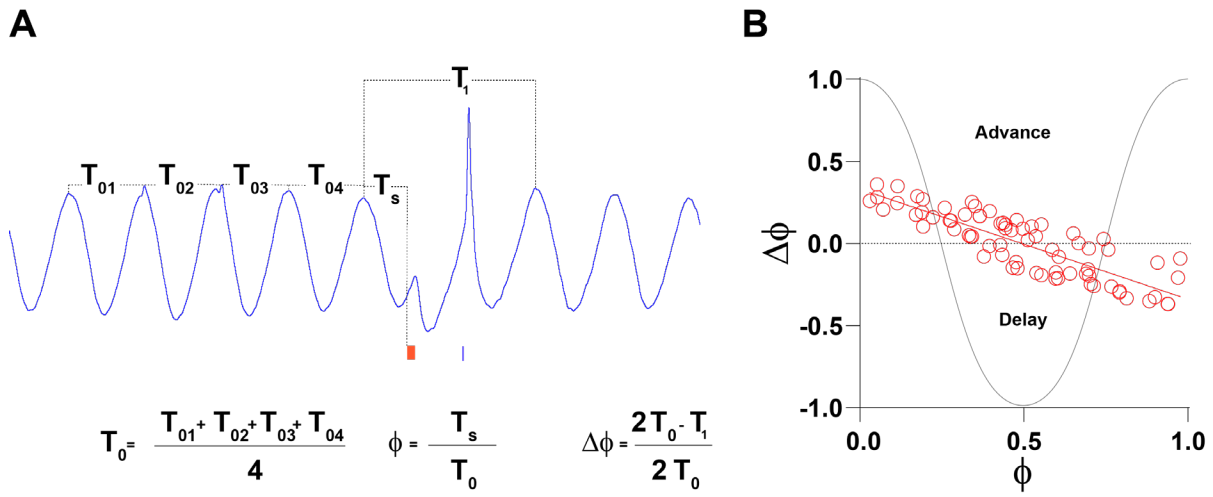

Appendix 1. PRC calculation. A, Period previous to stimulation (T_0) was calculated as the average of 4 periods preceding the stimuli. Period containing the synaptic responses caused by either single or dual stimuli (T_1) was calculated as the period from the peak cycle before stimulation to the peak cycle following the rebound peak caused by either single or dual stimulus. Time at which stimulation hit the STO (T_s) was calculated as the period from the peak cycle before stimulation to the onset of the first stimulus. B, PRC curve in which changes in the period containing the synaptic responses with respect to the period previous to stimulation (ΔΦ) is plotted against the phase at which stimulus hit the STO (Φ). Based in our convention shown in the formulas of panel a, positive ΔΦ values indicate a phase advance (period containing the synaptic response is shorter than previous one) whereas negative ΔΦ values indicate a phase delay (period containing the synaptic response is longer than previous one).

Materials and Methods

Animals

All performed experiments were licensed by the Dutch Competent Authority and approved by the local Animal Welfare Body, following the European guidelines for the care and use of laboratory animals Directive 2010/63/EU.

GAD2-Cre x Ai32 transgenic mice

For a subset of experiments GAD2-Cre animals were crossed with the Ai32 line (#012569, Jackson laboratory, Maine, US) expressing the ChR2(H134R)-EYFP fusion protein to allow selective light-activation of inhibitory nucleo-olivary afferents.

Viral transduction

Animals received bilateral 50-100 nl injections of AAV1-Synapsin-Chronos-GFP in the mesodienchepealic junction (bregma: -2.46 to -2.54, lateral: 0.6 to 0.7, depth: 3.8 to 4 mm) and AAV1-Synapsin-ChrimsonR-tdTomato in the cerebellar nuclei (bregma: -6.1 lateral: 2, depth: 3.3 mm). Virus was injected using a Nanoject II (Drummond Scientific) and glass capillaries (3-000-203-G/X, Drummond Scientific) backfilled with mineral oil. The virus was injected at 24.7 nl/s four times spaced at intervals spaced one minute apart. The pipette was slowly retracted over the course of 5 minutes after the last of the four injections. Injected animals were not used in experiments until at least 4 weeks after injection.

In vitro slice electrophysiology

Brainstem sagittal sections (300 µm) were cut in ice-cold cutting solution (in mM: 252 Sucrose, 5 KCl, 1.25 NaH_2PO_4, 26 $NAHCO_3$, 10 Glucose, 0.5 $CaCl_2$, 3.5 $MgSO_4$, pH=7.4) of mice (1-3 months) using a vibratome (Microm HM 650V, Thermo scientific).Slices were then transferred to a slice chamber with ACSF (in mM: 126 NaCl, 3 KCl, 1.2 kH_2PO_4, 26 $NaHCO_3$, 10 Glucose, 2.4 $CaCl_2$, 1.3 $MgSO_4$, pH = 7.4) in a water bath and kept first for 30 minutes at 34 ℃ and then 30 minutes at room temperature prior to use. Experiments were performed at 32 ℃. Fire-polished patch pipettes (4-5 MΩ) were backfilled with internal solution (in mM: 140 K-Gluconate, 4 NaCl, 0.5 CaCl2, 5 EGTA, 4 Mg-ATP, 10 Hepes, pH=7.2, osmolarity: 290 mOsm). Data were acquired using a multiclamp 700B patch clamp amplifier and digitized at 50 kHz using a 1440A digidata digitizer. Giga-seals were obtained in voltage-clamp configuration. After break-in current-clamp was used to monitor membrane voltage fluctuations.

Pharmacology

Stocks of CNQX (20 mM, Hello Bio #HB0205-50mg) and D-APV (50 mM, Hello Bio #HB0225-50mM) were prepared in water whereas Picrotoxin (100 mM, Sigma #P1675-5G) was prepared in DMSO in order to be dissolved in 100 ml of ACSF to reach concentrations of 20 µM, 50 µM and 100 µM, respectively. Drugs were perfused for at least 15 minutes prior to recording of synaptic responses.

Neuron labeling

Neurons were labeled by adding 0.5% (w/v) biocytin (Sigma) into the internal solution. Once the experiment was completed, patch-pipette was withdrawn carefully in order to reseal the neuronal membrane. Brainstem slices were then fixed overnight in 0.1M PBS containing 4% PFA. After the fixing period, they were washed three times in 0.1M PB (10 minutes per wash at 4°C) and then incubated with Alexa Fluor 594 or 633- conjugated streptavidin (Life technologies, 2mg/ml) in 0.1M PB containing 0.6% Triton X-100. The choice of the fluorophore depended on whether the experiments were carried out in either transgenic or viral transduced animals, respectively. Finally, slices were washed three times in 0.1M PB (10 minutes per wash at 4°C), mounted with Dako glycergel fluorescence mounting medium (RI 1.47-1.50; Dako) and coverslipped.

Images of labeled neurons and olivary afferents were obtained using confocal microscopy (Leica SP8). High magnification image stacked were obtained with 40 or 63X plan-Apochromat objectives at high resolution (ranged from 0.11 - 0.38 µm/pixel in the XY plane and 0.1 - 0.5 µm /z step).

Electrical stimulation

Bipolar stimulation electrodes were placed at the rostral border of the olivary subnucleus in order to stimulate the descending pathways originating from the mesodiencephalic junction (medial and central tegmental tracts). Brief 100 µs current pulses of 0.3 to 1.2mA were applied using an ISO-flex stimulus isolator.

In vitro optogenetics

We used a three-wavelength microscopy LED system in combination with a control box (Mightex Systems, Toronto) exciting chronos at 470 nm and ChrimsonR at 625 nm using TTL pulse triggering. Slices were illuminated through a 40 x objective (N.A.=0.5, Zeiss).

Data analysis

Data were analyzed using Clampfit 11.0.3 and custom scripts written in Matlab. All data and charts are expressed as Mean ± Standard deviation.

Phase response curve: Please refer to appendix 1.

Phase lag distribution: Phases were extracted using DAMOCO MatLab toolbox, then phase lags were calculated across trials for three cycles before and after stimulation using custom script written in MatLab.

Statistics

All statistical analysis were performed in GraphPad Prism 8.3.0. In order to test whether the data was normally distributed, D'Agostino-Pearson omnibus normality test was performed. For comparisons of two groups showing normally distributed data, unpaired or paired t-test was performed, whereas for comparison of two groups showing non-normally distributed data, Mann-Whitney U test or Wilcoxon matched-paired rank test was performed depending if data was unpaired or paired, respectively. When multiple groups normally distributed were compared, One-Way ANOVA test followed by post-hoc Fisher's LSD multiple comparison test was used. When multiple groups were not normally distributed, Kruskal-Wallis test followed by post-hoc Dunn's test was used. To determine whether the slope and intercept of two linear regressions were significantly different ANCOVA test was used, whereas for multiple comparisons one-way ANOVA test followed by post-hoc Fisher's LSD multiple comparison test was used. ANCOVA test was used to determine whether phase lags distributions pre and post stimulation were significantly different. For all the aforementioned tests, P values below 0.05 were considered statistically significant.

In vivo optogenetics

Custom probes were fabricated with two μLEDs (230 μm on a side) emitting at 470 and 625 nm respectively (Chips4Light) and flexible wires of 160 μm thickness. The LEDs were controlled and powered using a modified Arduino DUE board.

The probes were inserted after the ventral surgery described below. Prior to the ventral incision, a small incision was made to guide the probe under the skin. The probe was pulled until it reached the ventral surface of the neck. After exposing the neck the probe was placed directly above the

olive and embedded in a drop of slicone elastomer (Kwik-Sil, WPI). The muscles were then released to cover the probe end. A probe connector was attached to the head of the skull of the animal with dental cement (Super-Bond C&B, Sun-Medical).

Ventral approach surgery

To implant custom optogenetic probes with µLEDs above the inferior olive a small incision was first made in the dorsal neck for routing the probe underneath the skin to the site of the ventral implantation. A longitudinal ventral incision was made that extended from just below the jaw to the clavicles. The animal was put on it side and a blunt tipped forceps was used to guide the probe -under constant superfusion of sterile saline- subcutaneously to the side of the ventral incision. The probe connector was sutured using a U-stitch to the skin of the dorsal neck. Vetbond was applied to cover the dorsal suture and aid healing of the skin. The animal was then turned belly side up with the head at a slight backward inclination and the area was continuously rinsed with sterile saline. The salivary glands were pulled aside and held in place with hooks made out of bent and blunt syringe needles. Neck muscles were gently pulled apart taking care not to cause damage to the carotid artery and right vagal nerve. The artery and nerve were carefully pulled to the right side of the opening in the neck and the m. sternocephalicus covering trachea and esophagus were pulled to the left. A final set of m. longus capitis connected by connective tissue were pulled aside to reveal the membrana atlantoöccipitalis anterior, which was removed by scraping at the level of the occipital bone with a needle. The probe was inserted in a secure position with the LED dies facing downward. A drop of Kwik-Sil (WPI) was then deposited around the probe to provide extra stability. Subsequently the muscles were gently released into their original position taking care to cover the LED probe.

Whisker Stimulation and tracking

Air-puff stimulation was delivered to the whisker pad by a tube with a diameter of roughly 1mm located at an angle of approximatety 35˚ with respect to the body axis. The puffs had a pressure of 2 bar roughly and a duration of 30 ms. During the induction period, consisting of 4Hz stimulation for 20 s, air puffs were delivered in conjunction with MDJ afferents optogenetic stimulation either 50 ms or 150 ms following CN stimulation. Wavelength of 625 nm and a pulse duration of 20 ms was used to stimulate CN afferents whereas a wavelength of 470 nm and a pulse duration of 5 ms was used to stimulate the MDJ afferents.

Histology

Following the behavioral experiments, mice were perfused with 4% PFA an then 100 µm coronal sections of the brainstem were obtained. MDJ afferents expressing Chronos-GFP and CN afferents expressing Chrimson-TdTomato were visualized in the IO using confocal microscopy (Leica SP8) . High magnification images were obtained using 10X objective plan-Apochromat at high resolution.

Chapter 4

Sleep stage dependent modulation of complex spike ensemble activity

Sebastián Loyola, Tycho Hoogland, Cathrin Canto, Hugo Hoedemaker
Chris De Zeeuw

Abstract

Sleep is a ubiquitous animal behavior integral to a diverse set of physiological functions that are necessary for an animal's survival. Brain-wide changes occur during sleep and various studies have described the contribution of cortical and subcortical regions to various aspects of sleep. The physiological changes that occur in the cerebellum during sleep are less well understood relying on only a handful of undersampled studies with sometimes contradictory results. Cerebellar loss-of-function disrupts sleep patterns and sleep disruption interferes with cerebellar learning suggesting an integral role for the cerebellum in the regulation of sleep. Nevertheless it remains unknown how the activity of ensembles of cerebellar neurons changes across the different sleep stages. Here, we addressed how sleep modulates activity in the olivocerebellar loop by monitoring complex spikes in Purkinje cell dendrites using a combination of miniaturized fluorescence microscopes, electromyograph (EMG) as well as cortical electroencephalogram (EEG) and hippocampal LFP recordings. We find that sleep is associated with significant changes in complex spike firing, complex-spike evoked calcium transients, co-activation rates and pairwise correlations within a cerebellar microzone during sleep. Motor twitches coincided with triggered calcium transients in Purkinje cell dendrites across all sleep stages, but dropped in frequency from the wake to sleeping states. The modulation of excitability of the olivocerebellar circuit during sleep is likely to have a significant impact on the consolidation of motor memories.

Introduction

All vertebrates sleep and invertebrates also display periods of inactivity (Miyasaki et al., 2017, Keen and Doboue, 2018). Sleep is required for the clearing of metabolic waste, synapse pruning and the consolidation of memories and in humans cognitive performance is strongly impaired following sleep deprivation (Xie et al., 2013; Li et al., 2017; Basedovsky et al., 2019; Klinzing et al., 2019; Scammel et al., 2017). Sleep is therefore essential for the survival of animals. Neural correlates of sleep have been widely documented in the cerebral cortex and various subcortical brain regions (Ji and Wilson, 2007; Saper et al., 2005; Monti, 2011; Sullivan et al., 2014; Cox et al., 2016; Nagai et al., 2017). How the physiology of the cerebellum is affected during sleep has not been fully resolved (Canto et al. 2017), although cerebellar loss-of-function has been associated with disrupted sleep patterns (Sonni et al., 2014, Del Rosso and Hoque, 2014) and sleep disruption itself affects cerebellar learning (De Zeeuw and Canto, 2020). The pons, which gives rise to the mossy fiber pathway (Cicirata et al., 2005) one of the major afferent pathways to the cerebellum and whose ventral part has been implicated in the generation of eye movements during REM sleep, shows strong modulation of responses when transitioning from wakefulness to sleep and vice versa, with inhibitory and excitatory neuron subpopulations showing opposing changes in activity (Cox et al., 2016). Cerebellectomy in cats (Cunchillos and De Andres, 1982) only had a mild impact on the sleep-wake cycle, probably due to the fact that removal of both cerebellar cortex and the cerebellar nuclei has a smaller net effect than only removing the inhibitory drive of the cerebellar cortex. By contrast, direct recordings from cat cerebellum revealed modulation during synchronized (NREM) and desynchronized (REM) sleep states in Purkinje cell simple and complex spiking (Marchesi and Strata, 1971). Complex spike firing during REM sleep displayed increases in the absence of eye movement and decreases when eye movements were present. A contrasting study in macaques failed to find such a distinction (Mano, 1970) and instead found a reduced rate of complex firing during both NREM and REM stages of sleep in a select set of eight Purkinje cells. Later follow up studies in cat cerebellum revealed mostly a suppression of simple spikes and complex spikes during NREM stages of sleep and an increase during REM sleep that was partially attributable to eye movements. A recent study presented the first cerebellar electrophysiological recordings during sleep in mice (Zhang et al., 2020). Purkinje cell activity displayed an overall decrease during both NREM and REM sleep, but in contrast to previous studies no modulation of complex spike activity was found. Moreover, none of the aforementioned work has clearly distinguished modulation of cerebellar Purkinje cell activity across the different stages of NREM sleep. Recently developed affordable imaging technologies

(Cai et al. 2016, De Groot et al., 2020) have accelerated the recording of neural circuits with cellular resolution during more natural behavior, while preserving the topology of activity. Here, we utilized miniaturized fluorescence microscopes to image complex spike activity in ensembles of Purkinje cells in the anterior vermis of the cerebellum. Recordings from many hundreds of Purkinje cells reveals that complex spikes are modulated across the different sleep stages both in their rate, amplitude, regularity and levels of co-activation. By imaging cerebellar microzones, we further demonstrate that spatial correlations are affected during sleep. Moreover, we show that twitch-like movements that occur both during NREM and REM sleep all trigger complex spike activity in Purkinje cells. With our work we present the first investigation of cerebellar microzone activity during sleep and set the stage for future dual region imaging experiments that investigate the impact of sleep on functional loops between cerebral cortex and cerebellum

Results

To increase the chance of spontaneous sleep, C57/BL6 mice were placed in a custom modified computer-controlled slowly rotating drum for a period of four hours (Figure 1A) during which the movement kept the animals awake. After this period of sleep deprivation, mice were allowed to sleep and recordings began. An open-source miniaturized fluorescence microscope (Cai et al. 2016) was used to image cerebellar ensemble activity. Both cortical electroencephalogram (EEG) and hippocampal local field potential (LFP) were recorded to monitor sleep stage. A webcam was mounted above the mouse to obtain video recordings of its behavior (Figure 1B). Electromyography (EMG) activity from the neck muscles was recorded to monitor muscle twitches during quiet wakefulness and sleep. The cortical EEG of animals during wakefulness was characterized by high frequency small amplitude waveforms, during NREM1 sleep by the presence of alpha and theta activity, NREM2 by the presence of K complexes and NREM3 by delta range high amplitude slow waves. REM sleep had non-continuous theta band activity of low amplitude. EMG activity was significantly reduced during all sleep stages, with clear movement signatures in the EMG of animals during wakefulness allowing discrimination of wake from REM sleep (Figure 1C).

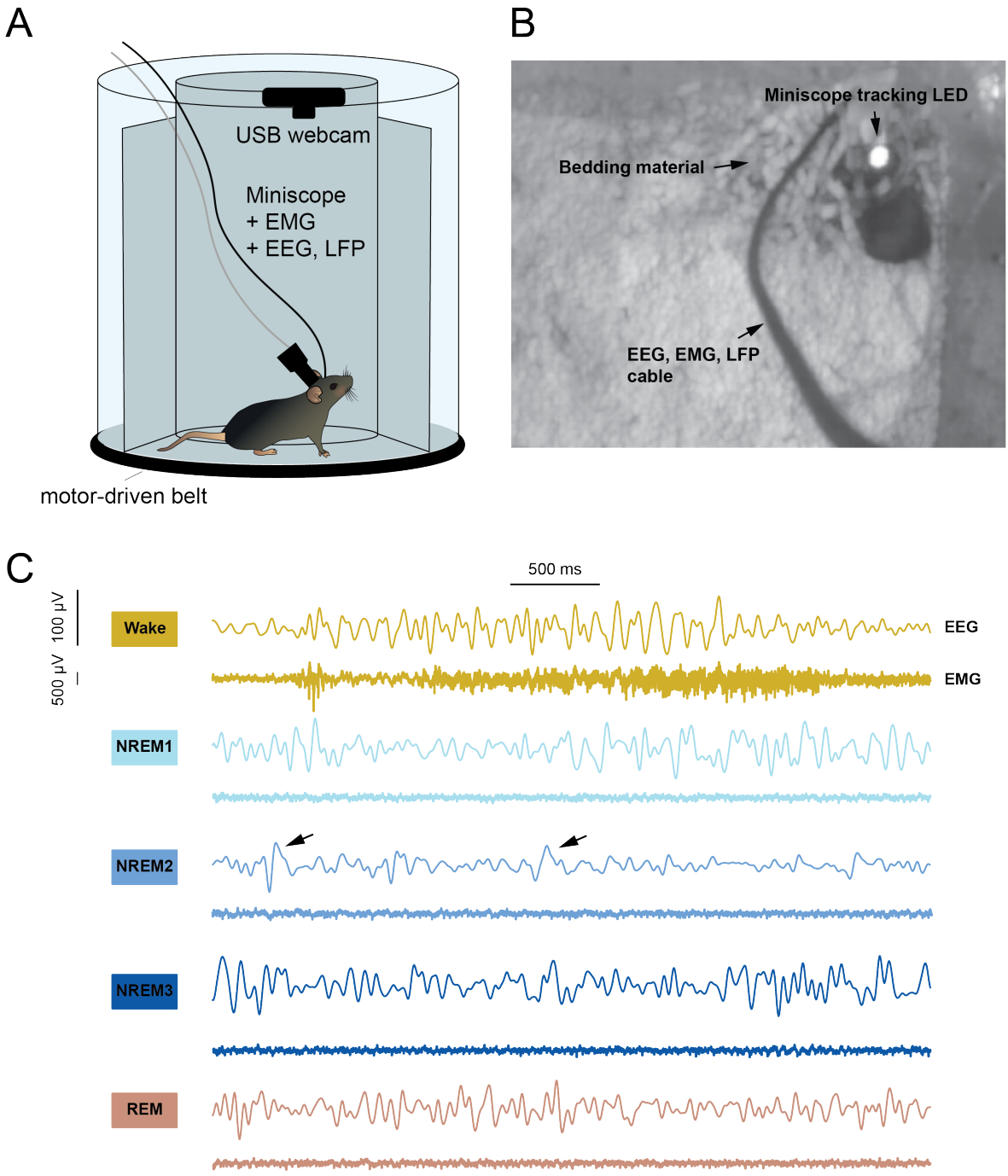

Figure 1, Sleep deprivation and scoring in C57/BL6 mice. A, Setup in which C57BL/6 (N=9) mice were subjected to constant slow rotation for a period of up to four hours to prevent them from falling asleep (for details refer to Materials and Methods). Data was recorded either in the same setup at rest or the home cage with bedding material. B, Webcam video recording used for a maximum image projection over a period of four minutes of a C57/BL6 mouse in its home cage with mounted miniscope and EMG/EEG cable. Note that the tracking LED of the miniscope stayed fixed in one location. C, Sleep was scored in four second epochs using Wonambi software and defined criteria to distinguish wakefulness, three stages of NREM sleep as well as REM sleep. Arrows denote K complexes during NREM2 sleep. EEG (top), EMG (bottom) for all states.

Across all our recordings, mice spent most of their time in NREM2 (49.4%), followed by NREM3 (20.1%), NREM1 (7.3%) and REM (5.3%) sleep. For the remainder of the time (17.9%), mice were in a quiet wakeful state (Figure 2A). Thus the highest fraction of scored sleep was spent in the NREM2 stage (NREM1: 6.5%, NREM2: 60.1%, NREM3: 24.5%, REM: 8.9 %). We performed miniscope imaging experiments from cerebellar lobule IV/V in conjunction with cortical EEG and neck muscle EMG recordings. Purkinje cell dendrites of cerebellar lobule IV/V (Figure 2B) were selectively transduced with the genetically encoded calcium indicator GCaMP6f (Figure 2C). Calcium transients were recorded from individual Purkinje cell dendrites that had large amplitude, fast onset times and kinetics separating them from other sources of calcium entry (Ju et al., 2019). Such transients were clearly resolvable and allowed us to extract complex spike onset times after signal deconvolution (Figure 2D). All data was passed through motion correction using NorMCorre (Pnvematikakis and Giovanucci, 2017) followed by signal extraction using CNMF-E as described previously (De Groot et al., 2020). Cellular resolution imaging of Purkinje cell dendrites allowed us to assess CS activity in dozens of cells at once while preserving the topology of the individual neurons with a field-of-view of 785 by 502 µm. Using our data we extracted 74±21.6 Purkinje cell dendrites on average (range: 44-119, N=9 animals).

A widely used standard in the sleep field is to sample epochs lasting four seconds and score them into sleep states (Moul et al., 2007). We adapted this approach for this study by scoring sleep into four second epochs and subsequently performing analyses on complex spike evoked calcium transient activity within them (Figure 2D, 2E). Transient movements, as found in the EMG recordings of the neck muscles, were associated with clearly discernible increases in complex spike activity during wakefulness (Figure 2E).

Our miniscope recordings from lobule IV/V in C57/BL6 mice (N=9 animals) allowed us to aggregate complex spike rates from many hundreds of Purkinje cell dendrites. During the transition from wake (Wake: 0.95±0.6 Hz, 1363 PC dendrites, mean±SD) to NREM1 sleep (1.0±0.5 Hz, 1277 PC dendrites) complex spike firing rates showed a small but significant increase (Figure 3A). Complex spike rates dropped significantly from NREM1 to NREM2 (0.77±0.5 Hz, 1836 PC dendrites) and NREM3 (0.81±0.5 Hz, 1418 PC dendrites) sleep. Complex spike rates increased to levels indistinguishable from wakefulness during REM sleep (0.94±0.5 Hz, 1498 PC dendrites). Significance was confirmed using a Kruskal-Wallis test comparing among groups followed by a Scheffe's procedure for multiple comparisons (α=0.01).

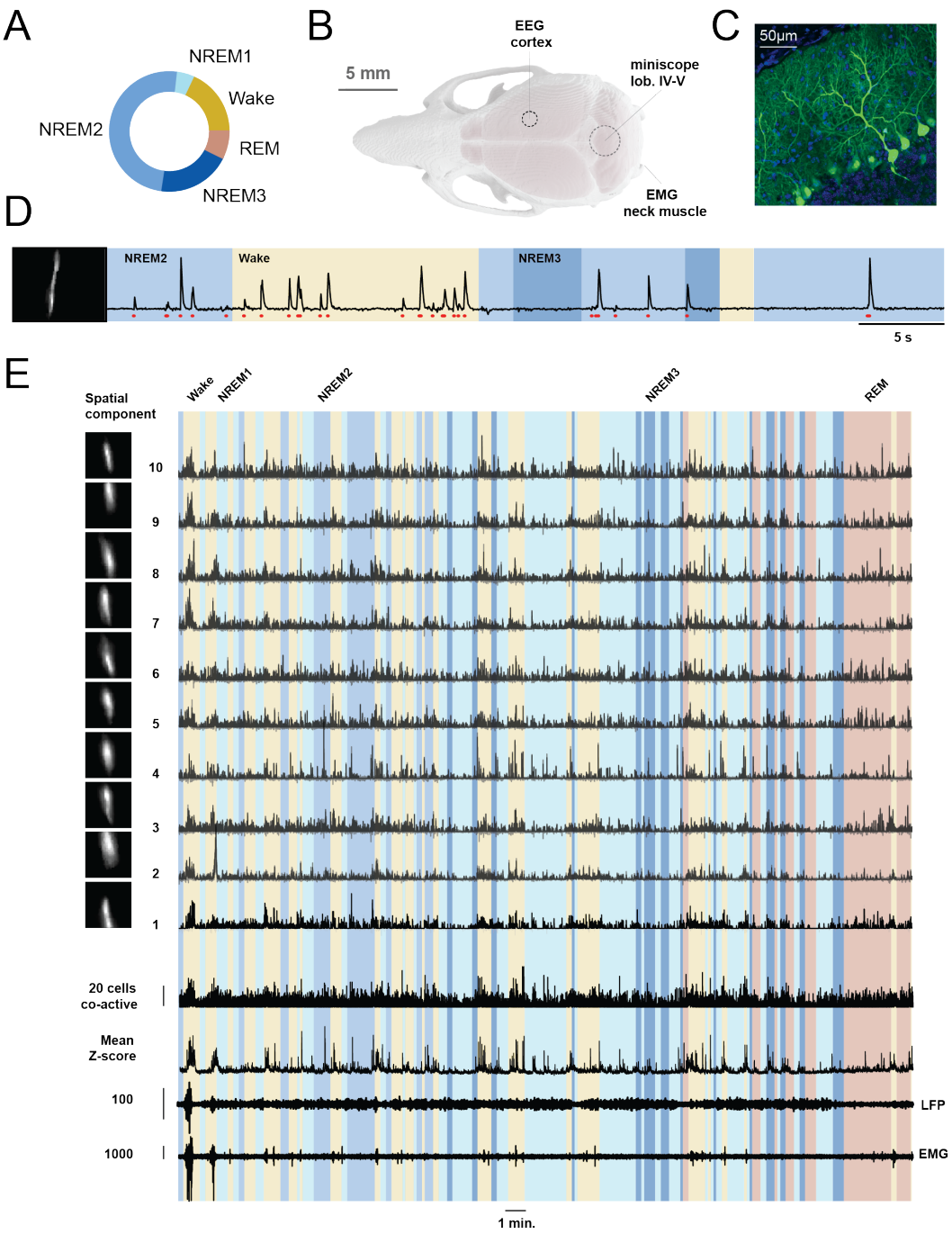

Figure 2. Miniscope imaging of complex spikes during cerebellar sleep. A, C57/BL6 mice stayed longest in NREM2 sleep (49.3%), followed in decreasing order by NREM3 (20.1%), REM (7.3%) and NREM1 sleep (5.3%). Animals transitioned several times from sleep to a wakeful state (17.9%) over the course of our recordings (N=9 animals). B, C57/BL6 mouse skull showing the recording positions for miniscope (cerebellar lobule IV/V), cortical EEG and neck muscles. C Expression of GCaMP6f selectively transduced in cerebellar Purkinje cells to allow imaging of complex spike associated calcium transients. D, Calcium transients associated with complex spike activity and their onsets (red dots) in a segmented Purkinje cell dendrite. E, Our data analysis pipeline consisted of motion correction with NoRMCorre, signal and spatial footprint extraction using CNMF-E. The spatial footprints of ten Purkinje cell dendrites are shown (left column) together with the extracted signal for these dendrites over a period lasting several minutes. Shaded color indicates behavioral (sleep) state with CS evoked calcium transients corresponding to a selection of ten Purkinje cell dendrites. All signals were deconvoluted and events representing the onset of a transient were extracted. Occurrences of CS events were summed to obtain the co-activation of CS associated calcium transients in Purkinje cells. Modulation of such co-activation, or the mean Z-scored signal were apparent during clear movements picked up in the EMG channel (units for LFP and EMG represented in µV).

Historically the complex spike has been seen as an all-or-none event, where the climbing fiber generates a massive synaptic response. Recent work has cast this idea aside suggesting that varying levels of sensory input to the inferior olive, which gives rise to the climbing fibers, could generate more graded complex spike responses (Najafi et al., 2014, Zang and Schutter 2019), as reflected potentially in a variable number of spikelet waves associated with a complex spike. Calcium imaging revealed that a graded response was reflected in the amplitude of complex spike evoked calcium transients (Najafi et al. 2014). We reasoned that if sensory input is gated during sleep (Van Luijtelaar et al., 1998) this should be associated with reduced complex spike -evoked calcium transient amplitudes. Indeed, relative to wakefulness (Wake: 12.4±9.7, 3972 transients, expressed as peak amplitudes of C, a denoised and scaled version of ΔF, mean±SD) the calcium transient amplitudes were reduced (Figure 3B) across all sleep states (NREM1: 11.1±10, 5517 transients; NREM2:10.8±7.7, 6082 transients; NREM3: 10±7.3, 5429 transients; REM: 10.6±8.2, 6272 transients). Inter-group differences were significant for Wake-NREM1, Wake-NREM2, Wake-NREM3, Wake-REM, NREM1-NREM2, NREM1-NREM3, NREM2-REM and NREM3-REM (Kruskal-Wallis test with post-hoc Scheffe test with α=0.01).

Given that our imaging approach allowed monitoring of multiple Purkinje cell dendrites we asked whether the rate at which at least 10% of all detected Purkinje cells co-fired within the imaging field-of-view changed during sleep (Figure 3C). There was a significant drop in co-activation rates from wakefulness (2.87±1.5 Hz) to NREM and REM (NREM1:1.5±1.8 Hz; NREM2: 1.0±1.2 Hz; NREM3: 0.77±1.2 Hz; REM: 0.96±1.4 Hz) sleep relative to wakefulness (Kruskal-Wallis test with post-hoc Scheffe test with α=0.01). The co-activation rate dropped significantly from NREM1 to NREM2 and NREM3 sleep. Thus, even though there were several instances of co-activation encompassing more than 10% of Purkinje cells during sleep they became more sparse.

We next looked at the regularity of complex spike firing across sleep stages (Figure 3D). This is of interest given that slow wave cortical activity has the potential to reduce complex spike regularity via cortical inputs to the inferior olive. Moreover, neocortical upstates have been shown to be permissive for driving complex spike firing (Ros et al., 2009) even during sleep (Levenstein, 2019). Recent work has suggested brain region-specific and sleep stage-dependent differences in neuron firing rates (Miyawaki et al., 2016). We used the CV_2 value (Holt, 1996) as a measure for the regularity of complex firing. CV_2 values during NREM1 (0.77±0.1, 898 PC dendrites, mean±SD) and REM (0.80±0.2, 1196 PC dendrites) sleep did not differ significantly from wakefulness (0.79±0.1, 962 PC dendrites), but CV_2 values during NREM2 (0.83±0.2, 1744 PC dendrites) and NREM3 (0.81±0.1, 1345 PC dendrites) had significantly different mean ranks

(Kruskal-Wallis test with post-hoc Scheffe test with α=0.01) when compared to the wake state suggesting that complex spikes fire in less regular fashion during deep stages of sleep.

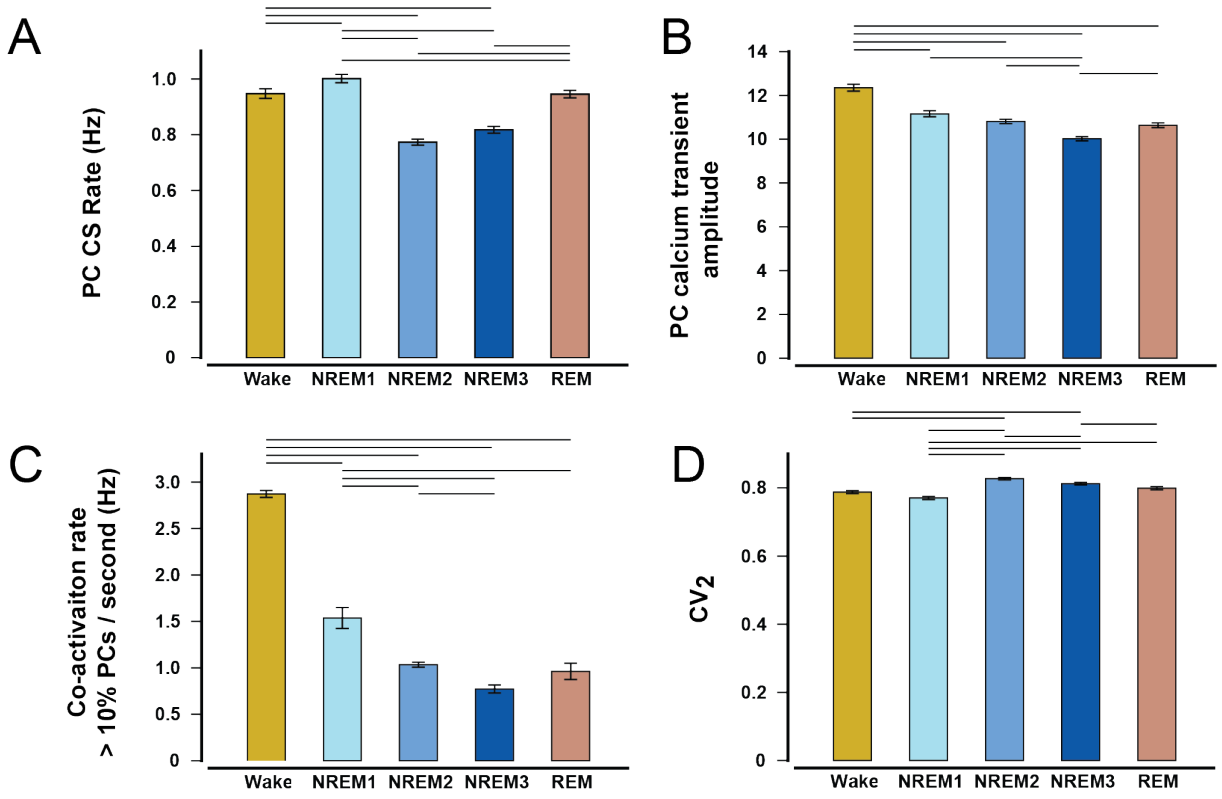

Figure 3. Quantification of complex spike activity imaged during sleep. A, Complex spike (CS) rates were suppressed most strongly during NREM2 and NREM3 sleep before increasing again during REM sleep. CS rates remained elevated during NREM1 sleep B, CS evoked calcium transient amplitudes were suppressed across all sleep stages. C, The rate of having more than 10% of PCs co-firing a CS decreased significantly from wakefulness to NREM and REM sleep. D, The regularity of firing decreased as indicated by an increase of CV_2 value (Holt et al., 1996) during NREM2, NREM3 and REM. Lines above the bar graphs indicate significance between groups as established using a Sheffe's test for multiple comparisons. Error bars represent standard error of the mean.

An organization into parasagittal bands of Purkinje cells as functional subdivisions of the cerebellum has been proposed in the past century (Oscarsson, 1979), with microzones comprising zones of input from specific parts of the inferior olive and projecting to specific targets in the cerebellar nuclei. Such cerebellar micrzones have later been demonstrated using imaging techniques that allowed finer scale measurements at cellular resolution (Ozden et al. 2009, De Gruijl et al. 2014). We leveraged the ability of our imaging approach to determine the pairwise correlations of complex spike events in neighbouring Purkinje cell dendrites during wakefulness and sleep (Figure 4). As expected and shown previously nearby Purkinje dendrites were more strongly correlated than those at greater mediolateral separation during wakefulness and this principle also held for all sleep states. There were some notable differences however, when

comparing for example wakefulness to late stages of NREM sleep. The pairwise cell-to-cell event correlations over the first ~200 µm were all significantly reduced (KS test for every 10 µm bin). The event correlations during NREM1 and REM sleep were closer to those observed during wakefulness and dropped off less steeply at greater distances than during wakefulness. Comparing the event correlations as a function of a mediolateral separation, extending to 400 µm for all sleep states showed that the spatial structure of complex spike firing was significantly different among groups (Kruskal-Wallis test, with Scheffe's procedure for multiple comparisons with α=0.01). Both REM and NREM1 sleep states were associated with significantly elevated correlation values relative to NREM2 and NREM3 sleep states. REM and NREM1 sleep had correlation values relative to wakefulness that remained significantly higher at greater distances of mediolateral separation.

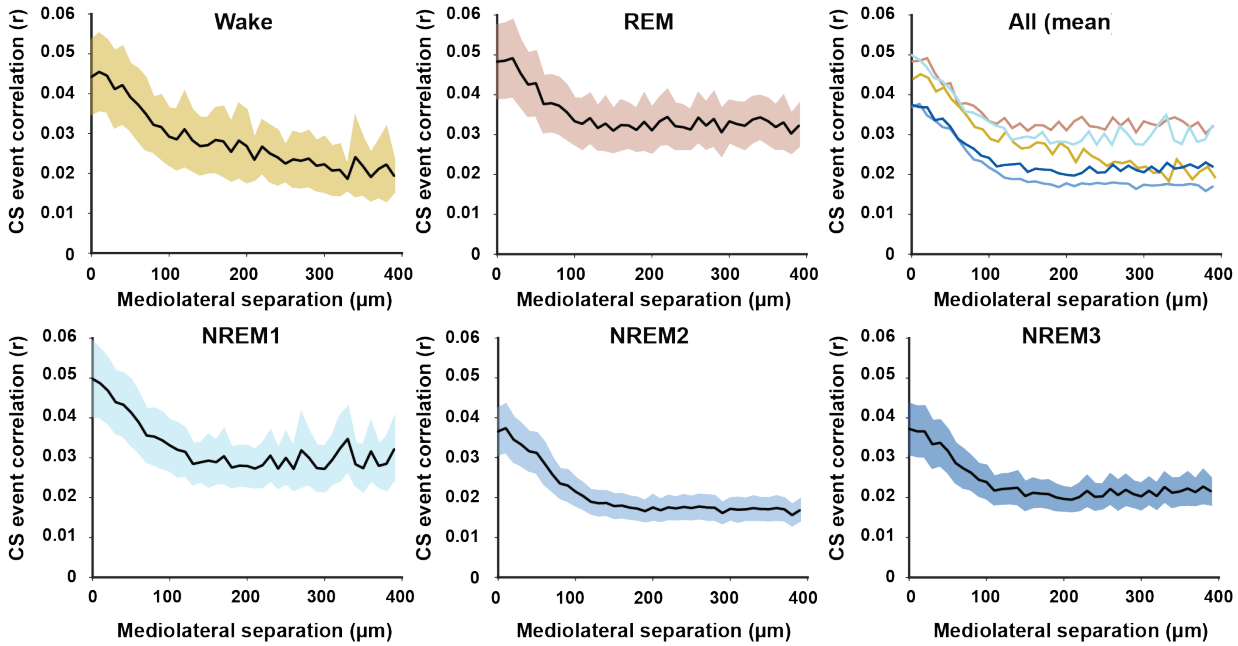

Figure 4. Spatial correlations of complex spike events during sleep. Pairwise correlations of complex spike events as a function of mediolateral separation during wakefulness, NREM sleep and REM sleep. Shaded areas represent standard error of the mean.

Animals twitch during sleep, but the extent to which this happens appears to vary by sleep state (Reiter et al., 2020) and type of animal (Libourel et al., 2018). We therefore scoured the neck muscle EMG for brief high frequency deflections reflecting a twitch and used these as onsets to determine if complex spike-evoked calcium transients could be triggered off of these twitches (Figure 5). The sharp breaks in the rectified EMGs at t=0 highlight the onset of the twitches. The largest fraction of twitches occurred during wakefulness (1.2 Hz, twitches per second). The rate was significantly suppressed, but present in both NREM and REM stages (NREM1: 0.4 Hz,

NREM2: 0.5 Hz, NREM3: 0.3 Hz, REM: 0.3 Hz). During wakefulness and across all sleep stages, twitches were associated with complex spike-evoked calcium transients that peaked after twitch onset. During REM a pronounced double peak response was found after twitch onset. Eye movement has been associated with increased CS complex spike firing during REM sleep as well as bursts of mossy fiber activity (Hobson and McCarley, 1972). One possibility is that due to the reciprocal nature of complex spike and simple spike firing (Badura et al., 2013) the twitches that occurred during REM sleep were associated with a reverberation of activity in the olivocerebellar network as a result of alternating climbing fiber and mossy fiber activation.

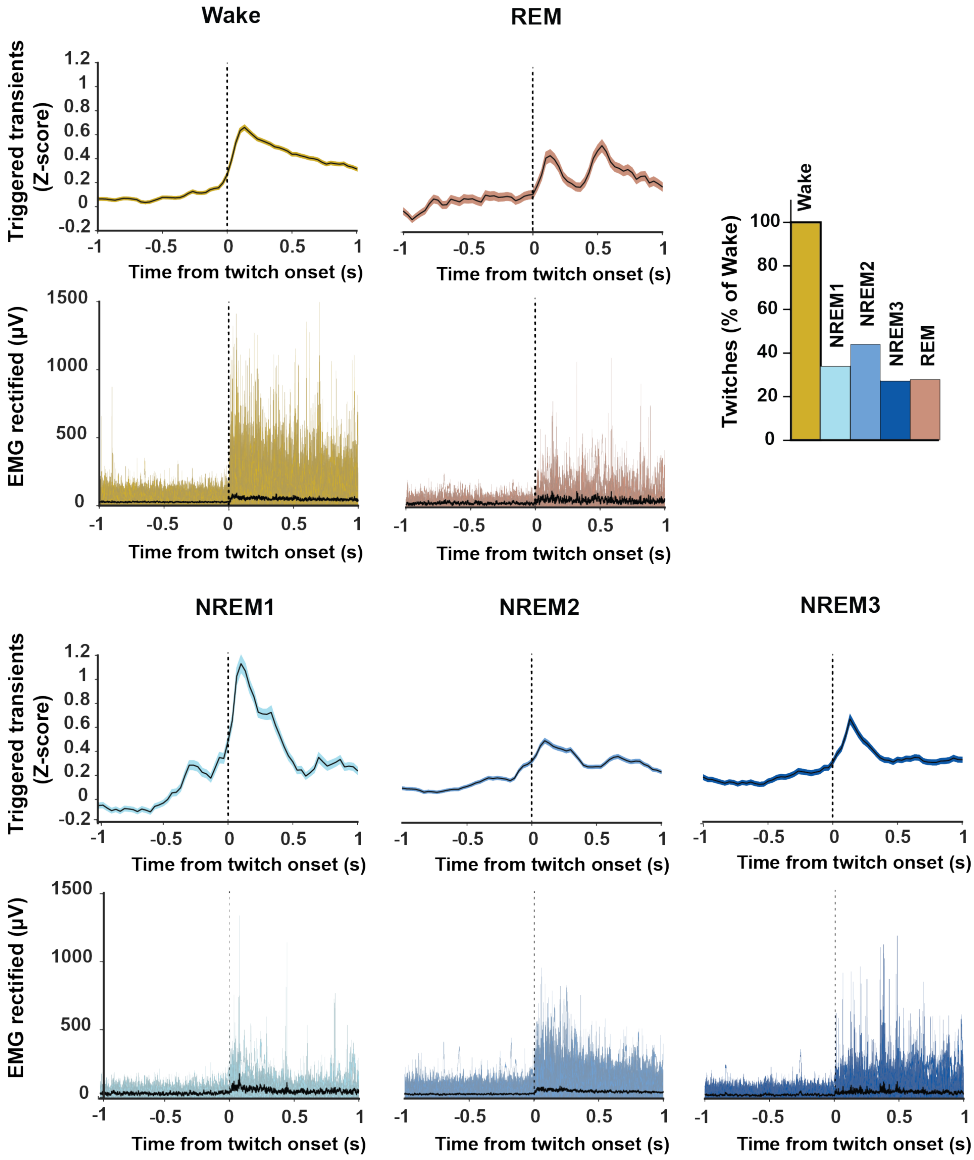

Figure 5. Twitch onset-triggered complex spike evoked calcium transient responses during sleep. Complex spike evoked calcium transients in Purkinje cell dendrites (top) were triggered off the onset of twitches detected in neck muscle EMG recordings (bottom, showing rectified EMG). Most twitches occurred during wakefulness and their number dropped substantially across all sleep states. Peak responses occurred after onset of the movement. Shaded areas in top panels represents standard error of the mean.

Discussion

Sleep is important for the consolidation and retrieval of cerebellar-dependent motor memories and such learning is facilitated by extending the permitted sleep period after cerebellar motor learning (De Zeeuw and Canto, 2020). It is important therefore, to understand the physiological changes that occur in cerebellar neurons that store such memories. Previous studies used rather small scale sampling of cerebellar activity during sleep in a variety of species (Mano 1970; Marchesi and Strata, 1971; Hobson and McCarley, 1972; Zhang et al., 2020) and some of the outcomes of these studies differed. In one study simple spikes showed a small decrease during NREM sleep, but increased strongly during REM sleep, while complex spike firing was most strongly reduced during REM sleep (Mano et al., 1970). Simple spikes were found to both fire in regularly or in bursts during wakefulness and REM sleep in this study. Marchesi and Strata (1970) by contrast reported a strong increase of complex spike firing during REM sleep in the absence of eye movements and this rate decreased when eye movements were present. Yet another study (Hobson and McCarley, 1972) found that complex firing increased during REM sleep, but only when eye movements were present. Only recently has the impact of state changes during sleep on simple spike and complex firing been investigated in mice (Zhang et al. 2020). Here no effect was seen of sleep on complex firing, but simple spikes were reduced both during REM and NREM sleep.

In the present work, we applied cellular resolution imaging of complex spikes from many hundreds of Purkinje cells to monitor the olivocerebellar circuit during sleep. We recorded in the anterior vermis of the cerebellum using miniaturized fluorescence microscopes as these permitted recording spatiotemporal patterns of complex spike activity during sleep under more natural circumstances than when animals are head-fixed (Yüzgeç et al., 2018) while the imaging modality also avoided noisy surroundings of the cooled infrared pulsed laser used with a two-photon microscope. Thus while we were not able to record simple spike activity we were able to look at population level dynamics of complex spike firing during sleep.

Attenuation of complex spike firing during slow wave sleep

While previous studies have defined only two categories of sleep NREM (slow wave) and REM (paradoxical), we here distinguish the three separate NREM sleep states individually. Our data show that complex spike rates are only depressed during NREM2 and NREM3 sleep. By contrast the complex spike rates during NREM1 sleep were slightly elevated relative to wakefulness and

REM sleep. Complex spikes rates were not different between wakefulness and REM sleep. Despite the strongest depression of complex spike firing during late stages of NREM sleep, the actual firing rate changes were rather modest suggesting tight homeostasis of complex spike generation in the inferior olive (Ju et al., 2019). What explains the reduction in firing rate? It is likely that ionic conductances such as Ih, which help to sustain subthreshold oscillations in the inferior olive, are affected during sleep (Lewis et al., 2010; Garden et al. 2018) and could result in a reduced firing frequency. Indeed sleep has been associated with regulation of specific ion channels and their kinetics across animal phyla (Kempf et al., 2019; Lancel, 1999) and various neuromodulators such as acetylcholine, noradrenaline, serotonin, orexin and dopamine are also likely to affect cerebellar excitability during sleep through downstream mechanisms on cell excitability (van Neerven et al., 1990, Tan et al., 1991; Barik et al.,2005; Silva-Marques, 2016). The arousal threshold (the occurrence of the arousal from sleep with a small rise in ventilatory drive) was found to be highest during slow wave sleep, but lower during NREM1 and REM sleep (Rechtschaffen et al., 1966; Franco et al., 2010; Scammel et al., 2007) which is consistent with a reduced excitability during NREM2 and NREM3 relative to NREM1 and REM sleep. In how far complex spikes follow the slow waves of synchronized activity in the cortex is unknown. In anesthetized animals, complex spike rates do seem to follow cortical up and down states (Ros et al., 2009). However, entrainment of activity in the inferior olive by cortical stimulation could be ineffective for the slow frequencies typically associated with late NREM sleep (Steriade and Hobson, 1976; Marshall and Lang, 2004). Thus, it is likely that at the level of the inferior olive cortical input is likely to be partially gated during slow wave sleep.

Reduced amplitudes of complex spike evoked calcium transients during NREM and REM sleep

Climbing fibers have typically been considered to trigger all-or-none complex spike responses in Purkinje cells. However, recent calcium imaging of sensory evoked complex spikes have challenged this assumption and suggest that a more graded response can be elicited by modulating the complex spike waveform and its number of spikelets (Najafi et al., 2014). We find that the amplitude of complex spike elicited calcium transients imaged from Purkinje cell dendrites is indeed reduced across both NREM and REM sleep. This could suggest that perhaps the number of spikelets riding on the climbing fiber induced complex spikes is reduced during sleep. There is only limited electrophysiological evidence for this in vivo. Mano (1970) reported that the number of spikelets in a complex spike waveform was reduced only during REM sleep with a

similar distribution in the number of spikelets during wakefulness and slow wave sleep. Najafi et al. (2014) proposed two explanations for an increased amplitude of sensory evoked calcium transients. They suggest a small component of the increase could be attributed to a route other than the complex spike itself, most likely by way of parallel fiber to Purkinje cell inputs (Davie et al., 2008). However, for stronger sensory stimulation this contribution was deemed insufficient and that more likely an additional complex spike spikelet could contribute to the observed increase in calcium transient amplitude. Indeed, previous work supports a role for spikelets in driving additional calcium influx associated with complex spikes whose number was dependent on IO oscillation phase (Mathy et al., 2009). Both the phase (Mathy et al., 2009) and amplitude (Bazzigalupi et al (2012) of inferior olive subthreshold oscillations have been suggested to affect spikelet number. Given that we see a reduced calcium transient amplitude throughout sleep and not just during late NREM when cortical activity is likely to be partially gated (Marshall and Lang, 2018), a reduced excitability of IO neurons could be an additional contributing factor to a reduced number of spikelets and reduced calcium transients amplitudes across all sleep stages. Such reductions may be significant for memory consolidation during sleep since the induction of plasticity is affected by the number of spikelets (Mathy et al., 2009).

Attenuation of the rate of co-activation during sleep

With our imaging approach it was possible to examine the level of co-activation of Purkinje cell dendrites within a cerebellar microzone (Oscarsson, 1979). In our current analysis we looked at the rate of occurrence of co-activations where at least 10% of Purkinje cell dendrites participated. Recent work suggests that the inferior olive in awake mice displays quasiperiodic rhythms in response to sensory input (Negrello et al., 2019), which are relatively short lasting. Thus if the level of cortical and midbrain input to the inferior olive is reduced during specific stages of sleep one could also expect an overall reduction in the level of synchronization of inferior olive oscillations and synchronous firing. We found that the co-activation rate was significantly greater during wakefulness even though synchronous firing still occurred during sleep. Synchronized firing in the inferior olive during sleep is likely to occur at specific time intervals during which cortical drive is strongly elevated such as at the cusp of synchronized cortical oscillations (Ros et al., 2009), or during eye movement related bursts of activity that occur during desynchronized, or REM sleep (Marchesi and Strata, 1970).

Increase of irregularity of complex spike firing during slow wave sleep

We looked at the regularity of complex spike firing during wakefulness and sleep by calculating CV_2 values (Shin et al. 2007), finding that during NREM2 and NREM3 firing of complex spikes became slightly more irregular relative to wakefulness, NREM1 and REM sleep. Recent work has examined how firing rate changes in the hippocampus and frontal cortex during sleep state cycling (Miyawaka et al., 2019). The authors found that sleep states and state transitions don't affect neurons uniformly, but depend on both the brain region and the relative activity of cells as well as the degree to which this activity is regulated by sleep-associated changes in neuromodulators. One would expect that the cortical synchronization during slow wave sleep might lead to more regular complex spike firing patterns, yet the ability of the inferior olive to preferentially gate cortical input frequencies above those of slow wave sleep could have contributed to a more irregular pattern of complex spike firing. Moreover, firing occurring during the up-state of a cortical oscillation is also likely to be irregular in nature (Steriade et al., 1993).

Spatial correlations change during sleep

Behavioral state can have a significant impact on complex spike firing in cerebellar microzones. Animals that are actively engaged in locomotion have higher pairwise correlations between complex spike firing Purkinje cells as a function of mediolateral distance than at rest (Ozden et al., 2012). Animals in which Cx36 gap junctions in the inferior olive are genetically knocked out display more desynchronized complex spike firing during locomotion (De Gruijl et al., 2014) and the same holds true when irregular simple spike firing patterns in Purkinje cell trigger desynchronized complex spike firing (Hoogland et al., 2015). It was therefore expected that during the state change from wakefulness to sleep we could see an effect on event correlations as a function of mediolateral distance between Purkinje cells. For wakefulness and across all sleep states, Purkinje cells that were closer together had higher correlation values. The anatomical clustering in the inferior olive (Vrieler et al., 2019) and arrangement of olivocerebellar projections impose this correlation structure on nearby Purkinje cells. During NREM2 and NREM3 sleep, when complex firing rates were most strongly suppressed and firing was also found to be more irregular, pairwise correlations between Purkinje cell dendrites as a function of mediolateral separation were significantly suppressed relative to wakefulness. By contrast, during NREM1 and REM sleep when complex spike firing rates remain relatively unchanged during sleep, event correlations follow those seen during wakefulness at least over the distances spanning a

cerebellar microzone. In addition to co-firing bands of nearby Purkinje cells, we sometimes observed widely separated Purkinje cell dendrites during early stages of NREM and REM sleep with similar firing patterns. This could explain why we saw event correlations drop off less steeply during NREM and REM sleep than during wakefulness at greater distances of mediolateral separation.

Complex spike activity in relation to twitching movements

Our EMG recordings monitored movement of the neck muscles. We found that twitch-like nuchal movements triggered complex spike-evoked calcium transients both during wakefulness and sleep. Our findings mirror recordings of the inferior olive in juvenile rats where activity increased sharply at the onset of nuchal activity during both wakefulness and sleep (Mukherjee et al., 2018). The authors proposed that the twitches are accompanied by a corollary discharge that is relayed to the cerebellar cortex guiding predictions on the sensory consequences of movements (Blakemore et al., 2001). Previous work also found strong modulation of complex spike activity during REM sleep in juvenile rats (Sokoloff et al., 2014). Twitching movements persist in the adult during sleep and thus may also contribute in adults to motor learning refinements (Brooks and Peever, 2016). Such a role in learning to distinguish self-generated movements. Studies in adult rats reported mostly ocular and masseter muscle rather than neck muscle activity during REM sleep (Anaclet et al., 2010). Implanting electrodes in the musculus rectus superior and musculus rectus lateralis could ease the association of REM state related movements with complex spike activity (Fulda et al., 2011). One distinguishing feature in our recordings during REM sleep were two clearly discernible peaks in the triggered calcium response. The desynchronized cortical activity observed during REM sleep (Frauscher et al., 2010) could generate lags that contribute to such a response. In addition, reverberation after a mossy fiber volley in the olivocerebellar loop could possibly contribute to such a secondary peak.

Future perspectives

We relied on a common practice to score sleep in epochs lasting four seconds. This allowed us to look at general trends in the data over many epochs. However, some of the scored epochs could have contained a mixture of sleep signatures, where some hallmarks of one type of sleep (such as K complexes during NREM2) were more clearly defined than others. Moreover, in the present study we did not specifically look at changes in activity around state transitions. A large

modulation of activity can occur around these transitions as has been recently demonstrated for simple spike firing in Purkinje cells (Zhang et al., 2020). While these authors did not find modulation in complex spike firing, our imaging approach would probably be more sensitive to pick up such changes, given the large number of cells that can be recorded from at once. The cerebellum and cortex are functionally and anatomically strongly interconnected through cortico-cerebellar loops (Hoover and Strick, 1999; Gao et al., 2018) and the activity in these two brain regions might engage and disengage over the course of sleep. The possibility to image from both the cerebellum and cortex concurrently was recently demonstrated in unrestrained animals (De Groot et al., 2020). Such recordings could reveal how, during transitions from wakefulness to synchronized (slow wave sleep, NREM3) and desynchronized (REM) sleep, complex firing in cerebellar microzones covaries with cortical activity. Longitudinal studies of complex spike firing, together with recordings from cerebral cortex after a learning paradigm could help to link activity changes in the olivocerebellar circuit and cerebello-cortical loops during sleep to consolidation of procedural memories (Ackerman and Rasch, 2014). In this study, we did not follow up on global increases in fluorescence that were sometimes observed in Purkinje cell dendrites during REM sleep. Such recurring fluorescence increases could represent increased parallel fiber to Purkinje cell drive associated with ponto-geniculo occipital waves, or P waves whose function remains enigmatic. It has been proposed they subserve a function in the retention of learning (Datta 2006; Lim et al 2007, Gott et al., 2017). It would therefore be valuable to perform a more detailed quantification of their occurrence during REM sleep.

Materials and Methods

Animals

All performed experiments were licensed by the Dutch Competent Authority and approved by the local Animal Welfare Body, following the European guidelines for the care and use of laboratory animals Directive 2010/63/EU.

Electrophysiology

During wake/sleep cycles, the electroencephalogram (EEG) was measured in the frontal cortex and motor cortex in conjunction with the hippocampal LFP. Electromyogram (EMG) signals were recorded from the neck muscles. Data were acquired using a multiclamp 700B patch-clamp

amplifier and digitized at 50 kHz using a 1440A digidata digitizer. LFP recordings were filtered using a low-pass filter at 30 Hz and a high-pass filter at 0.5 Hz. EMG recordings were not filtered.

Virus injections and GRIN lens implantation

Prior to surgeries mice were anesthetized with 3% Isoflurane before being transferred to a stereotactic apparatus after which anesthesia was maintained at 1.5% Isoflurane (flow rate: 0.3 ml/min O_2). For imaging of the cerebral and cerebellar cortex, a GRIN objective lens (1.8 mm diameter, 0.25 pitch, 64-519, Edmund Optics) was implanted on the brain surface. A small incision was made in the skin after shaving hair removal and disinfection of the skin with iodine solution (5%) and alcohol (70%). Lidocaine (100 mg/ml, Astra Zeneca, UK) was then applied to the exposed skull and the periosteum removed. The center coordinates for GRIN lens placement were located and a small ink dot was placed at the correct location relative to bregma (cerebellar lobule IV/V AP: -6.3 mm ML: 0 mm). Coordinates were scaled relative to the mean bregma-lambda distance (of 4.21 mm) as specified in Paxinos mouse brain atlas. Prior to drilling of the bone, mice received i.p. Injections of 15% D-Mannitol in saline (0.55 ml/25gr) to aid diffusion of virus particles after virus injection. A 2 mm circular craniotomy was then drilled centered around the marked location. In between drilling the skull was kept moist with sterile saline. The skull flap and dura were then removed and virus (Cerebellum: AAV1.CAG.FLEX.GCaMP6f / AAV1.CMV.PI.Cre.rBG mixed 1:1 and diluted in saline 1:3; Cortex: AAV1.Syn.GCaMP6f.WPRE.SV40 diluted in saline 1:3, UPenn Vector Core) was injected at four locations. At each location 25 nl of virus was injected once at 350, twice at 300 and once at 250 µm depth at a rate of 25 nl/min.The craniotomy was covered with gelfoam (Pfizer, USA) soaked in sterile saline (0.9 % NaCl, B. Braun Medical Inc., USA). The GRIN lens was lowered using a vacuum holder placed in the stereotactic apparatus until the lens surface touched the brain and then lowered an additional 50 µm. The edges of the craniotomy were sealed with Kwik-Sil (WPI, USA). Dental cement (Super-Bond C&B, Sun Medical, Japan) was then applied around the lens to secure it in place. Kwik-Cast (WPI, USA) was used to cover and protect the lens. At the end of the surgery animals received an s.c. injection of 5mg/kg Metacam.

Miniscope imaging and signal extraction

We used the UCLA Miniscope V3 (https://www.miniscope.org) for imaging complex spike activity in Purkinje cell dendrites. Movies were motion-corrected using NoRMCorre (Pnevmatikakis and

Giovanucci, 2017) and signal extracted using CNMF-E (Zhou et al., 2018). Events were detected after deconvolution of raw fluorescence traces (Vogelstein et al., 2009). Since we recorded the frame output of the miniscopes as an analog signal together with the electrophysiological measurements it was possible to readily align miniscope frames with the analyzed sleep epochs. In this way, for every dendrite, events could be extracted belonging to a particular behavioral state (Wake, NREM1, NREM2, NREM3 and REM).

Sleep deprivation

Animals were sleep deprived by placing them in a rotating drum (diameter: 39 cm, height: 37 cm) divided into four compartments by Plexiglass walls (Techniplast, France, University of Grenoble). The drum was rotated through a bidirectional computer-controlled motor (MACDO-B1, JVL, Denmark) and belt. The drum was set to rotate at 2 rotations per minute for the duration of 1 minute clockwise, followed by a 10 second pause and a subsequent 1 minute counter-clockwise rotation. Water and food were provided *ad libitum* and home cage bedding material was included in the enclosure.

Sleep scoring

The Wonambi 6.11 suite was used to score sleep stages by visualizing LFP and EMG recordings as well as their power spectrum. Epochs of 4 seconds were used to score sleep. Based on LFP and EMG recordings, sleep stages were classified as Wake, NREM1, NREM2, NREM3, REM, and Undefined. Wakefulness was characterized by small amplitude waves at high frequencies while different levels of continuous muscle activity were exhibited. NREM1 was characterized by a mixture of alpha activity (8-13 Hz) and theta activity (4 - 7 Hz), NREM2 was mainly characterized by the presence of K complexes and NREM3 was characterized by the high amplitude waves at low frequencies corresponding to the delta range (0.5 – 3 Hz). During these NREM stages, occasional muscle activity was present and was also annotated. REM sleep was characterized by small amplitude waves showing non-continuous but abundant theta activity (4 – 7 Hz). Muscle activity also occurred occasionally and was also annotated. Epochs were scored as Unknown when none of the hallmarks of the sleep stages described above was present which almost always was caused because of transient noise of the recording making it difficult to score.

Analysis

Analysis was performed on 9 animals in which sleep was scored and signals extracted from our miniscope recordings. Complex spike rates were calculated on a per-dendrite basis, while co-activation rates were determined for scored sleep epochs by taking the sum of the extracted complex spike event occurrences per frame across all Purkinje cell dendrites. CV_2 values were calculated using the approach by Holt (1996) using events corresponding to a specified sleep state for every imaged Purkinje cell dendrite.

References

Ackermann S, Rasch B (2014) Differential effects of non-REM and REM sleep on memory consolidation? Curr Neurol Neurosci Rep 14(2):430.

Anaclet C, Pedersen NP, Fuller PM, Lu J (2010) Brainstem circuitry regulating phasic activation of trigeminal motoneurons during REM sleep. PloS One 5(1):e8788.

Badura A, Schonewille M, Voges K, Galliano E, Renier N, Gao Z, Witter L, Hoebeek FE, Chédotal A, De Zeeuw CI (2013) Climbing fiber input shapes reciprocity of Purkinje cell firing. Neuron 78(4):700-13.

Bazzigaluppi P, De Gruijl JR, van der Giessen RS, Khosrovani S, De Zeeuw CI, de Jeu MTG (2012) Olivary subthreshold oscillations and burst activity revisited. Front Neural Circuits 6:91.

Blakemore SJ, Frith CD, Wolpert DM (2001) The cerebellum is involved in predicting the sensory consequences of action. Neuroreport 12(9):1879-84.

Brooks PL, Peever J (2016) A Temporally Controlled Inhibitory Drive Coordinates Twitch Movements during REM Sleep. Curr Biol 26(9):1177-82.

Cai DJ, Aharoni D, Shuman T, Shobe J, Biane J, Song W, Wei B, Veshkini M, La-Vu M, Lou J, Flores SE, Kim I, Sano Y, Zhou M, Baumgaertel K, Lavi A, Kamata M, Tuszynski M, Mayford M, Golshani P, Silva AJ (2005) A shared neural ensemble links distinct contextual memories encoded close in time. Nature 534(7605):115-8.

Cicirata F, Zappalà A, Serapide MF, Parenti R, Pantò MR, Paz C (2005) Different pontine projections to the two sides of the cerebellum. Brain Res Brain Res Rev 49(2):280-94.

Cox J, Pinto L, Dan Y (2016) Calcium imaging of sleep–wake related neuronal activity in the dorsal pons. Nat Commun 7:10763.

Cunchillos JD, De Andrés I. Participation of the cerebellum in the regulation of the sleep-wakefulness cycle (1982) Results in cerebellectomized cats. Electroencephalogr Clin Neurophysiol 53(5):549-58.

Datta S (2006) Activation of phasic pontine-wave generator: A mechanism for sleep-dependent memory processing. Sleep and Biological Rhythms, 4: 16-26.

Davie JT, Clark BA, Häusser M (2008) The origin of the complex spike in cerebellar Purkinje cells. J Neurosci 28(30):7599-609.

De Groot A, Den Boom BJG, Van Genderen RM, Coppens J, Van Veldhuijzen J, Bos G, Hoedemaker H, Negrello M, Willuhn I, De Zeeuw CI, Hoogland TM (2020) NINscope: a versatile miniscopes for multi-region circuit investigations. eLife 9: e49987.

De Gruijl JR, Hoogland TM, De Zeeuw CI (2014a) Behavioral correlates of complex spike synchrony in cerebellar microzones. J Neurosci 34:8937–8944.

De Zeeuw CI, Canto CB (2020) Sleep deprivation directly folowing eyeblink-conditioning impairs memory consolidation. Neurobiol Learn Mem 170:107165.

DelRosso LM, Hoque R. The cerebellum and sleep (2014) Neurol Clin 32(4):893-900.

Franco P, Kato I, Richardson HL, Yang JS, Montemitro E, Horne RS (2010) Arousal from sleep mechanisms in infants. Sleep Med 11(7):603-614.

Frauscher B, von Ellenrieder N, Dubeau F, Gotman J (2016) EEG desynchronization during phasic REM sleep suppresses interictal epileptic activity in humans. Epilepsia 57(6):879-888.

Fulda S, Romanowski CP, Becker A, Wetter TC, Kimura M, Fenzel T (2011) Rapid eye movements during sleep in mice: high trait-like stability qualifies rapid eye movement density for characterization of phenotypic variation in sleep patterns of rodents. BMC Neurosci 12:110.

Gao Z, Davis C, Thomas AM, Economo MN, Abrego AM, Svoboda K, De Zeeuw CI, Li N (2018) A cortico-cerebellar loop for motor planning. Nature 563(7729):113-116.

Garden DLF, Rinaldi A, Nolan MF (2018) Inferior olive HCN1 channels coordinate synaptic integration and complex spike timing. Cell Rep 22: 1722-1733.

Gott JA, Liley DT, Hobson JA (2017) Towards a Functional Understanding of PGO Waves. Front Hum Neurosci 11:89.

Kempf A, Song SM, Talbot CB, Miesenböck G (2019) A potassium channel β-subunit couples mitochondrial electron transport to sleep. Nature 568(7751):230-234.

Hobson JA, McCarley RW (1972). Spontaneous discharge rates of cat cerebellar Purkinje cells in sleep and waking. Electroencephalogr Clin Neurophysiol 33(5): 457-469.

Holt GR, Softky WR, Koch C, Douglas RJ (1996) Comparison of discharge variability in vitro and in vivo in cat visual cortex neurons. J Neurophysiol 75(5):1806-1814.

Hoogland TM, De Gruijl JR, Witter L, Canto CB, De Zeeuw CI (2015) Role of synchronous activation of cerebellar Purkinje cell ensembles in multi-joint movement control. Curr Biol 25: 1157–1165.

Hoover JE, Strick PL (1999) The organization of cerebellar and basal ganglia outputs to primary motor cortex as revealed by retrograde transneuronal transport of herpes simplex virus type 1. J Neurosci 19(4):1446-63.

Ji D, Wilson MA (2007) Coordinated memory replay in the visual cortex and hippocampus during sleep. Nat Neurosci 10(1): 100-107.

Ju C, Bosman LWJ, Hoogland TM, Velauthapillai A, Murugesan P, Warnaar P, van Genderen RM, Negrello M, De Zeeuw CI (2019) Neurons of the inferior olive respond to broad classes of sensory input while subject to homeostatic control. J Physiol 597(9):2483-2514.

Keene AC, Duboue ER (2018) The origins and evolution of sleep. J Exp Biol 221(Pt 11):jeb159533.

Lancel M (1999) Role of GABAA receptors in the regulation of sleep: initial sleep responses to peripherally administered modulators and agonists. Sleep 22(1):33-42.

Levenstein D, Buzsáki G, Rinzel, J (2019). NREM sleep in the rodent neocortex and hippocampus reflects excitable dynamics. Nat Commun 10 **:** 2478.

Lewis AS, Estep CM, Chetkovich DM. The fast and slow ups and downs of HCN channel regulation. Channels (Austin). 2010 May-Jun;4(3):215-31.

Li W, Ma L, Yang G, Gan WB (2017) REM sleep selectively prunes and maintains new synapses in development and learning. Nat Neurosci 20(3):427-437.

Libourel PA, Barrillot B, Arthaud S, Massot B, Morel AL, Beuf O, Herrel A, Luppi PH (2018) Partial homologies between sleep states in lizards, mammals, and birds suggest a complex evolution of sleep states in amniotes. PloS Biology 16(10): e2005982.

Lim AS, Lozano AM, Moro E, Hamani C, Hutchison WD, Dostrovsky JO, Lang AE, Wennberg RA, Murray BJ (2007) Characterization of REM-sleep associated ponto-geniculo-occipital waves in the human pons. Sleep 30(7):823-7.

Mano N (1970) Changes of simple and complex spike activity of cerebellar Purkinje cells with sleep and waking. Science 170(3964):1325-7.

Marchesi GF, Strata P (1971) Mossy and climbing fiber activity during phasic and tonic phenomena of sleep. Pflugers Arch 323(3):219-40.

Marshall SP, Lang EJ (2004) Inferior olive oscillations gate transmission of motor cortical activity to the cerebellum. J Neurosci 24(50):11356-67.

Mathy A, Ho SSN, Davie JT, Duguid IC, Clark BA, Häusser M (2009) Encoding of oscillations by axonal bursts in inferior olive neurons. Neuron 62:388–399.

Miyasaki S, Liu CY, Hayashi Y (2017). Sleep in vertebrate and invertebrate animals, and insights into the function and evolution of sleep. Neuroscience Research 188:3-12.

Miyawaki H, Diba K (2016) Regulation of Hippocampal Firing by Network Oscillations during Sleep. Curr Biol 26(7):893-902.

Miyawaki H, Watson BO, Diba K (2019) Neuronal firing rates diverge during REM and homogenize during non-REM. Sci Rep 9 : 689.

Monti JM (2011) Serotonin control of sleep-wake behavior. Sleep Med Rev 15(4): 269-281.

Moul DE, Germain A, Cashmere JD, Quigley M, Miewald JM, Buysse DJ (2007) Examining initial sleep onset in primary insomnia: a case-control study using 4-second epochs. J Clin Sleep Med 3(5):479-88.

Mukherjee D, Sokoloff G, Blumberg MS (2018) Corollary discharge in precerebellar nuclei of sleeping infant rats. Elife 7:e38213.

Nagai H, de Vivo L, Bellesi M, Ghilardi MF, Tononi G, Cirelli C (2017) Sleep Consolidates Motor Learning of Complex Movement Sequences in Mice. Sleep 40(2):zsw059.

Najafi N, Giovanucci A, Wang SS, Medina F (2014) Coding of stimulus strength via analog calcium signals in Purkinje cell dendrites of awake mice. Elife 3:e03663.

Oscarsson O (1979) Functional units of the cerebellum - sagittal zones and microzones. Trends Neurosci 2 : 143-145.

Ozden I, Dombeck DA, Hoogland TM, Tank DW, Wang SS (2012) Widespread state-dependent shifts in cerebellar activity in locomoting mice. PLoS One 7:e42650.

Ozden I, Sullivan MR, Lee HM, Wang SSH (2009) Reliable coding emerges from coactivation of climbing fibers in microbands of cerebellar Purkinje neurons. J Neurosci 29:10463–10473

Pnevmatikakis EA, Giovanucci A (2017) NoRMCorre: An online algorithm for piecewise rigid motion correction of calcium imaging data. J Neurosci Methods 291:83-94.

Rechtschaffen A, Hauri P, Zeitlin M (1966) Auditory awakening thresholds in REM and NREM sleep stages. Percept Mot Skills 22(3): 927-942.

Reiter AM, Roach GD, Sargent C, Lack L. Finger Twitches are More Frequent in REM Sleep Than in Non-REM Sleep (2020) Nat Sci Sleep 12:49-56.

Ros H, Sachdev RN, Yu, Sestan N, McCormick DA (2009). Neocortical networks entrain neuronal circuits in cerebellar cortex. J Neurosci 29(33): 10309-10320.

Saper CB, Scammell TE, Lu J (2005) Hypothalamic regulation of sleep and circadian rhythms. Nature 427(7063): 1257-1263.

Scammell TE, Arrigoni E, Lipton JO (2017). Neural circuitry of wakefulness and sleep. Neuron 93(4): 747-765.

Shin SL, Hoebeek FE, Schonewille M, De Zeeuw CI, Aertsen A, De Schutter E (2007) Regular patterns in cerebellar Purkinje cell simple spike trains. PLoS One 2(5):e485.

Sonni A, Kurdziel LB, Baran B, Spencer RM (2014) The effects of sleep dysfunction on cognition, affect, and quality of life in individuals with cerebellar ataxia. J Clin Sleep Med 10(5):535-43.

Steriade M, Hobson J (1976) Neuronal activity during the sleep-waking cycle. Prog Neurobiol 6(3-4):155-376.

Sullivan D, Mizuseki K, Sorgi A, Buzsáki G (2014) Comparison of sleep spindles and theta oscillations in the hippocampus. J Neurosci 34(2):662-74.

Tiriac A, Del Rio-Bermudez C, Blumberg MS (2014) Self-generated movements with “unexpected” sensory consequences. Curr Biol 24(18): 2136-2141.

Van Luijtelaar EL, Miller CA, Coenen AM, Drinkenburg WH, Ellenbroek BA (1998). Differential effects of non-REM and REM sleep on sensory gating in rats. Acta Neurobiol Exp (Wars) 58(4):263-270.

Vogelstein JT, Watson BO, Packer AM, Yuste R, Jedynak B, Paninski L. 2009. Spike Inference from Calcium Imaging Using Sequential Monte Carlo Methods. Biophysical Journal 97:636–655.

Vrieler N, Loyola S, Yarden-Rabinowitz Y, Hoogendorp J, Medvedev N, Hoogland TM, De Zeeuw CI, De Schutter E, Yarom Y, Negrello M, Torben-Nielsen B, Uusisaari MY (2019).Variability and directionality of inferior olive neuron dendrites revealed by detailed 3D characterization of an extensive morphological library. Published in Brain structure and function. 224(4):1677-1695.

Xie L, Kang H, Xu Q, Chen MJ, Liao Y, Thiyagarajan M, O'Donnell J, Christensen DJ, Nicholson C, Iliff JJ, Takano T, Deane R, Nedergaard M (2013) Sleep drives metabolite clearance from the adult brain. Science 342(6156) : 373-377.

Yüzgeç Ö, Prsa M, Zimmermann R, Huber D (2018) Pupil Size Coupling to Cortical States Protects the Stability of Deep Sleep via Parasympathetic Modulation. Curr Biol 28(3):392-400.e3.

Zang Y, De Schutter E (2019) Climbing Fibers Provide Graded Error Signals in Cerebellar Learning. Front Syst Neurosci 13:46.

Zhang L, Zhang J, Sun M, Chen H, Yan J, Luo FL, Yao ZX, Wu YM, Hu B (2020) Neuronal Activity in the Cerebellum During the Sleep-Wakefulness Transition in Mice. Neurosci Bull 36: 919–931.

Zhou P, Resendez SL, Rodriguez-Romaguera J, Jimenez JC, Neufeld SQ, Giovannucci A, Friedrich J, Pnevmatikakis EA, Stuber GD, Hen R, Kheirbek MA, Sabatini BL, Kass RE, Paninski L (2018) Efficient and accurate extraction of in vivo calcium signals from microendoscopic video data. eLife 7:e28728.

Chapter 5

General Discussion

In this thesis, I address various anatomical and functional aspects of the inferior olive (IO) nucleus, a brain stem structure that is essential for motor coordination and learning. I study inferior olive function at the level of individual neurons, in vivo circuits and during behavior in awake and sleeping mice. I also present a new tool for improved animal pose estimation, which can be applied towards better quantification of animal movement. In Chapter 2, I show that olivary neurons cannot be clustered in two distinct morphological categories based on their dendrite morphology (‘straight’, and ‘curly’, e.g. Scheibel and Scheibel, 1955; Devor and Yarom, 2002a), but rather lie along a morphological continuum. Moreover, I demonstrate that the dendritic trees of IO neurons have a strong directionality supporting the hypothesis that IO neurons form anatomical clusters. In Chapter 3, I show how excitatory and inhibitory inputs to the IO, arising from the mesodiencephalic junction (MDJ) and cerebellar nuclei (CN) respectively, affect subthreshold oscillations (STOs) in IO neurons and how their output is modulated. I find that both excitatory (MDJ) and inhibitory (CN) afferents to the IO can elicit transient STOs in a subset of non-oscillating neurons. The hyperpolarizing component of synaptic responses evoked by either of these inputs determines the amplitude and timing of such induced oscillations. In spontaneously oscillating IO neurons, the excitation or inhibition presented either independently or jointly at specific intervals differentially affect the oscillation amplitude, phase resetting and phase-locking. Here, inhibition causes strong phase-resetting, setting a specific time window during which ensuing excitation either mildly affects the amplitude of subsequent oscillation cycles, reduces phase-locking and suppresses spike generation, or alternatively, boosts oscillation amplitude, facilitates phase-locking and increases the generation of spikes. Using the timing intervals between inhibition and excitation that depress or facilitate the generation of spikes in the IO in vitro, I demonstrate that such intervals can facilitate or suppress reflexive motor learning in vivo. In Chapter 4, I describe how complex spike firing changes in cerebellar microzones during sleep showing sleep state specific changes in complex spike firing and pairwise spatial correlations.

5.1 A morphological map of IO neuron morphology

5.1.1 IO dendritic morphology

It has been proposed that IO neurons can be classified into two groups based on the morphology of their dendritic trees: neurons with dendritic branches forming spirals that curl back, referred to as 'curly neurons', and neurons with more straight branches that radiate away from the soma, referred to as 'straight neurons' (Scheibel and Scheibel, 1955; Devor and Yarom, 2002a). In line with these anatomical categorizations, it was first proposed that these two groups could have distinct physiological properties with straight neurons lacking STOs (and T-, and N-type calcium channels) and exhibiting high firing frequencies whereas curly neurons exhibiting STOs and low firing frequencies (Urbano et al., 2006). Straight cells were believed to be localized in specific IO subnuclei such as ventrolateral outgrowth, dorsal cap of Kooy (Urbano et al. 2006) and caudal part of MAO (Scheibel and Scheibel, 1995), while curly neurons were thought to reside in the PO, rostral part of MAO and DAO (De Zeeuw et al., 1998). The anatomical and functional classification of IO neurons has since been challenged by others (Bazigaluppi and De Jeu, 2016) and also in our present study. From a functional perspective, T-type calcium channel (Cav3.1) density is highest in the DCK and required to sustain STOs (Choi et al., 2010) and would suggest that the largest fraction of oscillating neurons consequently lies in this IO subnucleus (Bazzigaluppi and De Jeu., 2016). However, this is not corroborated by electrophysiological recordings in this nucleus (Urbano et al., 2006). In Chapter 2, I present new evidence that IO neurons cannot be classified in two distinct classes of 'curly' or 'straight' cells, but rather form a continuum between these extremes. This discrepancy can in part be explained by the more quantitative rather than qualitative approach that I employed to chart IO neuron morphology by using high-resolution confocal imaging and 3D morphological reconstruction.

5.1.2 Anatomical clustering of IO neurons

Inferior olive neurons are electrically coupled through gap junctions but if these neurons are arranged in anatomical clusters is still a matter of debate. Although there is some support for the organization of IO neurons in clusters, the methods used to study them give highly variable outcomes. For example, voltage-sensitive dye imaging in brain slices revealed olivary clusters consisting of hundreds of neurons (Leznik and Llinás, 2002) while intracellular injection of small molecules (e.g. neurobiotin, or biocytin) that readily cross connexin 36 containing gap junctions -

that are densely expressed in IO neurons- exhibit smaller clusters that comprised up to a dozen neurons (Turecek et al., 2014; Devor and Yarom, 2002; Hoge et al., 2011; Placantonakis et al., 2006). Thus far, there has not been careful scrutiny of how the arrangement of dendritic morphology could add additional proof for the existence of anatomical clusters of IO neurons. In Chapter 2 I provide new evidence that supports the organization of IO neurons in anatomical clusters as indicated by a strong directionality of the dendritic trees of IO neurons irrespective of their proximity to the borders of the subnucleus in which they are localized. In one striking example of a big cluster of 28 IO biocytin-coupled neurons obtained during a whole-cell patch-clamp recording of a single neuron, this directionality was particularly well illustrated. This cluster was associated with two large cells with straighter dendrites that emanated away from the cluster and could hint at the existence of bridge cells that span clusters. This would be in line with theoretical models that suggest that such an organization is likely to exist and can account for spontaneous frequency changes and phase differences of STOs observed in simultaneous recordings of IO neurons (Torben-Nielsen et al., 2012). This would underlie the phenomenon of propagating waves of subthreshold activity in the IO (Devor and Yarom, 2002b).

5.2 The role of cerebellar nuclei and midbrain afferents in shaping the STOs and output of IO neurons.

5.2.1 Impact of CN and MDJ afferents on conditional oscillators

A significant fraction of IO neurons (~30%, as shown in Chapter 3) does not exhibit subthreshold oscillations. Within this population, a subset shows transient oscillations following negative current injection (Bazzigaluppi and De Jeu, 2016) and suggests that hyperpolarization is required to initiate these transient events. Both afferent stimulation of CN and MDJ axons can elicit synaptic responses in IO neurons that contain a hyperpolarizing component as evidenced by recordings obtained from non-oscillating neurons (Garden et al., 2017; Lefler et al., 2014). In Chapter 3 I assess whether these synaptic responses can induce transient STOs in IO neurons. I find that both CN and MDJ afferent stimulation can trigger transient STOs in a subset of otherwise non-oscillating neurons. The amplitude of the inhibitory component of these synaptic responses is critical in modulating the amplitude and onset of the subsequent STOs. STOs induced by inhibitory CN afferents outlast those induced by excitatory MDJ afferents. This difference could be caused by the more prolonged asynchronous release of GABA by CN terminals (Best and Regehr, 2009; Turecek and Regehr, 2019). The present results differ from a

previous study where stimulation of excitatory input to the IO did not elicit transient oscillations (Garden et al., 2017). A reason could be the reduced slice thickness in these studies that would result in a reduction in the number of gap-junction coupled IO neurons and consequently a reduced number of oscillating neurons (Lampl and Yarom, 1997).

In conclusion, these findings contribute to a better understanding of how transient oscillations can be induced by inhibitory and excitatory inputs in otherwise silent IO neurons. This is highly relevant given that there has not been any confirmation that IO neurons display intrinsic STOs in awake animals.

5.2.2 Impact of CN and MDJ afferents on oscillating neurons

STOs are modulated by single-cell properties such as capacitance (Turecek et al., 2016) and membrane potential (Choi et al., 2010) that control their frequency and amplitude respectively. Moreover, network properties, such as the level of gap-junctional coupling, can act as a homeostat for determining the sensitivity of STO amplitude to membrane voltage (De Zeeuw et al., 2003). To what extent synaptic inputs modulate STOs has not been studied in detail and comparatively little data exists on the phase-response properties in response to excitatory or inhibitory inputs. In Chapter 3, I show the differential impact of inhibitory and excitatory synaptic inputs on STOs. The level of impact also depends on whether the evoked responses are subthreshold or suprathreshold. Inhibitory subthreshold synaptic responses cause strong phase resetting and locking and a significant, albeit transient increase of the oscillation amplitude. Thus, CN subthreshold synaptic responses can reliably set the timing of the ensuing cycles and drive the cell to more readily reach spike. The probability to trigger output is further enhanced if an excitatory synaptic response hits the rebound of the reset oscillation, or the cycle following it. Indeed, it has been shown that the occurrence of evoked or spontaneous doublets (rebound spikes following another one) is increased when IO gap-junctional coupling is blocked (Van der Giessen et al., 2008) which resembles, on a shorter time scale, the transient decrease in coupling exerted by CN input (Lefler et al., 2014).

The present study differentiates itself from earlier work that used high frequency trains of inhibitory stimulation (trains of stimulation up to ~17Hz for ~ 2s) to block STOs (Lefler et al, 2014), a response that is not observed with the single-pulse stimulation used here. Short-duration, single-pulse stimulation is likely to cause gap-junctional shunting and a transient decoupling of the recorded neuron from its neighbors. This can contribute to strong phase-locking and phase-resetting (Bazzigaluppi et al., 2012) because it prevents STOs frequency from being modified by

electrical activity arising from other neurons (Torben-Nielsen et al., 2012). Oscillation amplitude increases are the result of the large rebound depolarization following a hyperpolarization elicited by CN input which in turn increase the driving force of the currents underlying the STOs (Llinás and Yarom, 1981; Bal and McCormic, 1997) for a period of at least 4 cycles following stimulation. In the case of more persistent inhibitory input, STOs are likely to shut down due to a mechanism that involves both gap-junctional decoupling and dendritic shaft shunting (Lefler et al., 2014).
CN synaptic responses can trigger spikes if the depolarizing rebound component is close to spike threshold. Suprathreshold synaptic responses evoked by CN inputs can also increase oscillation amplitude and elicit a strong phase reset, but unlike CN subthreshold synaptic responses, result in weak phase-locking. This suggests that a spike triggered by CN input mitigates the phase-locking effects seen with CN subthreshold synaptic stimulation. The underlying mechanism could involve modulation of the gap-junction coupling coefficient.

I show here that MDJ subthreshold synaptic responses have a weaker impact on STOs than CN synaptic responses. This is reflected by the smaller oscillation amplitude increase and weaker phase resetting and phase locking. The transient amplitude increase for the first oscillation cycle is similar in magnitude to the persistent oscillation amplitude increase observed during pharmacological activation of NMDA receptors (Turecek et al., 2014). Phase resetting and phase-locking are weak with excitatory input because the hyperpolarizing component of the synaptic response is small in the presence of STOs. An explanation can come from the fact that ion channels underlying this component -SK and I_h channels (Garden et al., 2017 and Garden et al., 2018)- are also involved in the generation of STOs (Marshall and Lang, 2004; Bal and McCormick, 1997). The rhythmic deactivation and inactivacion of SK and I_h channels respectively reduce the probability to elicit calcium spikes in olivary dendritic spines which could result in a significantly reduced hyperpolarizing component (Kistler and De Zeeuw, 2005). The size of the hyperpolarizing component also depends on the number of electrically coupled neurons (Kistler and De Zeeuw, 2005; Garden et al., 2018) and thus not only single cell biophysics, but also the state of the IO network. When MDJ afferent stimulation triggers spikes, the oscillation amplitude of the first post-stimulus cycles is more strongly enhanced and the phase strongly reset, while phase-locking is weak. The large afterhyperpolarization that follows the spike elicited by MDJ afferent stimulation can account for the first two observations, whereas the weak phase locking could be associated with a transient increase in electrical coupling (Turecek et al., 2014).

5.2.3 Temporal interactions of CN and MDJ afferents and their impact on STOs and output

One of the striking features of the inferior olive is the synaptic organization of its neuropil into “glomeruli”. Each glomerulus consists of 5 to 6 long and thin dendritic spines derived from different IO neurons that are electrically coupled through gap-junctions. In addition, olivary spines are contacted by synaptic boutons of MDJ and CN afferents and surrounded by a glial sheath (De Zeeuw et al., 1990). This arrangement is ideal to implement AND-NOT gates (Segev and Parnas, 1983; De Zeeuw et al., 1998). There is some experimental evidence for the existence of logic gates in neurons, such as the XOR gate in cortical L2/3 dendrites (Gidon et al.,2020) or AND gate mediating synaptic plasticity in striatal neurons (Girault et al., 2007), but so far no experimental verification of the existence of AND-NOT gate in the IO (Shepherd and Brayton, 1987), which is also dependent on the timing of the inputs. This type of time-dependent logic gate is referred as to ‘dynamic logic gates’ (Goldental et al., 2014). In Chapter 3, I address whether such logic exists in the inferior olive. Specific temporal intervals of inhibition followed by excitation tune oscillation amplitude, phase-locking, phase resetting and output. For example, phase-locking is weak, post-stimulus oscillation amplitude weakly increased and spike output suppressed when excitation arrives 50 ms after inhibition (+50 ms). When this time interval is extended to 150 ms (+150 ms) the oscillation phase is strongly reset, phase-locking is apparent, oscillation amplitude significantly increased and output facilitated. This phenomenon is readily explained by the fact that at the 50 ms interval excitation occurs at the trough of the inhibitory component of CN synaptic response. It is likely that the oscillation amplitude is only weakly increased at this time interval because MDJ afferent excitation deactivates and inactivate I_h and T-type calcium channels respectively, that drive intrinsic oscillations (Bal and McCormick, 1997; Bazzigaluppi and De Jeu, 2016, Llinás and Yarom, 1981). By contrast, when MDJ input arrives 150 ms after inhibition it typically occurs around the peak of the rebound that follows the CN inhibition. Thus, spike output is facilitated and the following cycle is boosted to lesser extent but significantly higher than second cycle boost following +50 ms stimulation thereby an increased probability of eliciting a doublet exists at +150 ms if membrane voltage is close to spike threshold. At this time interval, oscillation phase can be both delayed or advanced depending on the phase at which the paired stimulus is presented thereby providing enhanced temporal control over complex spike firing. This finding also becomes relevant even if the cell is not oscillating as it shows that this time interval controls the time lag from the stimulus onset to the rebound peak in a membrane voltage-dependent manner. Furthermore, when spikes are triggered at the +150 ms time window phase locking is even more

pronounced. This can be the result of an enhanced decoupling of IO neurons caused by a synergistic effect of both synaptic responses. Therefore, MDJ suprathreshold synaptic response following inhibition at this time interval would increase the phase-locking which contrasts with the low phase-locking caused by it in the absence of inhibition. This implies that MDJ suprathreshold synaptic response would have a dual function in increasing or decreasing phase-locking which might come from their ability to bidirectionally control coupling, a calcium-dependent process in dendritic spines that is mediated by NMDA receptors (Grujil et al., 2014). Furthermore, I test time windows other than +50 ms and +150 ms to assess their effect on STOs and output. I find that time intervals where MDJ synaptic response either precedes (-100 ms, -50 ms) or follows (0 ms, +30 ms, +70ms, +100, +200 ms) CN synaptic responses also modulate differentially STOs phase and amplitude whereas output probability remains low.

Taken together, specific time intervals of inhibition and excitation act differentially on the STO phase and amplitude as well as the output of IO neurons thereby providing a mechanism to gate signals entering the IO. Thus, IO neurons are set up to gate out predictable sensory signals during cerebellar-dependent behavior (Lawreson et al., 2016). The ability to control the degree of phase-locking and resetting with different combinations of inhibition and excitation is relevant for motor control, which is state-dependent. For example, synchronous activation of Purkinje cells triggers body movements at rest, but causes them to stop or slow down during ongoing locomotion (Hoogland et al. 2015). Moreover, controlling the timing of complex spikes generation by changing the temporal interplay of inhibition and excitation is also relevant for cerebellar-dependent motor learning. For example, acquired complex spike responses to conditioned stimulus (CS) during eyeblink conditioning would have important roles in modulating the conditioned response (Ten Brinke et al., 2015), anticipating the upcoming unconditioned stimulus (US) as well as encoding the novelty of the CS (Ohmae and Medina, 2015).

5.2.4 Temporal interactions of CN and MDJ afferents and their impact on motor learning

Synaptic plasticity at the parallel fiber (PF) to Purkinje cell (PC) synapses in the cerebellar cortex underlies cerebellar-dependent motor learning (Ito et al., 2001). Long-term depression (LTD) of these synapses occurs when parallel fiber input is jointly activated with the climbing fiber (CF) input within a specific time window (Safo and Regher, 2008; Wang et al., 2000). By contrast, long-term potentiation (LTP) occurs when PF input is activated in the absence of CF input. The dependence on the timing of CF and PF input means that mechanisms need to be in place to

control under which behaviorally relevant conditions CF and PF inputs are active to successfully adapt behavior in the future. In Chapter 3 I have shown how the presentation of CN inhibition and MDJ excitation at specific time intervals affect the timing and probability of complex spikes. In that Chapter I build on our knowledge of the time intervals that suppress, or facilitate complex spike output, to address what the consequences are for a specific motor learning paradigm. I employ a whisker-reflex learning paradigm, that has been previously described (Romano et al., 2018), in which presentation of a 20-s period of 4 Hz air-puff stimulation to the whisker pad results in enhanced whisker protraction through an LTP-dependent mechanism. I chose this paradigm because whisker representations in cerebellar lobules Crus I and Crus II receive olivary inputs from both subnuclei principal olive (PO) and rostral MAO (rMAO) (App and Hawkes et al., 2009), the subnuclei from which I also obtained in vitro recordings. I could thus address the hypothesis that specific input pairings to the IO differentially affect the capacity to adapt whisker movement, with increased protraction of whiskers at time intervals that suppress complex spike activity. Based on our knowledge of facilitatory and suppressing temporal intervals for spike initiation in the IO, I paired 4 Hz air-puff stimulation during an induction protocol with CN and MDJ input at +50, or +150 ms intervals, to respectively suppress or enhance spike output during the induction phase of learning. Preliminary results show that behavioral output following stimulation with both intervals was variable in terms of amplitude and direction of the whisker reflexes. However, and despite this variability, +50 ms stimulation induced a larger amplitude of the whisker reflexes than +150 ms stimulation, suggesting that specific temporal intervals of excitatory and inhibitory synaptic inputs would allow a LTP-dependent mechanism that would have a bigger influence on whisker reflex learning irrespective of the direction of the movement. High variability of the amplitude and direction of the movements can be due to multiple factors such as complex spike frenquency triggered by stimulation, IO subnuclei stimulated and their contra/ipsi lateral location with respect to the side of stimulation (Kitazawa et al., 1998; Romano et al., 2018; Kubo et al., 2018).

5.3 Modulation of complex spike activity during sleep

Sleep is an evolutionary conserved animal behavior that has been linked to fundamental functions such as memory consolidation, immnunity and the clearing of metabolites (Basedovsky et al., 2019; Klinzing et al., 2019; Xie et al., 2013). It can be divided into two main stages: rapid eye movement or REM sleep and non-rapid eye movement or NREM sleep. REM sleep is characterized by saccadic eye movements and cortical theta activity, which is noncontinuous but

abundant in rodents. In this sleep stage muscle activity is suppressed and dreams occur (Scammel et al., 2017). NREM sleep can be divided into three sub-stages (NREM1, NREM2 and NREM3), each of which is characterized by specific electroencephalogram (EEG) patterns such as K waves (NREM2), spindles (NREM2 and NREM3) and slow waves with high amplitudes (NREM3, Canto et al., 2017). These sub-stages of NREM sleep are thought to be crucial for the consolidation of memory and learning (Piantoni et al., 2016; Ulrich 2016; Klinzing et al., 2019). Considering that cerebellar dysfunctions can lead to sleep disorders (Pedroso at al., 2011; Sonni et al., 2014), surprisingly little is known about the engagement of the olivo-cerebellar circuit during sleep. To address this knowledge gap EEG and electromyograph (EMG) recordings were performed in mice in conjunction with miniscope imaging of complex spike (CS) activity in Purkinje cell dendrites during sleep. The aggregate rate of CS decreased from NREM 1 to NREM 2 and increased from NREM3 to REM stages of sleep. This higher CS rate exhibited during REM sleep with respect to late stages of NREM sleep are in line with previous studies which have also revealed a more elevated rate of CS firing during REM sleep. This could be partially attributed to the presence of rapid eye movements during this sleep stage (Hobson and McCarley, 1972). A drop in CS firing rates from NREM1 to NREM2 and an increase from NREM3 to REM is expected if one considers that the arousal threshold (defined as the occurrence of arousal from sleep with a small rise in ventilatory drive) and therefore the ability for sensory stimuli to trigger CS differs by sleep stage (Scammel et al., 2017). Indeed, previous studies haves shown that the arousal threshold is lower during the light phase of NREM sleep (NREM1) and most elevated at the latest stage of NREM sleep (NREM3) (Scammel et al., 2017; Franco et al., 2010; Rechtschaffen et al., 1966).

By imaging from dozens of neighboring Purkinje cell dendrites at the same time it was possible to determine the level of co-activation of complex spikes. Co-activation rate -expressed as the co-firing of more than 10% of all segmented dendrites per second- was reduced from NREM1 to NREM2 and from NREM2 to NREM3 whereas REM sleep showed co-activation rates similar to NREM3. Low co-activation rates during NREM3 seems to reflect the slow and highly synchronized neocortical waves observed during this sleep stage. Indeed, previous studies in anesthetized mice have shown that CS activity follows the up and down states of slow waves by increasing or decreasing its rate (Ros et al., 2009). Low co-activation rate during REM might be caused by the desynchronized cortical activity observed during this sleep stage (Frauscher et al., 2010).

The amplitude of calcium transients triggered by complex spikes were previously shown to relate to the strength of sensory stimulation (Nafaji et al., 2014), presumably due to a stronger resetting of the inferior olive. We looked at calcium transient amplitudes across the different sleep

stages. The largest amplitude transients were found during wakefulness in line with increased sensory gating during sleep (Allada and Wu., 2017). Lower amplitudes were observed during both NREM and REM sleep. This contrasts with findings in rats where REM sleep showed a lower sensory gating in comparison to NREM sleep (van Luijtelaar et al., 1998). Finally, CV_2 values were measured to assess the regularity of the CS. Even with this rather crude approach, we found that complex spike firing during NREM2 and NREM3 was more irregular relative to other sleep stages. This is in line with previous studies showing irregular firing during the up state of the slow waves typical of NREM3 sleep (Steriade et al., 1993).

Pairwise correlations of complex spike events were analyzed as a function of mediolateral separation of Purkinje cell dendrites during wakefulness and each of the four analyzed sleep stages. Although nearby dendrites were more strongly correlated than those separated by greater distances across all stages, event correlations remained elevated across greater medio-lateral distances during NREM1 and REM. By contrast, event correlations spanning a cerebellar micrzone (~200 μm) were more suppressed during NREM2 and NREM3 relative to wakefulness, NREM1 and REM sleep. The reduced spatial correlations seen in the cerebellar cortex do not reflect the widespread waves of synchronous activity in the cerebral cortex observed during deeper stages of sleep (i.e. NREM2 and NREM3; Ioannides et al., 2017; Canto et al., 2017) suggesting it is at least partially gated at the level IO (Marshall and Lang, 2004) during sleep.

We measured neck muscle (EMG) activity in the wake state and across sleep stages during miniscope recordings of cerebellar cortical activity. Neck muscle activity was observed across all sleep stages, including REM sleep. This contrasts with previous work where muscle activity during REM was found mainly in the masseter and ocular muscle but not in the neck (Anaclet et al., 2010). We cannot exclude however, that some of the signal picked up by our electrode recordings from the neck muscle reflect cross-over signal from masseter muscle contraction. Using our EMG recordings, we triggered calcium transients off of movement onsets. This allowed us to determine during each sleep stage to what extent complex spikes are triggered by and if such activity precedes or follows the onset of a movement. Across all sleep stages the peak CS response occurred after onset of a movement. The peak response varied from one stage to the next, with the largest response seen during NREM1 sleep. During REM sleep two clearly discernible peaks were observed separated by several hundreds of milliseconds. These peaks did not correspond to repetitions in movement observed in the EMG signal. Moreover, there was no clear distinction in terms of average movement when comparing mean EMG responses across all stages of sleep. These could potentially arise from the cortical desynchronized activity observed during this stage

(Frauscher et al., 2010), which could lead to generate responses in the cerebellum with different lags.

5. 4 Future perspectives

In this thesis, I present new data on crucial anatomical and functional aspects of the inferior olive that helps to understand how the network is anatomically organized and how synaptic integration of excitatory and inhibitory inputs and its temporal interplay affects subthreshold and suprathreshold activity. In addition, I introduce a tool that more accurately tracks animal behavior than current available programs. However, there are still open questions waiting to be addressed. For example, the distribution of straighter cells and curlier cells among different IO subnuclei has not been investigated but would be useful to test the hypothesis that anatomical clusters of IO neurons consist mainly of curlier bridged to other clusters via more sparse straighter cells. Moreover, it is not clear if such anatomical arrangement is present across all IO subnuclei. Serial-sectioning EM of IO neuropil in combination with computational tools now available to more readily reconstruct small anatomical circuits at high resolution could add evidence for the existence of straight cells linking clusters of IO neurons. In addition, electrophysiological experiments should reveal whether anatomical variety across IO neurons coincides with a different functional phenotype. Finally, it remains to address the question of whether the putative anatomical cluster of IO neurons supports the dynamic changes of the spatial arrangement of clusters observed in the cerebellar cortex during movement (Welsh et al., 1995).

A question that has still not been addressed due to the complex nature of the required whole-cell patch-clamp recordings, or voltage imaging is whether IO neurons display intrinsic oscillations in the awake state. Overcoming this challenge will provide direct proof for the role of oscillatory activity during ongoing motor control and motor learning. Irrespective of the outcome of these studies, I show that a subset of IO neurons do respond to synaptic input with transient oscillations. Both inhibition and excitation can elicit this oscillatory behavior and their relative timing could dictate oscillation phase and spike probability over the course of a few oscillation cycles. These findings have been supported by a recent in vivo study, which demonstrated that sensory stimulation induces a transient and rhythmic firing of complex spikes (Negrello et al., 2019). On the other hand, the existence of persisting oscillations in the IO has been indirectly supported by a study that shows a highly rhythmic and synchronous complex spike activity in the cerebellar cortex during licking (Welsh et al., 1995).

Another outstanding question is what mechanisms determine the level of phase-locking when synaptic inputs are stimulated individually or in combination. This could be contingent on changes in the coupling coefficient of gap junctions that are widely expressed in IO neurons. Experiments thus remain to prove how fluctuations in the coupling coefficient affect phase locking.

Apart from continuing the studies of the impact of synaptic inputs on IO neurons in awake animals during a learning paradigm, from which should be elucidated the contribution of each IO subnuclei, it would be also important to focus on their impact on motor performance. Moreover, it has been shown that complex spikes are also involved in encoding non-motor tasks such as reward expectation, reward size, delivery, and omission (Kostadinov et al., 2019; Larry et al., 2019). This gives rise to further questions about the impact of the excitatory and inhibitory synaptic inputs and its temporal interplay on the modulation of these non-motor tasks.

Although in this thesis the first data on sleep stage dependent changes in complex spike firing in cerebellar microzones are presented, further studies are required to unravel the contribution of the olivo-cerebellar circuit to memory formation, consolidation and learning during sleep. The ability to record concurrently from the cerebellum and cortex (De Groot et al., 2020) will permit future investigations into how the cerebral cortex and cerebellum engage and disengage during such consolidation during sleep.

5.5 References

Anaclet C, Pedersen NP, Fuller PM, Lu J (2010) Brainstem circuitry regulating phasic activation of trigeminal motoneurons during REM sleep. Plos One 5(1):e8788.

Allada R, Wu M (2017) Genetics and genomic basis of sleep in simple model organisms. Principle and practice of sleep medicine (VI edition). ISBN: 978-0-323-24288-2.

Apps R and Hawkes R (2009) Cerebellar cortical organization: a one-map hypothesis. Nat Rev Neurosci. 10(9): 670-681.

Bal T and McCormick DA (1997) Synchronized oscillations in the inferior olive are controlled by the hyperpolarization-activated cation current I(h). J Neurophysiol 77: 3145–3156.

Basedovsky L, Lange T, Born J (2012). Sleep and immune function. Pflugers Arch 463(1): 121-137

Bazzigaluppi P, de Jeu MTG (2016) Heterogeneous expression of T-type Ca2+ channels defines different neuronal populations in the inferior olive of the mouse. Front Cell Neurosci 10: 192.

Bazzigaluppi P, Ruigrok T, Saisan P, De Zeeuw CI, de Jeu M (2012) Properties of the nucleo-olivary pathway: an in vivo whole-cell patch-clamp study. PLoS One 7: e46360.

Canto CB, Onuki Y, Bruinsma B, van der Werf De Zeeuw CI (2017). The sleeping cerebellum. Trends Neurosci. 40(5): 309-323.

Choi S, Yu E, Kim D, Urbano FJ, Makarenko V, Shin HS, Llinás RR (2010) Subthreshold membrane potential oscillations in inferior olive neurons are dynamically regulated by P/Q- and T-type calcium channels: a study in mutant mice. J Physiol 588: 3031–3043.

De Groot A, Den Boom BJG, Van Genderen RM, Coppens J, Van Veldhuijzen J, Bos G, Hoedemaker H, Negrello M, Willuhn I, De Zeeuw CI, Hoogland TM (2020) NINscope: a versatile miniscopes for multi-region circuit investigations. eLife 9: e49987.

De Grujil JR, Sokól PA, Negrello M, De Zeeuw CI (2014) Modulation of electrotonic coupling in the inferior olive by inhibitory and excitatory inputs: integration in the glomerulus. Neuron 81(6): 1215-1217.

De Zeeuw CI, Holstege JC, Ruigrok TJH, Voogd J (1990) Mesodiencephalic and cerebellar terminals terminate upon the same dendritic spines in the glomeruli of the cat and rat inferior olive: an ultrastructural study using a combination of [3H]leucine and wheat germ agglutinin coupled horseradish peroxidase anterograde tracing. Neuroscience 34: 645–655.

De Zeeuw CI, Simpon J, Hoogenraad C, Galjart N, Koekkoek S.K.E, Ruigrok T (1998). Microcircuitry and function of the inferior olive. Cerebellum 21: 391-400.

Devor A and Yarom Y (2002a) Electrotonic coupling in the inferior olive nucleus revealed by simultaneous double patch recordings. J Neurophysiol 87: 3048-3058.

Devor A and Yarom Y (2002b) Generation and propagation of subthreshold waves in a network of inferior olivary neurons. J Neurophysiol 87(6): 3059-3069.

Franco P, Kato I, Richardson HL, Yang JS, Montemitro E, Horne RS (2010) Arousal from sleep mechanisms in infants. Sleep Med 11(7):603-614.

Frauscher B, von Ellenrieder N, Dubeau F, Gotman J (2016) EEG desynchronization during phasic REM sleep suppresses interictal epileptic activity in humans. Epilepsia 57(6):879-888.

Garden DLF, Rinaldi A, Nolan MF (2017) Active integration of glutamatergic input to the inferior olive generates bidirectional postsynaptic potentials. J Physiol 595: 1239–1251.

Garden DLF, Rinaldi A, Nolan MF (2018) Inferior olive HCN1 channels coordinate synaptic integration and complex spike timing. Cell Rep 22: 1722-1733.

Gidon A, Zolnik TA, Fidzinski P, Bolduan F, Papoutsi A, Poirazi P, Holtkamp M, Vidal I, Larkum ME (2020) Dendritic action potentials and computation in human layer 2/3 cortical neurons. Science 367(6473): 83-87.

Girault JA, Valjent E, Caboche J, Hervé D (2007) ERKS2: a logical AND gate critical for drug-induced plasticity. Curr Opin Pharmacol 7(1): 77-85.

Goldental A, Guberman S, Vardi R, Kanter I (2014) A computational paradigm for dynamic logic-gates in neuronal activity. Front Comput Neurosci 8:52.

Hobson JA, McCarley RW (1972). Spontaneous discharge rates of cat cerebellar Purkinje cells in sleep and waking. Electroencephalogr Clin Neurophysiol 33(5): 457-469

Hoogland TM, De Gruijl JR, Witter L, Canto CB, De Zeeuw CI (2015) Role of synchronous activation of cerebellar Purkinje cell ensembles in multi-joint movement control. Curr Biol 25: 1157–1165.

Hoge GJ, Davidson KG, Yasumura T, Castillo PE, Rash JE, Pereda AE (2011) The extent and strength of electrical coupling between inferior olivary neurons is heterogenous. J Neurophysiol 105: 1089-1101.

Ioannides AA, Liu L, Poghosyan V, Kostopoulos GK (2017) Using MEG to understand the progression of light sleep and the emergence and functional roles of spindles and K-complexes. Front Hum Neurosci 11: 313.

Ito M (2001) Cerebellar long-term depression: characterization, signal transduction, and functional roles. Physiol Rev 81(3): 1143-1195.

Kistler WM and De Zeeuw CI (2005) Gap junctions synchronize synaptic input rather than spike output of olivary neurons. Prog Brain Res 148: 189-197.

Kitazawa S, Kimura T, Yin PB (1998) Cerebellar complex spikes encode both destinations and erros in arm movements. Nature 392 (6675): 494-497.

Klinzing JG, Niethard N, Born K (2019). Mechanisms of systems memory consolidation during sleep. Nat Neurosci 22(10): 1598-1610.

Kubo R, Aiba A, Hashimoto K (2018) The anatomical pathway from the mesodiencephalic junction to the inferior olive relays perioral sensory signals to the cerebellum in the mouse. J Physiol 596(16): 3775-3791.

Kostadinov D, Beau M, Blanco-Pozo M, Häusser M (2019) Predictive and reactive reward signals coveyed by climbing fiber input to cerebellar Purkinje cells. Nat Neurosci 22(6): 950-962.

Lampl I and Yarom Y (1997) Subthreshold oscillations and resonant behavior: two manifestations of the same mechanism. Neuroscience 78(2): 325-341.

Larry N, Yarkoni M, Lixenberg A, Joshua M (2019) Cerebellar climbing fibers encode expected reward size. Elife 8: e46870.

Lawrenson C, Watson T, Apps R (2016) Transmission of predictable sensory signals to the cerebellum via climbing fiber pathways is gated during exploratory behavior. J Neurosci. 36(30): 7841-7851.

Lefler Y, Yarom Y, Uusisaari MY (2014) Cerebellar inhibitory input to the inferior olive decreases electrical coupling and blocks subthreshold oscillations. Neuron 81: 1389–1400.

Leznik E, Makarenko V, Llinás R (2002). Electrotonically mediated oscillatory patterns in neuronal ensembles: An in vitro voltage-dependent dye-imaging study in the inferior olive. J Neurosci. 22(7): 2804-2815.

Llinás R and Yarom Y (1981) Properties and distribution of ionic conductances generating electroresponsiveness of mammalian inferior olive neurones in vitro. J Physiol 315: 569-584.

Marshall SP and Lang EJ (2004) Inferior olive oscillations gate transmission of motor cortical activity to the cerebellum. J Neurosci 24(50): 11356-11367.

Najafi N, Giovanucci A, Wang SS, Medina F (2014) Coding of stimulus strength via analog calcium signals in Purkinje cell dendrites of awake mice. Elife 3:e03663.

Negrello M, Warmaar P, Romano V, Owens CB, Lindeman S, Lavarone E, et al (2019) Quasiperiodic rhythms of the inferior olive. PloS Comput Biol 15(5): e1006475.

Ohmae S and Medina JF (2015) Climbing fibers encode a temporal-difference prediction error during cerebellar learning in mice. Nat Neurosci 18(2): 1798-1803.

Pedroso JL, Braga-Neto P, Felício AC, Aquino CC, Prado LB, Prado GF, Barsottini OG (2011). Sleep disorders in cerebellar ataxia. Arq Neuropsiquiatr 69(2A): 253-257

Piantoni G, Halgren E, Cash SS (2016). The contribution of thalamocortical core and matrix pathways to sleep spindles. Neural Plast. 2016: 3024342.

Placantonakis, D.G., Bukovsky, A.A., Aicher, S.A., Kiem, H.P., and Welsh, J.P. (2006). Continuous electrical oscillations emerge from a coupled network: a study of the inferior olive using lentiviral knockdown of connexin36.J Neurosci 26: 5008–5016.

Prsa M, Thier P (2011). The role of the cerebellum in saccadic adaptation as a window into neural mechanisms of motor learning. Eur J Neurosci 33(11): 2114-2128.

Rechtschaffen A, Hauri P, Zeitlin M (1966) Auditory awakening thresholds in REM and NREM sleep stages. Percept Mot Skills 22(3): 927-942.

Van Luijtelaar EL, Miller CA, Coenen AM, Drinkenburg WH, Ellenbroek BA (1998). Differential effects of non-REM and REM sleep on sensory gating in rats. Acta Neurobiol Exp (Wars) 58(4):263-270.

Romano V, De Propris L, Bosman LWJ, Warnaar P, ten Brinke MM, Lindeman S, Ju C, Velauthapillai A, Spanke JK, Guerra EM, Hoogland TM, Negrello M, D'Angelo E, De Zeeuw CI (2018) Potentiation of cerebellar Purkinje cells facilitates whisker reflex adaptation through increased simple spike activity. eLife 7: e38852.

Ros H, Sachdev RN, Yu, Sestan N, McCormick DA (2009). Neocortical networks entrain neuronal circuits in cerebellar cortex. J Neurosci 29(33): 10309-10320

Safo S and Regher WG (2008) Timing dependence of the induction of cerebellar LTD. Neuropharmacology 54(1): 213-218

Scammell TE, Arrigoni E, Lipton JO (2017). Neural circuitry of wakefulness and sleep. Neuron 93(4): 747-765.

Scheibel ME and Scheibel AB (1955) The inferior olive: a Golgi study. J Comp Neurol 102(1): 77-131.

Segev I and Parnas I (1983) Theoretical and experimental investigation of temporal postsynaptic interactions between excitatory and inhibitory inputs. Biophys J 41: 41-50.

Shepherd GM and Brayton RK (1987) Logic operations are properties of computer-simulated interactions between excitable dendritic spines. Neuroscience 21(1): 151-165.

Sonni A, Kurdziel LB, Baran B, Spencer RMC (2014). The effects of sleep dysfunction on cognition, affect, and quality of life in individuals with cerebellar ataxia. J Clin Sleep Med 10(5): 535-543.

Steriade M, Nuñez A, Amzica F (1993). A novel slow (<1 Hz) oscillation of neocortical neurons in vivo: depolarizing and hyperpolarizing components. J Neurosci 13(8): 3252-3265.

Ten Brinke MM, Boele HJ, Spanke JK, Potters JW, Kornysheva K, Wulff P, IJpelaar AC, Koekkoek SK, De Zeeuw CI (2015) Evolving models of pavlovian conditioning: Cerebellar cortical dynamics in awake behaving mice. Cell Rep 13(9): 1977-1988.

Torben-Nielsen B, Segev I, Yarom Y (2012) The generation of phase differences and frequency changes in a network model of inferior olive subthreshold oscillations. PloS Comput Biol 8(7): e1002580.

Turecek J, Han VZ, Cuzon Carlson VC, Grant KA, Welsh JP (2016) Electrical coupling and synchronized subthreshold oscillations in the inferior olive of the rhesus macaque. J Neurosci 36: 6497–6502.

Turecek J, Yuen GS, Han VZ, Zeng XH, Beyer KU, Welsh JP (2014) NMDA receptor activation strengthens weak electrical coupling in mammalian brain. Neuron 81: 1375–1388.

Ulrich D (2016). Sleep spindles as facilitators of memory formation and learning. Neural Plast 2016: 1796715

Urbano FJ, Simpson JI, Llinás RR (2006) Somatomotor and oculomotor inferior olivary neurons have distinct electrophysiological phenotypes. Proc Natl Acad Sci U S A 103: 16550–16555.

Wang SS, Denk W, Häusser M (2000) Coincidence detection in single dendritic spines mediated by calcium release. Nat Neursci 3(12): 1266-1273.

Welsh JP, Lang EJ, Suglhara I, Llinás R (1995) Dynamic organization of motor control within the olivocerebellar system. Nature 374: 453–457.

Xie L, Kang H, Xu Q, Chen MJ, Liao Y, Thiyagarajan M, O'Donnell J, Christensen DJ, Nicholson C, Iliff JJ, Takano T, Deane R, Nedergaard M (2013) Sleep drives metabolite clearance from the adult brain. Science 342(6156) : 373-377.

Zhou H, Lin z, Voges K, Ju C, Gao Z, Bosman LW, Ruigrok TJ, Hoebeek FE, De Zeeuw CI, Schonewille M (2014). Cerebellar modules operate at different frequencies. Elife 3: e02536.

Summary

In this thesis, I address fundamental aspects of the inferior olive nucleus (IO) that have previously not been studied in detail. These include how the anatomy of IO neurons define IO network organization, how the IO integrates multiple inputs, how such integration affects motor learning ,and how IO activity changes during sleep.

In Chapter 1, I provide an introductory overview of the known functional and anatomical aspects of the IO and highlight the knowledge gaps, some of which have been addressed in this thesis.

In Chapter 2, I demonstrate that classifying IO neurons in two distinct groups based on their dendritic morphology (‘curly’ and ‘straight’) is inaccurate. Using 3D morphological reconstructions and quantitative measures, I show that IO neurons exhibit dendritic morphologies spanning a continuum of morphologies that lies between these two cellular archetypes. Moreover, I show that IO dendrites have a strong directionality which supports the idea that IO neurons form clusters. Using preliminary evidence I propose that ‘straight’ cells bridge clusters of IO neurons.

In Chapter 3, I investigate how the IO integrates inhibitory and excitatory synaptic afferents, originating respectively in the cerebellar nuclei (CN) and mesodiencephalic junction (MDJ). In a subset of non-oscillating neurons, or ‘conditional oscillators’, synaptic afferents can induce transient sub-threshold oscillations (STOs) whose amplitude and timing depend on the magnitude of the hyperpolarizing component ($V_{hyp.}$) of the evoked synaptic potential. I further show that synaptic responses triggered by CN and MDJ afferent stimulation modulate the STOs of intrinsically oscillating neurons affecting both their oscillation amplitude and phase. The degree to which STOs are affected depends strongly on whether inhibitory (CN) or excitatory (MDJ) afferents are stimulated as well as on whether the evoked responses are subthreshold or suprathreshold. I then look at how the timing of CN and MDJ synaptic responses modulates the amplitude and phase of STOs and the output of IO neurons. I find that there are specific intervals that either suppress or enhance the STO amplitude, amount of phase-locking and initiation of spikes. If excitatory input from the MDJ is triggered 50 ms after inhibitory input from the CN (+50 ms) there is a decreased boost of the oscillation amplitude as well as reduced phase-locking and the generation of spikes is suppressed. By contrast, when excitation is triggered 150 ms after inhibition (+150 ms), we see the inverse, with boosted post-stimulus STO amplitudes, increased phase-locking and an increase in the generation of spikes. These findings demonstrate for the

first time how the IO, through its unique oscillatory behavior, sets specific timing intervals for inhibitory and excitatory inputs to generate IO output. My data supports previous hypotheses that predicted an important role for the temporal interplay of these afferents in modulating IO activity. This is especially relevant in light of the close approximation of excitatory and inhibitory afferents on the gap-junction coupled dendritic spines of IO neurons.

Finally, using the knowledge gained on the specific time intervals that suppress or facilitate IO output, I turn to the impact of such interval timing on motor learning. For this purpose, I use a whisker reflex learning paradigm that relies on long-term potentiation (LTP) of parallel fiber to Purkinje Cell (PC) synapses and is associated with an increase of simple activity of Purkinje cells in lobule Crus I and Crus II. This increase in firing is associated with increased whisker protraction. Based on preliminary data, I find that stimulating CN and MDJ input at intervals that suppress IO output are indeed associated with larger sensory evoked whisker protractions and retractions. This suggests that the temporal interplay of CN and MDJ synaptic afferents that projects to the IO play an important role in motor learning.

In Chapter 4, I tackle an important topic that has been largely ignored in sleep research, which is the engagement of the olivo-cerebellar circuit during sleep. By using EEG and EMG along with miniscope recordings, I find that complex spike frequency, complex spike evoked calcium transient amplitude, co-activation and spatial correlations of complex spike firing change during sleep. I also show that, despite such changes, spontaneous twitches are still associated with complex spike activity.

In Chapter 5, I provide an overview of the main findings of my previous Chapters and discuss them in relation to earlier work and previously postulated hypotheses on olivary function. I highlight some of the limitations of the present work and propose topics of future investigation.

Samenvatting

In dit proefschrift behandel ik een aantal fundamentele vraagstukken over de functie van de inferieure olijfkern (IO) die nog niet eerder in detail zijn bestudeerd. Ik laat zien hoe de anatomie van zenuwcellen de netwerk organisatie van de IO kunnen bepalen, hoe de IO excitatoire en inhibitoire inputs integreert en in welke mate deze integratie van invloed is op de output van de IO en motorisch leren. Daarnaast beschrijf ik hoe de activiteit van de IO verandert tijdens slaap.

In Hoofdstuk 1 geef ik een uitgebreid overzicht van de bekende functionele en anatomische karakteristieken van de IO. Ik geef ook aan waar kennis ontbreekt in aanloop naar het adresseren van de vraagstukken in dit proefschrift.

In Hoofdstuk 2 laat ik zien dat de traditionele manier van onderverdelen van IO neuronen in twee types met ‘gekrulde’ en ‘rechte’ dendrieten niet accuraat is. Door gebruik te maken van 3D morfologische reconstructies en kwantitatieve metingen laat ik zien dat de morfologie van IO neuronen op een continuüm ligt. Tevens laat ik zien dat de dendrieten van IO neuronen een sterke directionaliteit vertonen. Dit pleit voor het idee dat IO neuronen zijn gerangschikt in clusters. Ik lever hiervoor experimenteel bewijs aan en poneer de hypothese dat IO neuronen met ‘rechte’ dendrieten een brug vormen tussen clusters.

In Hoofdstuk 3 doe ik verslag hoe inhibitoire en excitatoire synaptische inputs, respectievelijk uit de cerebellaire nuclei (CN) en mesodiencephalische junction (MDJ) worden geïntegreerd in de IO. In een subset van cellen, zogenaamde ‘conditionele oscillatoren’, leidt stimulatie van synaptische afferenten tot de inductie van transiente oscillaties van het membraan potentiaal, waarbij de hyperpolarizerende component van de synaptische response van invloed is op de amplitude en timing van de oscillatie. Ook in cellen die al intrinsiek oscillaties vertonen heeft stimulatie van CN en MDJ afferenten een grote impact op de amplitude en timing van de oscillaties. De mate waarin hangt voor een groot deel af van welke afferenten worden gestimuleerd en of deze onder of boven de vuurdrempel van de cel liggen. Na het in kaart brengen van de impact van de afzonderlijke afferenten laat ik zien hoe de gelijktijdige presentatie en timing ervan IO cellen beïnvloedt. Specifieke intervallen van CN en MDJ stimulatie hebben een tegengesteld effect op de amplitude van oscillaties in de IO, de fase en het vuurgedrag. Als MDJ stimulatie valt in een interval 50 ms na presentatie van CN stimulatie (+50ms) wordt de amplitude verhoging van de oscillatie onderdrukt, lopen de oscillaties minder in fase en wordt de

vuurdrempel verhoogt. Wordt de MDJ stimulatie gepresenteerd met 150 ms na presentatie van CN stimulatie (+150 ms) dan neemt de oscillatie amplitude toe, lopen de oscillaties meer in fase en wordt de vuurdrempel verlaagt. Deze resultaten laten voor het eerst zien dat de IO middels haar intrinsieke oscillaties specifieke tijdsintervallen dicteert die de output van de IO beïnvloeden. Mijn data onderschrijft eerdere hypothesen die een belangrijke rol toeschreven aan de temporele interactie tussen de CN en MDJ afferenten die beiden synaptische contacten maken op gap junction gekoppelde IO spines.

Gebruikmakend van de kennis over de onderdrukkende of faciliterende intervallen van deze contacten kijk ik vervolgens naar hoe deze in rol kunnen in spelen in motorisch leren. Hierbij maak ik gebruik van een snorhaar reflex paradigma waarbij versterkte protractie afhankelijk is van parallel vezel naar Purkinje cell synapse lange termijn potentiatie (LTP). In verkennende experimenten vind ik dat intervallen van CN en MDJ stimulatie die IO output onderdrukken snorhaar protractie en retractie faciliteren. Hieruit kan worden geconcludeerd dat motorisch leren sterk kan worden beïnvloed door de temporele interactie van CN en MDJ afferenten.

In Hoofdstuk 4, snijd ik een belangrijk thema aan dat onderbelicht is in het slaaponderzoek, de de veranderingen die tijdens slaap plaatsvinden in het olivo-cerebellaire netwerk. Door middel van electroencephalogram (EEG), electromyograph (EMG) en calcium imaging met geminiaturiseerde fluorescentie microscopen (miniscopes) vind ik dat het vuren van complex spikes, de amplitude van complex spike gedreven calcium transienten, co-activatie van complex spikes in Purkinje cellen en spatiele correlaties veranderen. Ondanks deze veranderingen zijn kortstondige bewegingen tijdens slaap geassocieerd met complex spike activiteit.

In Hoofdstuk 5 geef ik een overzicht van al mijn bevindingen en plaats deze in de context van eerder werk en bestaande hypothesen over de functie van de olijfkern. Ik zet ook uiteen hoe de uitkomsten van de beschreven experimenten de basis kun.

Personal Information

Name: Sebastián Enrique Loyola Arroyo

Date and place of birth: April 18th, 1985. Santiago, Chile.

Education

- December 2013 – Present: Ph.D student at Erasmus MC and Netherlands Institute for Neuroscience. Promotor: Prof. dr. C.I. De Zeeuw. Copromotor: Dr. Tycho M. Hoogland.

- March 2003- April 2010: Biochemist and Bsc in Biochemistry. University of Santiago, Chile.

Research experience

December 2013 - Present. PhD student in Chris De Zeeuw lab (Cerebellar coordination and cognition group) at Erasmus MC and Netherlands Institute for Neuroscience. Thesis project: *"Impact of excitatory and inhibitory inputs on inferior olive subthreshold oscillations (STOs), output, and motor learning"*.

October 2013 –December 2013. PhD internship in Yosef Yarom's lab at Hebrew University of Jerusalem. Research project*: "Dynamic Control of electrotonic coupling in the Inferior Olive".*

April 2013 –September 2013. Research assistant of Patricio Rojas, Ph.D. at University of Santiago, Chile. Research project: *"Bumetanide as an antipsychotic and antiepileptic drug".*

November 2012 – February 2013. Research assistant in Rudolf Deisz's lab at Charité-Universitätsmedizin Berlin. Research project: *"Functional and molecular characterization of activity induced by KCC2 modulation".*

April 2012 – October 2012. DAAD short term scholarship for young scientists in Rudolf Deisz's lab at Charité-Universitätsmedizin Berlin. Research project: *"Functional and molecular characterization of activity induced by KCC2 modulation".*

July 2011 – February 2012. Research assistant of Patricio Rojas, Ph.D. at University of Santiago, Chile. Research project: *"GABAA characterization and chloride dynamics in the axon initial segment of pyramidal neurons"*.

April 2011 – June 2011. Short term internship in Alfredo Kirkwood lab at Johns Hopkins University. Research projects: *"LTD in NARP mice in visual cortex" and "LTP independent on NMDA receptors in hippocampus"*.

May 2010 – March 2011. Research assistant in Bernardo Morales lab at University of Santiago, Chile. Research projects: *"Molecular and cellular basis of the effect of MDMA (extasis) on synaptic plasticity in visual cortex and hippocampus", "Effects of Methylphenidate on synaptic plasticity in hippocampus and prefrontal cortex*", and *"Effects of gold nanoparticles on synaptic plasticity in hippocampus".*

Honors and awards

2013. Erasmus Mundus's Ph.D fellowship for the Joint Doctorate "Neural Processing of Time".
2012. DAAD short term scholarship for young scientists and doctoral students.
2011. Johns Hopkins University short term scholarship at Zanvyl Krieger Mind/Brain Institute.
2010. IBRO scholarship to attend the course "Mechanisms of Neuroplasticity" at University of Valparaíso. Valparaíso. Chile
2010. SINPOSPq 2010 award for the research "An Acetylated sauroine derivate generates Chem LTP".International Symposium of Pos-graduation and Research (SINPOSPq) .Ribeirao Preto, Brasil.

Publications

Liu X,* Yu S*, Flierman N, Loyola S, Kamermans M, Hoogland T, De Zeeuw CI (2020*).optiFlex: video-based animal pose estimation using deep learning enhanced by optical flow*. Submitted to *Frontiers in Cellular Neuroscience.* *These authors contributed equally to this work.

Zessin M, Strauß, Deisz RA, Rodan Aylin RR, Pleinis JM, Borschewski A, Torsten G, Loyola S, Schindler M, Endlich N, Mrowka R, Maillet M, McCormick JA, Mutig K (2019*).Calcineurin inhibitor cyclosporine A impairs neuronal chloride homeostasis*. Submitted to *Journal of clinical investigation*.

Loyola S, Bosman WJ, De Gruijl JR, De Jeu MTG, Negrello M, Hoogland TM, De Zeeuw CI (2019*).Inferior Olive: All Ins and Outs*. Published in the *Handbook of the Cerebellum and Cerebellar Disorders. Springer, Cham.*

Vrieler N, Loyola S, Yarden-Rabinowitz Y, Hoogendorp J, Medvedev N, Hoogland TM, De Zeeuw CI, De Schutter E, Yarom Y, Negrello M, Torben-Nielsen B, Uusisaari MY (2019*).Variability and directionality of inferior olive neuron dendrites revealed by detailed 3D characterization of an extensive morphological library*. Published in *Brain structure and function.* 224(4):1677-1695.

Vallejo M, Loyola S, Contreras D, Ugarte G, Cifuente D, Ortega G, Cabrera JL, Zeise ML, Tonn C, Carreño M, Morales Band Agnese M (2014*). A new semi-synthetic derivative of sauroine induces LTP in hippocampal slices and improves learning perfomance in the Morris water maze*. Published in *Journal of Neurochemistry.*129(5):864-76.

Loyola S*, Rozas C*, Ugarte M, Zeise ML, Reyes-Parada M, Pancetti F, Morales B (2011). *MDMA acutely applied enhances long term potentiation in the rat hippocampus involving D1 and 5HT-2 receptors through a polysynaptic mechanisms.* Published in *European Neuropsycopharmacology.* 22(8):584-95. *These authors contributed equally to this work.

Lorca RA, Rozas C, Loyola S, Moreira- Ramos, Zeise ML, Kirkwood A, Huidobro-Toro JP and Morales B (2010). *Zinc enhances long term potentiation through P2X receptor modulation in the hippocampal CA1 region*. Published in *European Journal of Neuroscience*. 33(7):1175-1185.

Arias-Cavieres A, Rozas C, Reyes-Parada M, Barrera N, Pancetti f, Loyola S, Lorca R, Zeise M, Morales B (2009). *MDMA ("ecstasy") impairs learning in the Morris Water Maze and reduces hippocampal LTP in young rats*. Published in *Neuroscience Letters*. 469(3):375-9.

Meeting presentations

Loyola S (2019). Modulación de las oscilaciones del núcleo olivar inferior y su impacto en la coordinación motora. *Conversatorio de postgrado en neurociencias y psicología*. Universidad Diego Portales. Santiago. Chile.

Zessin M, Strauss U, Deisz R, Borschweski A, Schindler M, Endlich N, Loyola S, Plennis J, Rondan A, Giesecke T, McCormick J, Mrowka R, Mutig K. Calciuneurin inhibitor impairs the function of neuronal potassium-Chloride Cotransporter 2. Experimental Biology meeting. Orlando, Florida. USA.

Loyola S, Negrello M, Nassirinia F, Isope P, De Zeeuw CI, Hoogland TM (2018*)*.Impact of excitatory and inhibitory afferents on inferior olive subthreshold oscillations (STOs) and motor behavior*. 11th Forum of european neuroscience (FENS). Berlin*. Germany.

Loyola S, Hoedemaker H, Hoogland T, De Zeeuw CI, (2018*)*.Impact of excitatory and inhibitory inputs on inferior olive subthreshold oscillations (STOs).*Peer review meeting. Amsterdam*. The Netherlands.

Loyola S, Negrello M, Hoedemaker H, De Zeeuw CI, Hoogland T (2017*)*.Impact of excitatory and inhibitory inputs on inferior olive subthreshold oscillations (STOs*).Procedural learning summer school. Amsterdam*. The Netherlands

Loyola S (2017). Impact of excitatory and inhibitory inputs on inferior olive subthreshold oscillations (STOs) .*V Annual Meeting of Neurotime PhD program*. Amsterdam. The Netherlands.

Loyola S (2016). Impact of excitatory and inhibitory inputs on inferior olive subthreshold oscillations (STOs) .I*V Annual Meeting of Neurotime PhD program*. Strasbourg. France.

Loyola S (2015). Dynamic Control of electrotonic coupling in the Inferior Olive. *III Annual Meeting of Neurotime PhD program*. Basel. Switzerland.

Loyola S (2014). Dynamic Control of electrotonic coupling in the Inferior Olive. *II Annual Meeting of Neurotime PhD program*. Amsterdam. The Netherlands.

Lara Marcelo, Loyola S, Mantellero C, Morales M, Pertusa M, Rojas P,.(2013).Role of Chloride Cotransporter NKCC1 in excitability of Dentate Gyrus in chronic Epilepsy in rats. *IX Annual Meeting of the Chilean Neurosience society*. Valparaiso. Chile.

Salas E, Loyola S, Guerreo S, Velasco C, Riveros A, Zeise M, Morales B; kogan M.(2012). Estudio del efecto de nanosesferas de oro sobre la Sobre la Memoria y el Aprendizaje: Un Acercamiento para Posibles Aplicaciones en la Enfermedad de Alzheimer. *II Latino American symposium of Nanomedicine*. San Luis. Argentina

Salas E, Loyola S, Guerreo S, Velasco C, Riveros A, Zeise M, Morales B; kogan M.(2012). Estudio del efecto de nanosesferas de oro sobre la plasiticdad sináptica para posibles aplicaciones en la enfermedad de alzeheimer. *II National congress of nanotechnology*. Valparaíso. Chile.

Loyola S, Zeise M, Arias-Cavieres A, Rozas C, Sanchez C, Maureira F, Ugarte G, Rojas P, Morales M.(2011).Acute and chronic effects of methylphenidate on the synaptic plasticity at hippocampus and prefrontal cortex. *VII Annual Meeting of the Chilean Neurosience society*. Santa Cruz. Chile.

Zeise M, Arias-Cavieres A, Rozas C, Loyola S, Sanchez C, Maureira F, Ugarte G, Rojas P, Morales M.(2011). Acute application and chronic application of methylphenidate influence long term potentiation in rat hippocampus slices in opposite ways. *VIII World Congress of Neuroscience*. Florence. Italy.

Zeise M, Arias-Cavieres A, Rozas C, Loyola S, Morales M.(2010). Effects of methylphenidate in the Morris water Maze task are not congruent with synaptic plasticity in hippocampus in young rats*. VI Annual Meeting of the Chilean Neuroscience society* .Valdivia. Chile.

Loyola S, Solano L, Rozas C, Arias-Cavieres A , Zeise M ,Morales B. (2010). The increase of long term potentiation induced by MDMA (“Ecstasy”) involves phosphorylation of the 845 serine residue in GLUR1 subunit in the AMPA receptor via PKA in the CA1 area of rat hippocampus. *VI Annual Meeting of the Chilean Neurosience society*.Valdivia. Chile.

Vallejo M, Ortega G, Loyola S, Rozas C, Cifuente D, Ardanaz C, Cabrera JL, Tonn C, Morales B, Agnese M. (2010). An Acetylated sauroine derivate generates Chem LTP.*IV International Symposium of Pos-graduation and Research (SINPOSPq)* .Ribeirao Preto, Brasil.

Morales B., Loyola S , Arias-Cavieres, A , Zeise M.(2010). The increase of long term potentiation induced by MDMA (“Ecstasy”) involves phosphorylation of the 845 serine residue in the AMPA receptor via PKA in the CA1 area of rat hippocampus. *7th Forum of european neuroscience (FENS)*. Amsterdam. The Netherlands.

Zeise M, Arías A , Espinoza S, Loyola S, Morales B (2009). Metilfenidato, distinto de MDMA, no influencia la adquisición de una tarea visuo-espacial en el laberinto de Morris en ratas. *IV congreso Chileno de Psicología del Consorcio de Universidades del Estado*. UFRO. Temuco. Chile

Morales B, Arias A., Rozas C., Reyes-Parada M., Loyola S., Acuña-Castillo, C., Madrid R., Zeise M. (2009). Chronic application of MDMA impairs visuo-spatial learning and memory retrieval in the Morris Water Maze and abolishes hippocampal LTP in rats. *Society for Neuroscience*. Chicago. USA.

Arias-Cavieres A., Rozas C., Reyes-Parada M., Loyola S., Pancetti F.,Acuña-Castillo C., Madrid R., Zeise M., Morales B.(2009). MDMA impairs visuo-spatial learning and memory in the Morris Water Maze and abolishes hippocampal LTP in rats without neurotoxic action. *V Annual Meeting of the Chilean Neurosience society.* Coquimbo. Chile.

Rozas C., Arias-Cavieres, Loyola S., Morales B (2009). 5-HT2 and D1 receptors participate in the modulatory effect of MDMA on synaptic plasticity. *International worshop "Motivated behavior, stress and addiction: from molecules to behavior*". Milenium Nucleus in stress and addiction, NEDA. Faculty of Biological Science, Catholic University of Chile.Santiago. Chile.

Acknowledgments

Agradecimientos

First, I would like to thank you Chris for giving me the chance to work in your lab. Your optimism, confidence and kindness towards my project and me were crucial to keep going and complete it. I wish you all the best in your life and your cerebellar adventure.

Tycho, I would like to thank you for all the scientific and personal support you have provided me along my PhD path. Thanks for all the nice conversations and invitations to your place where I could meet your beautiful family. I wish you all the best in your life and upcoming projects.

Huguito, Thank you so much for your fundamental contribution and enthusiasm for our project, which meant doing surgeries until very late in the evening and during weekends as well as discussing about experimental design and results. Our wonderful friendship led us to go to visit my home country, Chile, and those amazing memories will always be in my heart. I am sure you will do great in your new job at the VU. ¡¡¡Espero volver a verte en Chile, querido Huguito!!!.

Thanks to all the CCC group for the nice work environment as well as our fruitful scientific discussions. Nico, it was very nice to attend some concerts with you and thanks for showing me one of the best places in Amsterdam, the 5 € pizza place in Leidseplein. I always recommend it. Laura and Emilie, Thanks for your good vibes and nice moments you bring into the lab. I wish both all the best as well as I wish all the best for the rest of the CCC group: Cinthya, Rachel, Cathrin and Beerend.

To the 'Lunch times group', thank you very much for being like a second family for me during my stay in Amsterdam. Sreedeep, I will miss our long conversations at the black coach, thanks for always being supportive and giving me wise advice about different aspects of my life. Nemanja, thank you very much for being such a nice friend and for showing me very cool music and radio shows. Prem, I will always remember your enthusiasm for science and good vibes. Sehrazat, amiga, it has been a pleasure to meet you, you are a wonderful friend and I hope you can accomplish all your goals. Dani, thanks for always being there for me, you are an amazing person and friend. We have lived some many things together and I'm sure you will succeed on whatever goal you want to accomplish. I will miss you my dear friends.

I would also like to remember and thank other amazing friends whom I met here but some have left quite some time ago. Tomás, thanks for all the musical and nice moments together. Javier, thanks for all the dinners and joyful moments. Wilson, thanks for the music and deep conversations about life. I hope to see you guys soon.

Alessandro, Victor and Cristián, thanks for your friendship and nice moments we had playing together. I will miss you guys.

I would like to express my gratitude towards all the people working at the NIN and AMC that made possible my daily work, which encompasses different areas such as the workshop (Marteen, John and Stephan), Depot (Hanneke), animal facility (Rainier), cleaning personnel (Joyce, Elvis and Gabi), ICT department (Giuliano and Marteen) and AMC cantine (Helen, Abdel and Lina).

Ahora en español (Now in Spanish)

Me gustaría agradecer a mi familia, en especial a mis Padres, Nancy y Alberto, por siempre haberme dado mucho amor, cuidados y apoyo durante toda mi vida, los cual se extiende hasta el día de hoy. Sin ellos, no podría haber logrado todo lo que me he propuesto lograr. También me gustaría agradecer a mis hermanos Luis, Felipe, Nancy y Cristóbal por todo el amor y preocupación que he recibido de ellos. Este agradecimiento se extiende a sus respectivas familias donde incluyo a mis cuñadas Marcelina y Riko y a mis cuñados Daniel y Pepe, así como también a mis 5 sobrinas, Amparo, Ángela, Luna, Marina y Noelia; y a mis 2 sobrinos, Luis Alberto ('Beto') y Santiago. Además, me gustaría agradecer a personas que ya no están entre nosotros. Una de esas personas es mi querida Nani, quien fue como una segunda madre para mí. Querida Nani, no sé si puedes leer esto, pero si pudieses hacerlo me gustaría decirte que te extraño mucho y que siempre te siento junto a mí. Otra persona a quien me gustaría recordar y agradecer es a mi abuelita Zoila, quien siempre me entregó mucho amor y a quien también extraño mucho. Asimismo, me gustaría poder agradecer también a Valentina ('Vale') a quien ha sido mi amor y compañera durante este largo camino y viaje, Muchas gracias por todo tu amor, comprensión y ayuda durante todo este período, tal como se dice has estado en las buenas y en las malas. A pesar de haber estado alejados físicamente por mucho tiempo, hemos sido capaces de construir una muy linda relación. Eres una hermosa mujer a quien admiro mucho por su bondad, inteligencia y perseverancia. Tal como te he dicho algunas veces anteriormente, en esta relación que hemos mantenido en la distancia he podido experimentar de forma vívida la subjetividad del tiempo y disfrutar cada segundo que estamos juntos, así tal como lo decía Víctor Jara, 'La vida es eterna en cinco minutos'. Ahora, luego de un largo camino, finalmente ya podemos estar físicamente juntos y así poder construir una vida juntos.

También me gustaría agradecer a la familia de Vale, en especial a sus Padres, Luis y Patricia; Abuela, Irma, Hermano, Matías; hermana, Bárbara, cuñado, Juan y sobrino, Salvador, por todo el amor, cariño y preocupación que he recibido de ellos.

También me gustaría agradecer a mis amigos Chilenos en Amsterdam: Ricardo, Carolina y Gabriel. Muchas gracias por los buenos momentos y todos los partidos de FIFA y pizzas que hemos compartido.

Por último, me gustaría agradecer a mis amigos en Chile, quienes siempre han estado allí cuando tenemos la oportunidad de vernos y que siempre han estado allí de alguna u otra forma. Max, querido amigo, nos conocemos hace bastante tiempo y a pesar de la distancia física que vivimos durante mucho tiempo por nuestros estudios, y ahora por la pandemia, siempre hablamos y nos apoyamos en las distintas etapas que hemos vivido. Muchas gracias por estar siempre allí y por tu apoyo. Diego, muchas gracias por ser un gran amigo,ya que sé que siempre puedo contar contigo, ya nos veremos pronto para comer algo en la fuente Suiza. Nando, muchas gracias por tu apoyo y por ser un gran amigo, espero que pronto toquemos de nuevo en DelaCosta. Mr. Dani Liebner, muchas gracias también por tu apoyo y valiosa amistad. Espero pronto conocer a Laurita. Cristián (Moreno), muchas gracias compadre por toda la buena onda y el apoyo, mucho éxito en tu nueva etapa de postdoc. Milenco, muchas gracias por tu amistad, buena onda y por la buena música. Bélgica, Xime, Pauli y Marcelo muchas gracias por su gran amistad y buena onda.